The Dissertation Committee for Danielle Kristin Smith Certifies that this is the approved version of the following dissertation:

Synthesis and Characterization of Carbon Nanotubes, Gold Nanorods, Silica Coated Nanocrystals, and Binary Nanocrystal Superlattices

Committee:

Brian A. Korgel, Supervisor

Adela Ben-Yakar

George Georgiou

Miguel José Yacamán

Konstantin V. Sokolov

Synthesis and Characterization of Carbon Nanotubes, Gold Nanorods, Silica Coated Nanocrystals, and Binary Nanocrystal Superlattices

by

Danielle Kristin Smith, B.S.

Dissertation

Presented to the Faculty of the Graduate School of

The University of Texas at Austin

in Partial Fulfillment

of the Requirements

for the Degree of

Doctor of Philosophy

The University of Texas at Austin

May 2009

Dedication

For my mother

Acknowledgements

Though one can set their dreams and goals high, they are often not reached without the help, support, and love of others. I personally am indebted to many people, particularly my adviser, lab mates, friends, my boyfriend, and my family.

Dr. Brian Korgel has provided me with guidance, motivation, and a paycheck for the last five years, for which I will be forever grateful. His passion for science and prowess in the field of nanotechnology are never-ending. I am also grateful to him for encouraging me to be a role model for future female chemical engineers. I have learned much from him and enjoyed my time in his research group.

My fellow Korgelites have also helped me to finally make it to this moment. I especially want to thank those who graduated before me and taught me much around the lab including Tobias Hanrath, Cindy Stowell, Aaron Saunders, April Shricker, Ali Ghezelbash, Felice Shieh, Dayne Fanfair, and especially Doh C. Lee, who was my first and best mentor in this group, and my officemate Hsing-Yu Tuan for his endless optimism and friendship. My current lab mates continue to make working in the lab a pleasant experience and I am so glad to have found good friends and hearty scientific discussion with Reken Patel, Bonil Koo, Damon Smith, Mike Rasch, Matt Panthani, Vahid Akhavan, Vince Holmberg, Aaron Chockla, Justin Harris, Alex Knoop, Colin Hessel, and Jose-Luis Hueso Martos. I especially want to thank lab mates Brian

(Chadsworth) Goodfellow for all of his work on our BSL paper and Andy Heitsch, who strove for perfection on our Rubpy paper (no smurged data points). I also thank Andy for all the many minutes I spent in front of his chalkboard discussing some of the final subtleties of nanotechnology as well as for being such a good sport during all the endless teasing.

I also want to thank Dr. Paul Chan, my undergraduate advisor at the University of Missouri, who relentlessly encouraged me to go to graduate school and continues to still give great advice.

And most heartfelt and special thanks go out to my family, especially my mother, who encouraged me to pursue my goal of getting a Ph.D. at any cost. Their support was truly selfless and endless, and I have learned much from the examples that they have set for me. I also want to thank my boyfriend who has been there for me through all the días buenos y días malos and has picked me up so many times when I was down. Without the support and help of my loved ones and all of my blessings from God, I would have never been able to complete my Ph.D.

Synthesis and Characterization of Carbon Nanotubes, Gold Nanorods, Silica Coated Nanocrystals, and Binary Nanocrystal Superlattices

Publication No._____________

Danielle Kristin Smith, Ph.D.
The University of Texas at Austin, 2009

Supervisor: Brian A. Korgel

Nanomaterials such as carbon nanotubes, gold nanorods, magnetic nanocrystals, and binary nanocrystal superlattices have exciting potential applications. However, before these ideas can be applied, it is imperative to fully understand the materials synthesis.

Multiwall carbon nanotubes were synthesized in supercritical toluene using cobaltocene, nickelocene, ferrocene, or metal nanocrystals as catalysts. Toluene served as both the solvent and carbon source for nanotube growth. The reaction was optimized by introducing supplemental carbon sources; either hexane or ethanol increased the yield relative to pure toluene and catalytic amounts of water minimized carbon filament and amorphous carbon formation.

Gold nanorods were synthesized by the colloidal seed-mediated, surfactant-assisted approach using cetyltrimethylammonium bromide (CTAB) obtained from ten different suppliers. The gold nanorod yield depended strongly on the CTAB used: with the same recipe, three of the CTABs produced only spherical particles, whereas the other

CTABs produced nanorods with nearly 100% yield. Inductively coupled plasma mass spectrometry revealed a trace iodide impurity in the CTABs that did not yield nanorods. Further experiments introducing potassium iodide to the nanorod synthesis verified the detrimental effect of iodide on nanorod formation.

Multifunctional colloidal core-shell nanoparticles of magnetic nanocrystals or gold nanorods coated with a fluorescent dye (Tris(2,2′-bipyridyl)dichlororuthenium(II) hexahydrate) doped silica shells were also synthesized. The as-prepared magnetic nanocrystals were initially hydrophobic and silica coated using a microemulsion approach, while the gold nanorods were hydrophilic and silica coated using a Stöber process. These colloidal heterostructures have the potential to be used as dual-purpose tags, exhibiting a fluorescent signal that could be combined with either dark-field optical contrast or enhanced contrast in magnetic resonance imaging.

Binary superlattices (BSLs) of large iron oxide and small gold nanocrystals were assembled by slow evaporation of colloidal dispersions on tilted substrates. SEM and grazing incidence small angle X-ray scattering (GISAXS) confirmed the BSLs were simple hexagonal AB_2 superlattices with long range order. GISAXS also revealed that the superlattice was slightly contracted perpendicular to the substrate as a result of solvent drying during the deposition process. Additionally, in some BSLs nearly periodic superlattice dislocations consisting of inserted half-planes of gold nanocrystals were observed.

Table of Contents

List of Tables

List of Figures

Chapter 1: Introduction

The exciting field of nanotechnology encompasses materials that are metallic, magnetic, or semiconducting which have applications in microelectronics, photovoltaics, magnetics, or biology. The interesting properties that these nanostructures possess arise from their size, shape, or constituent material. Controlled, reproducible, and tunable synthesis is imperative for integration and application of nanomaterials to real world systems.

One fundamental challenge in this field is to control the nanostructure size and shape. Seeded growth has been used for the synthesis of semiconductor nanowires such as Si[1, 2] and Ge[3] and carbon nanotubes.[4, 5] By varying the reaction time and precursor concentrations, nanowire and nanotube lengths can be controlled. Additionally, by varying the diameter of the catalyst seed, carbon nanotubes have been produced with varying widths.[6]

Arrested precipitation is another approach that can yield size and shape control: capping ligands coat the surface of nanocrystals as they nucleate and grow, thus stabilizing their size and shape. The shape of semiconductor quantum dots can be tuned by varying the choice of capping ligand[7] or precursor injection rate[8].

Shape control can also be achieved through oriented attachment. In this mechanism, particles aggregate in a preferential crystallographic orientation and fuse into single crystal nanorods or nanowires.[9]

No matter what the approach, to efficiently design and engineer the properties of nanomaterials, their synthesis must be well understood. High quality materials produced in high yield are critical for future applications of nanomaterials. This dissertation focuses on engineering nanomaterials synthetic pathways to optimize yield and quality of the final product.

1.1 CARBON NANOTUBES

Though carbon nanotubes have been produced and observed under a variety of conditions prior to 1991, Sumio Iijima's reports on the syntheses of multiwall[10] and single wall nanotubes[11] using an arc discharge process brought these materials to the scientific forefront. Interest grew further when Richard Smalley's group showed that metal catalyzed single wall carbon nanotubes could be produced by a laser vaporization method, providing more controllable growth conditions than the arc discharge process.[12]

Multiwall nanotubes can be conceptualized as concentric layers of seamless cylindrical graphene sheets. Single walled carbon nanotubes possess only one graphene sheet and are thus only one atom thick. In both types of nanotubes, the covalent sp^2 bonds formed between the individual carbon atoms result in very high carbon nanotube tensile strength. The electrical properties of carbon nanotubes arise from the unique electronic structure of graphene. Single walled carbon nanotubes may be metallic or semiconducting depending on their chirality. Additionally, all nanotubes are very good thermal conductors.

These properties suggest that carbon nanotubes could potentially be useful in nanoelectro-mechanical systems or as structural/functional composites.[13-15] For example, carbon nanotubes have been suggested for use in field-effect transistors, integrated circuits, reinforced polymers and concrete, bullet proof vests, and stronger and lighter sports equipment. Additionally, carbon nanotubes have been suggested as drug delivery vessels by either tethering the drug to the nanotubes surface or placing it in the nanotubes core.[16]

Many synthetic approaches to carbon nanotubes currently exist, including arc discharge, laser ablation, and chemical vapor deposition. Though some of these techniques can produce nanotubes in sizeable quantities their high manufacturing costs still prohibits widespread carbon nanotube commercialization.

1.1.1 Supercritical Fluids

Solution-phase synthetic routes have the potential for continuous processing with high precursor concentrations, making them perhaps more scalable than vapor-phase routes. In the supercritical fluid, the carbon reactant and dispersed metal catalyst concentrations can be orders of magnitude higher than those possible in vapor-phase processes.

A supercritical fluid is a material that is at a temperature and pressure above its critical point. Supercritical fluids possess the properties of both liquids and gases; they can diffuse through solids as a gas does and they can dissolve materials like a liquid.[17] At reaction conditions near the critical point, small changes in pressure or temperature result in large changes in the supercritical fluid's density. To date, supercritical fluids have been used for applications such as extraction, drying, and for biodiesel production.[18] The high-temperature availability, high precursor concentration, and possibility for continuous processing make supercritical fluids attractive media for nanomaterials synthesis. Work by Korgel et al. has demonstrated the supercritical fluids can be used for the synthesis of silicon[1] and germanium nanowires[3] as well as carbon nanotubes.[19] For the synthesis of carbon nanotubes, supercritical toluene is used. A phase diagram of toluene appears in Appendix A.

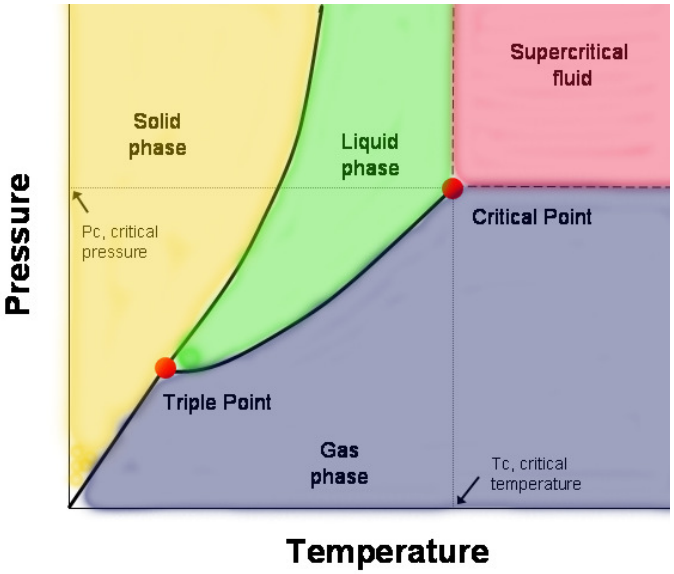

Figure 1.1. Phase diagram or pressure-temperature plot. A supercritical fluid is a phase of material that is heated and pressurized above its critical point.

1.1.2. Carbon Nanotube Growth Mechanism

Supercritical toluene serves as both the reaction medium and as a carbon source for nanotube growth. Catalytic hydrocarbon decomposition occurs at the surface of the metal nanoparticles, which are introduced as preformed nanocrystals of iron or cobalt, or formed *in situ* from metallocenes such as ferrocene, cobaltocene, or nickelocene. Carbidization of the catalyst saturates the particle surface with carbon and gives rise to surface-directed graphitization and nanotube formation. In the “folded growth mode”[19, 20] which we observed, curved graphite layers form on the surface and wrap the seed particle, ultimately extruding to form a carbon nanotube.

1.2 GOLD NANORODS

1.2.1 Gold Nanorod Optical Properties

Gold is an interesting material because of its optical properties, which arise from its unique electron configuration.[21] Collective oscillations of the conduction electrons in response to an optical excitation are known as surface plasmons.[22] The presence of these surface plasmons causes light to be reflected from the surface of gold, giving rise to the shine and luster of this material. Because gold nanorods have an elongated shape, they absorb light at two different wavelengths, one in the visible regime and the other at near-infrared wavelengths, each corresponding to one dimension of the nanorod. Figure 1.2 reveals a typical absorbance spectra of gold nanorods, the two peaks in the spectra correspond to plasmon resonances: the shorter wavelength peak at 520 nm to plasmon oscillations in the shorter transverse direction, and the longer wavelength peak (typically between 700 nm and 1300 nm) to longitudinal oscillations. The position of the second plasmon peak can be varied by tuning the nanorod aspect ratio.[23-26] Using the Drude free electron model[27, 28] and theory derived by Mie[22] and Gans,[29] the position of the plasmon peaks as a function of aspect ratio can be predicted (see Appendix B).

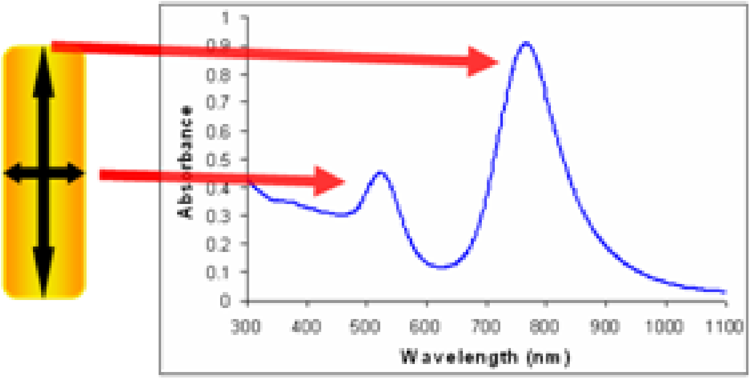

Figure 1.2. Typical absorbance spectra of gold nanorods, with the schematic showing how each peak corresponds to a different nanorod dimension.

1.2.2. Gold Nanorod Applications

Hemoglobin and water, the major absorbers in biological systems of visible and infrared light, respectively, have their lowest absorption coefficient in the NIR region around 650–900 nm.[30] Therefore, when the second plasmon peak is tuned in this range, gold nanorods can serve as contrast agents for biological imaging. The use of nanocrystals as biological contrast agents is advantageous because these materials are the same order of magnitude as biological macromolecules,[31, 32] and they have surfaces that can be functionalized with nucleic acids[33] or antibodies[34] to serve as cellular targeting molecules, suggesting that disease diagnostics and therapy are possible on a *cellular* level. Already gold nanorods have been demonstrated for use as bright contrast agents for two-photon luminescence (TPL) diagnostic imaging[35] (see Figure 1.3) and photothermal therapy of cancer cells.[36]

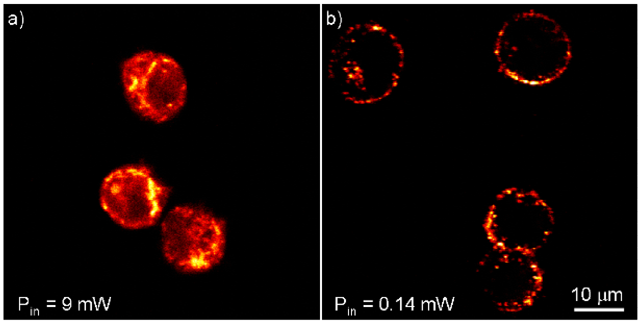

Figure 1.3. Two-photon images of cancer cells placed on a coverslip from a cell suspension. (a) TPAF (autofluorescence) images of unlabeled cells. (b) TPL images of nanorod labeled cells. Imaging required 9 mW of excitation power in unlabeled cells to get same signal level obtained with only 140 μW for nanorod labeled cells, indicating that TPL from nanorods is more than 4,000 times brighter than TPAF from autofluorescence. Reproduced with permission from Durr, N. J.; Larson, T.; Smith, D. K.; Korgel, B. A.; Sokolov, K.; Ben-Yakar, A., *Nano Lett.* **2007,** *7*, (4), 941-945. Copyright 2007 American Chemical Society.

1.3 SILICA COATING OF MAGNETIC NANOCRYSTALS AND GOLD NANORODS

As mentioned, gold nanorods can be used as biological contrast agents for two-photon luminescence imaging. Magnetic nanocrystals such as iron oxide and iron platinum can also serve as biological contrast agents using magnetic resonance imaging (MRI). Iron oxide and iron platinum are superparamagnetic, meaning their spins align with an externally applied magnetic field. In the absence of a field, they will not retain any magnetization because thermal motion causes the spins to randomly orient. Superparamagnetic materials enhance contrast in MRI by changing the relaxation rate of the protons in the surrounding water.[37] However, highly crystalline magnetic nanocrystals are synthesized in high-temperature organic solvents[38, 39] and capped with organic molecules such as oleic acid, which renders the particles hydrophobic. Therefore, before they can be introduced to the body they must be made hydrophilic. One strategy for this is ligand exchange, such as with 2,3-dimercaptosuccinic acid.[40] Alternatively, the as-synthesized nanocrystals can be coated with a silica shell (see Figure 1.4).

Silica coating of nanocrystals such as gold,[41] iron platinum,[42] and cadmium selenide[43] has been demonstrated. In addition to the hydrophilicity, silica coating is advantageous because silica is biologically inert and provides a surface that can easily be functionalized with antibodies that could serve as biological recognition agents.[44]

These benefits also apply to silica coating gold nanorods. Though as-synthesized gold nanorods are hydrophilic, they are capped with a cetyltrimethylammonium bromide bilayer which has been shown to be cytotoxic to cells.[45] Silica coating thus shields the cells from the potentially dangerous capping ligands.

Fluorescent dyes have been embedded in silica nanocrystals to create a new class of hydrophilic biological imaging agents.[46, 47] By embedding a fluorescent dye in the silica, there is minimal interaction of the dye with the body enhancing the photostability and reducing the photobleaching of the dye. We have adapted this chemistry to produce embedded fluorescent dyes in the silica coating of our nanocrystals.

The presence of the dye embedded in the silica shell introduces a second imaging modality. Thus, these fluorescent dye-doped silica coated nanocrystals can be thought of as dual-mode imaging agents that could potentially be used to map cellular components and track them in real time, as traceable drug delivery vehicles, or as therapeutic agents. The advantage of having two imaging modalities in one heterostructure allows for characterizing cellular systems at different length and time scales, and a second verification of the cellular targeting, diagnostics, or therapy performed with these materials.

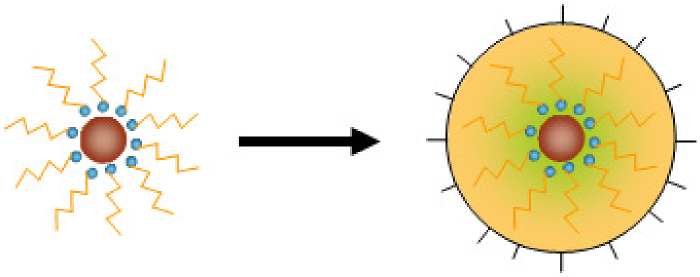

Figure 1.4. Silica coating of magnetic nanocrystals. The silica surface can be further functionalized.

1.4 BINARY NANOCRYSTAL SUPERLATTICES

Binary micrometer sized hard spheres will self-assemble into superlattices based on spaced filling principles and entropically driven processes; the resulting superlattice has a higher free volume entropy than the free-floating spheres.[48] Hard sphere binary superlattices have been observed for radii size ratios (r/R where $r<R$) varies between 0.2

and 0.624, resulting in superlattices with ordered structures of either AB, AB_2, or AB_{13} geometry and packing fractions as high as 0.782 (AB_{13}).[49, 50]

Colloidal nanocrystals have also been observed to self-assemble into binary superlattices, suggesting a promising new route to "bottom-up" nanomaterials engineering. By combining two different types of nanocrystals in a binary superlattice, *metamaterials*[51] may be made with new properties that result from their nanoscale organization and interplay of their constituent properties. For example, films of semiconductor nanocrystals could be made for higher performance photovoltaics, or mixtures of magnetic nanocrystals could be used for higher energy density magnets.[52]

The primary driving force for colloidal nanocrystal superlattice formation is the same as that of hard spheres. Additionally, the "soft" shell of capping ligands that nanocrystals possess may play a secondary role in the superlattice formation. Interactions such as van der Waals forces, ligand-ligand interactions, capillary forces, electrostatic interactions, and kinetic factors have also been suggested to play a role. Therefore, careful characterization is needed to fully understand the driving forces behind binary nanocrystal superlattice formation.

1.5 DISSERTATION OVERVIEW

The optimization of the synthesis of multiwall carbon nanotubes in supercritical toluene is discussed in Chapter 2. The introduction of supplemental carbon sources such as hexane or ethanol increased the yield of nanotubes relative to that of pure toluene alone. Also, catalytic amounts of water minimized carbon filament and amorphous carbon formation, thus improving the product quality.

Factors affecting the synthesis of gold nanorods, especially iodide impurities in CTAB, are discussed in Chapter 3. When trace iodide impurities were present in CTAB, nanorod formation did not occur and only spherical gold nanocrystals resulted, suggesting that the presence of iodide can disrupt nanorod formation and growth.

The silica coating of gold nanorods and magnetic nanocrystals such as iron oxide and iron platinum is discussed in Chapter 4. Embedding fluorescent dyes in the silica shells rendered these heterostructured materials as dual mode imaging agents; the fluorescent signal of the silica shell could be combined with either dark-field optical contrast or two-photon luminescence imaging for the gold nanorods or enhanced contrast in magnetic resonance imaging for the magnetic nanocrystals. The optical and magnetic properties of these heterostructures were studied.

The synthesis of simple hexagonal binary nanocrystal superlattices made from 11.5 nm iron oxide and 6.1 nm gold nanocrystals is discussed in Chapter 5. Long range order of the superlattices was confirmed by TEM, SEM, grazing incidence small angle X-ray scattering (GISAXS). Uniaxial contraction of the superlattice perpendicular to the substrate as a result of residual solvent evaporation was discovered with GISAXS. Au nanocrystal half plane defects were also discovered and attributed to strain induced by the curvature of a drying droplet of colloidal nanocrystal solution at the air-liquid-substrate interface.

1.6 REFERENCES

1. Holmes, J. D.; Johnston, K. P.; Doty, R. C.; Korgel, B. A., *Science* **2000,** *287*, (5457), 1471-1473.

2. Hu, J. T.; Odom, T. W.; Lieber, C. M., *Acc. Chem. Res.* **1999,** *32*, (5), 435-445.

3. Hanrath, T.; Korgel, B. A., *J. Amer. Chem. Soc.* **2002,** *124*, (7), 1424-1429.

4. Dai, H.; Rinzler, A. G.; Nikolaev, P.; Thess, A.; Colbert, D. T.; Smalley, R. E., *Chem. Phys. Lett.* **1996,** *260*, (3-4), 471-475.

5. Dresselhaus, M. S.; Dresselhaus, G.; Avouris, P., *Carbon Nanotubes: Synthesis, Structure, Properties, and Applications*. Springer: New York, 2002.

6. Cheung, C. L.; Kurtz, A.; Park, H.; Lieber, C. M., *J. Phys. Chem. B.* **2002,** *106*, (10), 2429-2433.

7. Peng, X. G.; Manna, L.; Yang, W. D.; Wickham, J.; Scher, E.; Kadavanich, A.; Alivisatos, A. P., *Nature* **2000,** *404*, (6773), 59-61.

8. Shieh, F.; Saunders, A. E.; Korgel, B. A., *J. Phys. Chem. B* **2005,** *109*, (18), 8538-8542.

9. Cho, K. S.; Talapin, D. V.; Gaschler, W.; Murray, C. B., *J. Am. Chem. Soc.* **2005,** *127*, (19), 7140-7147.

10. Iijima, S., *Nature* **1991,** *354*, (6348), 56-58.

11. Iijima, S.; Ichihashi, T., *Nature* **1993,** *363*, (6430), 603-605.

12. Guo, T.; Nikolaev, P.; Thess, A.; Colbert, D. T.; Smalley, R. E., *Chem. Phys. Lett.* **1995,** *243*, (1-2), 49-54.

13. Andrews, R.; Jacques, D.; Qian, D. L.; Rantell, T., *Acc. Chem. Res.* **2002,** *35*, (12), 1008-1017.

14. Ouyang, M.; Huang, J. L.; Lieber, C. M., *Acc. Chem. Res.* **2002,** *35*, (12), 1018-1025.

15. Avouris, P., *Acc. Chem. Res.* **2002,** *35*, (12), 1026-1034.

16. Dai, H. J., *Acc. Chem. Res.* **2002,** *35*, (12), 1035-1044.

17. Kotz, J. C.; Treichel, P., *Chemistry and Chemical Reactivity*. 3rd ed.; Saunders College Publishing: Fort Worth, 1996; p 619.

18. Bunyakiat, K.; Makmee, S.; Sawangkeaw, R.; Ngamprasertsith, S., *Energy Fuels* **2006,** *20*, (2), 812-817.

19. Lee, D. C.; Mikulec, F. V.; Korgel, B. A., *J. Am. Chem. Soc.* **2004,** *126*, 4951-4957.

20. Louchev, O. A.; Hester, J. R., *J. Appl. Phys.* **2003,** *94*, (3), 2002-2010.

21. Schaaff, T. G.; Shafigullin, M. N.; Khoury, J. T.; Vezmar, I.; Whetten, R. L.; Cullen, W. G.; First, P. N.; Gutierrez Wing, C.; Ascensio, J.; Jose Yacaman, M. J., *J. Phys. Chem. B* **1997,** *101*, (40), 7885-7891.

22. Mie, G., *Ann. Phys.* **1908,** *25*, 377-455.

23. Burda, C.; Chen, X.; Narayanan, R.; El-Sayed, M. A., *Chem. Rev.* **2005,** *105*, (4), 1025-1102.

24. Link, S.; El-Sayed, M. A., *Annu. Rev. Phys. Chem.* **2003,** *54*, (1), 331.

25. Schwartzberg, A. M.; Zhang, J. Z., *J. Phys. Chem. C* **2008,** *112*, (28), 10323-10337.

26. Xia, Y. N.; Halas, N. J., *MRS Bull.* **2005,** *30*, (5), 338-344.

27. Alvarez, M. M.; Khoury, J. T.; Schaaff, T. G.; Shafigullin, M. N.; Vezmar, I.; Whetten, R. L., *J. Phys. Chem. B* **1997,** *101*, (19), 3706-3712.

28. Ziman, J. M., *Theory of Solids*. University Press: Cambridge, 1979; p 278.

29. Gans, R., *Ann. Phys.* **1915,** *47*, 270-84.

30. Weissleder, R., *Nat. Biotechnol.* **2001,** *19*, (4), 316-317.

31. Duguet, E.; Vasseur, S.; Mornet, S.; Devoisselle, J. M., *Nanomed.* **2006,** *1*, (2), 157-168.

32. Jaiswal, J. K.; Goldman, E. R.; Mattoussi, H.; Simon, S. M., *Nat. Methods* **2004,** *1*, (1), 73-78.

33. Alivisatos, P., *Nat. Biotechnol.* **2004,** *22*, (1), 47-52.

34. Xing, Y.; Chaudry, Q.; Shen, C.; Kong, K. Y.; Zhau, H. E.; Wchung, L.; Petros, J. A.; O'Regan, R. M.; Yezhelyev, M. V.; Simons, J. W.; Wang, M. D.; Nie, S., *Nat. Protocols* **2007,** *2*, (5), 1152-1165.

35. Durr, N. J.; Larson, T.; Smith, D. K.; Korgel, B. A.; Sokolov, K.; Ben-Yakar, A., *Nano Lett.* **2007,** *7*, (4), 941-945.

36. Huang, X. H.; El-Sayed, I. H.; Qian, W.; El-Sayed, M. A., *J. Am. Chem. Soc.* **2006,** *128*, (6), 2115-2120.

37. Kuperman, V., *MRI: Physical Principles and Applications*. Academic Press: Chicago, Illinois, 2000.

38. Chen, M.; Liu, J. P.; Sun, S. H., *J. Am. Chem. Soc.* **2004,** *126*, (27), 8394-8395.

39. Hyeon, T.; Lee, S. S.; Park, J.; Chung, Y.; Bin Na, H., *J. Am. Chem. Soc.* **2001,** *123*, (51), 12798-12801.

40. Huh, Y. M.; Jun, Y. W.; Song, H. T.; Kim, S.; Choi, J. S.; Lee, J. H.; Yoon, S.; Kim, K. S.; Shin, J. S.; Suh, J. S.; Cheon, J., *J. Am. Chem. Soc.* **2005,** *127*, (35), 12387-12391.

41. Liz-Marzan, L. M.; Giersig, M.; Mulvaney, P., *Langmuir* **1996,** *12*, (18), 4329-4335.

42. Lee, D. C.; Mikulec, F. V.; Pelaez, J. M.; Koo, B.; Korgel, B. A., *J. Phys. Chem. B* **2006,** *110*, (23), 11160-11166.

43. Selvan, S. T.; Patra, P. K.; Ang, C. Y.; Ying, J. Y., *Angew. Chem.* **2007,** *46*, (14), 2448-2452.

44. Arruebo, M.; Fernandez-Pacheco, R.; Velasco, B.; Marquina, C.; Arbiol, J.; Irusta, S.; Ibarra, M. R.; Santamaria, J., *Adv. Funct. Mater.* **2007,** *17*, (9), 1473-1479.

45. Mirska, D.; Schirmer, K.; Funari, S. S.; Langer, A.; Dobner, B.; Brezesinski, G., *Colloids Surf., B* **2005,** *40*, (1), 51-59.

46. Ow, H.; Larson, D. R.; Srivastava, M.; Baird, B. A.; Webb, W. W.; Wiesner, U., *Nano Lett.* **2005,** *5*, (1), 113-117.

47. Zhao, X. J.; Bagwe, R. P.; Tan, W. H., *Adv. Mater.* **2004,** *16*, (2), 173-176.

48. Schofield, A. B.; Pusey, P. N.; Radcliffe, P., *Phys. Rev. E* **2005,** *72*, (3).

49. Cottin, X.; Monson, P. A., *J. Chem. Phys.* **1995,** *102*, (8), 3354-3360.

50. Murray, M. J.; Sanders, J. V., *Philos. Mag.* **1980,** *42*, (6), 721-40.

51. Redl, F. X.; Cho, K. S.; Murray, C. B.; O'Brien, S., *Nature* **2003,** *423*, (6943), 968-971.

52. Zeng, H.; Li, J.; Liu, J. P.; Wang, Z. L.; Sun, S. H., *Nature* **2002,** *420*, (6914), 395-398.

Chapter 2: Multiwall Carbon Nanotube Synthesis in Supercritical Fluids

Reproduced in part with permission from: Smith, D.K.; Lee, D.C.; Korgel, B.A. "High Yield Multiwall Carbon Nanotube Synthesis in Supercritical Fluids." *Chemistry of Materials* **2006,** *18(14)*, 3356-3364. Copyright 2006 American Chemical Society.

2.1 INTRODUCTION

Carbon nanotubes are potentially useful in nanoelectro-mechanical systems (NEMS) and structural/functional composites[1]; they exhibit high mechanical strength and modulus[2], high electrical conductivity[3], and high thermal conductivity.[4] Many synthetic approaches to carbon nanotubes exist, including arc discharge, laser ablation and chemical vapor deposition (CVD) and some of these techniques can produce nanotubes in sizeable quantities; yet their high manufacturing costs still prohibit widespread commercialization, particularly in the case of single wall carbon nanotubes (SWNTs).[5]

Solution-phase synthetic routes have the potential for continuous processing with high precursor concentrations, making them perhaps more scalable than vapor-phase routes. Carbon nanotube synthesis, however, typically requires temperatures much higher than the boiling point of conventional solvents, which makes solution routes difficult to conceive. One approach for reaching high solution temperatures is to pressurize the solvent. In water for example, multiwall carbon nanotubes (MWNTs) have been made under hydrothermal conditions at 700 to 800 ºC from reactants such as amorphous carbon, polyethylene, ethylene glycol, and polyethylene glycol either in the presence of a catalyst or without one.[6-10] There have been efforts to decrease the reaction temperature needed to generate nanotubes and recently a low temperature hydrothermal MWNT synthesis was reported at 160 ºC.[10] MWNTs have also been produced by solvothermal routes (i.e., pressurized organic solvents), for example by catalyzed reduction of ethanol (both the solvent and the carbon source) using metal oxides at 550 ºC,[11] hexachlorobenzene using nickel chloride in cyclohexane at 230 ºC,[12] hexachlorobenzene using a Co/Ni catalyst in benzene at 350 ºC,[13] tetrachloroethylene using metallic potassium in benzene at 200 ºC,[14] and the thermal decomposition of ethoxylated alcohol polyoxyethylene at 310 ºC using hexane as a solvent without the presence of a catalyst.[15] A benzene thermal reduction catalysis route at 200 ºC using tetrachloroethylene with a metallic potassium catalyst[14] and the magnesium reduction of ethanol (both the solvent and the carbon source) at 600 ºC have also been reported.[16]

In our laboratory, we recently demonstrated ferrocene-catalyzed MWNT synthesis in supercritical toluene at ~625 ºC and 12.4 MPa.[17, 18] Toluene serves as both a solvent and a carbon source for nanotube growth. Toluene is chemically stable up to about 650 ºC, but metallocenes such as ferrocene catalyze decomposition to carbon and promote nanotube formation at slightly lower temperatures. Therefore, carbon formation occurs only at the catalyst. In the supercritical fluid, the carbon reactant and dispersed metal catalyst concentrations can be orders of magnitude higher than those possible in vapor-phase processes. In our previous work, the yield of MWNTs obtained from supercritical toluene had a low conversion of toluene to carbonaceous product (less than 1%) and low purity, only 2% of the carbon product was nanotubes.[18]

Here, we show that MWNTs can be synthesized with relatively high yield—up to 65% conversion of toluene to MWNTs—in supercritical toluene by using cobaltocene as a catalyst with the addition of ethanol (30 vol%) and catalytic amounts of water (0.75 vol%). Nickelocene, ferrocene, cobaltocene, Co and Fe nanocrystals all work as catalysts, but cobaltocene gives the highest yields and purity, followed by nickelocene. Relative to these catalysts, ferrocene is actually not very effective. Water was found to be a critical additive, preventing to a large extent amorphous carbon and carbon filament formation. The addition of ethanol increased the yield by almost an order of magnitude relative to pure toluene.

2.2 EXPERIMENTAL DETAILS

2.2.1 Starting materials

Hexane, anhydrous toluene, ferrocene (98%) and cobaltocene were used as received from Aldrich Chemical Co. (Milwaukee, WI). Water was doubly-distilled and deionized (DI-H_2O). Ethanol was purchased from Fisher Scientific (Pittsburgh, PA) and anhydrous nickelocene (97%) was purchased from Fluka (Milwaukee, WI). Anhydrous toluene, ferrocene, cobaltocene, and nickelocene were stored under nitrogen prior to use. Fe nanocrystals were synthesized by thermal decomposition of iron pentacarbonyl ($Fe(CO)_5$) (Aldrich) in octyl ether (Fluka) and oleic acid (Fluka) at 100 °C.[19] Co nanocrystals were synthesized by the decomposition of dicobalt octacarbonyl (Aldrich, 90-95% Co, stabilized with hexane) in the presence of anhydrous o-dichlorobenzene (Aldrich, 99%), oleic acid (Aldrich, 99%), and trioctylphosphine oxide (Strem Chemicals, 99%) at 182 °C.[20]

2.2.2 MWNT synthesis

MWNTs were synthesized using a continuous flow-through process similar to the one we described in Ref. 21. A high-pressure 10 ml stainless steel vessel (High-Pressure Equipment Company, Erie, PA) is connected to 1/8” O.D. and 0.060” size I.D. stainless steel high pressure tubing (High Pressure Equipment Company, HiP) via stainless steel reducers (HiP) and stainless steel high-pressure valves as shown in Figure 2.1. The inlet is connected to a 6-way valve (Valco) with a 10 ml injection loop. The outlet is connected to a micrometering valve (HiP). The reactor is pressurized using a high-pressure liquid chromatography (HPLC) pump (Alcott) connected to a piston filled with anhydrous toluene. The piston is pressurized using water to avoid having to run solvent through the HPLC pump. The reactor pressure is measured with a digital pressure gauge (Sensotech) and the temperature of the brass heating block is monitored with a type K thermocouple and temperature controller (Omega). A silicon wafer cut to 1 cm x 5 cm was placed inside the reactor to facilitate nanotube collection.

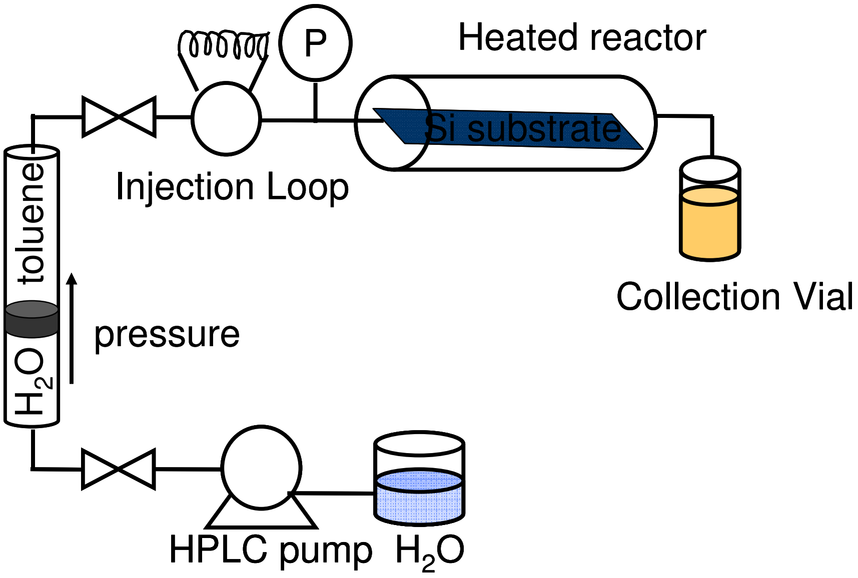

Figure 2.1. Schematic of the continuous flow through supercritical fluid reactor system.

The reactor was loaded with toluene and preheated to the reaction temperature (between 600 and 645 °C) and pressurized to 1200 psig (8.3 MPa) with anhydrous toluene. (Extreme caution must be exercised in all reactions close to 650 °C, as these conditions are close to the equipment limitations of the reactor connections.) Catalyst was dissolved in anhydrous toluene, and the supplemental carbon source and DI-H_2O (if present) were added and vigorously mixed. This reactant solution was then immediately injected from a 10 ml injection loop at a rate of 1 ml/min. As the reaction proceeded, product was collected in a vial at the outlet of the reactor. Reactions were always performed in a fume hood and the collection vial was sealed, yet vented to prevent pressure buildup upon cooling. The reaction was carried out for 10 minutes before removing the reactor from the heating block and cooling to room temperature. The reactor was then opened under ambient conditions, the deposition substrate was removed and the remaining loose product of black soot, was collected by rinsing with chloroform.

2.2.3 Purification

The nanotubes were treated with nitric acid and hydrogen peroxide to remove residual soot—purification that enabled high resolution imaging of the nanotubes. Approximately 3 mg of product was refluxed at 120 °C in 10 ml of 7 M nitric acid (Aldrich) for 3 hours. The solution was cooled to room temperature and centrifuged at 8000 rpm for 10 minutes. The supernatant was discarded and the precipitate was redispersed in DI-H_2O with brief sonication and centrifuged again. This precipitation/centrifugation step was repeated again to ensure that residual acid, amorphous carbon, and catalyst particles were removed. The nanotubes were then dispersed in a 9% hydrogen peroxide (H_2O_2) solution and refluxed at 80 °C for 6 hours. The solution was cooled to room temperature and centrifuged at 8000 rpm for 10 minutes. The supernatant was discarded and the precipitate was redispersed in ethanol and centrifuged again. This precipitation/centrifugation step was repeated again. The nanotubes were then ultrasonicated for 2 hours using a Cole Parmer 8891(Vernon Hills, IL) sonication bath and 10 minutes using a Branson Sonifer 250 (Danbury, CT) sonication horn. The horn was set to a duty cycle of 10% with an output control of 2.

2.2.4 Characterization

The reaction products were characterized by thermogravimetric analysis (TGA), high-resolution scanning electron microscopy (HRSEM), transmission electron microscopy (TEM), and energy dispersive X-ray spectroscopy (EDS). For HRSEM, the product was imaged on the silicon substrate removed directly from the reactor and no additional treatment was performed to the substrate or product prior to imaging on a LEO 1530 HRSEM at 3 kV with working distance between 7 to 12 mm using an in-lens detector. For TEM imaging, 4 µl of the sonicated nanotube dispersion was dropped onto a lacey carbon-coated TEM grid (Electron Microscopy Sciences). HRTEM imaging was performed on a JEOL 2010F TEM operating at a voltage of 200kV and EDS data were obtained on an attached Oxford INCA ED spectrometer. The images were acquired digitally by a GATAN digital photography system.

TGA was performed on 10 mg of unpurified cobaltocene-catalyzed MWNTs (synthesized in supercritical toluene at 640 °C and 8.3 MPa with 8.2 mM cobaltocene, 3.7 mM ethanol, and 0.2 mM DI-H_2O) and 10 mg of an amorphous carbon sample obtained from a failed nanotube reaction placed in an open-top alumina sample pan in a Perkin Elmer TGA 7. The samples were heated in air to 300 °C at a heating rate of 20 °C/min and allowed to equilibrate for one minute before being heated from 300 °C to 900 °C at 1 °C/min. Scan rates higher than 1 °C/min gave slightly elevated decomposition temperatures, as also noted previously by McKee and Vecchio.[22]

2.3 RESULTS AND DISCUSSION

2.3.1 Metallocene-catalyzed MWNT growth in supercritical toluene

Figure 2.2 shows an SEM image of multiwall carbon nanotubes (MWNTs) synthesized in supercritical toluene at 640 °C using cobaltocene as a catalyst. The nanotubes were synthesized with a catalytic amount of water (0.75 vol%) and 30 vol% ethanol. The carbon product consists of some amorphous carbon, but primarily MWNTs as shown in the TEM images in Figures 2.2b and 2.2c. Figure 2.3 shows SEM images of MWNTs synthesized in supercritical toluene at 640 °C using ferrocene, cobaltocene and nickelocene as catalysts in reactions carried out with water and ethanol (or hexane, with ferrocene). All three metallocenes catalyze MWNT formation, with toluene serving as both a solvent for the reaction and the primary carbon source for MWNT formation. In the cobaltocene-catalyzed reactions, approximately 4% of the toluene fed into the reactor was converted to carbonaceous product, and approximately 70% of this product was MWNTs, as determined from SEM. TGA also confirmed that the MWNT product was composed primarily of MWNTs: Figure 2.4 shows the mass loss profiles and oxidation rates of a MWNT sample compared to an amorphous carbon sample. Amorphous carbon burns off at ~450 °C, which is much lower than the MWNT decomposition temperature of ~630 °C. Very little decomposition occurs by TGA at temperatures below 500 °C, indicating that the MWNT sample is relatively pure. Further indicating a relatively high purity, the MWNT decomposition temperature is slightly higher than what has previously been reported for MWNTs synthesized by CVD.[22]

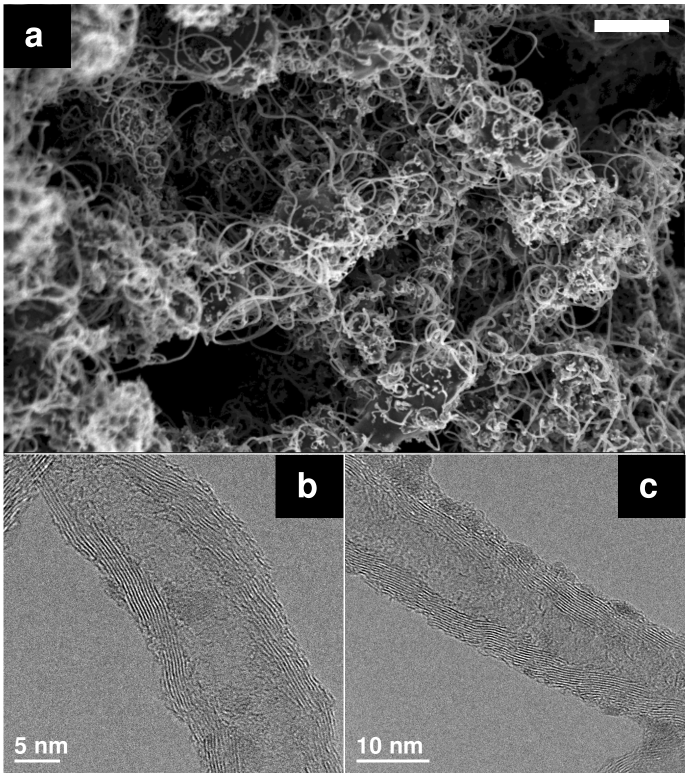

Figure 2.2. Multiwall carbon nanotubes synthesized in supercritical toluene. (a) SEM image of product collected on the deposition substrate in the reactor without further purification. (b, c) TEM images showing the multiwall nanotube structure of the product.

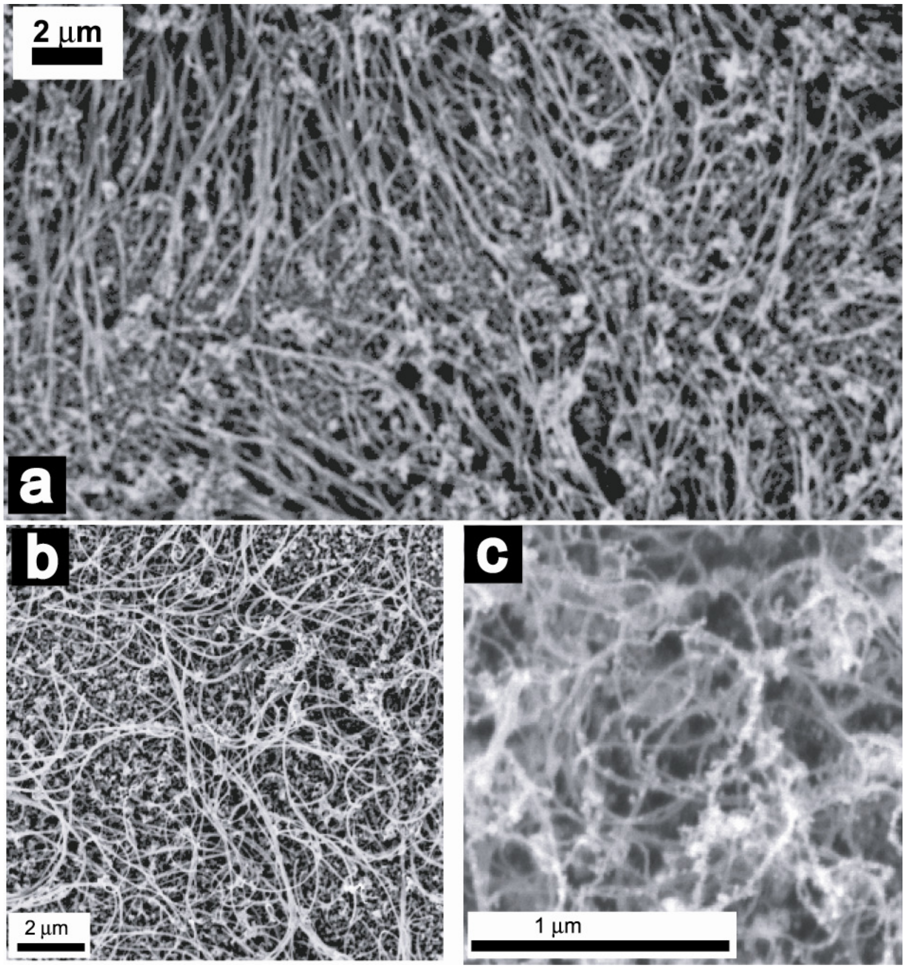

Figure 2.3. HRSEM images of MWNTs synthesized in supercritical toluene at 640 °C and 8.3 MPa with (a) 26 mM ferrocene, 1.6 mM hexane, and 0.2 mM DI-H_2O; (b) 8.2 mM cobaltocene, 3.7 mM ethanol, and 0.2 mM DI-H_2O; and (c) 8.2 mM nickelocene, 3.7 mM ethanol, and 0.2 mM DI-H_2O. The reaction product was imaged on the collection substrate taken from the reactor without further purification.

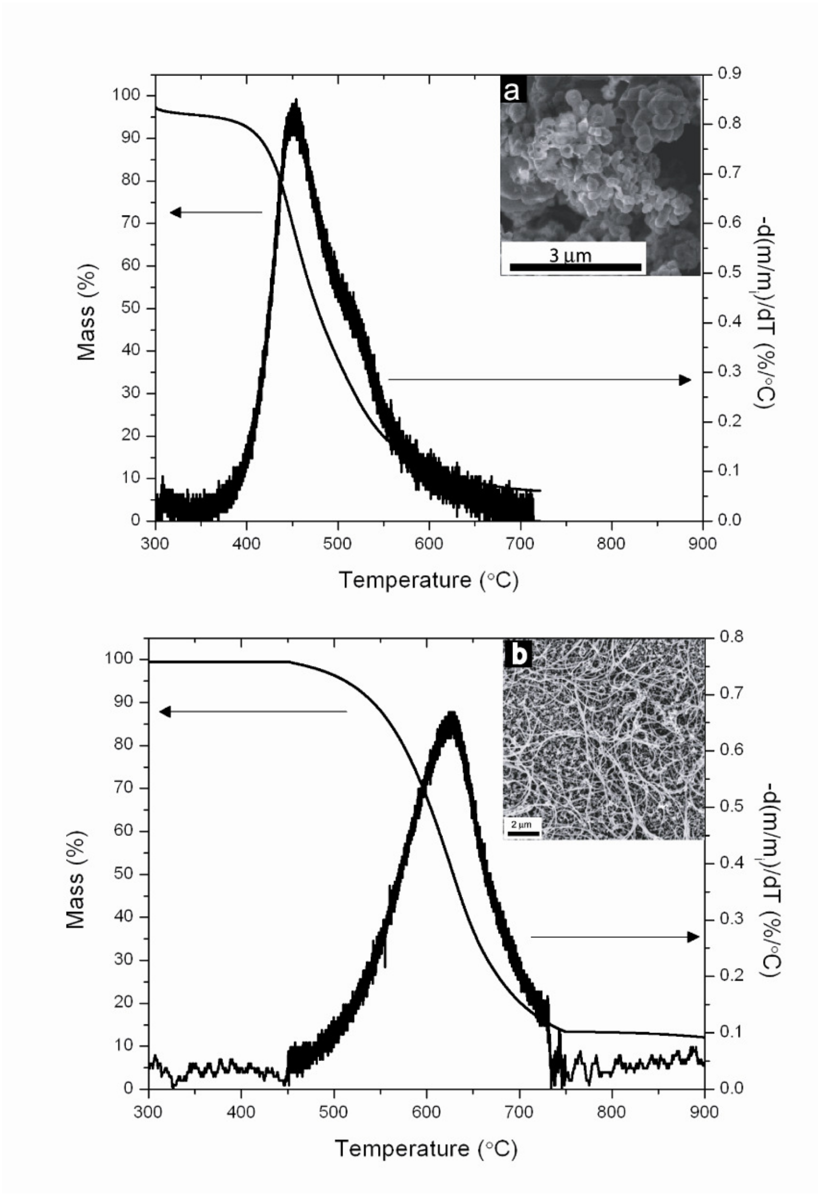

Figure 2.4. TGA of (a) amorphous carbon and (b) MWNTs produced from supercritical toluene reactions. (Insets) SEM images of the analyzed products. The samples were scanned at 1 °C/min. The quantity m/m_i is the mass fraction of the sample remaining. The peak in $-d(m/m_i)/dT$ versus T corresponds approximately to the decomposition temperature of the sample. The absence of significant thermal decomposition below ~500 °C in (b) indicates that the sample is primarily MWNTs.

The nanotube yield was significantly higher for cobaltocene-catalyzed reactions than the ferrocene-catalyzed reactions, which converted ~2% of the toluene into carbon, of which only about 35% of the product was MWNTs. Since toluene serves as the solvent for the reaction, a very high conversion of toluene to nanotubes is not necessarily expected or even desired. This amount of nanotubes, however, is quite significant—approximately 20 ml of toluene gives ~0.26 g of MWNTs.

Relative to reactions carried out in pure toluene, ethanol addition significantly increased the yield of MWNTs in cobaltocene and nickelocene catalyzed reactions and small amounts of hexane increased MWNT yields in ferrocene-catalyzed reactions. Mizuno et al[23] also found that nanotube yields were higher in gas-phase reactions when Fe catalysts were used in conjunction with straight-chain hydrocarbons and when Co catalysts were used in the presence of alcohols. In the supercritical reactions, ethanol and hexane both decompose much more rapidly than toluene to increase the MWNT yields; however, neither pure hexane nor ethanol when used as the solvent gave good results—hexane in particular is too reactive and decomposes primarily to amorphous carbon. In the case of ethanol, –OH radicals may form and speed the toluene decomposition rate and limit amorphous carbon formation, as Maruyama has suggested in gas phase reactions using alcohols.[24]

In low concentrations (~0.2 to 4 mM; 0.75 vol%), water greatly reduced the amount of amorphous carbon and carbon filaments formed during the reaction. Below ~0.1 mM, water did not improve the purity of the product; whereas, concentrations much above 5 to 10 mM poisoned the reaction and prevented nanotube formation. Qualitatively similar results have also been observed in gas-phase carbon nanotube reactions, with water limiting carbon sidewall deposition and carbonaceous byproduct formation.[25] In the supercritical toluene reactions, water addition was found to be critical to forming nanotubes at very high temperatures—close to 650 °C. In our previous work[18], nanotube reactions at 650 °C using pure toluene gave only amorphous carbon and some filaments and no observable nanotubes. With the addition of water, a relatively high yield of MWNTs could be obtained in this temperature range. In fact, the highest yield of MWNTs in the presence of water was obtained at 640 °C versus 625 °C in pure toluene.

Higher catalyst concentrations gave larger amounts of MWNTs. Cobaltocene was the best metallocene catalyst for MWNT growth, giving both the largest amount of MWNTs and the purest product with the highest proportion of carbon nanotubes relative to carbon filaments and amorphous carbon. The mole ratio between Co and C in the nanotubes is approximately 1:1000 in these reactions. Nickelocene produced more MWNTs than ferrocene. In gas-phase reactions, both cobaltocene and nickelocene have catalyzed single-walled nanotube (SWNT) synthesis under experimental conditions where ferrocene has not,[26-28] and the yield of SWNTs has been higher with cobaltocene than nickelocene.[28] Although fundamental understanding of nanotube growth is still being refined, these observations are consistent with expectations based on the C-Co, C-Ni, and C-Fe[29] phase diagrams: at temperatures between 600 and 650 °C, the carbon solubility is an order of magnitude higher in Co than Ni or α-Fe, ranging from 0.1 to 0.2 atomic % in Co down to 0.0~0.1 to 0.01~0.03 atomic % in Ni and Fe, respectively.

Within a rather narrow temperature range, the MWNT yield increased with higher reaction temperature. At 600 °C and below, toluene does not decompose, even in the presence of the catalyst. At temperatures above ~645 °C, good quality MWNTs are produced, but with excessive amounts of amorphous carbon due to homogeneous toluene decomposition. The highest yield of MWNTs with the least amount of amorphous carbon byproduct was obtained at 640°C. Figure 2.2 shows cobaltocene-catalyzed MWNTs grown at 640°C after purification.

2.3.2 Fe and Co nanocrystal catalyzed MWNT growth

Pre-formed Fe and Co nanocrystals, 5 to 6 nm in diameter, were also studied as catalysts for MWNT synthesis in supercritical toluene. The metallocenes decompose in the reactor to metal particles. This decomposition is relatively uncontrolled and the final catalyst particle size is limited by many factors such as their decomposition kinetics, concentration and effect of the nanotubes on metal aggregation. The nanocrystals on the other hand can be injected with a pre-specified size and are reasonably stable during the reaction, although aggregation and coalescence certainly occurs to some extent and increase the size and broaden the size distribution.[30] Somewhat surprisingly, Fe and Co nanocrystals gave significantly lower product yields compared to the metallocenes, by about an order of magnitude. Perhaps the capping ligand coating on the nanocrystals slows catalytic toluene decomposition at the metal surface. We found recently that the capping ligand coating on Ir nanocrystals significantly influences catalytic reactions, such as the hydrogenation of alkenes, on their surfaces.[31] More study is required to understand the underlying causes for the difference in reaction yields between the nanocrystals and the metallocenes. However, one significant observable difference was the metal seed diameter: the metallocenes were found to decompose into metal particles with diameters of 20~50 nm at the ends of the MWNTs, which are significantly larger than the injected nanocrystals. These observations agree with our previous work in pure supercritical toluene.[18]

2.3.3 Structural characterization of the MWNTs

Nanotubes extracted directly from the reactor were difficult to image by high resolution TEM. The nanotubes tend to agglomerate and tangle in a matrix of amorphous carbon, as shown in Figure 2.5. When isolated tubes could be imaged on the TEM grid, they would generally be coated with a few nanometers of amorphous carbon, most likely as a result of sidewall carbon deposition from homogeneously decomposing toluene, similar to what happens in CVD reactions.[32] To obtain high resolution TEM images, the MWNTs were purified using a process developed by Goto et al[33] to remove the carbonaceous byproducts. Several other methods were tried, but this one worked best. Care must be taken to avoid MWNT degradation (See Figure 2.8c) in the purification process, as noted in the literature for gas-phase produced nanotubes.[34-36]

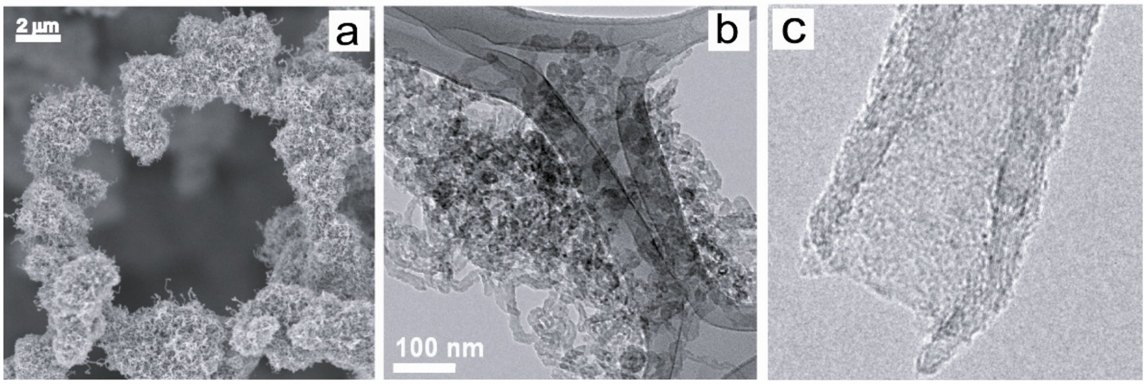

Figure 2.5 Aggregates of nanotubes imaged by (a) SEM and (b) TEM. Purification with nitric acid and hydrogen peroxide solutions and sonication was necessary to obtain better dispersed nanotubes suitable for high resolution TEM imaging. Very high acid concentrations, greater than ~16 M nitric acid, opened and damaged the nanotubes as shown in (c).

Very clean high resolution TEM images could be obtained from the purified MWNTs. For example, Figure 2.6 shows TEM images of cobaltocene-catalyzed carbon

MWNTs. The nanotube walls are composed of ordered graphitic sheets. However, closer examination reveals that the nanotubes exhibit a range of structural defects. Most MWNTs were curly. Cobaltocene-catalyzed MWNTs for example exhibited a variety of interesting shapes, including springs, hairpins, lassos, and coiled ropes (Figure 2.7). Many nanotubes exhibited kinks, as shown in Figure 2.8. Often near these kinks, the inner tube diameter would increase or decrease slightly. Iijima et al[37,38] has attributed curvature in nanotubes to the addition of either a pentagon or heptagon into the hexagonal carbon network. These kinds of "point defects" may be the source of the curvature in the MWNTs, however, much more structural characterization is required before such a conclusion can be made. Often, segments in the MWNTs had an orientation angle between the graphite basal planes and the tube axis (θ)[39,40] that deviated from zero (Figure 2.7). In gold nanocrystal-seeded Si nanowire synthesis in supercritical hexane, extended defects occurred as a result of starved growth.[41] To see if the precursor supply rate was too slow and was responsible for the large number of defects in the MWNTs, the flow rate was increased to 1.5 ml/min and both the amount of supplemental carbon source and reaction temperature were varied independently. No morphology difference was observed in the MWNTs with these changes in the reaction conditions. (MWNTs grown at higher flow rate are shown in Figure 2.6.) A significant difference in nanotube morphology most likely requires a large change in reaction conditions, for example Cui et al showed that significant differences in tube morphology occurred with synthesis temperature differences over a range of 400 °C.[42]

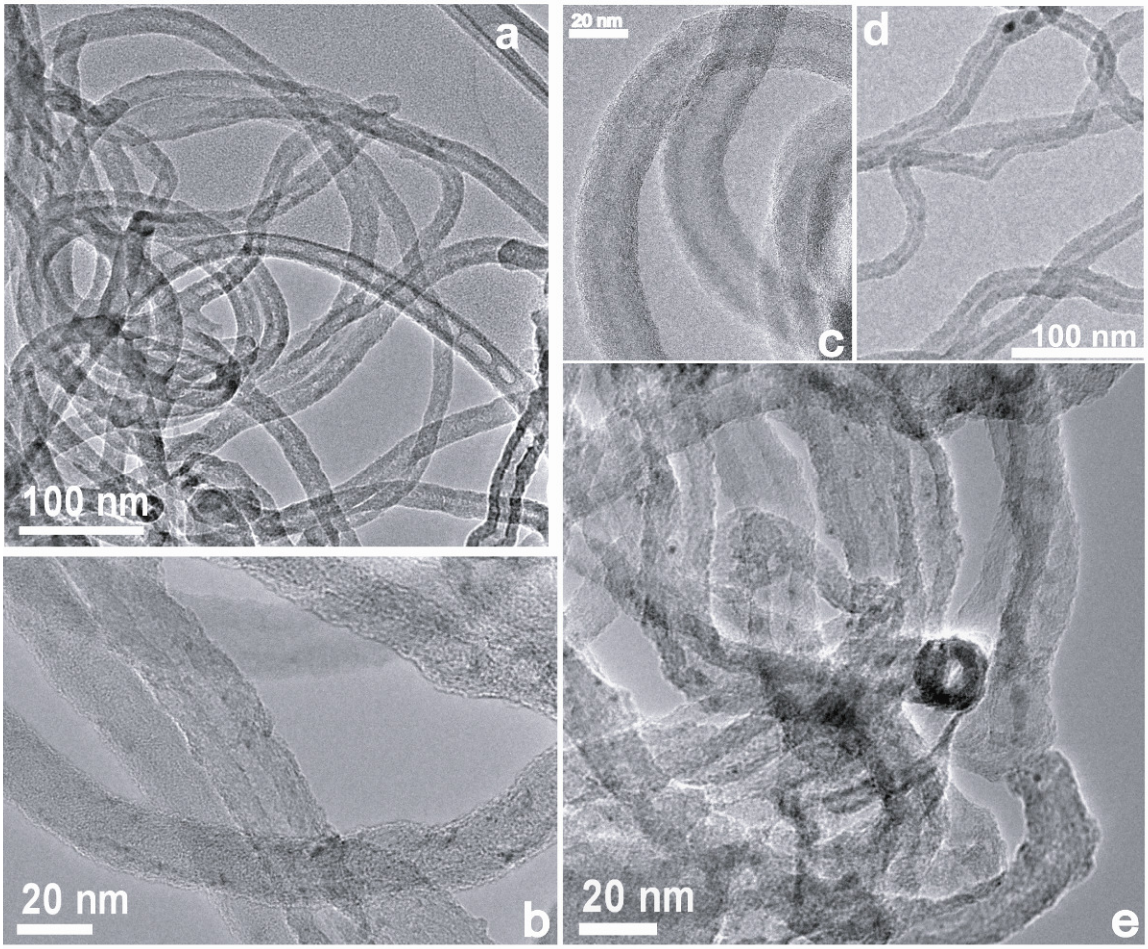

Figure 2.6 HRTEM images of MWNTs. Products obtained from reactions carried out under the following conditions: (a) 0.6 mM cobaltocene, 3.7 mM ethanol, 0.3 mM DI-H2O at 640 °C; (b,d) 8.2 mM cobaltocene, 3.7 mM ethanol, 0.2 mM DI-H2O, 640 °C with a flow rate of 1.5 ml/min; (c) 8.2 mM cobaltocene, 3.7 mM ethanol, 0.2 mM DI- H2O at 640 °C; (e) 8.2 mM cobaltocene, 3.7 mM ethanol, 0.04 mM DI-H2O at 640 °C. Lower amounts of DI-H2O gave more amorphous carbon intermixed with the nanotubes. The quality of the MWNTs did not appear to vary with reactant injection rate.

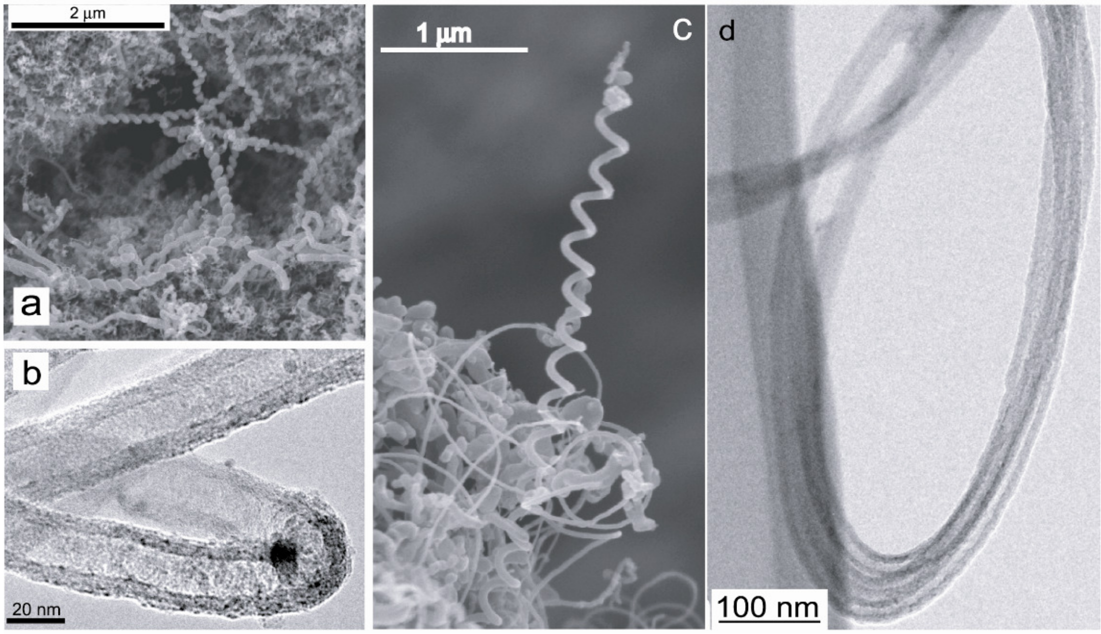

Figure 2.7 Different nanotube structures obtained in cobaltocene-catalyzed reactions: (a) coils (26 mM cobaltocene and 4.9 mM ethanol at 600 °C), (b) hairpins (8.2mM cobaltocene, 3.7 mM ethanol, 0.2 mM DI-H2O at 640 °C) (c) springs (17mM ferrocene, 3.7 mM ethanol at 630 °C), and (d) “lassos” (625 °C, 8 mM nickelocene, 3.7 mM ethanol, 0.2 mM DI- H2O).

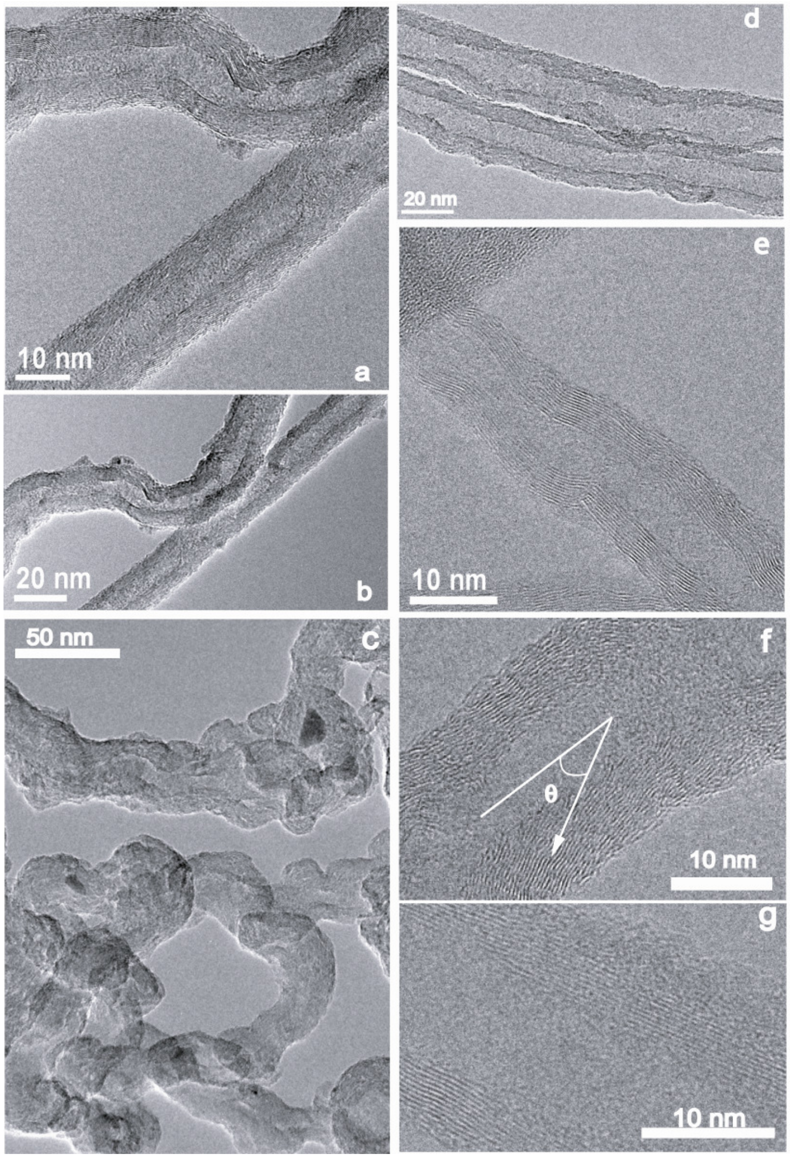

Figure 2.8 HRTEM images showing defects in MWNTs synthesized in supercritical toluene. (a-c) MWNTs synthesized in supercritical toluene with 12 mM cobaltocene, 3.7 mM ethanol and 4 mM DI-H_2O at 640 °C. (d) MWNTs synthesized with 8.2 mM cobaltocene, 3.7 mM ethanol, and 0.2 mM water at 640 °C. (e) MWNTs synthesized with 0.6 mM cobaltocene, 3.7 mM ethanol, and 0.3 mM DI- H_2O at 640 °C. In (f), θ is the angle between the tube axis and the graphite basal planes. Non-zero θ indicates a defect in the tube wall.

Figure 2.9 shows TEM images of MWNTs with bamboo morphology—sections of graphite bridge the interior of the nanotube at regular intervals. Bamboo morphology in MWNTs has been observed in many studies and has been attributed in some cases to a root growth mechanism of tubes from metal seed particles.[43-47] The MWNTs synthesized in supercritical toluene from metallocene catalysts, however, appear to grow by a folded-growth mechanism in which at the end of the MWNT the graphite sheets wrap around the metal seed particle.[17,18] Figure 2.9 shows several examples of these "folded-growth" structures where the metal seed particle at the tip of the MWNT is coated with graphite. However, it is possible that in some cases the MWNTs might be growing at exposed open ends of the tubes as well, as many nanotubes were observed by TEM with metal catalyst particles embedded in the middle of the nanotubes[48] (Figure 2.9h). Bamboo morphology in carbon nanotubes has been proposed to be the result of subtle changes in the growth conditions near the seed metal, for example a fluctuation in pressure, temperature or reactant concentration, might lead to a defect in the graphite sheet, resulting in a temporary "capping" of the nanotube. Louchev attributed bamboo layer formation to any change in the growth conditions that slows carbon addition to the nanotube edge and gives rise to a high probability of pentagon defect formation;[49] thus, resulting in a temporary capping of the tube resulting in the bamboo structure. Certainly, local temperature or reactant concentration fluctuations at the metal catalyst surface are possible in the supercritical toluene reactions.

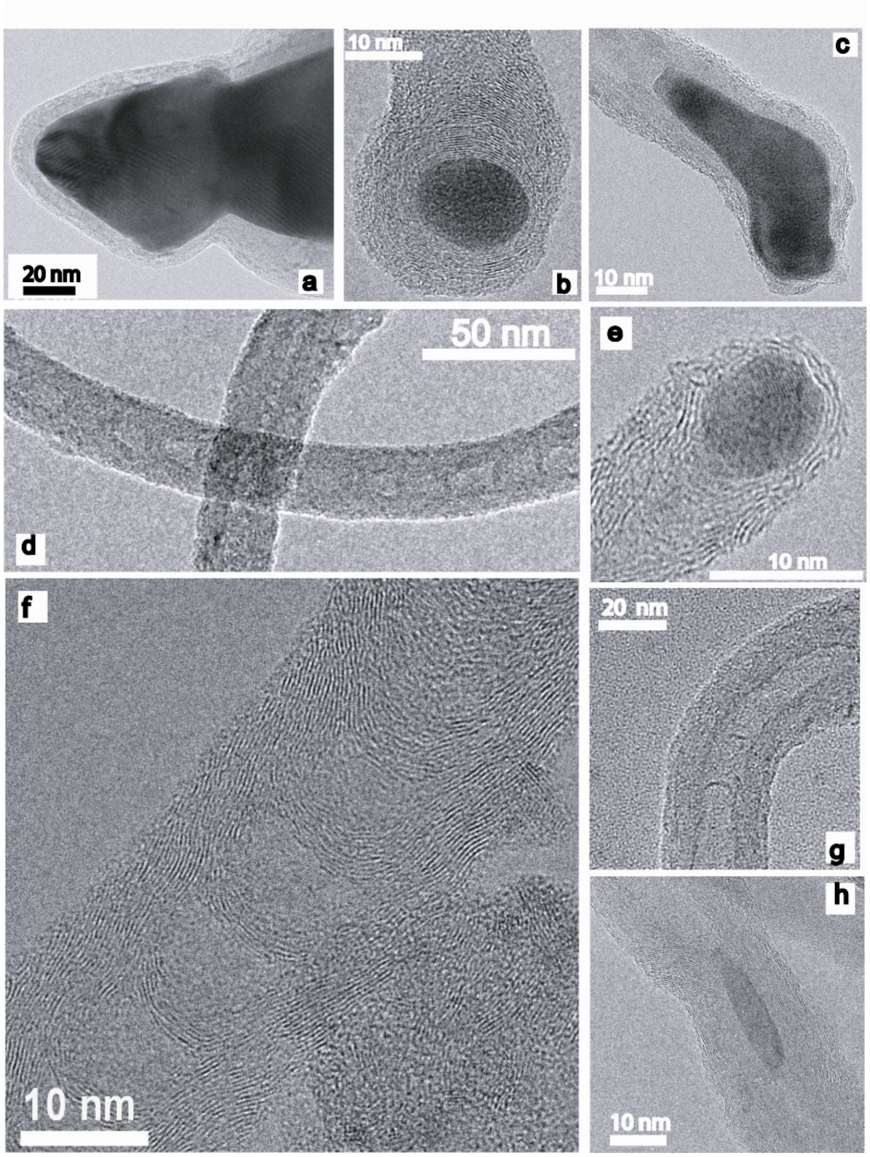

Figure 2.9 TEM images of metallocene-catalyzed MWNTs synthesized in supercritical toluene. The graphitic sheets generally are found folded around the metal seed particle, as shown in (a-c) and (e). (8.2 mM cobaltocene with 3.7 mM ethanol and 0.2 mM DI-H_2O at 640 °C). Many of the tubes exhibited bamboo morphology, as shown in (d), (f) and (g). (625 °C, 8 mM nickelocene, 3.7 mM ethanol, and 0.2 mM DI- H_2O). (h) In many cases, metal was found entrained in the middle of the nanotube as well (17 mM cobaltocene, 3.7 mM ethanol, 630 °C).

2.4 CONCLUSIONS

MWNTs were grown in supercritical toluene using ferrocene, cobaltocene, nickelocene, Fe, and Co nanocrystals as catalysts. A continuous flow reactor and cobalt and nickel precursors led to much higher yields than previous batch reactions in supercritical toluene. The addition of water significantly reduced amorphous carbon and nanofilament formation. Additional reactive carbon sources like hexane and ethanol gave higher MWNT yields. Cobaltocene was the best catalyst in terms of both the purity of the product and the conversion of toluene to nanotubes, which might be explained by higher carbon solubility into Co compared to Ni and Fe at temperatures of 600 to 650 °C. The nanotubes appear to grow by a folded growth mechanism. Many MWNTs exhibited significant defects in their graphitic layers, resulting in curly and kinked nanowires. In some cases, the nanowire bending was consistent along the length of the nanotube, resulting in coil, spring, and lasso structures.

In future work, conditions might be identified that will enable single wall carbon nanotube synthesis. However, the window of operating temperature is very limited. Reactions were carried out at the highest possible temperatures in our system (~650 °C) and as of yet no SWNTs have been observed. Kanzow and Ding suggest that single-walled carbon nanotube growth requires temperatures of at least 900 °C,[50] however, using catalytic chemical vapor deposition, Maruyama et al. reported the synthesis of single-walled carbon nanotubes at temperatures as low as 550 °C.[24] In the supercritical reactions, the relatively large size of the catalyst seeds may also be preventing SWNT formation.[51-53] Smaller metal seeds are needed to induce the extreme curvature of the graphitic sheets to form a single wall nanotube, yet it is difficult to obtain and stabilize <2 nm diameter metal seeds in the very high temperature solutions and may be another significant challenge facing SWNT growth in high temperature supercritical solvents.

Nonetheless, it seems possible that SWNTs could be produced in a supercritical organic solvent with the appropriate reactants and concentrations and is an area of ongoing study.

2.5 REFERENCES

1. Meyyappan, M., *Carbon Nanotubes: Handbook of Nanoscience, Engineering, and Technology.* CRC Press: Boca Raton, 2003.
2. Treacy, M. M. J.; Ebbesen, T. W.; Gibson, J. M., *Nature* **1996**, *381*, 678.
3. Ebbesen, T. W.; Ajayan, P. M., *Nature* **1992**, *358*, 220.
4. Ruoff, R. S.; Lorents, D. C., *Carbon* **1995**, *33*, 925.
5. Baughman, R. H.; Zakhidov, A. A.; de Heer, W. A., *Science* **2002**, *297*, 787.
6. Gogotsi, Y.; Libera, J. A.; Yoshimura, M., *J. Mater. Res.* **2000**, *15*, 2591.
7. Calderon Moreno, J. M.; Yoshimura, M., *J. Am. Chem. Soc.* **2001**, *123*, 741.
8. Libera, J.; Gogotsi, Y., *Carbon* **2001**, *39*, 1307.
9. Suchanek, W. L.; Libera, J. A.; Gogotsi, Y.; Yoshimura, M., *J. Solid State Chem.* **2001**, *160*, 184.
10. Wang, W.; Huang, J. Y.; Wang, D. Z.; Ren, Z. F., *Carbon* **2005**, *43*, 1328.
11. Zhang, W.; Ma, D.; Liu, J.; Kong, L.; Yu, W.; Qian, Y., *Carbon* **2004**, *42*, 2341.
12. Hu, G.; Cheng, M.; Ma, D.; Bao, X., *Chem. Mater.* **2003**, *15*, 1470.
13. Jiang, Y.; Wu, Y.; Zhang, S.; Xu, C.; Yu, W.; Xie, Y.; Qian, Y., *J. Am. Chem. Soc.* **2000**, *122*, 12383.
14. Wang, X.; Lu, J.; Xie, Y.; Du, G.; Guo, Q.; Zhang, S., *J. Phys. Chem. B* **2002**, *106*, 933.
15. Wang, W.; Kunwar, S.; Huang, J. Y.; Wang, D. Z.; Ren, Z. F., *Nanotechnology* **2005**, *16*, 21.
16. Liu, J.; Shao, M.; Chen, X.; Yu, W.; Liu, X.; Qian, Y., *J. Am. Chem. Soc.* **2003**, *125*, 8088.
17. Lee, D. C.; Korgel, B. A., *Mol. Simul.* **2005**, *31*, 637.

18. Lee, D. C.; Mikulec, F. V.; Korgel, B. A., *J. Am. Chem. Soc.* **2004**, *126*, 4951.

19. Hyeon, T.; Lee, S. S.; Park, J.; Chung, Y.; Na, H. B., *J. Am. Chem. Soc.* **2001**, *123*, 12798.

20. Puntes, V. F.; Zanchet, D.; Erdonmez, C. K.; Alivisatos, A. P., *J. Am. Chem. Soc.* **2002**, *124*, 12874.

21. Hanrath, T.; Korgel, B. A., *J. Am. Chem. Soc.* **2002**, *124*, 1424.

22. McKee, G. S. B.; Vecchio, K. S., *J. Phys. Chem. B* **2006**, *110*, 1179.

23. Mizuno, K.; Hata, K.; Saito, T.; Ohshima, S.; Yumura, M.; Iijima, S., *J. Phys. Chem. B* **2005**, *109*, 2632.

24. Maruyama, S.; Kojima, R.; Miyauchi, Y.; Chiashi, S.; Kohno, M., *Chem. Phys. Lett*. **2002**, *360*, 229.

25. Futaba, D. N.; Hata, K.; Yamada, T.; Mizuno, K.; Yumura, M.; Iijima, S., *Phys. Rev. Lett.* **2005**, *95*, 056104.

26. Satishkumar, B. C.; Govindaraj, A.; Sen, R.; Rao, C. N. R., *Chem. Phys. Lett.* **1998**, *293*, 47.

27. Vivekchand, S. R. C.; Cele, L. M.; Deepak, F. L.; Raju, A. R.; Govindaraj, A., *Chem. Phys. Lett*. **2004**, *386*, 313.

28. Rao, C. N. R.; Govindaraj, A.; Sen, R.; Satishkumar, B. C., *Mater. Res. Innovations* **1998**, *2*, 128.

29. *Binary Alloy Phase Diagrams*. 2nd ed.; ASM International: Materials Park, OH, 1990; Vol. 1.

30. Shah, P. S.; Hanrath, T.; Johnston, K. P.; Korgel, B. A., *J. Phys. Chem. B* **2004**, *108*, 9574.

31. Stowell, C. A.; Korgel, B. A., *Nano Lett.* **2005**, *5*, 1203.

32. Qin, L. C., *J. Mater. Sci. Lett.* **1997**, *16*, 457.

33. Goto, H.; Furuta, T.; Fujiwara, Y.; Ohashi, T. Method of purifying single wall carbon nanotubes from metal catalyst impurities. U.S. Patent Application 20030007924, January 9, 2003.

34. Zhang, X.; Sreekumar, T. V.; Liu, T.; Kumar, S., *J. Phys. Chem. B* **2004**, *108*, 16435.

35. Zhang, M.; Yudasaka, M.; Iijima, S., *J. Phys. Chem. B* **2004**, *108*, 149.

36. Lee, G.-W.; Kumar, S., *J. Phys. Chem. B* **2005**, *109*, 17128.

37. Iijima, S.; Ishihashi, T.; Ando, Y., *Nature* **1992**, *356*, 776.

38. Iijima, S.; Ajayan, P. M.; Ichihashi, T., *Phys. Rev. Lett.* **1992**, *69*, 3100.

39. Nolan, P. E.; Schabel, M. J.; Lynch, D. C., *Carbon* **1995**, *33*, 79.

40. Meyyappan, M.; Delzeit, L.; Cassell, A.; Hash, D., *Plasma Sources Sci. Technol.* **2003**, *12*, 205.

41. Lu, X.; Hanrath, T.; Johnston, K. P.; Korgel, B. A., *Nano Lett.* **2003**, *3*, 93.

42. Cui, H.; Eres, G.; Howe, J. Y.; Puretkzy, A.; Varela, M.; Geohegan, D. B.; Lowndes, D. H., *Chem. Phys. Lett.* **2003**, *374*, 222.

43. Liu, J.; Xu, L.; Zhang, W.; Lin, W. J.; Chen, X.; Wang, Z.; Qian, Y., *J. Phys. Chem. B* **2004**, *108*, 20090.

44. Wang, Y. Y.; Tang, G. Y.; Koeck, F. M.; Brown, B.; Garguilo, J. M.; Nemanich, R. J., *Diamond Relat. Mater.* **2004**, *13*, 1287.

45. Lee, C. J.; Park, J., *Appl. Phys. Lett.* **2000**, *77*, 3397.

46. Lee, C. J.; Park, J. H.; Park, J., *Chem. Phys. Lett.* **2000**, *323*, 560.

47. Lee, C. J.; Park, J., *J. Phys. Chem. B* **2001**, *105*, 2365.

48. Deck, C. P.; Vecchio, K. S., *J. Phys. Chem. B* **2005**, *109*, 12353.

49. Louchev, O. A., *Phys. Status Solidi A* **2002**, *193*, 585.

50. Kanzow, H.; Ding, A., *Phys. Rev. B* **1999**, *60*, 11180.

51. Li, Y. M.; Kim, W.; Zhang, Y. G.; Rolandi, M.; Wang, D. W.; Dai, H. J., *J. Phys. Chem. B* **2001**, *105*, 11424.

52. Li, Y.; Liu, J.; Wang, Y. Q.; Wang, Z. L., *Chem. Mater.* **2001**, *13*, 1008.

53. Cheung, C. L.; Kurtz, A.; Park, H.; Lieber, C. M., *J. Phys. Chem. B* **2002**, *106*, 2429.

Chapter 3: The Influence of Iodide Impurities in CTAB on the Colloidal Seed-Mediated Synthesis of Gold Nanorods

Reproduced in part with permission from: Smith, D.K. and Korgel, B.A. "The Importance of the CTAB Surfactant on the Colloidal Seed-Mediated Synthesis of Gold Nanorods." *Langmuir*, **2008**, *24*, 644-649. Copyright 2008 American Chemical Society.

3.1 INTRODUCTION

A broad goal in the field of nanomaterials chemistry is to develop chemical, *self-directed* approaches for producing nanostructures with controlled size and shape.[1-5] Arrested precipitation is one such approach that can yield metal[2, 6-12] and semiconductor[4, 13-19] nanocrystals with exquisite size and shape control. It relies on controlled reactions carried out in solution in the presence of capping ligands: the capping ligands coat the surface of nanocrystals as they nucleate and grow and stabilize their size and shape. Although this method can work very well, the underlying physical and chemical mechanisms that determine nanocrystal size, and particularly *shape*, are presently only crudely understood.

The shape of a gold nanorod is what gives rise to its interesting optical properties. Gold nanorods have two peaks in their absorbance spectra that correspond to plasmon resonances: one at approximately 520 nm from plasmon oscillations in the shorter transverse direction and a second at longer wavelengths (typically between 700 nm and 1300 nm) from longitudinal oscillations.[20-24] By varying the nanorod aspect ratio, the position of the longer wavelength plasmon peak can be tuned out to the near-infrared region, where absorbance by cells and tissue is minimal.[25] Thus, gold nanorods are attractive candidates for cellular and biological imaging.

To date, gold nanorods have been explored for biological and medical use as optical contrast agents for dark field[26-30] and two-photon luminescence diagnostic imaging[31] and photothermal therapy of cancer cells.[26] They are attractive candidates for biomedical imaging not only because their optical response can be tuned to near infrared wavelengths which penetrate deep into cells and tissue;[25] but furthermore, they do not photobleach or blink, and are chemically inert and biologically compatible.[32-35]

Gold nanorods can be made in large quantities with very narrow size and shape distributions by arrested precipitation via a seeded growth process with CTAB (cetyltrimethylammonium bromide) as a stabilizing surfactant. The chemistry, however, is rather complex and the shape-controlling factors are still being resolved. Murphy[36] first reported the approach, demonstrating that heterogeneous, facet-selective Au deposition could be induced on 2 to 4 nm diameter Au seed particles to produce Au nanorods. Their initial method, however, gives only a low yield of nanorods and the majority of the product is composed of spherical nanoparticles: it employs citrate-stabilized seed particles with twins that when added carefully in a controlled step-wise fashion to growth solutions, promote nanorod growth, but with a relatively low probability (only approximately 15% of the particles end up as nanorods). El-Sayed[37] later demonstrated that silver nitrate addition to the nanorod growth solution greatly enhances nanorod formation, with yields of nearly 100% nanorods. Silver adsorbs selectively to {110} Au facets by underpotential deposition (UPD) and inhibits Au deposition on those surfaces, but allows Au deposition on {100} and {111} surfaces, leading to nanorod growth in the [100] direction.[38] Au nanorods formed from citrate-stabilized Au nanoparticles in the absence of silver have a different, [110] growth direction.[39,40]

The reproducibility of the gold nanorod synthesis—i.e., the nanorod size, shape, and yield—has been a persistent challenge facing the technique.[41,42] Many studies have addressed this issue, attributing differences in reproducibility to a wide variety of factors including seed aging time,[43] the method of mixing the seed and growth solutions,[43] variations in salt concentration and temperature of the growth solution, as well as nanorod growth time.[41,42] It is true that many factors can affect the synthesis of gold nanorods including the concentration of Ag(I) in the growth solution, the amount of seeds added to the growth solution, pH, and the addition of salts such as Na_2S (see Appendix B). However, we discovered another very significant variable that is detrimental to gold nanorod production: impurities in the CTAB.

The role of CTAB in inducing nanorod growth has been debated in the literature.[43-45] CTAB is an interesting capping ligand, as it stabilizes the Au nanorods by forming a *bilayer* around the nanocrystals (see Figure 3.1). Polar headgroups attach CTAB to the Au surface and the bilayer structure also allows polar CTAB headgroups to interface with the surrounding water phase and provide aqueous dispersibility.[46] We found that CTAB from some chemical suppliers did not yield nanorods—only spherical particles formed—and our initial extensive chemical analysis showed that a trace impurity was present in these CTAB samples, but we were unable to identify what the impurity was.[47]

However, later chemical analysis using inductively coupled plasma mass spectroscopy (ICP-MS) revealed that iodide was present in all brands of CTAB with concentrations varying with chemical supplier. All iodide concentrations in solid CTAB were less than 900 ppm (which equates to 242 μM [I-] in the nanorod growth solutions), but iodide concentrations in the growth solution as low as 570 nM were found to prevent nanorod formation. Iodide adsorbs strongly to Au {111} surfaces and prevents nanorod growth. These findings agree with previous reports showing that iodide can prevent the formation of nanorods[48] and nanoprisms,[49] but contradict a recent paper[50] that suggests that iodide is *necessary* for Au nanorod formation.

3.2 EXPERIMENTAL SECTION

3.2.1. Materials and Supplies

Doubly-distilled deionized water (DI H_2O) was used in all preparations. Hydrogen tetrachloroaurate(III) hydrate ($HAuCl_4$, 99.9+%), sodium borohydride ($NaBH_4$, 98+%), silver nitrate ($AgNO_3$, 99.9999%), trisodium citrate ($HOC(COONa)(CH_2COONa)_2{\cdot}2H_2O$), ascorbic acid ($C_6H_8O_6$, 99+%), and tetramethylammonium hydroxide solution ($(CH_3)_4N(OH)$, 25% in H_2O) were obtained from Sigma-Aldrich and used as received. Nitric acid (HNO_3, trace metal grade, 69-70% anhydrous solute), potassium iodide (KI), and sodium hydroxide (NaOH, 97+%) were obtained from Fisher. Cetyltrimethylammonium bromide ($CH_3(CH_2)_{15}N(Br)(CH_3)_3$, CTAB) was obtained from various suppliers and purities as listed in Table 2.1.

3.2.2 Gold Nanorod Synthesis

3.2.2.1 Ag(I)-assisted growth method

Au nanorods were made by a Ag(I)-assisted approach as previously described. [51] An aqueous gold seed particle solution was first prepared by adding 250 μL of 0.01 M $HAuCl_4$ to 9.75 mL of 0.1 M CTAB solution. An aqueous growth solution was prepared by combining 9.5 ml of 0.1 M CTAB, 75 μL of 0.01 M $AgNO_3$, 500 μL of 0.01 M $HAuCl_4$ and 55 μL of 0.1 M ascorbic acid. 600 μL of aqueous 0.01 M $NaBH_4$ was added to the gold seed particle solution and stirred for 2 minutes. After two hours, 12 μL of this gold seed solution was then added to the growth solution and mixed by capping the reaction vessel and slowly inverting it two times. After seed addition, the growth solution was maintained at 24 ^{o}C without stirring overnight.

3.2.2.2 Step-wise additive growth method

Au nanorods were formed by a step-wise additive growth method as described previously.[52] An aqueous gold seed particle solution was formed by adding 500 μL of 0.1 M $NaBH_4$ to a solution of 18 ml DI water, 500 μL of 0.01 M $HAuCl_4$, and 500 μL of 0.01 M trisodium citrate. The solution was stirred for 2 minutes after adding the $NaBH_4$. Three aqueous growth solutions were prepared. Solutions "1" and "2" contain 9 ml of 0.1 M CTAB, 250 μL of 0.01 M $HAuCl_4$, 50 μL of 0.1 M ascorbic acid, and 50 μL of 0.1 M NaOH. Solution "3" was prepared with a ten fold increase in reagent concentration relative to solutions 1 and 2: 90 ml of 0.1 M CTAB, 2.5 mL of 0.01 M $HAuCl_4$, 500 μL of 0.1 M ascorbic acid, and 500 μL of 0.1 M NaOH. 1 ml of the gold seed solution was added to growth solution 1 and mixed by capping the reaction vessel and slowly inverting it two times. 1 ml of this mixed growth solution 1 was added to growth solution 2 and mixed as described. Finally, the new growth solution 2 was added to growth solution 3 and mixed as described. The nanorods grew overnight and the growth solution was maintained at 24 ^{o}C without stirring.

In some experiments, an aqueous solution of 0.1 M KI was added in various amounts to the growth solutions to control the iodide concentration. In other experiments, an aqueous solution of 0.1 M KI was added to the Au nanorod preparation after their synthesis.

3.2.3 Materials Characterization

Nanorods were purified by centrifuging at 10,000 RPM for 15 minutes, removing and discarding the supernatant, and redispersing the precipitate in DI H_2O. This process was repeated to ensure removal of excess CTAB from the Au nanorods. Transmission electron microscopy (TEM) was performed using either a Phillips EM208 TEM with 80 kV accelerating voltage or a JEOL 2010F HRTEM with the field emission gun operated at 200 kV. Images were digitally acquired. TEM samples were prepared by dropcasting the nanorods dispersed in DI H_2O onto carbon-coated copper 200 mesh TEM grids (Electron Microscopy Sciences). Absorbance spectra were acquired using a Varian Cary 50 Bio UV/Vis Spectrophotometer with samples dispersed in water in quartz cuvettes with a 1 cm path length. Absorbance spectra of the purified nanorods were measured the day after nanorod synthesis.

Identification of I^- an impurity in some CTAB formulations and subsequent quantification of I^- was achieved using an Agilent 7500ce quadrupole ICP-MS. Vendor CTAB formulations, dissolved in 2% HNO_3, were initially scanned across the entire atomic mass unit (AMU) range to identify elemental contaminants that may play a role in Au nanorod inhibition. Critical assessment of the resulting mass spectral peaks demonstrated that I^- was a distinctive component of several formulations. That these same formulations correspond to failed nanorod synthesis efforts suggested a causal role by I^-. Accordingly, the next step was to quantify CTAB I^- concentrations.

New CTAB aliquots (0.03 g) were dissolved in 2% HNO_3 (6 mL), then diluted 10-fold in an organic alkali (2% TMAH) to minimize volatile loss. ICP-MS operating conditions were 1500 W forward RF power, 13 L/min plasma gas flow, 0.2 L/min auxiliary gas flow and 0.92 L/min nebulizer gas flow, peristaltic pump speed 0.1 RPM. Indium-115 (0.5 ppm in 2% TMAH) was added in-line as an internal standard for drift compensation. Analytes were measured using an integration time of 0.1 sec, for three replicates, after a 12 second stabilization time. Prior to quantitative analysis, the instrument was tuned using a 10 ppb tune solution to optimize sensitivity across the mass range, and to normalize counts measured by the electron multiplier in pulse and analog counting modes. KI in 2% TMAH was used to make calibration solutions between 0.1 and 1000 ppb.

Five replicates of a low-end calibration standard (7.65 ppb) were within 3% (7.83 ± 0.07 ppb). An intermediate calibration standard check (76.66 ppb measured vs. 76.45 ppb actual) was better than 1%. The limit of detection, calculated from as three times the standard deviation of blank (2% TMAH) counts on replicates (n = 5), plus the overall average of replicates, was 1.35 ppb. A randomly selected CTAB sample (sample I, Sigma H5882) was spiked with 10 and 100 ppb I. Negative recoveries, both ~89% of the unspiked sample concentration (~414 ppb), suggest a moderate matrix suppression effect of the KI-TMAH matrix compared to the CTAB dilutions. Accordingly, derived I concentrations are considered to be minimum values. Samples above detection (samples H-J) ranged between 28 and 414 ppb I, or 58 to 840 ppm when dilution factor corrected.

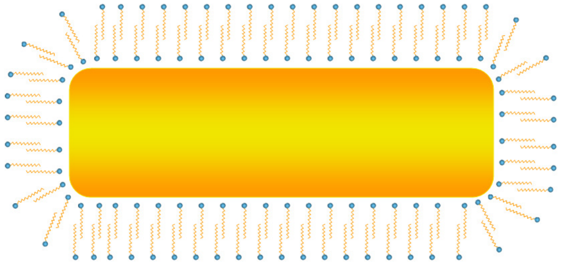

Figure 3.1. A gold nanorod created by a CTAB bilayer. The blue circles represent ammonium head groups and the orange zig zags are the hydrocarbon tails of the CTAB.

3.3 RESULTS AND DISCUSSION

3.3.1 Differences in the Ag(I)-Assisted and Step-wise Additive Synthesis Methods

As sketched in Figure 3.2, both synthesis methods rely on the initial preparation of ~1.5 nm diameter gold nanoparticle seeds. In the Ag(I)-assisted synthesis, these gold nanoparticles are capped with CTAB, and are added to a growth solution of concentrated CTAB, $AgNO_3$, $HAuCl_4$, and ascorbic acid. Ascorbic acid is a weak reducing agent that induces heterogeneous gold deposition at the surface of the seed particles.[53] Anisotropic nanorod growth results from facet-selective gold deposition promoted by the silver ions, which adsorb to the gold surfaces by an underpotential deposition (UPD) mechanism as elucidated by Liu and Guyot-Sionnest.[38] The nanorod aspect ratio can be increased to a certain extent, up to 4.5, by increasing the silver concentration,[37] and the absence of Ag+ from the reactions leads to only a very low yield of Au nanorods (see Figure B4 in the appendix).

In the step-wise additive method, the gold nanoparticle seeds are capped with trisodium citrate. The seed nanoparticles are added to a growth solution "A" containing CTAB, $HAuCl_4$, and ascorbic acid. A 1 mL aliquot of the growing nanorods is withdrawn from growth solution "A" and transferred into fresh growth solution "B" containing the same reagents as solution "A": CTAB, $HAuCl_4$, and ascorbic acid. All of solution "B" is then added to a fresh growth solution "C" which is a 10-fold scale up of the CTAB, $HAuCl_4$, and ascorbic acid amounts used for growth solutions "A" and "B." In this method, no Ag(I) is present and the nanorod growth is attributed to the pentafold twinning of the seed nanocrystals.[39,40,44]

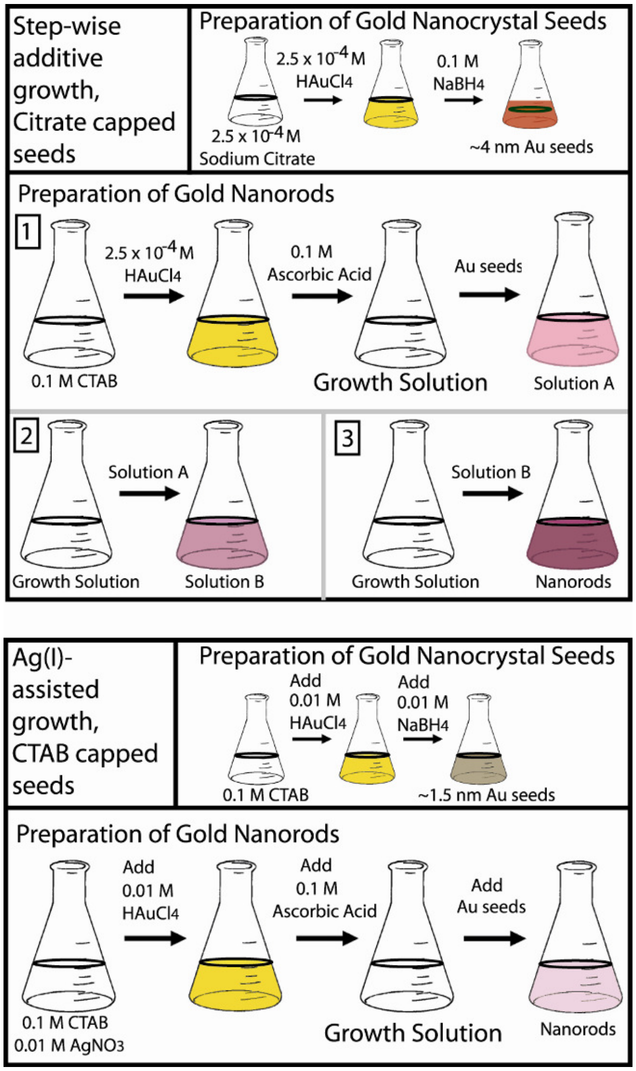

Figure 3.2. Comparison between the (Top) step-wise additive and (Bottom) Ag(I)-assisted Au nanorod synthesis procedures. Both methods require the preparation of a seed particle solution and a growth solution, but the step-wise additive synthesis requires three transfer steps to growth solutions in contrast to one for the Ag(I)-assisted growth method. The other important differences between the two methods are the seed particle stabilizer and the growth solution chemistry: the step-wise additive synthesis uses citrate-stabilized seed particles; whereas, the Ag(I)-assisted synthesis uses CTAB stabilized Au seed particles and $AgNO_3$ is added to the growth solution.

3.3.2 Iodide Impurity in CTAB Prevents Au Nanorod Formation by the Ag(I)-Assisted Approach

In our initial experiments, we discovered nanorods could only be produced when CTAB from certain suppliers was used. Using the same Ag(I) assisted recipe, CTAB from Acros, Sigma, and Aldrich did not yield nanorods, whereas CTAB from Fluka and MP Biomedicals did.[31]

We performed more extensive tests using the Ag(I)-assisted method to examine the influence of CTAB from ten different suppliers on seed and nanorod growth. Figure 3.3 shows a picture of seed particle solutions made using the last five CTABs listed in Table 3.1, along with their absorbance spectra before and after adding sodium borohydride. Prior to adding the reducing agent, the CTAB/$HAuCl_4$ solutions (Figure 3.3a) have distinctly different colors (Note: aqueous solutions of all five CTABs prior to the addition of hydrogen tetrachloroaurate are clear and have identical absorbance spectra.) However, after reduction, all of the solutions turned similar shades of brown, indicating that the seed particle sizes made during this step were roughly equal, as also confirmed by TEM (See Appendix B).

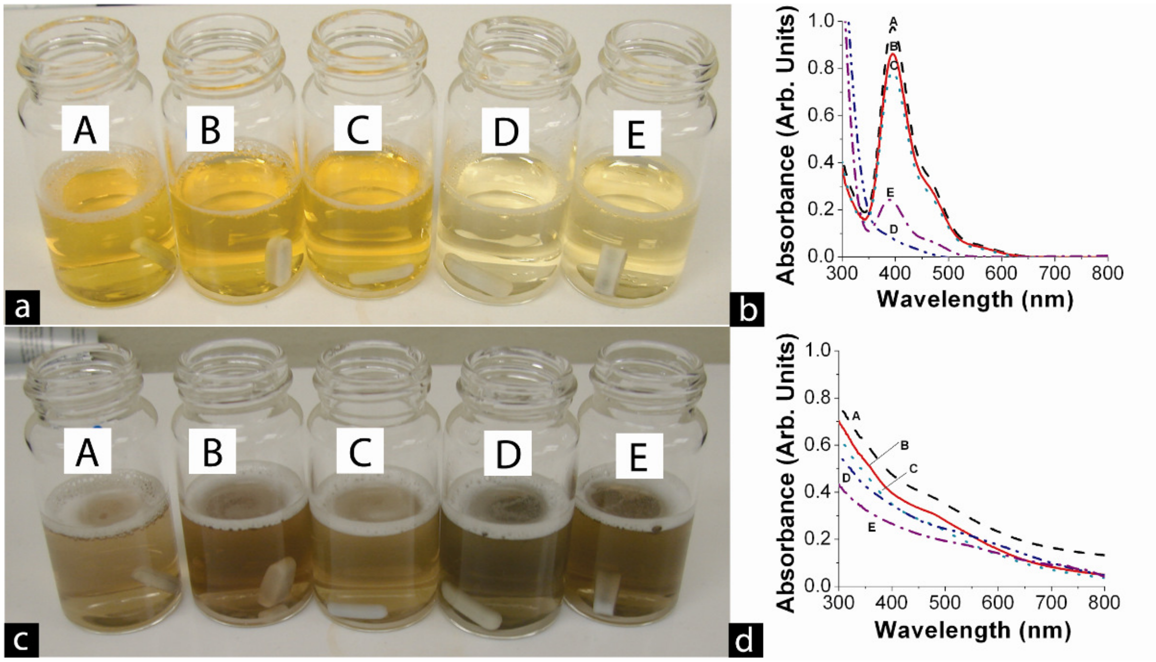

Figure 3.3. (a) Photographs of the reactant solutions for the gold seed particles made using the Ag(I)-assisted method (0.1 M CTAB and 0.01 M hydrogen tetrachloroaurate(III) hydrate) prior to sodium borohydride addition. Each solution was made using CTAB from a different supplier: (A) Fluka (52370), (B) MP Biomedicals, (C) Acros, (D) Sigma (H5882), and (E) Aldrich. (b) The corresponding absorbance spectra of the solutions in (a). (c) Reactant solutions after adding sodium borohydride (600 µL, 0.01 M) to induce particle formation, and (d) their corresponding absorbance spectra.

Figure 3.4 shows five vials of the growth solution six minutes and 30 minutes after adding 12 µL of the seed solution to the growth solution. The three vials on the right contain CTAB from Acros, Sigma (H5882), and Aldrich. CTAB from the different suppliers induced noticeably different gold colloid growth rates. After six minutes, the solutions with Fluka (52370) and MP Biomedicals CTAB were still clear, indicating that gold colloid growth had not yet occurred. In contrast, the solutions with CTABs from Acros, Sigma (H5882), and Aldrich were red six minutes after injection, indicating that larger diameter spherical gold particles had already formed. Thirty minutes after seed injection, the three vials on the right were still red, indicating that the gold colloids remained spherical. The two vials on the left became blue/purple after thirty minutes, indicating that nanorods had formed. TEM and SEM images of the final products (shown in Figure 3.5) confirmed that the two vials on the left contained nanorods and the three vials on the right had only spherical particles. These experiments show that the CTABs that do not yield nanorods exhibit a much faster rate of gold colloid growth during the "growth" step. The CTAB can influence the growth rate by either increasing (or decreasing) the rate of gold cation reduction in solution, or by enhancing (or decreasing) the bonding strength of the adsorbed surfactant layer, which can also change the growth rate of the particles (see Figure B7 in the Appendix).

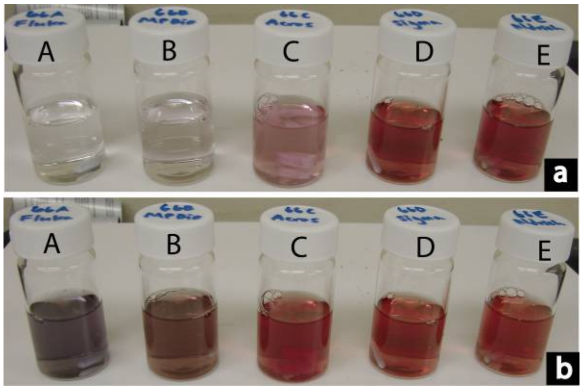

Figure 3.4. The growth solutions made using the Ag(I)-assisted method (a) six minutes and (b) 30 minutes after seed addition. The reactions were carried out using the same reactant concentrations and addition procedures with CTAB from five different suppliers: (A) Fluka (52370), (B) MP Biomedicals, (C) Acros, (D) Sigma (H5882), and (E) Aldrich. The red solution color is indicative of spherical particles, and the blue/purple color is characteristic of nanorods. Note that the formation of larger diameter spherical gold particles has occurred in vials C, D, and E after only six minutes.

Figure 3.5 shows TEM and SEM images of gold colloids made using CTAB from these different suppliers. In each preparation, the particles were monodisperse, but the shape was dramatically different—either spheres or rods—depending on the CTAB supplier. The only noticeable difference between the CTAB obtained from different suppliers seemed to be the purity. In our initial research, the CTAB that generated nanorods was relatively "impure" (~97%); therefore, we speculated[6] that an impurity in the CTAB was important for *inducing* nanorod formation.

In further experiments, however, we have found that relatively pure (>99%) CTAB from Sigma or Fluka also generated nanorods, and the role of impurities appeared to be a more complicated issue. Figure 3.6 shows UV-visible absorbance spectra of gold colloid dispersions made using CTAB from ten different suppliers. Dispersions of gold nanorods were easily distinguished from gold spheres because nanorods exhibit two absorbance peaks, one at ~520 nm and the other at ~700-1300 nm, depending on the aspect ratio[20]—as opposed to only one at ~520 nm for spheres. These peaks correspond to plasmon resonances: the shorter wavelength peak at 520 nm to plasmon oscillations in the shorter transverse direction, and the longer wavelength peak (between 700 nm and 1300 nm) to longitudinal oscillations. Table 3.1 summarizes our findings. Of the ten different CTABs sampled, three did not generate rods (the spectra labeled H, I, and J in Figure 3.6 with only one absorbance peak indicating that nanorods did not form in these reactions).

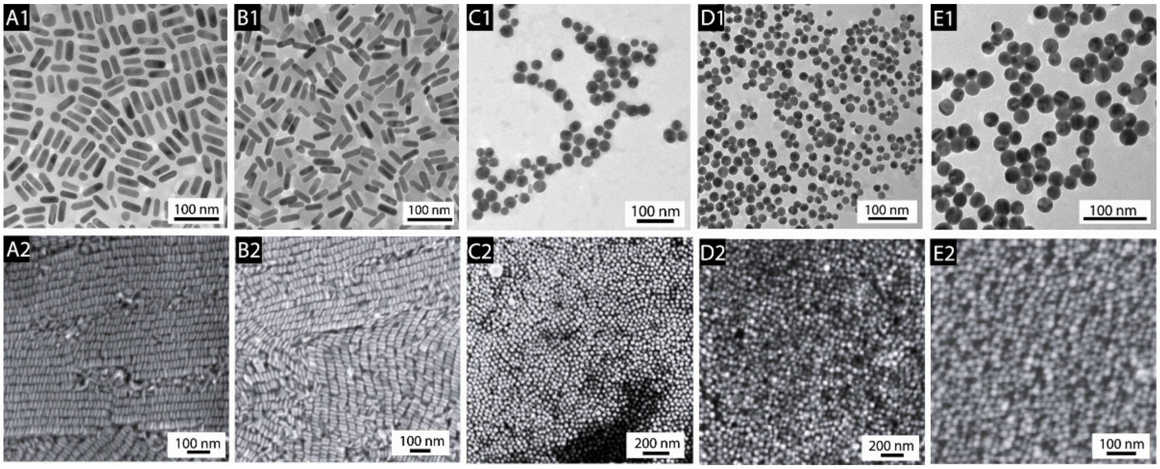

Figure 3.5. TEM (top images labeled with "1") and SEM (bottom images labeled with "2") images of gold colloids made using the Ag(I)-assisted method with CTAB from five different suppliers (see Table 3.1): (A) Fluka (52370), (B) MP Biomedicals, (C) Acros, (D) Sigma (H5882), and (E) Aldrich. Of these, only CTAB supplied by Fluka and MP Biomedicals yielded nanorods, while the others yielded only spherical particles.

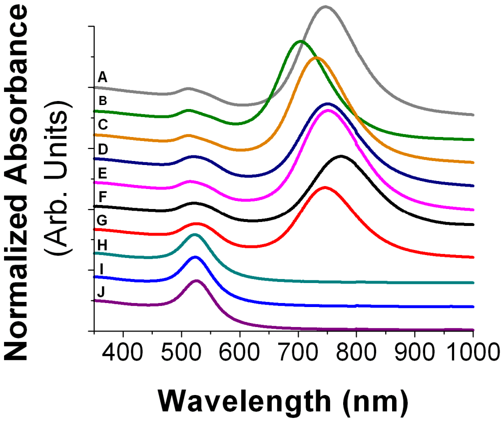

Figure 3.6. Absorbance spectra of gold nanorods synthesized using the Ag(I)-assisted method with CTAB from ten different suppliers, as listed in Table 2.1: (A) Sigma (H6269); (B) Sigma (H9151); (C) Fluka (52365); (D) Fluka (52367); (E) Fluka (52369); (F) Fluka (52370); (G) MP Biomedicals; (H) Acros, (I) Sigma (H5882); (J) Aldrich. The longer wavelength peak in samples A-G indicates that nanorods formed. The peak shifts to longer wavelength with increasing nanorod length.

Table 3.1. Purity noted in the catalog and the actual lot purity of CTAB from several different suppliers that were used to synthesize gold nanorods.

Sample	Supplier	Product #	Nanorods? [a)]	Catalog Purity	Actual Lot Purity
A	Sigma	H6269	Yes	~ 99%	100.0%
B	Sigma	H9151	Yes	~ 99%	100.3%
C	Fluka	52365	Yes	≥ 99%	99.4%
D	Fluka	52367	Yes	≥ 99%	99.7%
E	Fluka	52369	Yes	≥ 99%	99.7%
F	Fluka	52370	Yes	≥ 96%	97.1%
G	MP Biomedicals	194004	Yes	> 98%	98.9%
H	Acros	22716V	No	≥ 99%	99.0%
I	Sigma	H5882	No	≥ 99%	100%
J	Aldrich	855820	No	95%	100.3%

a) Nanorod formation is revealed by the color of the solution (spheres are red, rods are light purple), the appearance of the low energy plasmon peak (at 700-800 nm) in the absorbance spectra, and confirmed by TEM imaging.

These results are rather dramatic. If the "wrong" CTAB is used, then nanorods do not form. We did not find any mention in the literature about the importance of the CTAB supplier on the synthesis and this seemed completely unexpected. Thus, we sought to identify the difference between the CTABs. Additional experiments were performed to determine if the CTAB in the seed solution or growth solution was most important to nanorod growth (See Figure 3.7). When CTAB supplied by Acros, Sigma (H5882), or Aldrich was used in the growth solution, the final product always consisted entirely of spherical particles, regardless of the CTAB used to make the gold nanocrystal seeds. On the other hand, nanorods always formed when CTAB supplied by Acros, Sigma (H5882), or Aldrich was used to make the seeds but CTAB from Fluka (52370) or MP Biomedicals was used in the growth solution. The nanorods formed in these reactions, however, made up only a small percentage of the total product and the lengths of the nanorods that formed were relatively short. This indicates that CTAB is primarily important for nanorod formation, but is also important in the production of the seed particles as well. It is possible that this data reveal that different CTABs have slightly different binding strengths to the seed particles, which can influence to growth rates of the gold nanorods during the growth step.

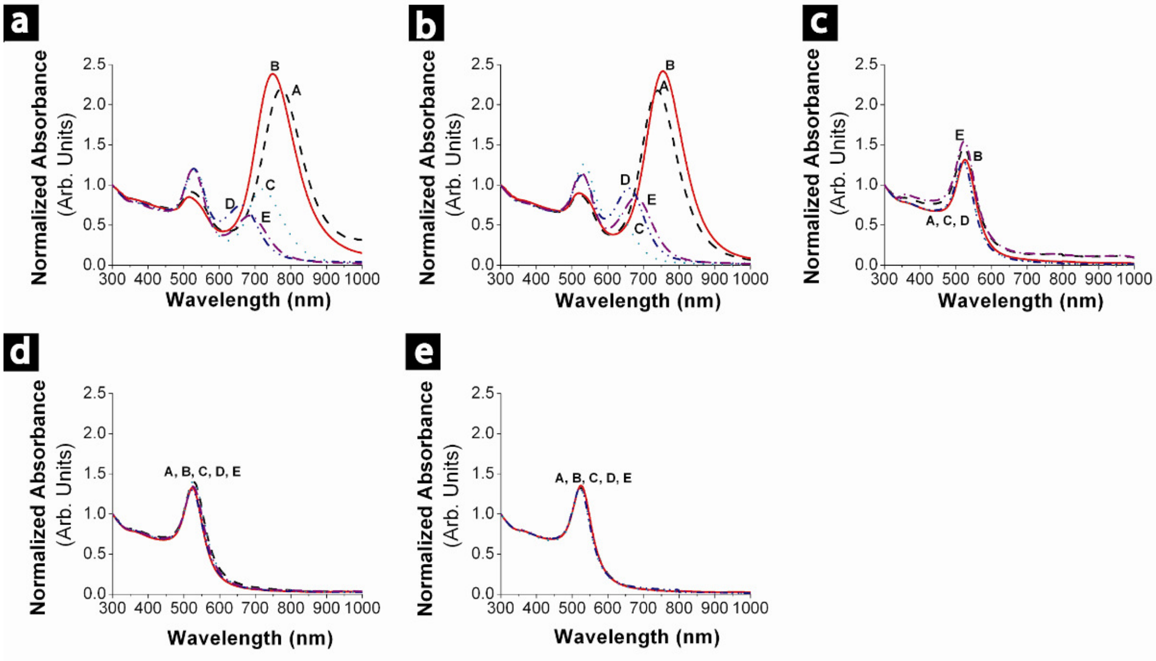

Figure 3.7. Absorbance spectra of gold nanorods produced in growth solutions made using the Ag(I)-assisted method with CTAB from five different suppliers: (a) Fluka (52370) (b) MP Biomedicals (c) Acros (d) Sigma (H5882) and (e) Aldrich. The curves labeled A-E in each plot correspond to spectra from nanorods that were made with gold seeds capped with CTAB from five different suppliers: (A) Fluka (52370); (B) MP Biomedicals; (C) Acros; (D) Sigma (H5882); (E) Aldrich.

We tried to determine if an impurity in the CTABs was giving these results and tried several different analytical techniques, including size exclusion chromatography, XRD, NMR, and mass spectrometry (see Appendix B), but did not observe any noticeable difference between the CTABs that generate nanorods and those that did not. Additionally, we tried adding different “impurities”, including NaBr, KBr, cetyldimethylamine,[54] and surfactants with differing head groups (benzyldimethylammonium, chloride (BDAC) and cetyltrimethylammonium chloride (CTAC)) in small amounts to the reactant solutions that did not yield nanorods (i.e., reactions with CTAB purchased from Sigma (H5882), Aldrich, and Acros), but we could not induce nanorod formation using any of these additives.

Finally, using inductively coupled plasma mass spectroscopy (ICP-MS), we were able to determine that an iodide impurity was present in all brands of CTAB. Table 3.2 summarizes the synthesis results and the corresponding solid CTAB/iodide concentrations determined by ICP-MS. CTAB that did not yield nanorods had significantly higher iodide concentration than CTAB that produced nanorods.

Table 3.2. Summary of nanorod growth reactions using CTAB from various suppliers and the iodide concentrations measured by ICP-MS.

Sample	**Supplier and Reported Purity**	**Product #**	**Nanorods? [1]**	**[I$^-$] (ppm) [2]**	**[I-] (μM) in the Au NR reaction [3]**
A	Sigma, ~99%	H6269	Yes	<2.75	<0.74
B	Sigma, ~99%	H9151	Yes	<2.75	<0.74
C	Fluka, ≥99%	52365	Yes	<2.75	<0.74
D	Fluka, ≥99%	52367	Yes	<2.75	<0.74
E	Fluka, ≥99%	52369	Yes	<2.75	<0.74
F	Fluka, ≥96%	52370	Yes	<2.75	<0.74
G	MP Biomedicals, >98%	194004	Yes	<2.75	<0.74
`H	Acros, , ≥99%	22716V	No	57.68	15.52
I	Sigma, ≥99%	H5882	No	839.27	225.78
J	Aldrich, 95%	855820	No	537.68	144.65

[1] Nanorod formation as evidenced by the color of the solution (spheres are red, rods are light purple), the presence of the low energy plasmon peak at 700~800 nm in the absorbance spectra, and the observation of nanorods in TEM images.

[2] Iodide concentration in solid CTAB measured by ICP-MS after correction for all dilutions (per methods). Samples 1-8 had [I-] ppb levels below the detection limit of 1.35 ppb, which corresponds to a 2.75 ppm limit when dilution factor corrected.

[3] The [I-] (μM) concentration in the (~10 mL) growth solution were calculated using the solid CTAB concentrations [I-] (ppm) determined from ICP-MS.

To confirm that iodide was indeed preventing nanorod growth, potassium iodide (KI) was added in controlled amounts to growth solutions with “good” CTAB prior to nanorod growth. Figure 3.8 shows absorbance spectra of the nanorod products obtained with varying KI concentration. The longer wavelength plasmon peak shifted to shorter wavelength as more KI was added to the reaction, indicating that the nanorod aspect ratio was decreased by increased I- concentration. The longer wavelength plasmon peak was absent when iodide concentrations in the growth solutions exceeded 0.57 μM, indicating that nanorods did not form under these conditions. This iodide concentration agrees with the ICP-MS measurements showing that the I^- concentration in the CTABs that do not work to make nanorods falls within a 0.57 to 860 μM range on a per reaction basis. (See Table 3.2). When iodide concentrations were further increased, above ~1720 μM, nanorods were observed to form again, but with relatively low yield and a large proportion of spherical nanocrystals.

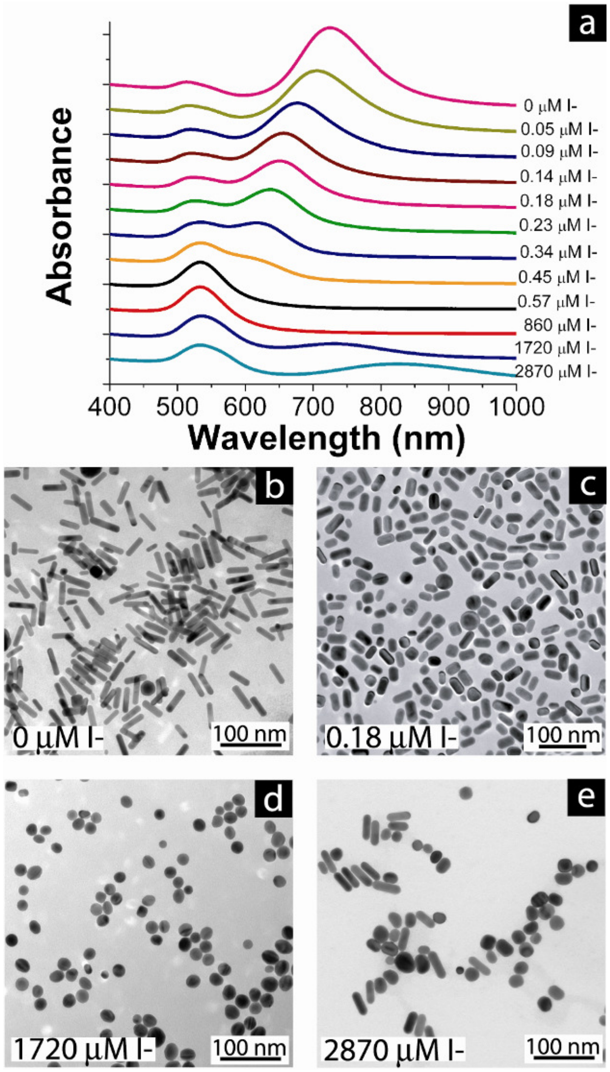

Figure 3.8. (a) Absorbance spectra and (b-e) TEM images of Au nanorods synthesized by the Ag(I)-assisted growth method with KI added to the growth solution. The iodide concentration in the growth solution is indicated next to each spectrum in (a).

3.3.3 Iodide Addition to CTAB-stabilized Au Nanorods

Iodide was also found to disrupt dispersions of Au nanorods. Figure 3.9 shows absorbance spectra and TEM images of Au nanorods after adding KI to dispersions at different concentrations. Iodide was found to transform the nanorods into spherical particles and cause aggregation, as has previously been reported.[55-57] Iodide adsorption competes with CTAB adsorption on the Au surface and displaces the capping ligands to destabilize the nanorod shape and dispersion stability.

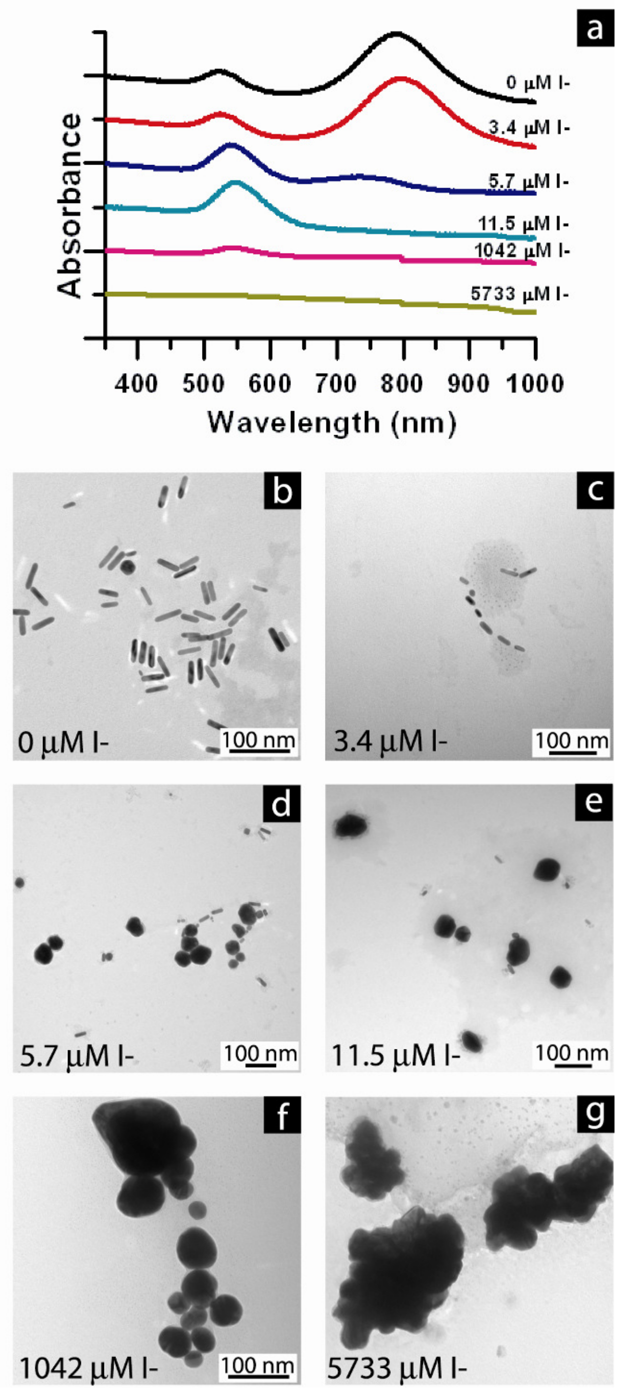

Figure 3.9. (a) Absorbance spectra and (b-g) TEM images of Au nanorods after adding KI to their dispersions. Iodide concentrations are provided next to each spectrum in (a).

3.3.4. The Role of Iodide in the Ag(I)-assisted versus Step-wise Additive Synthesis of Au Nanorods

Millstone, et al.[50] recently reported that iodide was *required* to form Au nanorods. Our results clearly contradict that assertion. In agreement with our ICP-MS findings, Millstone et al.[50] reported that iodide is present as a contaminant in CTAB from some suppliers and then studied the influence of iodide on nanorod formation. However, they were making Au nanorods by the step-wise additive growth method and not the Ag(I) assisted growth method.[58] This is a very important difference that explains the different conclusion drawn from their study.

Both Au nanorod synthesis approaches use gold nanocrystals (2~4 nm in diameter) to seed nanorod formation and CTAB to stabilize the nanorods; however, as illustrated in Figure 3.2 there are important differences in the chemistry of these two methods:

(1) The seed particles in the Ag(I)-assisted growth method are stabilized with CTAB, while the seed particles in the step-wise additive growth method are stabilized by citrate;

(2) In the Ag(I)-assisted growth method, seed particles are added to only one growth solution, while the step-wise additive growth method relies on transferring seed particles to a series of three different growth solutions;

(3) The growth solution in the Ag(I)-assisted growth method contains $AgNO_3$.

A much higher yield of monodisperse Au nanorods is obtained with the Ag(I)-assisted approach.[52, 59] As an illustration of this, Figure 3.10 shows absorbance spectra and TEM images of Au nanorods synthesized by the two methods. The longer wavelength plasmon peak in the absorbance spectra is associated with the nanorod length and its energy is determined by the nanorod aspect ratio (length/width ratio),[40-44] while the shorter wavelength peak arises from either spherical particles or from the plasmon resonating within the width of the nanorods. The relative heights of the two plasmon peaks indicate how many spherical particles are in the sample. The nanorods made by the Ag(I)-assisted approach exhibit a much more intense longer wavelength plasmon peak than the nanorods made by the step-wise additive method, clearly indicating a much higher concentration of nanorods. TEM images of the two nanorod samples corroborate that interpretation of the spectra.

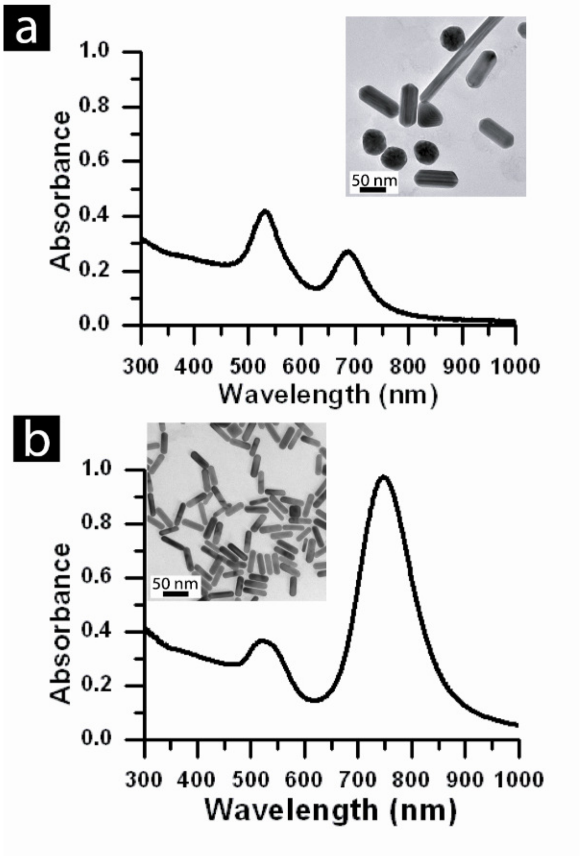

Figure 3.10. Absorbance spectra and TEM images (insets) of Au nanorods made by the (a) step-wise additive and (b) Ag(I)-assisted syntheses.

Confirmation that the two methods yield nanorods by different mechanisms is provided by the fact that the nanorods exhibit different growth directions: the Ag(I)-assisted nanorods are extended in the [100] direction and the step-wise additive nanorods grow in the [110] direction.[38, 39] Facet-selective Ag(I) underpotential deposition (UPD) on {110} Au facets promotes crystallization in the [100] direction[38] whereas the pentafold twin-induced growth of nanorods in the absence of Ag(I) occurs in the [110] direction.[39, 40, 60] Figure 3.11 shows TEM images of Au nanorods made using the two different methods.

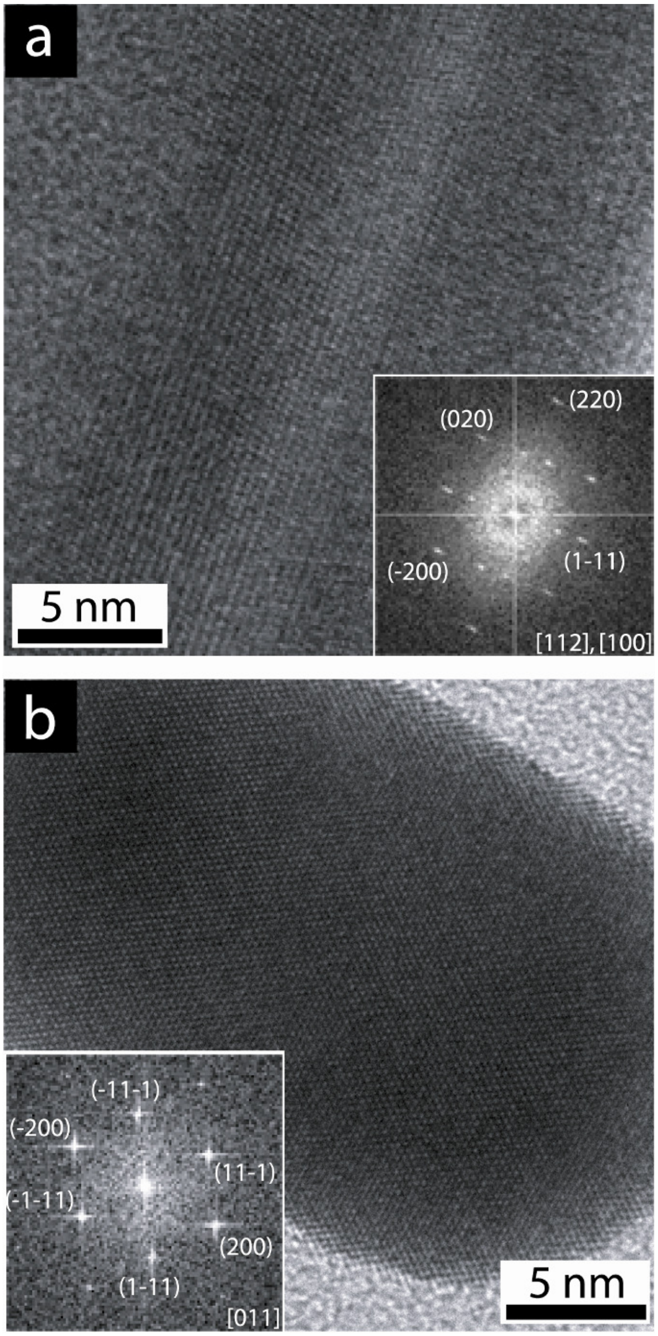

Figure 3.11. TEM images of Au nanorods synthesized by the (a) step-wise additive or (b) Ag(I)-assisted growth methods. (Insets) FFTs of the TEM images; zone axes are indicated in the bottom right. Figure 3.11a shows the superposition of two crystallographic zone axes, the [112] and [100] which has been previously observed for twinned nanorods made using the step-wise additive growth method.[23]

Although the yield of nanorods is low even in the absence of iodide in the step-wise additive synthesis, iodide addition to the growth solution further decreases the amount of nanorods obtained. When 5 µM I- was in the growth solution, the longer wavelength plasmon peak was absent, indicating that nanorods did not form. Consistent with Millstone,[50] the formation of some triangular nanoprisms was also observed with increasing I^- concentration, however, spherical nanocrystals were still the major product.

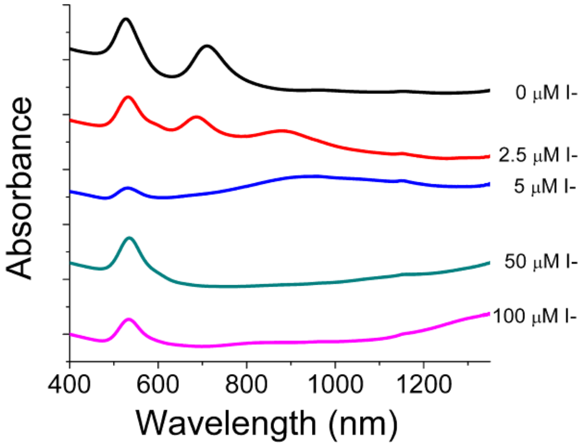

Figure 3.12. Absorbance spectra and of Au nanorods synthesized by the step-wise additive method with KI added to the growth solution. The iodide concentration in the growth solution is indicated next to each spectrum.

Four possible mechanisms exist by which iodide can affect gold nanorod formation.

(1) Iodide can etch the Au seed surfaces.

(2) I^- and Ag^+ can combine to form AgI nanocrystals that can seed Au nanocrystal formation and end up competing with Au seeds as sites for Au deposition. The presence of AgI would also reduce the amount of Ag available for UPD on the Au {110} surface.

(3) Iodide can act as a redox agent, changing the reduction rate of Au(III) to Au^0.

(4) Iodide can preferentially bind to Au {111} surfaces and prevent further Au deposition on this facet.

The use of iodine/potassium iodide solutions as gold etchants are well established[61-64] and have even been implemented in nanoscale systems.[65, 66] However, it is unlikely that iodide impurities present in CTAB are etching the gold surfaces during nanorod formation, because well-dispersed spherical nanocrystals are still produced in the reaction, indicating that the CTAB capping ligand layer has not been disrupted or the seeds etched to molecular byproducts. However, this etchant model may apply to the iodide-induced aggregation of nanorods post-synthesis. Iodide chemisorption displaces CTAB capping ligands on the Au surface, destabilizing the nanorod shape and promoting their aggregation and coalescence.

Grzelczak et al. recently published a report about the effect of iodide ions on the seeded growth of pre-formed gold nanorods made with Ag.[67] They found that when KI was present in the growth solution at low concentrations, the pre-formed nanorods became dumbbell shaped, indicating that gold salt reduction took place preferentially at the nanorod tips. When excess iodide was present in the growth solution, homogeneous rod growth was observed. The authors proposed a model whereby low concentrations of iodide bind preferentially to Au {111}, creating AuI and AgI on this facet, which lowers its redox potential. Thus when ascorbic acid was added, gold ions were reduced preferentially at the {111} resulting in dumbbell formation. When the iodide concentrations in the growth solution were higher, AgI deposited on all surfaces, resulting in homogeneous rod growth.

We considered the formation of insoluble AgI nanoparticles in the nanorod growth solution as an explanation for the blueshifting the second plasmon peak with increasing iodide concentration as shown in Figure 2. AgI formation would be analogous to AgBr formation, which has been proposed.[37, 68, 69] and observed[70] on Au nanorod surfaces. Formation of AgI would reduce the availability of Ag for UPD on Au {110} and thus lead to shorter nanorods or isotropic nanocrystal formation, as well as lower the redox potential[71] of Au(III) and increase the reaction kinetics. To examine this possibility, time dependent absorbance measurements at 400 nm were performed to study the Au^0 concentration[72, 73] (and thus the reduction rate of Au(III)) in nanorod growth solutions with and without iodide. However, increasing iodide concentration slowed the rate of Au(III) reduction, suggesting that AgI formation does not occur to a significant extent but that the presence of iodide does influence the reduction rate of Au(III) to Au^0.

Iodide is known to form strongly bound adlayers on Au surfaces[74-80] and others have also reported that iodide present in the growth solution can change the shape of gold nanocrystals.[48, 49] Rai et al.[49] found that 10^{-3} M iodide in the growth solution prevented nanotriangle formation and led to aggregated spherical nanocrystals. Ha et al.[48] added 20 μM iodide to an Au nanorod synthesis and found that nanotriangles formed instead of nanorods. Similar to Millstone et al., Rai and Ha did not add Ag(I) to their growth solutions. Some authors[48, 50] suggested that the data from Rai et al. and Ha et al. are contradictory. However, Rai and Ha used significantly different iodide concentrations, and as pointed out by Ha et al., the experimental details of the syntheses are not the same and. Our results in fact agree with both reports of Rai and Ha. Consistent with Rai et al., we found that 10 mM KI in the Au nanorod growth solution led to spherical nanocrystals. Consistent with the <5 uM iodide concentration reported by Ha et al., we observed that low iodide concentrations (570 nM) inhibit nanorod formation (see Figure 3.8). However, Ha et al. found in their experiments that triangular nanoprisms formed (with 20 μM I^-), whereas we only observed spherical nanocrystals at similar iodide concentrations. This difference stems from the fact that Ha et al. did not add Ag(I) and had excess ascorbic acid in their growth solution. When we performed an experiment adding 20 μM KI to an Au nanorod reaction without silver and with excess ascorbic acid, we also observed similar triangular nanoprisms.

Ha et al. first proposed that inhibition of Au deposition can result from strongly bound iodide ions on Au {111}.[48] Millstone later proposed that I^- can selectively bind to {111} faces of Au, which disrupts the CTAB bilayer formation on {111} Au facets and *gives rise* to Au nanorod growth in the [111] direction[50] (it should be noted that [111] growth directions have not been observed for Au nanorods.) However, based on our observations it appears that iodide adsorption on {111} Au facets is in fact preventing nanorod elongation. In both the Ag(I)-assisted and step-wise additive approaches, {111} surfaces are exposed at the tips of the Au nanorods (see Figure 3.13) and Au must deposit onto these surfaces for nanorods to grow. Au deposition is slowed significantly when the {111} facets are terminated by I^-; thus, explaining why CTAB with relatively high concentrations of iodide impurity does not yield Au nanorods.

Nanorods can still form in the presence of low concentrations of iodide when there is only partial surface coverage of the Au {111} surfaces; however, the resulting nanorods have shorter aspect ratios. Note the blueshift of the second plasmon peak with increasing iodide concentration in Figure 3.8. But once iodide completely covers the Au {111} surfaces, nanorod growth cannot occur. Therefore, because a smaller area of the tip is {111} in the Ag-assisted method, this procedure is more sensitive to iodide binding to the {111} than the step-wise additive method, as it requires less iodide to completely cover all the {111} facets.

Grzelczak et al. also did control experiments with KI using penta-twinned nanorods made in the absence of Ag as seeds for further gold overgrowth.[67] In this case, dumbbells did not form but the nanorod width increased while the length remained constant. This result indicate that iodide ions will completely block the {111} facets at the nanorod tips from further Au deposition when Ag is not present, which agrees with our proposed model.

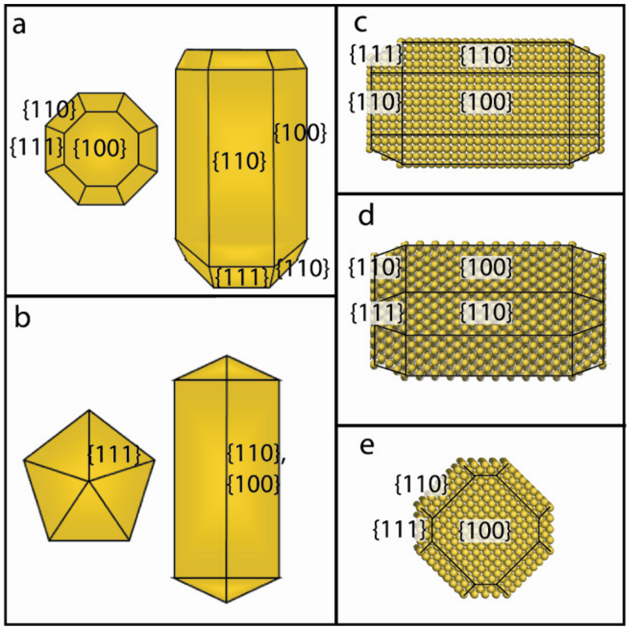

Figure 3.13. Top (left) and side (right) view of an Au nanorod synthesized with the (a) Ag(I)-assisted method or (b) step-wise additive method with the exposed facets labeled. Crystallographic models of an Au nanorod synthesized with the Ag(I)-assisted growth method on its (c) {100} side facet, (d) {110} side facet, or (e) {100} bottom facet.

3.4 CONCLUSION

Iodide disrupts the formation of Au nanorods made by seed-mediated, silver- and CTAB-assisted arrested precipitation. Iodide impurities at ppm concentrations present in CTAB obtained from some chemical suppliers prevent nanorod growth and yield only spherical nanocrystals. In the Ag(I)-assisted growth of Au nanorods, Ag UPD on {110} Au surfaces prevents Au deposition on these surfaces and leads to nanorod growth in the

[100] direction. Iodide adsorption on the growth facets prevents nanorod growth. Iodide adsorption was also found to prevent nanorod growth in the absence of Ag(I), as in the case of the step-wise additive growth process in which nanorod formation is induced by five-fold twin defects.

We note that the literature contains reports of gold nanorod synthesis using CTAB purchased from Acros[81] and Aldrich, [41,-44, 48, 52, 82-88] which we were never able to use to synthesize nanorods. This suggests that the presence of iodide impurities in the CTAB from a particular supplier can vary from lot to lot. Only three papers report the synthesis of nanorods using Fluka CTAB[37, 38, 89] while several use Sigma[27, 51, , 90-97] or other suppliers.[54, 98]

Our findings add to the mounting evidence that demonstrates how low concentration impurities can play a determining role in the shape of nanocrystals made by arrested precipitation. For example, adventitious impurities in tri-n-octylphosphine oxide (TOPO) are known to influence the synthesis of CdSe nanorods and nanowires.[13, 99] Peng, *et al.*[13] found that in the case of CdSe nanorods grown by high temperature arrested precipitation in the coordinating solvent, trioctylphosphine oxide (TOPO), that an impurity was needed to induce their formation. Without this impurity in the TOPO—which turns out to be a phosphonic acid—the particle growth rates were much faster and only spherical CdSe nanocrystals would form. The impurity in this case, slowed down nanocrystal growth and helped along the formation of the nanorods. In the case of Au nanorod growth, very low concentrations of iodide will prevent nanorod formation.

3.4 REFERENCES

1. Peng, X. G. *Adv. Mater.* **2003,** *15*, 459-463.

2. Lee, D. C.; Smith, D. K.; Heitsch, A. T.; Korgel, B. A. *Annu. Rep. Prog. Chem., Sect. C: Phys. Chem.* **2007,** *103*, 351-402.

3. Kwon, S. G.; Hyeon, T. *Acc. Chem. Res.* **2008,** *41*, 1696-1709.

4. Yin, Y.; Alivisatos, A. P. *Nature* **2005,** *437*, 664-670.

5. Lee, S. M.; Cho, S. N.; Cheon, J. *Adv. Mater.* **2003,** *15*, 441-444.

6. Cordente, N.; Respaud, M.; Senocq, F.; Casanove, M.-J.; Amiens, C.; Chaudret, B. **2001,** *1*, 565-568.

7. Brust, M.; Walker, M.; Bethell, D.; Schiffrin, D. J.; Whyman, R. *J. Chem. Soc.-Chem. Commun.* **1994,** 801-802.

8. Saunders, A. E.; Sigman, M. B.; Korgel, B. A. **2004,** *108*, 193-199.

9. Shah, P. S.; Husain, S.; Johnston, K. P.; Korgel, B. A. **2001,** *105*, 9433-9440.

10. Whetten, R. L.; Shafigullin, M. N.; Khoury, J. T.; Schaaff, T. G.; Vezmar, I.; Alvarez, M. M.; Wilkinson, A. *Acc. Chem. Res.* **1999,** *32*, 397-406.

11. Park, J.; Koo, B.; Yoon, K. Y.; Hwang, Y.; Kang, M.; Park, J.-G.; Hyeon, T. **2005,** *127*, 8433-8440.

12. Seo, J.-w.; Jun, Y.-w.; Ko, S. J.; Cheon, J. **2005,** *109*, 5389-5391.

13. Peng, X. G.; Manna, L.; Yang, W. D.; Wickham, J.; Scher, E.; Kadavanich, A.; Alivisatos, A. P. *Nature* **2000,** *404*, 59-61.

14. Shieh, F.; Saunders, A. E.; Korgel, B. A. *J. Phys. Chem. B* **2005,** *109*, 8538-8542.

15. Carbone, L.; Nobile, C.; De Giorgi, M.; Sala, F. D.; Morello, G.; Pompa, P.; Hytch, M.; Snoeck, E.; Fiore, A.; Franchini, I. R.; Nadasan, M.; Silvestre, A. F.; Chiodo, L.; Kudera, S.; Cingolani, R.; Krahne, R.; Manna, L. *Nano Lett.* **2007,** *7*, 2942-2950.

16. Kan, S.; Mokari, T.; Rothenberg, E.; Banin, U. *Nat. Mater.* **2003,** *2*, 155-158.

17. Murray, C. B.; Norris, D. J.; Bawendi, M. G. *J. Am. Chem. Soc.* **1993,** *115*, 8706-8715.

18. Peng, Z. A.; Peng, X. G. *J. Am. Chem. Soc.* **2002,** *124*, 3343-3353.

19. Yong, K.-T.; Sahoo, Y.; Choudhury, K. R.; Swihart, M. T.; Minter, J. R.; Prasad, P. N. **2006,** *6*, 709-714.

20. Burda, C.; Chen, X.; Narayanan, R.; El-Sayed, M. A. *Chemical Reviews* **2005,** *105*, 1025-1102.

21. Link, S.; El-Sayed, M. A. *Annu. Rev. Phys. Chem.* **2003,** *54*, 331.

22. Schwartzberg, A. M.; Zhang, J. Z. *J. Phys. Chem. C* **2008,** *112*, 10323-10337.

23. Stewart, M. E.; Anderton, C. R.; Thompson, L. B.; Maria, J.; Gray, S. K.; Rogers, J. A.; Nuzzo, R. G. *Chemical Reviews* **2008,** *108*, 494-521.

24. Xia, Y. N.; Halas, N. J. *MRS Bulletin* **2005,** *30*, 338-344.

25. Weissleder, R. *Nat. Biotechnol.* **2001,** *19*, 316-317.

26. Huang, X. H.; El-Sayed, I. H.; Qian, W.; El-Sayed, M. A. *J. Am. Chem. Soc.* **2006,** *128*, 2115-2120.

27. Huang, X. H.; El-Sayed, I. H.; Qian, W.; El-Sayed, M. A. *Nano Lett.* **2007,** *7*, 1591-1597.

28. Ding, H.; Yong, K. T.; Roy, I.; Pudavar, H. E.; Law, W. C.; Bergey, E. J.; Prasad, P. N. *J. Phys. Chem. C* **2007,** *111*, 12552-12557.

29. Yu, C. X.; Nakshatri, H.; Irudayaraj, J. *Nano Lett.* **2007,** *7*, 2300-2306.

30. Yu, C. X.; Varghese, L.; Irudayaraj, J. *Langmuir* **2007,** *23*, 9114-9119.

31. Durr, N. J.; Larson, T.; Smith, D. K.; Korgel, B. A.; Sokolov, K.; Ben-Yakar, A. *Nano Lett.* **2007,** *7*, 941-945.

32. Cytotoxicity is a complicated issue. Gold itself is biocompatible,[9] but CTAB is toxic,[10,11] therefore CTAB-coated gold nanorods may in fact not be useful for *in vivo* diagnostics and therapy.

33. Connor, E. E.; Mwamuka, J.; Gole, A.; Murphy, C. J.; Wyatt, M. D. *Small* **2005,** *1*, 325-327.

34. Cortesi, R.; Esposito, E.; Menegatti, E.; Gambari, R.; Nastruzzi, C. *Int. J. Pharm.* **1996,** *139*, 69-78.

35. Mirska, D.; Schirmer, K.; Funari, S. S.; Langer, A.; Dobner, B.; Brezesinski, G. *Colloid Surface B* **2005,** *40*, 51-59.

36. Jana, N. R.; Gearheart, L.; Murphy, C. J. *J. Phys. Chem. B* **2001,** *105*, 4065-4067.

37. Nikoobakht, B.; El-Sayed, M. A. *Chem. Mater.* **2003,** *15*, 1957-1962.

38. Liu, M. Z.; Guyot-Sionnest, P. *J. Phys. Chem. B* **2005,** *109*, 22192-22200.

39. Johnson, C. J.; Dujardin, E.; Davis, S. A.; Murphy, C. J.; Mann, S. *J. Mater. Chem.* **2002,** *12*, 1765-1770.

40. Lofton, C.; Sigmund, W. *Adv. Funct. Mater.* **2005,** *15*, 1197-1208.

41. Jiang, X. C.; Pileni, M. P. *Colloid Surface A* **2007,** *295*, 228-232.

42. Jiang, X. C.; Brioude, A.; Pileni, M. P. *Colloids Surface* **2006,** *277*, 201-206.

43. Perez-Juste, J.; Liz-Marzan, L. M.; Carnie, S.; Chan, D. Y. C.; Mulvaney, P. *Adv. Funct. Mater.* **2004,** *14*, 571-579.

44. Gao, J. X.; Bender, C. M.; Murphy, C. J. *Langmuir* **2003,** *19*, 9065-9070.

45. Hubert, F.; Testard, F.; Spalla, O. *Langmuir* **2008,** *24*, 9219-9222.

46. Nikoobakht, B.; El-Sayed, M. A. *Langmuir* **2001,** *17*, 6368-6374.

47. Smith, D. K.; Korgel, B. A. *Langmuir* **2008,** *24*, 644-649.

48. Ha, T. H.; Koo, H. J.; Chung, B. H. *J. Phys. Chem. C* **2007,** *111*, 1123-1130.

49. Rai, A.; Singh, A.; Ahmad, A.; Sastry, M. *Langmuir* **2006,** *22*, 736-741.

50. Millstone, J. E.; Wei, W.; Jones, M. R.; Yoo, H. J.; Mirkin, C. A. *Nano Lett.* **2008,** *8*, 2526-2529.

51. Gou, L. F.; Murphy, C. J. *Chem. Mater.* **2005,** *17*, 3668-3672.

52. Busbee, B. D.; Obare, S. O.; Murphy, C. J. *Adv. Mater.* **2003,** *15*, 414-416.

53. Murphy, C. J.; Sau, T. K.; Gole, A. M.; Orendorff, C. J.; Gao, J.; Gou, L.; Hunyadi, S. E.; Li, T. *J. Phys. Chem. B* **2005,** *109*, 13857-13870.

54. Zweifel, D. A.; Wei, A. *Chem. Mater.* **2005,** *17*, 4256-4261.

55. Cheng, W. L.; Dong, S. J.; Wang, E. K. *Angew. Chem., Int. Ed.* **2003,** *42*, 449-452.

56. Singh, S.; Pasricha, R.; Bhatta, U. M.; Satyam, P. V.; Sastry, M.; Prasad, B. L. V. *J. Mater. Chem.* **2007,** *17*, 1614-1619.

57. Wang, J.; Li, Y. F.; Huang, C. Z. *J. Phys. Chem. C* **2008,** *112*, 11691-11695.

58. Millstone also stated that I^- can selectively bind to {111} faces of Au, thus disrupting CTAB bilayer formation on {111} Au facets and giving rise to Au nanorod growth in the [111] direction. [111] growth directions have not been observed for Au nanorods.

59. The Ag(I)-assisted approach to Au nanorod synthesis has been cited 150 more times than the step-wise additive growth method. The Ag(I)-assisted approach, however, cannot produce nanorods with aspect ratios greater than ~5; whereas the step-wise additive approach has been reported to yield nanorods with aspect ratios as high as 19.[52] But the problem is that the yields of nanorods from the synthesis using the step-wise additive growth method are very low, with significant amounts of nanocrystals that are not rod-shaped.

60. Grzelczak, M.; Perez-Juste, J.; Mulvaney, P.; Liz-Marzan, L. M. *Chem. Soc. Rev.* **2008,** *37*, 1783-1791.

61. McGrew, K. J.; Murphy, J. W. Iodine leach for the dissolution of gold. US Patent 4557759, **1985**.

62. Pal, T.; Jana, N. R.; Sau, T. K. *Corros. Sci.* **1997,** *39*, 981-986.

63. Umeno, A.; Hirakawa, K. *Appl. Phys. Lett.* **2005,** *86*.

64. Yoshimatsu, N.; Kawasaki, T.; Ban, K.; Kusaka, T.; Ikeda, T. E. *J. Surf. Sci. Nanotechnol.* **2005,** *3*, 524-526.

65. Cho, E. C.; Xie, J. W.; Wurm, P. A.; Xia, Y. N. *Nano. Lett.* **2009**, *9*, 1080-1084.

66. Figuerola, A.; Franchini, I. R.; Fiore, A.; Mastria, R.; Falqui, A.; Bertoni, G.; Bals, S.; Van Tendeloo, G.; Kudera, S.; Cingolani, R.; Manna, L. *Adv. Mater.* **2009,** *21*, 550-554.

67. Grzelczak, M.; Sanchez-Iglesias, A.; Rodriguez-Gonzalez, B.; Alvarez-Puebla, R.; Perez-Juste, J.; Liz-Marzan, L. M. *Adv. Funct. Mater.* **2008,** *18*, 3780-3786.

68. Jana, N. R.; Gearheart, L.; Murphy, C. J. *Adv. Mater.* **2001,** *13*, 1389-1393.

69. Sau, T. K.; Murphy, C. J. *Langmuir* **2004,** *20*, 6414-6420.

70. Niidome, Y.; Nakamura, Y.; Honda, K.; Akiyama, Y.; Nishioka, K.; Kawasaki, H.; Nakashima, N. *Chem. Commun.* **2009,** *13*, 1754-1756.

71. Sibbald, M. S.; Chumanov, G.; Cotton, T. M. *J. Phys. Chem.* **1996,** *100*, 4672-4678.

72. Rodriguez-Fernandez, J.; Perez-Juste, J.; Mulvaney, P.; Liz-Marzan, L. M. *J. Phys. Chem. B* **2005,** *109*, 14257-14261.

73. Grzelczak, M.; Perez-Juste, J.; Rodriguez-Gonzalez, B.; Liz-Marzan, L. M. *J. Mater. Chem.* **2006,** *16*, 3946-3951.

74. Bravo, B. G.; Michelhaugh, S. L.; Soriaga, M. P.; Villegas, I.; Suggs, D. W.; Stickney, J. L. *J. Phys. Chem.* **1991,** *95*, 5245-5249.

75. Gao, X. P.; Edens, G. J.; Liu, F. C.; Hamelin, A.; Weaver, M. J. *J. Phys. Chem.* **1994,** *98*, 8086-8095.

76. Gao, X. P.; Edens, G. J.; Weaver, M. J. *J. Phys. Chem.* **1994,** *98*, 8074-8085.

77. Gao, X. P.; Weaver, M. J. *J. Am. Chem. Soc.* **1992,** *114*, 8544-8551.

78. McCarley, R. L.; Bard, A. J. *J. Phys. Chem.* **1991,** *95*, 9618-9620.

79. Tao, N. J.; Lindsay, S. M. *J. Phys. Chem.* **1992,** *96*, 5213-5217.

80. Wang, J. X.; Watson, G. M.; Ocko, B. M. *J. Phys. Chem.* **1996,** *100*, 6672-6677.

81. Yang, Z. S.; Lin, Y. W.; Tseng, W. L.; Chang, H. T. *J. Mater. Chem.* **2005,** *15*, 2450-2454.

82. Spuch-Calvar, M.; Perez-Juste, J.; Liz-Marzan, L. M. *J. Colloid Interface Sci.* **2007,** *310*, 297-301.

83. Kou, X. S.; Zhang, S. Z.; Tsung, C. K.; Yang, Z.; Yeung, M. H.; Stucky, G. D.; Sun, L. D.; Wang, J. F.; Yan, C. H. *Chem-Eur. J.* **2007,** *13*, 2929-2936.

84. Vial, S.; Pastoriza-Santos, I.; Perez-Juste, J.; Liz-Marzan, L. M. *Langmuir* **2007,** *23*, 4606-4611.

85. Iqbal, M.; Chung, Y. I.; Tae, G. *J. Mater. Chem.* **2007,** *17*, 335-342.

86. Wu, H. Y.; Huang, W. L.; Huang, M. H. *Cryst. Growth Des.* **2007,** *7*, 831-835.

87. Yu, C. X.; Irudayaraj, J. *Anal. Chem.* **2007,** *79*, 572-579.

88. Khanal, B. P.; Zubarev, E. R. *Angew. Chem. Int. Edit.* **2007,** *46*, 2195-2198.

89. Miranda, O. R.; Dollahon, N. R.; Ahmadi, T. S. *Cryst. Growth Des.* **2006,** *6*, 2747-2753.

90. Orendorff, C. J.; Murphy, C. J. *J. Phys. Chem. B* **2006,** *110*, 3990-3994.

91. Park, H. J.; Ah, C. S.; Kim, W. J.; Choi, I. S.; Lee, K. P.; Yun, W. S. *J. Vac. Sci. Technol. A* **2006,** *24*, 1323-1326.

92. Gole, A.; Murphy, C. J. *Chem. Mater.* **2004,** *16*, 3633-3640.

93. Gole, A.; Murphy, C. J. *Langmuir* **2005,** *21*, 10756-10762.

94. Gole, A.; Murphy, C. J. *Chem. Mater.* **2005,** *17*, 1325-1330.

95. Orendorff, C. J.; Hankins, P. L.; Murphy, C. J. *Langmuir* **2005,** *21*, 2022-2026.

96. Jebb, M.; Sudeep, P. K.; Pramod, P.; Thomas, K. G.; Kamat, P. V. *J. Phys. Chem. B* **2007,** *111*, 6839-6844.

97. Pierrat, S.; Zins, I.; Breivogel, A.; Sonnichsen, C. *Nano Lett.* **2007,** *7*, 259-263.

98. Wang, C. G.; Wang, T. T.; Ma, Z. F.; Su, Z. M. *Nanotechnology* **2005,** *16*, 2555-2560.

99. Wang, F. D.; Tang, R.; Buhro, W. E. *Nano Lett.* **2008,** *8*, 3521-3524.

Chapter 4: Multifunctional Particles: Magnetic Nanocrystals and Gold Nanorods Coated with Fluorescent Dye-Doped Silica Shells

Reproduced in part with permission from: Heitsch, A.T.†; Smith, D.K. †; Patel, R.N.; Ress, D.; and Korgel, B.K. "Multifunctional particles: Magnetic nanocrystals and gold nanorods coated with fluorescent dye-doped silica shells." *Journal of Solid State Chemistry*, **2008**, *181*, 1593-1602. Copyright 2008 Elsevier.
†These authors contributed equally to this work.

4.1 INTRODUCTION

Colloidal nanoparticles are useful tools for studying biological systems.[1-3] Their size is similar to biological macromolecules[3,4] and their surfaces provide a bioconjugation scaffold to tether biocompatible coatings[2,5,6] and biologically-relevant recognition molecules like nucleic acids,[6,7] peptide fragments,[4] and antibodies.[2,3,8] Nanoparticles can be used to map cellular components and monitor and track them in real time[5,9] and can also be used as drug delivery vehicles[10,11] and therapeutic agents.[12-14] For example, superparamagnetic iron oxide nanoparticles are commercially available as magnetic resonance imaging (MRI) contrast agents;[15,16] although higher contrast is still desired and new magnetic nanoparticles are being studied and developed for these purposes.[17-21] Recently, colloidal nanomaterials have been synthesized with complicated structure and composition, designed to exhibit multiple functionality—for example, nanoparticles that both fluoresce and respond to magnetic fields.[22,23] These multifunctional nanoparticles provide the opportunity for multiple imaging and therapeutic modalities from a single unit[23-25] for unprecedented opportunities for medical advancement.

Examples of multifunctional nanoparticles include FePt-Au heterodimers with the FePt domain for magnetic resonance imaging (MRI) contrast and Au as a docking point for thiolated polyethylene glycol and neutravidin ligands,[26] and gold nanoshells on a silica-coated iron oxide core for both MRI and photothermal therapy.[12] For combined MR and fluorescence imaging, a variety of multifunctional nanomaterials have been made, including fluorescent semiconductor nanocrystals doped with magnetic impurity atoms,[22] fluorescent dye-doped silica-coated magnetic Fe_3O_4 nanoparticles[27,28] and fluorescent dye-doped silica particles decorated with paramagnetic gadolinium[29] or iron oxide particles[30] on their surfaces. Silica has been utilized rather extensively as a nanoparticle material for biological applications[31,32] because it provides both a surface for bioconjugation and a host matrix for fluorescent molecules that can improve dye photostability and biocompatibility.[33-44] Furthermore, several strategies to coat colloidal nanocrystals with silica have also been developed in recent years,[33,47-49] which makes silica an interesting material to integrate into multifunctional heterostructure nanoparticles for biological applications.

Here, we report the coating of FePt and Fe_2O_3 nanocrystals and Au nanorods with uniform silica shells embedded with fluorescent dye. The nanocrystals or nanorods are first synthesized and then coated with silica. Two different coating techniques were utilized because the FePt and Fe_2O_3 nanocrystals are initially passivated with hydrophobic ligands and are only dispersible in organic solvents, while the Au nanorods are coated with hydrophilic ligands are disperse only in polar solvents. Both coating techniques yielded uniform silica shells with incorporated dye. The optical absorbance and luminescence of these multifunctional colloidal heterostructure nanoparticles were measured. The magnetic properties of the Fe_2O_3 and FePt core dye-doped silica shell nanoparticles are also reported and their potential suitability for use as MRI contrast agents is described.

4.2 EXPERIMENTAL SECTION

4.2.1 Materials and Supplies

All chemicals were used as received. Platinum acetylacetonate (Pt(acac)$_2$, 97%), iron pentacarbonyl (Fe(CO)$_5$, 99.999%), oleylamine (70%), oleic acid (99%), Igepal CO-520, Tris(2,2′-bipyridyl)dichlororuthenium(II) hexahydrate (Rubpy, 99.95%), fluorescein 5(6)-isothiocyanate (FITC, >90%), tetraethyl orthosilicate (TEOS, 98%), hydrogen tetrachloroaurate(III) hydrate (99.9+%), sodium borohydride (98+%), silver nitrate (99+%), cetyltrimethylammonium bromide (CTAB, batch number H6269, 99%), ascorbic acid (99+%), poly(allylamine hydrochloride) (PAH, MW 15,000), and octadecyltrimethoxysilane (OTMOS, 90%) were purchased from Sigma-Aldrich. Ethanol (ACS grade), 2-propanol (ACS grade), and chloroform (ACS grade) were purchased from Fisher Scientific. Dioctyl ether (>97%), poly(vinylpyrollidone) (PVP, MW 10,000), and cyclohexane (ACS grade) were purchased from Fluka. Poly(styrenesulfonic acid) sodium salt (PSS, MW 18,000) was purchased from Polysciences, Inc. Sodium Chloride (NaCl, 99%) was purchased from Mallinckrodt. Ammonium hydroxide (NH_4OH, aqueous solution (30%)) was purchased from EMD Chemicals. 3-aminopropyltriethoxysilane (APTES) was purchased from Gelest. Doubly-distilled deionized water (DI-H_2O) was used in all preparations. FePt and Fe_2O_3 nanocrystals were synthesized under inert (N_2) atmosphere using standard glovebox and Schlenk line techniques with continuous stirring using a Teflon-coated magnetic stir bar.

4.2.2 FePt and Fe_2O_3 Nanocrystal Synthesis

FePt nanocrystals were prepared as previously described.[50] In a 50 mL three neck flask, 0.197 g (0.50 mmol) Pt(acac)$_2$ and 10 mL of dioctyl ether were degassed under reduced pressure (200 mTorr) and at elevated temperature (45 °C) for 1 hour. This solution was heated to 120 °C under N_2 flow at atmospheric pressure. Next, 0.15 mL (1.15 mmol) $Fe(CO)_5$, 1.45 mL (4.40 mmol) oleylamine, and 1.35 mL (4.25 mmol) oleic acid were prepared in three separate syringes in a fume hood and injected into the reaction solution sequentially. Caution must be taken when preparing $Fe(CO)_5$, as it is extremely volatile and potentially hazardous (refer to MSDS before use). The temperature was raised (~15 °C/min) to 240 °C and maintained for 1 hour, before heating to reflux (~297 °C) and stirring for an additional hour. The reaction flask was cooled to room temperature.

Fe_2O_3 nanocrystals were prepared as previously described.[51] In a 25 mL three neck flask, 10 mL of dioctyl ether and 960 μL (4.56 mmol) of oleic acid were heated to 100 °C under N_2 flow at atmospheric pressure. Next, 0.2 mL (1.52 mmol) of $Fe(CO)_5$ was injected into this solution and the temperature was raised to 300 °C. The solution was refluxed for one hour before removing the reaction flask from the heating mantle and allowing it to cool to room temperature. The flask was then opened to air to oxidize the as-made Fe nanocrystals.

FePt and Fe_2O_3 nanocrystals were purified as follows. After reaching room temperature, the reaction solution was centrifuged for 5 minutes at 8000 rpm (8228 g). The precipitate—consisting of solid byproducts and poorly capped nanocrystals—was discarded. Excess ethanol was then added to the supernatant and this mixture was centrifuged for 10 minutes at 8000 rpm (8228 g) to precipitate the nanocrystals. The supernatant was discarded. The nanocrystals were further purified in two additional washing steps by redispersing in hexane followed by the addition of ethanol as an antisolvent and then centrifugation. Nanocrystals were stored as a concentrated (~10 mg/mL) dispersion in hexane for later use.

4.2.3 Gold Nanorod Synthesis

Au nanorods were synthesized as previously described.[52] Colloidal Au seed particles were first prepared by mixing an aqueous solution of CTAB (0.1 M, 9.75 mL) with hydrogen tetrachloroaurate(III) hydrate (0.01 M, 250 μL) and then adding sodium borohydride (0.01 M, 600 μL) to reduce the gold and induce seed nucleation. 12 μL of this seed solution was then injected into an aqueous growth solution of CTAB (0.1 M, 9.5 ml), silver nitrate (0.01 M, 75 μL), hydrogen tetrachloroaurate(III) hydrate (0.01 M, 500 μL), and ascorbic acid (0.1 M, 55 μL). This solution was stirred at room temperature for 24 hours.

4.2.4 Rubpy-doped silica coating of FePt and Fe_2O_3 nanocrystals and Au nanorods

FePt and Fe_2O_3 nanocrystals were encapsulated within a Rubpy doped amorphous silica (SiO_2) shell in inverse micelle microemulsion media.[34,47,53] 4 mL of Igepal CO-520 was added to 80 mL of cyclohexane in a 250 mL Erlenmeyer flask and stirred at room temperature for 5 minutes. 2 mL of a cyclohexane dispersion of FePt or Fe_2O_3 nanocrystals (5 mg/mL) was added to the 80 mL cyclohexane mixture and stirred for 5 minutes. 1.75 mg of Rubpy dissolved in 0.65 mL of aqueous NH_4OH solution (30% by volume) was added dropwise to the nanocrystal dispersion, followed by the dropwise addition of 0.75 mL of tetraethyl orthosilcate (TEOS). The mixture was stirred for 48 hours. The Rubpy-doped SiO_2-coated nanocrystals (FePt@SiO_2(Rubpy) or Fe_2O_3@SiO_2(Rubpy)) were then purified by extraction: 30 mL of methanol was added to induce phase separation between cyclohexane-rich and methanol-rich phases and the methanol-rich phase containing the nanocrystals was collected. The solvent was then partially evaporated from the nanoparticle dispersion on a rotary evaporator. Once the dispersion appeared turbid it was removed from the rotary evaporator and centrifuged for 15 minutes at 8000 rpm (8228 g). The supernatant was discarded. Excess Rubpy and surfactant were removed by redispersing the particles in 1:1 vol% methanol:hexane and then centrifuging at 8000 rpm (8228 g) for 15 minutes and discarding the supernatant. This washing procedure was repeated 5 times. The silica-coated nanocrystals were stored as a concentrated dispersion for further characterization in ethanol or DI-H_2O.

The as-prepared CTAB-coated Au nanorods disperse only in polar solvents and cannot be coated with silica in inverse micelle microemulsions. Therefore, the nanorods were coated using a modification of a previously published strategy, which utilizes the adsorption of a polyelectrolyte layer followed by a modified Stöber method for silica deposition.[48,54] 10 mL of as-synthesized Au nanorods were centrifuged at 8000 rpm (8228 g) for 15 minutes and redispersed in 5 mL of DI-H_2O. *PSS coating*: the Au nanorod dispersion was added dropwise to a 5 mL aqueous solution of 111 μM PSS and 6 mM NaCl and stirred for 3 hours. The PSS-coated Au nanorods were collected by centrifugation at 8000 rpm (8228 g) for 15 minutes. The supernatant was discarded and the nanorods were redispersed in 5 mL of DI-H_2O. *PAH coating*: the aqueous dispersion of PSS coated Au nanorods was then added dropwise to 5 mL of aqueous 133 μM PAH and 6 mM NaCl solution and stirred for 3 hours. The nanorods were precipitated by centrifugation at 8000 rpm (8228 g) for 15 minutes. The supernatant was discarded and the nanorods were then redispersed in 5 mL of DI-H_2O. *PVP coating*: the dispersion of PSS/PAH-coated Au nanorods was then added dropwise to 5 mL of aqueous 400 μM PVP solution and stirred overnight. The nanorods were precipitated by centrifugation at 8000 rpm (8228 g) for 15 minutes and the supernatant was discarded. The nanorods were redispersed in 0.1 mL of DI-H_2O. This aqueous dispersion of PSS/PAH/PVP polyelectrolyte-coated Au nanorods was added dropwise to 0.5 mL of isopropyl alcohol under vigorous stirring. 0.46 mL of DI-H_2O was then added. Separately, Rubpy was dissolved in aqueous 30 vol% NH_4OH at a concentration of 2 mg/mL. 384 μL of the

NH_4OH/Rubpy solution was mixed with 9.62 mL of isopropyl alcohol. 0.72 mL of this NH_4OH/Rubpy/isopropyl alcohol solution and 0.1 mL of a 0.97 vol% TEOS in isopropyl alcohol solution were added to the Au nanorod dispersion and stirred for 12 hours. The silica coated Au nanorods were collected by centrifuging at 8000 rpm (8228 g) for 15 minutes and the supernatant was discarded. Excess Rubpy was removed by redispersing the particles in ethanol or DI-H_2O and then centrifuging at 8000 rpm (8228 g) for 15 minutes and discarding the supernatant. This washing procedure was repeated 5 times. The silica-coated Au nanorods were stored as a concentrated dispersion for further characterization in ethanol or DI-H_2O.

In some cases, the surfaces of the silica-coated nanocrystals and nanorods were further treated by exposure to OTMOS using procedures described in the literature.[47] The silica-coated magnetic nanocrystals or Au nanorods were dispersed in 3 mL of ethanol at a concentration of 1 mg/mL and mixed with 30 μL of 30 vol% NH_4OH aqueous solution. Approximately 150 μL of 10 vol% OTMOS in chloroform was added dropwise to the nanoparticle dispersion, followed by 24 hrs of stirring. The nanoparticles were collected by centrifugation at 8000 rpm (8228 g) for 8 minutes. The nanoparticles were washed by an additional step consisting of redispersion in 1:1 vol% chloroform:ethanol and centrifuging at 8000 rpm (8228 g) for 8 minutes. The supernatant was discarded.

4.2.5 FITC-doped Silica coating of Fe_2O_3 and Au nanorods

Fe_2O_3 nanocrystals were encapsulated in silica shells doped with the dye FITC using the same inverse micelle microemulsion coating method described for the Rubpy-doped silica coatings with the exception that the dye was not dissolved in the aqueous ammonium hydroxide solution and in the final reaction step, TEOS was not immediately added. Rather, FITC was first covalently linked to the silane coupling agent APTES by dissolving 10 mg of FITC in 48 μL of APTES (a 1:4 molar ratio). Cyclohexane was then added to create a 10 vol% FITC/APTES in cyclohexane solution. This FITC/APTES/cyclohexane solution was stirred for 24 hours in the glovebox in the dark prior to use.

4 mL of Igepal CO-520 was added to 80 mL of cyclohexane in a 250 mL Erlenmeyer flask and stirred at room temperature for 5 minutes. Then 2 mL of a cyclohexane dispersion of Fe_2O_3 nanocrystals (5 mg/mL) were added to the 80 mL cyclohexane mixture and stirred for an additional 5 minutes. 750 μL of the FITC/APTES/cyclohexane solution was added dropwise to the nanocrystal dispersion, followed by the dropwise addition of 0.65 mL of aqueous ammonium hydroxide solution (30% by volume). Because the hydrolysis rate of APTES is five times slower than that of TEOS,[40] the reaction was stirred for 24 hours prior to the TEOS addition to ensure that the APTES bound to the FITC was hydrolyzed and would be incorporated in the SiO_2 shell. Then 0.75 mL of TEOS was added dropwise to the solution and then the mixture was stirred for 48 hours.

Similarly, FITC was incorporated in the silica coating on the Au nanorods by first making a FITC/APTES/ethanol solution. FITC was covalently linked to APTES by dissolving 10 mg of FITC in 48 μL of APTES (a 1:4 molar ratio). Anhydrous ethanol was then added to create a 10 vol% FITC/APTES in ethanol solution. This FITC/APTES/ethanol solution was stirred for 24 hours in the glovebox in the dark prior to use.

0.1 mL of PSS/PAH/PVP polyelectrolyte-coated Au nanorods in DI-H_2O was added dropwise to 0.5 mL of isopropyl alcohol under vigorous stirring. 0.46 mL of DI-H_2O was then added. Separately, 384 μL of the aqueous 30 vol% ammonium hydroxide was mixed with 9.62 mL of isopropyl alcohol, and 0.72 mL of this NH_4OH//isopropyl alcohol solution was added dropwise to the Au nanorod dispersion. Also in a separate flask, 100 μL of FITC/APTES/ethanol solution was mixed with 9.9 mL of isopropyl alcohol. 200 μL of this FITC/APTES/ethanol/isopropyl alcohol solution was added to the nanorod dispersion, and the reaction was stirred for 24 hours before adding 0.1 mL of a 0.97 vol% TEOS in isopropyl alcohol solution. The Au nanorod dispersion was stirred for 12 hours.

4.2.6 Transfer Printing FePt@SiO_2(Rubpy) Nanoparticles Arrays

Langmuir Blodgett films of OTMOS coated FePt@SiO_2(Rubpy) nanoparticles were made using a system 2 KSV minitrough filled with DI-H_2O. A 0.5 mg/ml solution of OTMOS coated FePt@SiO_2(Rubpy) nanoparticles in chloroform was spread drop-wise onto the water surface and the solvent was allowed to evaporate for 10 minutes (total dispersion volumes ranged from 300 to 600 μl). Films were then compressed at a rate of 5 mm/min until reaching a surface pressure of 37 mN/m. Pre-patterned poly(dimethylsiloxane) (PDMS) stamps were carefully brought into contact with the water surface to transfer the nanoparticle film to the PDMS stamp. The PDMS stamp coated with the nanoparticle monolayer was then gently brought into conformal contact with clean silicon or glass substrates. After 30 seconds of contact, the PDMS stamps were slowly removed leaving behind densely packed arrays of FePt@SiO_2(Rubpy) nanoparticles.

4.2.7 Sample Characterization

Nanoparticles were imaged using transmission electron microscopy (TEM) and scanning electron microscopy (SEM). TEM was performed using either a Phillips EM208 TEM with 80 kV accelerating voltage or a JEOL 2010F HRTEM with the field emission gun operated at 200 kV. Images were digitally acquired. TEM samples were prepared by dropcasting the nanoparticles (uncoated FePt or Fe_2O_3 were dispersed in hexane, uncoated gold nanorods were dispersed in DI-H_2O, and the Rubpy-doped silica coated nanoparticles were dispersed in ethanol) onto carbon-coated copper 200 mesh TEM grids (Electron Microscopy Sciences). EDS data were acquired on the JEOL 2010F TEM with an Oxford Inca EDS detector. SEM images were obtained from nanoparticles dropcast on silicon substrates using a Zeiss Supra 40 SEM with an in-lens arrangement at 3 keV working voltage and 5 mm lens to detector distance.

The optical properties of the nanoparticles were determined using optical fluorescence microscopy and UV-visible absorbance and photoluminescence (PL) spectroscopy. Absorbance and photoluminescence spectra were acquired at room temperature using a Varion Cary 50 Bio UV/Vis Spectrophotometer and Varion Cary Eclipse Fluorescence Spectrophotometer, with samples dispersed in water in quartz cuvettes with a 1 cm path length. Optical fluorescence microscopy was performed with a Leica DM IRBE microscope with 40X or 100X oil objective, 100 Watt Hg lamp, and 1.5" x 1.5" cover slides. The samples where excited with blue light and the emission was imaged with a black and white Leica DFC350 FX camera after filtering with a 515 nm long pass FITC filter.

The magnetization properties were measured on a superconducting quantum interference device (SQUID) magnetometer (Quantum Design). Samples were prepared by transferring 3 to 7 mg of dry SiO_2 encapsulated nanocrystals into gelatin capsules (Capsuline #4) and filling the remainder of the capsule with cotton. At applied fields of ~5 T, the magnetic signal from the FePt@SiO_2(Rubpy) or Fe_2O_3@SiO_2(Rubpy) nanoparticles was two orders of magnitude larger than the contribution from the sample holder and background; therefore, background subtraction was not necessary.

T_1 and T_2 relaxation times of the FePt@SiO_2(Rubpy) and Fe_2O_3@SiO_2(Rubpy) nanoparticles were measured by performing MRI of aqueous nanocrystal dispersions at The University of Texas at Austin Imaging Research Center on a General Electric Signa EXCITE 3 T scanner. 2 mL snap shut centrifuge tubes were completely filled with varying nanoparticle concentrations in DI-H_2O and inserted into tight fitting holes bored into solid 3" H x 6" D cylindrical shaped high density hard polymer material. The sample holder was then positioned in the center of the standard GE-product head coil. Images of all samples were obtained by prescribing a set of 2-mm-thick slices in a quasi-coronal orientation that was nearly normal to vertical axis of the sample tubes. 128×128 images were then obtained in a 160-mm field-of-view to yield 1.25-mm pixels. Imaging data was analyzed by measuring the mean intensity values averaged over a 5×5-pixel region on one slice near the center of each tube. T_1 was obtained by running inversion-prepared spin-echo sequences at minimum echo time (T_E = 50 ms), and inversion times (TI) varying from 50 to 1750 ms in eight roughly linear steps. The resulting intensity values were fit to the function $I_0\left(1-2e^{-T_I/T_1}\right)$ using the "fminsearch" non-linear optimization routine in Matlab (Mathworks Inc, Natick MA) and a least-square-error metric. T_2 was obtained by running spin-echo sequences with T_E varying from 50 to 2000 ms in eight roughly logarithmic steps, and fitting the data to an exponential decay function using non-linear optimization with a least-square-error metric.

4.3. RESULTS AND DISCUSSION

4.3.1 Synthesis and structural analysis

The as-made FePt and Fe_2O_3 nanocrystals are hydrophobic and disperse in organic solvents; whereas, the Au nanorods are hydrophilic and disperse only in polar solvents. Therefore, different silica coating methods were needed for these different classes of nanomaterials. Figure 4.1 illustrates the two coating strategies used. Magnetic nanocrystals were coated in microemulsion media and Au nanorods were coated using a modified Stöber method in a polar mixture of alcohol and water.

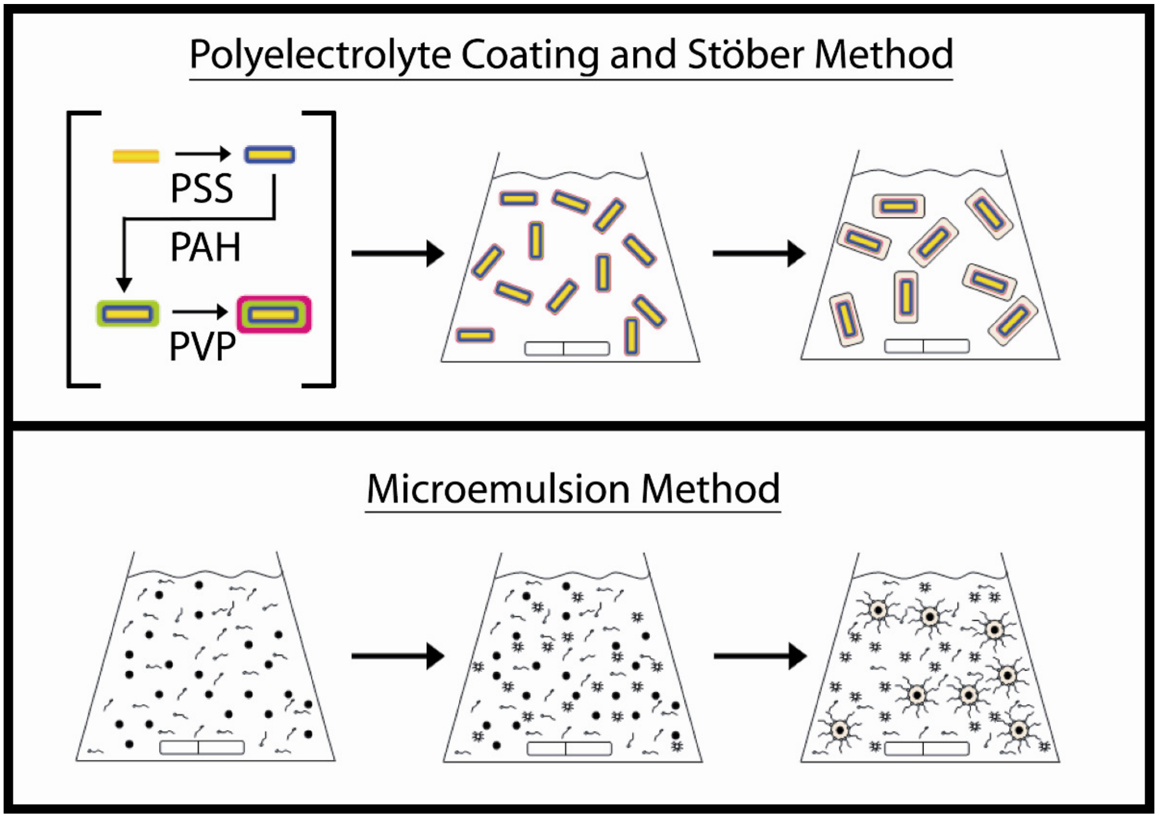

Figure 4.1. Illustration of the two different silica coating strategies used for magnetic nanocrystals and Au nanorods. (Top row) As-prepared CTAB-covered Au nanorods were first primed with the adsorption of a polyelectrolyte layer and then coated with silica using a modified Stöber method in a mixture of water and alcohol. The polyelectrolyte layers are represented with different colors, and the silica shell is shown in tan. (Bottom row) Hydrophobic Fe_2O_3 and FePt nanocrystals were coated with silica in microemulsion reaction media. The surfactant (squiggly lines) stabilizes inverse micelles (gray dots) and controls the silica deposition (tan circles) and prevents aggregation of the nanocrystals (black dots).

Figure 4.2 shows TEM images of FePt and Fe_2O_3 nanocrystals, and Au nanorods, before and after coating with Rubpy-doped silica shells. Both of the silica-coating approaches—the microemulsion approach and the Stöber approach—provide uniform silica coatings. One important key to obtaining size- and shape-monodisperse coated nanoparticles is to begin with core nanocrystals (and nanorods) that are monodisperse. Silica deposits heterogeneously on the surface of the core nanocrystals at a steady and uniform rate on particles throughout the dispersion; therefore, the final size distribution of coated nanoparticles will be narrow provided that the initial nanocrystal size distribution is narrow.

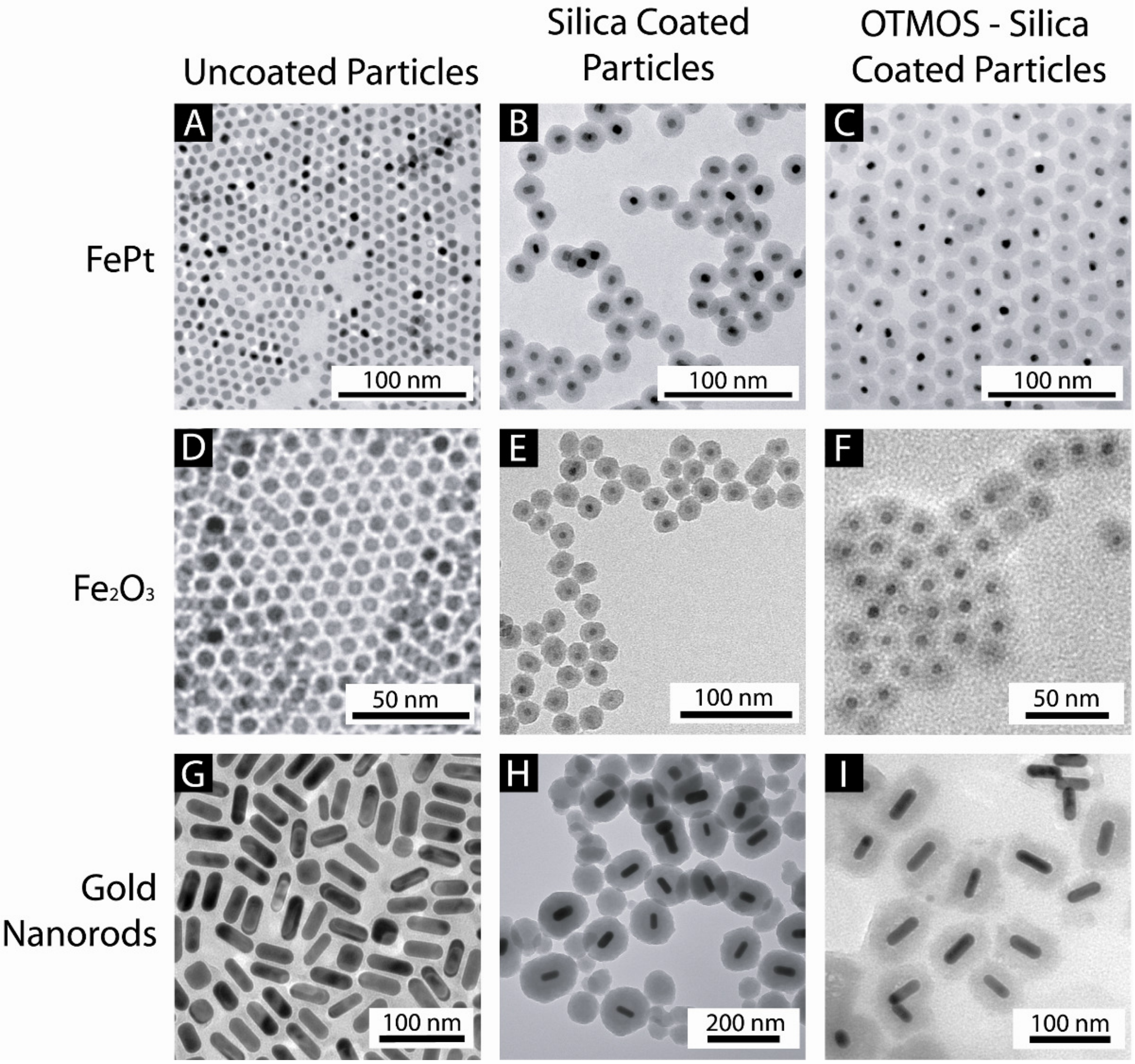

Figure 4.2. TEM images of (A, B, C) FePt and (D,E,F) Fe_2O_3 nanocrystals and (G,H,I) Au nanorods before and after coating with Rubpy-doped silica. The average diameters of the FePt and Fe_2O_3 nanocrystals are 6.6 nm and 6.5 nm, respectively. The Au nanorods have an average length of 44 nm and width of 15 nm (aspect ratio = 3). The FePt composition was determined by EDS to be 40% Fe and 60% Pt.

The inverse micelle microemulsion method provides a method for coating hydrophobic nanocrystals because the nanoparticles disperse initially in the continuous organic phase of the inverse microemulsion. The silica coating chemistry, however, occurs in the aqueous reaction compartments within the inverse micelles. It is interesting and perhaps somewhat unexpected that this coating approach works, as the nanocrystals must interface with the aqueous compartments of the inverse micellar media to a significant extent to enable heterogeneous silica deposition on their surfaces. The microemulsion method provides a high yield of silica-coated FePt and Fe_2O_3 nanocrystals with uniform shell thickness. Using the recipe described here, 10 mg of nanocrystals were coated with uniform silica shell thickness. The shell thickness could be tuned from 3 nm to 20 nm by varying the concentration of TEOS, similar to what has been previously described.[47] The presence of Rubpy does not affect the silica deposition chemistry.

CTAB-coated Au nanorods required significantly different silica coating chemistry than the FePt and Fe_2O_3 nanocrystals. First of all, CTAB-coated Au nanorods do not disperse in organic solvents. Secondly, CTAB inhibits silica deposition[48] and can lead to mesoporous coatings (See Appendix C).[24] It is not possible to remove CTAB from the nanorod surface without destroying the nanorods; therefore, the only way to coat CTAB-coated Au nanorods with a uniform, continuous silica coating is to first protect the surface with another surfactant layer. Pastoriza-Santos et al.[48] found that a series of polyelectrolyte layers does this well, and this was the strategy applied to achieve the silica coatings on the Au nanorods shown in Figure 4.2. Once the Au nanorod surface is modified with a polyelectrolyte coating, the nanorods can be coated using a modification of the Stöber method.[54] The polyelectrolyte layer also provides good nanorod dispersibility in isopropanol, as needed for the Stöber-based silica coating method. Rubpy was found to increase the silica deposition rate, and the silica shells were about a factor of two thicker when Rubpy was present than when it was not added during the silica deposition step. The coating recipe described in the experimental section produces 20 nm thick shells, but thicker SiO_2 shells were also possible with subsequent addition of TEOS/isopropyl alcohol solution after coating with a first layer of silica; for example, 40 nm thick shells were obtained by adding 0.1 mL of TEOS/isopropyl alcohol solution 3 hours after the first TEOS/isopropyl alcohol solution was added.

The as-synthesized silica-coated nanoparticles disperse only in polar solvents. To render them hydrophobic, a hydrocarbon monolayer was adsorbed to the particle surface by exposure to OTMOS. OTMOS chemisorbs to the silica surface via the siloxane moiety to leave a C_{18} hydrocarbon brush layer exposed on the particle surface. Figure 4.2 shows TEM images of OTMOS surface-modified Rubpy-doped silica-coated nanoparticles. This data indicates that the silica surface can be easily modified with siloxyl terminated ligands, thus providing a platform for various surface functionalities, including biological molecules.[55,56]

4.3.2 Optical properties

The $FePt@SiO_2$(Rubpy), $Fe_2O_3@SiO_2$(Rubpy) and $AuNR@SiO_2$(Rubpy) nanoparticles all fluoresce, indicating that the dye is indeed incorporated in the silica shell. Figure 4.3 shows examples of dispersions of these nanoparticles under room light and under excitation by a black light source. The emission is visible by the eye.

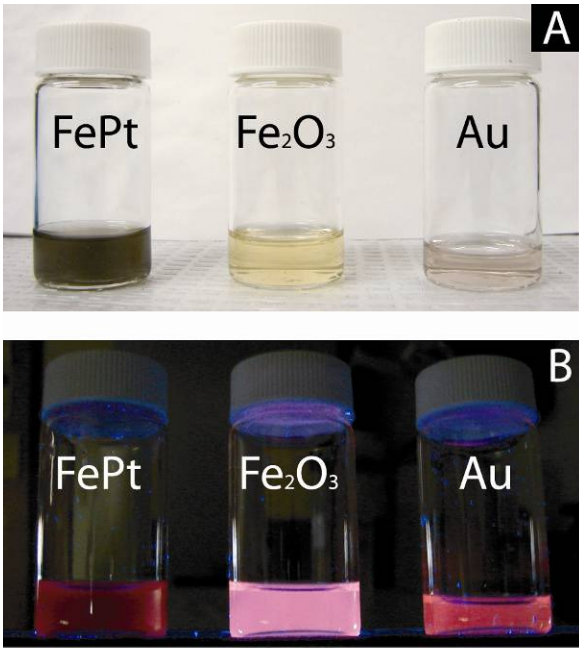

Figure 4.3. Photographs of FePt and Fe_2O_3 nanocrystals and Au nanorods coated with Rubpy-doped silica shells under (A) room light and (B) under a black lamp (λ_{exc} = 365 nm). All three different kinds of nanoparticles are fluorescent.

Figure 4.4 shows absorbance and PL emission spectra of the FePt@SiO_2(Rubpy), Fe_2O_3@SiO_2(Rubpy) and AuNR@SiO_2(Rubpy) nanoparticles. Rubpy exhibits an absorption peak at 458 nm, which appears in all of the samples. The AunNR@SiO_2(Rubpy) nanoparticles show two additional absorption peaks at 522 nm and 782 nm, which correspond to the transverse and longitudinal plasmon bands of the Au nanorods.[52] The red absorbance band of the Au nanorods has been of significant interest for in vivo medical optical imaging[58-63] because biological tissue is relatively transparent to light with these wavelengths.[57]

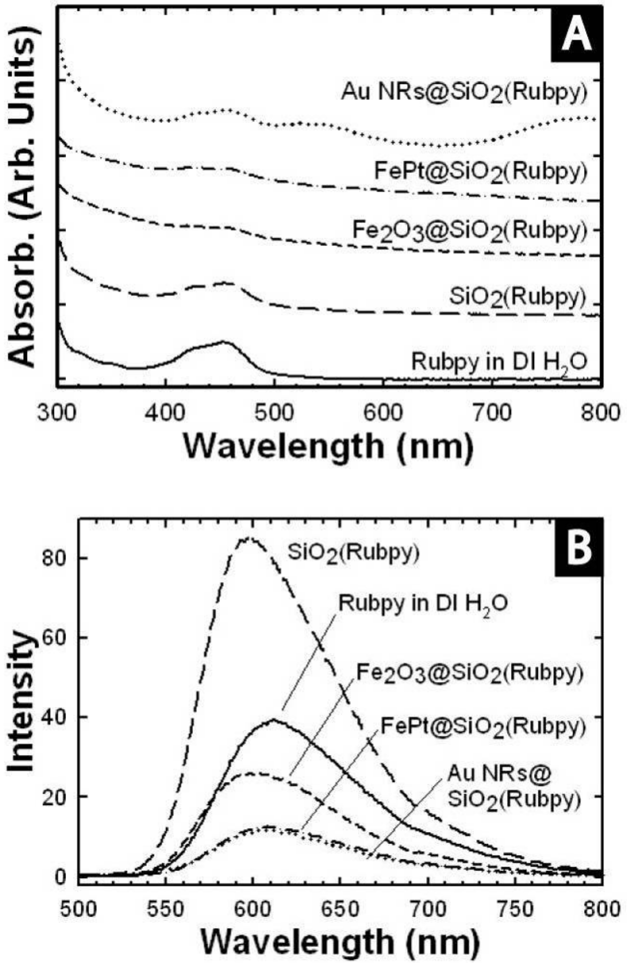

Figure 4.4. Room temperature (A) absorbance and (B) PL emission spectra (λ_{exc} = 458 nm) of FePt@SiO_2(Rubpy), Fe_2O_3@SiO_2(Rubpy) and AuNR@SiO_2(Rubpy) nanoparticles dispersed in water. Free Rubpy dissolved in water and silica spheres with Rubpy made in the absence of the core magnetic nanocrystals or Au nanorods (SiO_2(Rubpy)) were also measured for comparison.

Rubpy emits 610 nm light and all of the Rubpy-doped silica coated nanoparticles emit light with a peak wavelength near 610 nm. The emission peaks of the FePt@SiO_2(Rubpy), Fe_2O_3@SiO_2(Rubpy) and AuNR@SiO_2(Rubpy) nanoparticles are slightly blueshifted from the peak emission wavelength of Rubpy free in solution, as has been observed previously for Rubpy embedded in silica.[35] This data further confirms that Rubpy is embedded into the silica shell and is not free in solution or physisorbed on the particle surface.

Two additional tests were carried out to ensure that the emitting Rubpy was indeed embedded in the silica shell and was not free in solution or adsorbed to the particle surface. First, a control experiment was performed in which nanocrystals were coated with silica shells in the absence of Rubpy and were then dispersed in a solution of free Rubpy. This dispersion was washed following the standard procedures used here and there was no visible PL emission from these washed particles. This "wash test" indicated that Rubpy physisorption on the silica surface is weak and adsorbed dye molecules are easily removed during the purification procedure.

As another test, FePt@SiO_2(Rubpy) nanoparticles were floated on a Langmuir Blodgett trough and then transferred using a polydimethylsiloxane (PDMS) stamp to either a glass substrate for fluorescence microscopy imaging or a silicon substrate for SEM imaging. Pre-patterned PDMS stamps containing micrometer-sized features were fabricated using previously published soft-lithography techniques.[64] Figure 4.5A shows an SEM image of 20 μm diameter stamped circular features with 5 micrometer spacing. Each of these disks is composed of a monolayer of FePt@SiO_2(Rubpy) nanoparticles. The inset shows a high magnification SEM image of the nanoparticles within one of the circular features in Fig. 4.5A. The nanoparticles exhibit close-packed order in the stamped film layer. Figures 4.5B-G show optical fluorescence microscopy imaging of FePt@SiO_2(Rubpy) printed into various geometrical patterns, including square and circular features of various dimensions, spacing, and periodicities. The fluorescence images confirm that Rubpy embedded in the silica coating is emitting light. It is also worth noting that the patterned structures can be printed on any substrate, including plastics, glass and metals using any of the multifunctional nanoparticles described here. This makes it possible to envision potential schemes for bioassays, dual mode imaging, and even micrometer-size optical and electronic data storage using these kinds of features patterned with such nanomaterials with novel optical and magnetic response.

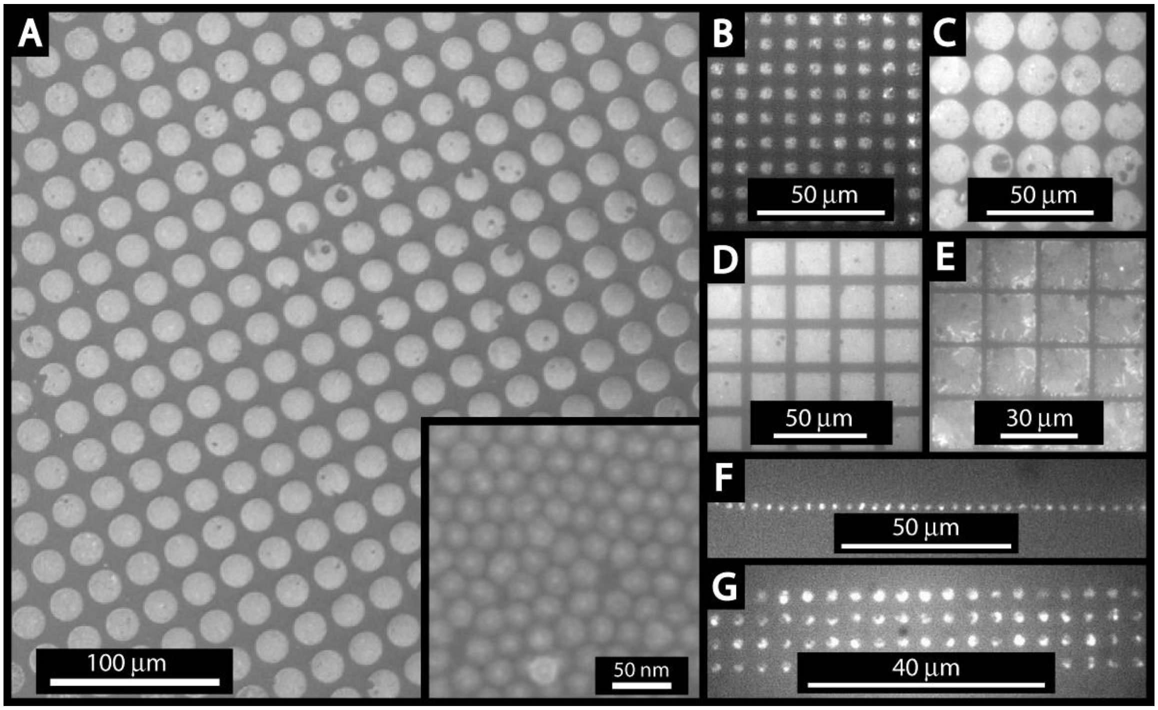

Figure 4.5. (A) SEM and (B-G) fluorescence microscopy images of FePt@SiO_2(Rubpy) nanoparticles patterned using PDMS stamps. High resolution SEM imaging of the circular patterns of FePt@SiO_2(Rubpy) nanoparticles in (A) are shown in the inset, which reveal the individual particles.

The fluorescent dye fluorescein 5(6)-isothiocyanate (FITC) could also be embedded into the silica shells using similar coating strategies as developed for the Rubpy-doped silica shells. Figure 4.6 shows data for Fe_2O_3@SiO2(FITC) and AuNR@SiO_2(FITC) nanoparticles. The TEM images show that both the iron oxide nanocrystals and the Au nanorods could be coated uniformly with the FITC-doped silica shells. The absorbance and PL spectra confirm FITC incorporation into the silica coatings, as the characteristic FITC absorption and emission peaks are present in the spectra in Figure 4.6. FITC incorporation in the silica-coated nanocrystals shows that the coating methods can be extended to other dyes with different emission wavelengths.

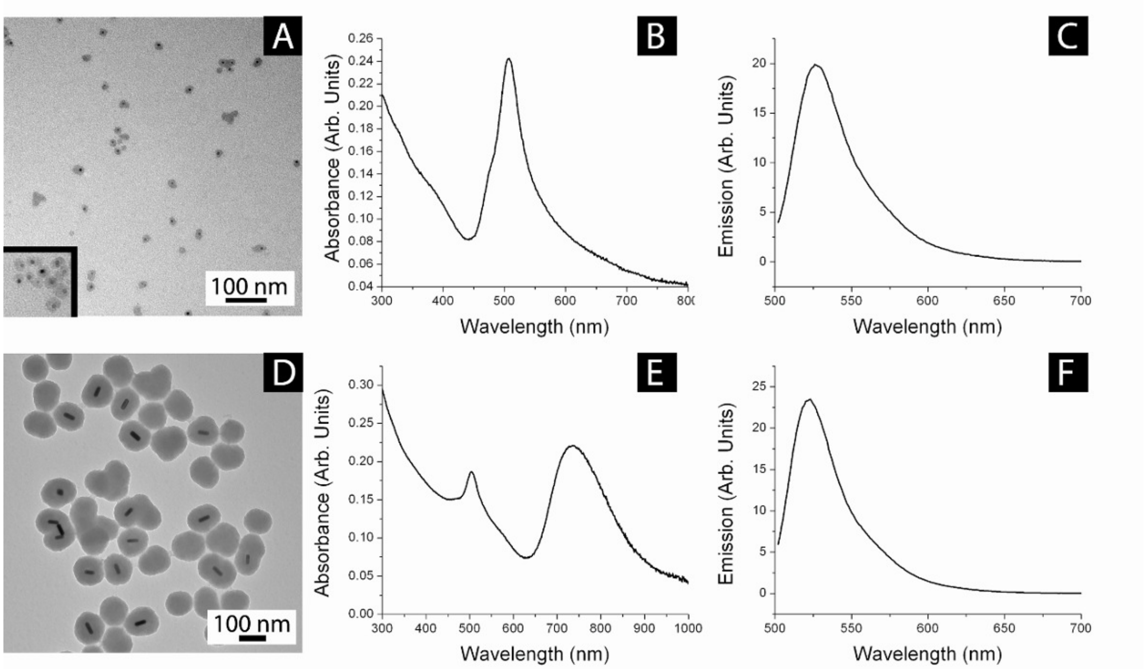

Figure 4.6. (A-C) $Fe_2O_3@SiO_2$(FITC) and (D-F) AuNR@SiO_2(FITC) nanoparticles: (A,D) TEM images, (B,E) absorbance spectra and (C,F) PL emission spectra (λ_{exc} = 492 nm). The absorbance peak at ~505 nm corresponds to the absorbance peak of FITC. The absorbance peak in (E) at ~730 nm corresponds to the longitudinal plasmon peak of the core Au nanorods. Note that there is also an absorption feature at ~520 nm, which is the transverse plasmon peak of the Au nanorods, which overlaps slightly with the FITC absorbance peak at ~505 nm. The emission peak at ~523 nm in (F) is the PL emission from the FITC dye.[40]

4.3.3 Magnetic resonance imaging (MRI) properties of FePt@SiO$_2$(Rubpy) and Fe$_2$O$_3$@SiO$_2$(Rubpy) nanoparticles

The magnetic/fluorescent heterostructure nanoparticles synthesized here might be used as dual-mode contrast agents for magnetic resonance and optical fluorescence imaging. For MRI, there are two important materials-dependent parameters, the longitudinal and transverse spin relaxation times, T$_1$ and T$_2$.[65,66] These parameters were measured for the FePt@SiO$_2$(Rubpy) and Fe$_2$O$_3$@SiO$_2$(Rubpy) nanoparticles in water at room temperature.

Both FePt@SiO$_2$(Rubpy) and Fe$_2$O$_3$@SiO$_2$(Rubpy) nanoparticles exhibited $T_{1(meas)}$ values nearly identical to the values measured for pure water ($T_{1(H_2O)}$=1759 msec), as expected for superparamagnetic nanoparticles in this size range at high field.[67,68] T$_2$ on the other hand exhibited increased relaxation due to the nanoparticles. Figure 4.7 shows R$_2$ = T$_2^{-1}$ plotted as a function of dispersed Fe concentration for the FePt@SiO$_2$(Rubpy) and Fe$_2$O$_3$@SiO$_2$(Rubpy) nanoparticles. The T$_2$ relaxivity, r_2, indicates how strongly the paramagnet influences the proton spin relaxation of the surrounding water and is determined from the concentration dependence of R$_2$: [66,67,69]

$$r_2 = T_2^{-1}[Fe]^{-1} \tag{1}$$

Linear fits to the data in Figure 4.7 give values of r_2= 30.7 ± 2.0 mM^{-1}s^{-1} for FePt@SiO$_2$(Rubpy) and r_2= 26.1 ± 1.6 mM^{-1}s^{-1} for Fe$_2$O$_3$@SiO$_2$(Rubpy). These r_2 values are similar to those of ultrasmall superparamagnetic iron oxide particles (44.1 mM^{-1}s^{-1} [70]), and slightly lower than commercially available superparamagnetic iron oxide (SPIO) MRI contrast agents (70~150 mM^{-1}s^{-1} [71]) and other water-soluble iron oxide (WSIO) nanocrystals with diameters between 6 and 9 nm studied in the literature (82.0–116.0 mM^{-1}s^{-1} [21,30,72]). However, r_2 scales approximately as the inverse of the separation distance between the paramagnet surface (i.e., the magnetic nanocrystal core) and the water protons,[73] and thinner shells would enhance r_2 and bring it within the neighborhood of new manganese ferrite nanoparticles of $MnFe_2O_4$,[21,74] and bimagnetic FePt-iron oxide[75] nanoparticles that have recently been the subject of interest as new high T_2 contrast agents for MRI.

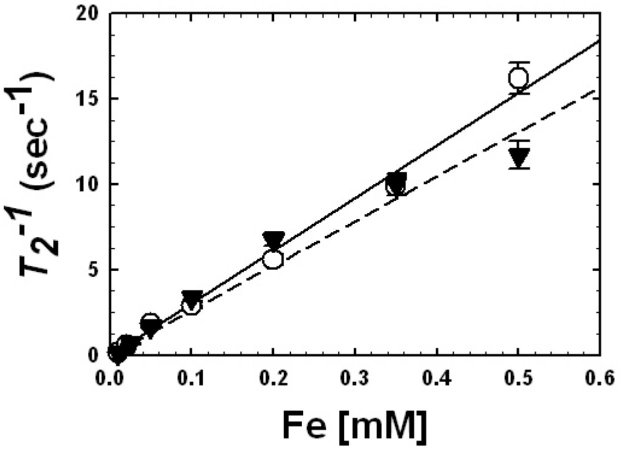

Figure 4.7. T_2 relaxivities measured as a function of Fe concentration in water dispersions of (○) FePt@SiO_2(Rubpy) or (▼) Fe_2O_3@SiO_2(Rubpy) nanoparticles.[66] The core diameters and silica shell thicknesses were 6.6 and 7.9 nm for FePt@SiO_2(Rubpy) and 6.5 and 6.4 nm for the Fe_2O_3@SiO_2(Rubpy) nanoparticles. From Eqn (1), linear fits ((___), FePt@SiO_2(Rubpy) and (_ _ _), Fe_2O_3@SiO_2(Rubpy)) were used to determine r_2: 30.7 $mM^{-1}s^{-1}$for FePt@SiO_2(Rubpy) and 26.1 $mM^{-1}s^{-1}$ for Fe_2O_3@SiO_2(Rubpy).

Magnetization measurements were performed on the FePt@SiO_2(Rubpy) and Fe_2O_3@SiO_2(Rubpy) nanoparticles to gain some insight into the difference in r_2 values measured for the two different types of nanoparticles. Figure 4.8 shows room temperature field sweeps of the magnetization of FePt@SiO_2(Rubpy) and Fe_2O_3@SiO_2(Rubpy) nanoparticles. Both nanoparticles are superparamagnetic and behave like paramagnets at room temperature. At room temperature, the magnetization on a per Fe atom basis of the iron oxide cores is 1.2 times higher than the FePt cores (Figure 4.8). But r_2 for the FePt@SiO_2(Rubpy) nanoparticles was slightly higher than r_2 for the Fe_2O_3@SiO_2(Rubpy) nanoparticles, despite the fact that the FePt@SiO_2(Rubpy) nanoparticles also had slightly thicker silica shells (7.9 nm vs. 6.4 nm).

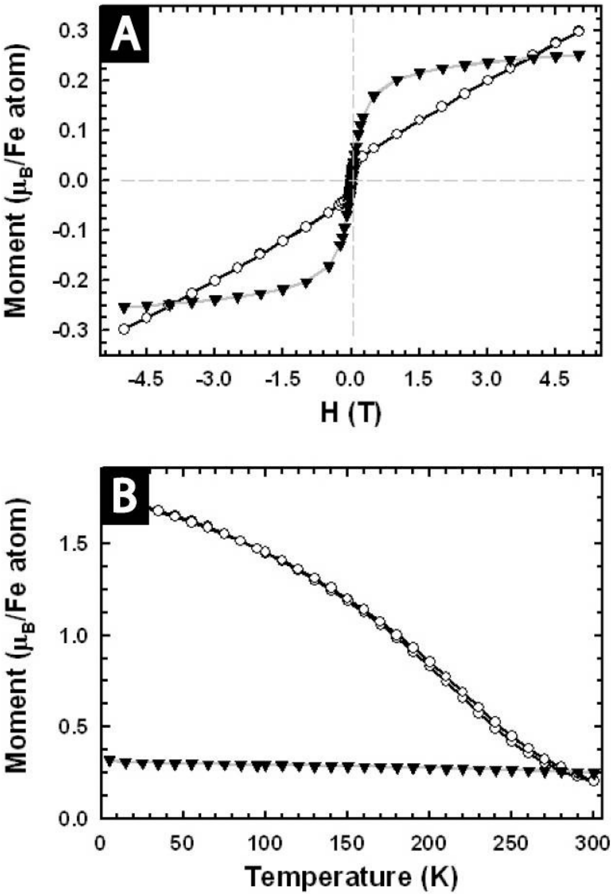

Figure 4.8. Magnetization of (○) FePt@SiO_2(Rubpy) and (▼) Fe_2O_3@SiO_2(Rubpy) nanoparticles: (A) measured at room temperature at different applied magnetic fields and (B) measured under a applied field of 3 T as a function of temperature cooled under the applied field (i.e., field-cooled conditions). The magnetization at 3 T of Fe_2O_3@SiO_2 (Rubpy) and FePt@SiO_2(Rubpy) at room temperature are 0.24 µB/Fe atom (1347 µB/particle) and 0.20 µB/Fe atom (785 µB/particle), respectively.

The reason for the difference in r_2 between these materials requires further study. But apart from the difference in room temperature saturation magnetization, there is also a very significant qualitative difference in the magnetic properties of the Fe_2O_3@SiO_2(Rubpy) and FePt@SiO_2(Rubpy) nanoparticles. The FePt nanocrystals exhibit two distinct magnetic behaviors in the field sweeps in Figure 4.8A: at low field (<~0.1 T), the material exhibits a high susceptibility similar to that the Fe_2O_3 nanoparticles, but at high fields (>~0.1 T), the magnetization does not saturate (even at fields greater than 5 T) and the magnetization exhibits a low susceptibility. The two distinct magnetic behaviors could indicate two distinctly different material regions within the FePt nanoparticle (Fe-rich and Pt-rich regions or Fe_xO_x and Pt-rich regions), similar to what has been observed in annealed or partially annealed FePt nanocrystals.[47,76,77] The possibility of an Fe-rich and Pt-rich region within the FePt core could result from the particle growth process, in which a Pt nanocrystal is first formed, followed by heterogeneous Fe deposition and subsequent Fe-Pt alloying during the particle growth process.[25,50,78] A Fe-rich shell surrounding a Pt-rich core could increase the local magnetic field gradient at the surface of the FePt@SiO_2 nanoparticles, increasing the proton dephasing rate and causing a higher r_2.[65,79] Because the SQUID measurements correspond to the volume average of the nanoparticles, they are not sensitive to the local field gradients at the surface of the particle. The lower bulk magnetization of the FePt on a per Fe basis compared to that of Fe_2O_3 at 3T may be compensated by the spatial configuration of the crystal to produce larger field gradients in the surrounding water molecules.

The magnetization of the iron oxide particles saturates at fields of less than 1 T. The temperature dependence of the magnetization is also qualitatively different for the two materials. Field-cooled and zero field-cooled (FC and ZFC) magnetization measured under an applied field of 3T overlapped for both materials, confirming that the particles are superparamagnets. A blocking temperature of 5 K was measured for the FePt@SiO_2(Rubpy) and the blocking temperature of the Fe_2O_3@SiO_2(Rubpy) nanoparticles was less than 5K and was not determined. The magnetization of the FePt core particles exhibits a much stronger temperature dependence than the Fe_2O_3 core particles, and once the temperature drops below ~280K, the FePt magnetization overtakes the magnetization of the iron oxide particles. This phenomenon may also relate to the r_2 properties of the materials, but requires further study.

4.3.4 Magnetic separations

Figure 4.9 shows 3 mg of FePt@SiO_2(Rubpy) nanoparticles magnetically separated in an aqueous dispersion using a SmCo magnet. The response to the external magnetic field indicates that the nanoparticles might be suitable for targeted drug delivery using magnetic fields.[80] Additionally, the nanoparticles redisperse after removing the magnetic field, which could be advantageous for inexpensive purification procedures, such as protein separations and water treatments that would enable the materials to be recycled.[81,82] For example, Fe_3O_4 nanocrystals have been shown to be good absorbers of arsenic from contaminated water[83] and these fluorescent/magnetic nanoparticles might be used for such a purpose.

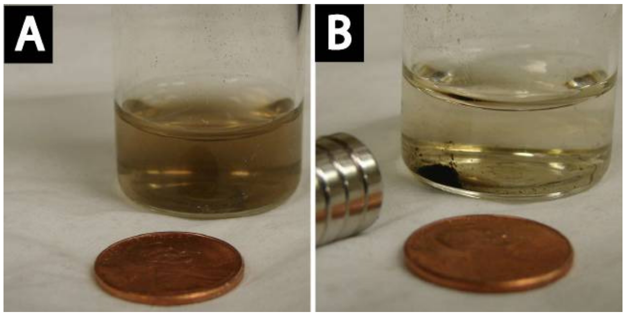

Figure 4.9. Photographs of dilute aqueous dispersions of FePt@SiO_2(Rubpy) nanoparticles (A) before and (B) after exposure to a SmCo magnet. The magnet pulls the colloidal nanoparticles to the side of the vial. The separation occurs in less than 4 hours.

4.4 CONCLUSION

The data presented here show that various nanocrystals and nanorods can be conformally coated with fluorescent dye-doped silica. Silica is a useful material for biological applications in particular because it provides a biocompatible host for the dye molecules, which has been shown to aid in the photostability of the dye, and also serves as a convenient surface for bioconjugation. However, this study also shows that significantly different silica coating chemistry can be required for nanoparticles depending on their initial surface coatings. In some cases, like the CTAB-coated Au nanorods, the nanocrystals must be "primed" for silica deposition. Nonetheless, despite these challenges, multifunctional nanoparticles can be designed and synthesized with the addition of dye-doped silica. Specifically, the FePt@SiO_2(Rubpy) and Fe_2O_3@SiO_2(Rubpy) nanoparticles synthesized in this study might serve as dual-mode imaging contrast agents that are suitable for fluorescence and magnetic resonance imaging. Preliminary proton relaxivity measurements confirm that these materials are indeed suitable for MRI imaging. Further studies, however, are required to understand the details of how the relaxivity relates to the magnetic properties of the core nanocrystals and the silica shell thickness.

4.5 REFERENCES

1. Duguet, E.; Vasseur, S.; Mornet, S.; Devoisselle, J. M. *Nanomed.* **2006,** *1*, 157-168.

2. Jaiswal, J. K.; Goldman, E. R.; Mattoussi, H.; Simon, S. M. *Nat. Methods* **2004,** *1*, 73-78.

3. Michalet, X.; Pinaud, F. F.; Bentolila, L. A.; Tsay, J. M.; Doose, S.; Li, J. J.; Sundaresan, G.; Wu, A. M.; Gambhir, S. S.; Weiss, S. *Science* **2005,** *307*, 538-544.

4. Winter, J. O.; Liu, T. Y.; Korgel, B. A.; Schmidt, C. E. *Adv. Mater.* **2001,** *13*, 1673-1677.

5. Dubertret, B.; Skourides, P.; Norris, D. J.; Noireaux, V.; Brivanlou, A. H.; Libchaber, A. *Science* **2002,** *298*, 1759-1762.

6. Chu, T. C.; Shieh, F.; Lavery, L. A.; Levy, M.; Richards-Kortum, R.; Korgel, B. A.; Ellington, A. D. *Biosens. Bioelectron.* **2006,** *21*, 1859-1866.

7. Alivisatos, P. *Nat. Biotechnol.* **2004,** *22*, 47-52.

8. Xing, Y.; Chaudry, Q.; Shen, C.; Kong, K. Y.; Zhau, H. E.; Wchung, L.; Petros, J. A.; O'Regan, R. M.; Yezhelyev, M. V.; Simons, J. W.; Wang, M. D.; Nie, S. *Nat. Protocols* **2007,** *2*, 1152-1165.

9. Fu, A. H.; Gu, W. W.; Boussert, B.; Koski, K.; Gerion, D.; Manna, L.; Le Gros, M.; Larabell, C. A.; Alivisatos, A. P. *Nano Lett.* **2007,** *7*, 179-182.

10. Hu, S.-H.; Liu, T.-Y.; Huang, H.-Y.; Liu, D.-M.; Chen, S.-Y. *Langmuir* **2008,** *24*, 239-44.

11. Smith, D. K.; Rasch, M. R.; Korgel, B. A. *Nanomed.* **2007,** *2*, 943-9.

12. Ji, X. J.; Shao, R. P.; Elliott, A. M.; Stafford, R. J.; Esparza-Coss, E.; Bankson, J. A.; Liang, G.; Luo, Z. P.; Park, K.; Markert, J. T.; Li, C. *J. Phys. Chem. C* **2007,** *111*, 6245-6251.

13. Gobin, A. M.; Lee, M. H.; Halas, N. J.; James, W. D.; Drezek, R. A.; West, J. L. *Nano Lett.* **2007,** *7*, 1929-1934.

14. Sokolov, K.; Nida, D.; Descour, M.; Lacy, A.; Levy, M.; Hall, B.; Dharmawardhane, S.; Ellington, A.; Korgel, B.; Richards-Kortum, R., In *Adv. Cancer Res.*, 2007; Vol. 96, pp 299-344.

15. Huh, Y. M.; Jun, Y. W.; Song, H. T.; Kim, S.; Choi, J. S.; Lee, J. H.; Yoon, S.; Kim, K. S.; Shin, J. S.; Suh, J. S.; Cheon, J. *J. Am. Chem. Soc.* **2005,** *127*, 12387-12391.

16. Jun, Y. W.; Huh, Y. M.; Choi, J. S.; Lee, J. H.; Song, H. T.; Kim, S.; Yoon, S.; Kim, K. S.; Shin, J. S.; Suh, J. S.; Cheon, J. *J. Am. Chem. Soc.* **2005,** *127*, 5732-5733.

17. Bulte, J. W. M.; Kraitchman, D. L. *NMR Biomed.* **2004,** *17*, 484-499.

18. Qin, J.; Laurent, S.; Jo, Y. S.; Roch, A.; Mikhaylova, M.; Bhujwalla, Z. M.; Muller, R. N.; Muhammed, M. *Adv. Mater.* **2007,** *19*, 1874-1878.

19. Song, H. T.; Choi, J. S.; Huh, Y. M.; Kim, S.; Jun, Y. W.; Suh, J. S.; Cheon, J. *J. Am. Chem. Soc.* **2005,** *127*, 9992-9993.

20. Hu, F. Q.; Wei, L.; Zhou, Z.; Ran, Y. L.; Li, Z.; Gao, M. Y. *Adv. Mater.* **2006,** *18*, 2553-2556.

21. Lee, J. H.; Huh, Y. M.; Jun, Y.; Seo, J.; Jang, J.; Song, H. T.; Kim, S.; Cho, E. J.; Yoon, H. G.; Suh, J. S.; Cheon, J. *Nat. Med.* **2007,** *13*, 95-99.

22. Santra, S.; Yang, H. S.; Holloway, P. H.; Stanley, J. T.; Mericle, R. A. *J. Am. Chem. Soc.* **2005,** *127*, 1656-1657.

23. Quarta, A.; Di Corato, R.; Manna, L.; Ragusa, A.; Pellegrino, T. *IEEE T. Nanobiosci.* **2007,** *6*, 298-308.

24. Lin, Y. S.; Wu, S. H.; Hung, Y.; Chou, Y. H.; Chang, C.; Lin, M. L.; Tsai, C. P.; Mou, C. Y. *Chem. Mater.* **2006,** *18*, 5170-5172.

25. Lee, D. C.; Smith, D. K.; Heitsch, A. T.; Korgel, B. A. *Annu. Rep. Prog. Chem., Sect. C: Phys. Chem.* **2007,** *103*, 351-402.

26. Choi, J. S.; Jun, Y. W.; Yeon, S. I.; Kim, H. C.; Shin, J. S.; Cheon, J. *J. Am. Chem. Soc.* **2006,** *128*, 15982-15983.

27. Zhang, L. H.; Liu, B. F.; Dong, S. J. *J. Phys. Chem. B* **2007,** *111*, 10448-10452.

28. Lu, C. W.; Hung, Y.; Hsiao, J. K.; Yao, M.; Chung, T. H.; Lin, Y. S.; Wu, S. H.; Hsu, S. C.; Liu, H. M.; Mou, C. Y.; Yang, C. S.; Huang, D. M.; Chen, Y. C. *Nano Lett.* **2007,** *7*, 149-154.

29. Kim, J. S.; Rieter, W. J.; Taylor, K. M. L.; An, H.; Lin, W. L.; Lin, W. B. *J. Am. Chem. Soc.* **2007,** *129*, 8962-8963.

30. Lee, J. H.; Jun, Y. W.; Yeon, S. I.; Shin, J. S.; Cheon, J. *Angew. Chem., Int. Ed.* **2006,** *45*, 8160-8162.

31. Wang, L.; O'Donoghue, M. B.; Tan, W. H. *Nanomed.* **2006,** *1*, 413-426.

32. Yan, J. L.; Estevez, M. C.; Smith, J. E.; Wang, K. M.; He, X. X.; Wang, L.; Tan, W. H. *Nano Today* **2007,** *2*, 44-50.

33. Santra, S.; Tapec, R.; Theodoropoulou, N.; Dobson, J.; Hebard, A.; Tan, W. H. *Langmuir* **2001,** *17*, 2900-2906.

34. Santra, S.; Wang, K. M.; Tapec, R.; Tan, W. H. *J. Biomed. Optics* **2001,** *6*, 160-166.

35. Bagwe, R. P.; Yang, C. Y.; Hilliard, L. R.; Tan, W. H. *Langmuir* **2004,** *20*, 8336-8342.

36. Yao, G.; Wang, L.; Wu, Y. R.; Smith, J.; Xu, J. S.; Zhao, W. J.; Lee, E. J.; Tan, W. H. *Anal. Bioanal. Chem.* **2006,** *385*, 518-524.

37. Bottini, M.; Cerignoli, F.; Mills, D. M.; D'Annibale, F.; Leone, M.; Rosato, N.; Magrini, A.; Pellecchia, M.; Bergamaschi, A.; Mustelin, T. *J. Am. Chem. Soc.* **2007,** *129*, 7814-7823.

38. Ow, H.; Larson, D. R.; Srivastava, M.; Baird, B. A.; Webb, W. W.; Wiesner, U. *Nano Lett.* **2005,** *5*, 113-117.

39. Zhao, X. J.; Bagwe, R. P.; Tan, W. H. *Adv. Mater.* **2004,** *16*, 173-176.

40. Wang, L.; Tan, W. H. *Nano Lett.* **2006,** *6*, 84-88.

41. Chen, X. L.; Zou, J. L.; Zhao, T. T.; Li, Z. B. *J. Fluores.* **2007,** *17*, 235-241.

42. Bagwe, R. P.; Hilliard, L. R.; Tan, W. H. *Langmuir* **2006,** *22*, 4357-4362.

43. Zhao, X. J.; Hilliard, L. R.; Mechery, S. J.; Wang, Y. P.; Bagwe, R. P.; Jin, S. G.; Tan, W. H. *Proc. Natl. Acad. Sci. U. S. A.* **2004,** *101*, 15027-15032.

44. Zhao, X. J.; Tapec-Dytioco, R.; Tan, W. H. *J. Am. Chem. Soc.* **2003,** *125*, 11474-11475.

45. Santra, S.; Zhang, P.; Wang, K. M.; Tapec, R.; Tan, W. H. *Anal. Chem.* **2001,** *73*, 4988-4993.

46. Deng, T.; Li, J. S.; Jiang, J. H.; Shen, G. L.; Yu, R. Q. *Adv. Funct. Mater.* **2006,** *16*, 2147-2155.

47. Lee, D. C.; Mikulec, F. V.; Pelaez, J. M.; Koo, B.; Korgel, B. A. *J. Phys. Chem. B* **2006,** *110*, 11160-11166.

48. Pastoriza-Santos, I.; Perez-Juste, J.; Liz-Marzan, L. M. *Chem. Mater.* **2006,** *18*, 2465-2467.

49. Yi, D. K.; Lee, S. S.; Papaefthymiou, G. C.; Ying, J. Y. *Chem. Mater.* **2006,** *18*, 614-619.

50. Chen, M.; Liu, J. P.; Sun, S. H. *J. Am. Chem. Soc.* **2004,** *126*, 8394-8395.

51. Hyeon, T.; Lee, S. S.; Park, J.; Chung, Y.; Bin Na, H. *J. Am. Chem. Soc.* **2001,** *123*, 12798-12801.

52. Smith, D. K.; Korgel, B. A. *Langmuir* **2008,** *24*, 644-649.

53. Tago, T.; Hatsuta, T.; Miyajima, K.; Kishida, M.; Tashiro, S.; Wakabayashi, K. *J. Am. Ceram. Soc.* **2002,** *85*, 2188-2194.

54. Stöber, W.; Fink, A.; Bohn, E. *J. Colloid Interface Sci.* **1968,** *26*, 62-9.

55. Gupta, A. K.; Naregalkar, R. R.; Vaidya, V. D.; Gupta, M. *Nanomed.* **2007,** *2*, 23-39.

56. Arruebo, M.; Fernandez-Pacheco, R.; Velasco, B.; Marquina, C.; Arbiol, J.; Irusta, S.; Ibarra, M. R.; Santamaria, J. *Adv. Funct. Mater.* **2007,** *17*, 1473-1479.

57. Lim, Y. T.; Kim, S.; Nakayama, A.; Stott, N. E.; Bawendi, M. G.; Frangioni, J. V. *Mol. Imaging* **2003,** *2*, 50-64.

58. Wang, H. F.; Huff, T. B.; Zweifel, D. A.; He, W.; Low, P. S.; Wei, A.; Cheng, J. X. *Proc. Natl. Acad. Sci. U. S. A.* **2005,** *102*, 15752-15756.

59. Durr, N. J.; Larson, T.; Smith, D. K.; Korgel, B. A.; Sokolov, K.; Ben-Yakar, A. *Nano Lett.* **2007,** *7*, 941-945.

60. Yu, C. X.; Nakshatri, H.; Irudayaraj, J. *Nano Lett.* **2007,** *7*, 2300-2306.

61. Ding, H.; Yong, K. T.; Roy, I.; Pudavar, H. E.; Law, W. C.; Bergey, E. J.; Prasad, P. N. *J. Phys. Chem. C* **2007,** *111*, 12552-12557.

62. Huang, X. H.; El-Sayed, I. H.; Qian, W.; El-Sayed, M. A. *J. Am. Chem. Soc.* **2006,** *128*, 2115-2120.

63. Huang, X. H.; El-Sayed, I. H.; Qian, W.; El-Sayed, M. A. *Nano Lett.* **2007,** *7*, 1591-1597.

64. Yang, H.; Deschatelets, P.; Brittain, S. T.; Whitesides, G. M. *Adv. Mater.* **2001,** *13*, 54-58.

65. Kuperman, V. *MRI: Physical Principles and Applications*. Academic Press: Chicago, Illinois, 2000.

66. T_1 and T_2 are reported in reference to the solvent values, ${T_{1,2(H_2O)}}^{-1}$, where $T_{1,2(meas)}$ are the measured values: ${T_{1,2}}^{-1} = {T_{1,2(meas)}}^{-1} - {T_{1,2(H_2O)}}^{-1}$.

67. Koenig, S. H.; Kellar, K. E. *Magn. Reson. Med.* **1995,** *34*, 227-233.

68. Koenig, S. H. *Invest. Radiol.* **1998,** *33*, 822-827.

69. Bloembergen, N.; Purcell, E. M.; Pound, R. V. *Curr. Cont.* **1977,** 7.

70. Weissleder, R.; Elizondo, G.; Wittenberg, J.; Rabito, C. A.; Bengele, H. H.; Josephson, L. *Radiology* **1990,** *175*, 489-493.

71. Wang, Y. X. J.; Hussain, S. M.; Krestin, G. P. *Eur. Radiol.* **2001,** *11*, 2319-2331.

72. Wan, J.; Cai, W.; Meng, X.; Liu, E. *Chem. Comm.* **2007,** 5004-5006.

73. Koenig, S. H.; Schillin.We. *J. Biol. Chem.* **1969,** *244*, 6520-6526.

74. Tromsdorf, U. I.; Bigall, N. C.; Kaul, M. G.; Bruns, O. T.; Nikolic, M. S.; Mollwitz, B.; Sperling, R. A.; Reimer, R.; Hohenberg, H.; Parak, W. J.; Forster, S.; Beisiegel, U.; Adam, G.; Weller, H. *Nano Lett.* **2007,** *7*, 2422-2427.

75. Figuerola, A.; Fiore, A.; Di Corato, R.; Falqui, A.; Giannini, C.; Micotti, E.; Lascialfari, A.; Corti, M.; Cingolani, R.; Pellegrino, T.; Cozzoli, P. D.; Manna, L. *J. Am. Chem. Soc.* **2008,** *130*, 1477-1487.

76. Zeng, H.; Li, J.; Liu, J. P.; Wang, Z. L.; Sun, S. H. *Nature* **2002,** *420*, 395-398.

77. Yamamoto, S.; Morimoto, Y.; Tamada, Y.; Takahashi, Y. K.; Hono, K.; Ono, T.; Takano, M. *Chem. Mater.* **2006,** *18*, 5385-5388.

78. Chen, M.; Kim, J.; Liu, J. P.; Fan, H. Y.; Sun, S. H. *J. Am. Chem. Soc.* **2006,** *128*, 7132-7133.

79. Bushong, S. *Magnetic Resonance Imaging: Physical and Biological Principles.* The C.V. Mosby Company: St. Louis, 1988.

80. Alexiou, C.; Jurgons, R.; Schmid, R. J.; Bergemann, C.; Henke, J.; Erhardt, W.; Huenges, E.; Parak, F. *J. Drug Targeting* **2003,** *11*, 139-149.

81. Bao, J.; Chen, W.; Liu, T. T.; Zhu, Y. L.; Jin, P. Y.; Wang, L. Y.; Liu, J. F.; Wei, Y. G.; Li, Y. D. *ACS Nano* **2007,** *1*, 293-298.

82. Yantasee, W.; Warner, C. L.; Sangvanich, T.; Addleman, R. S.; Carter, T. G.; Wiacek, R. J.; Fryxell, G. E.; Timchalk, C.; Warner, M. G. *Environ. Sci. Technol.* **2007,** *41*, 5114-5119.

83. Yavuz, C. T.; Mayo, J. T.; Yu, W. W.; Prakash, A.; Falkner, J. C.; Yean, S.; Cong, L. L.; Shipley, H. J.; Kan, A.; Tomson, M.; Natelson, D.; Colvin, V. L. *Science* **2006,** *314*, 964-967

Chapter 5: Self-Assembled Simple Hexagonal AB_2 Binary Nanocrystal Superlattices: SEM, GISAXS and Defects

Reproduced in part with permission from: Smith, D.K.; Goodfellow, B.W.; Smilgies, D.M.; and Korgel, B.A. "Self-Assembled Simple Hexagonal AB_2 Binary Nanocrystal Superlattices: SEM, GISAXS, and Defects. *Journal of the American Chemical Society*, **2009**, *131*, 3281-3290. Copyright 2009 American Chemical Society.

5.1 INTRODUCTION

Binary nanocrystal superlattices (BSLs)—*e.g.*, periodically-ordered arrays of nanocrystals with two different well-defined diameters—have been reported with astonishingly diverse structures, including those that are isostructural with AlB_2,[1-8] CaB_6,[2,3] $CaCu_5$,[1-3,5,7,9,10] CuAu,[2,3,5,10] Cu_3Au,[2,3] $NaZn_{13}$,[1-4,7,11] Fe_4C,[2,3] $MgNi_2$,[2] $MgZn_2$,[2,3,7] NaCl,[2-4,12,13] and NiAs[4] compounds. Since nanocrystals can be synthesized with a wide variety of chemical and physical properties, including magnets,[14] metals,[15] semiconductors,[16] and even more complex multifunctional heterostructures,[16-25] they provide a library of assorted materials suited for new technologies in the biological sciences,[26-29] computing and information storage,[14,30] photovoltaics,[31] and thermoelectrics.[13] By merging nanocrystals into BSLs, *metamaterials* may be fabricated with new, unique characteristics that result from their nanoscale organization and interplay of their constituent properties.[32] For example, magnetic and semiconductor nanocrystals might be mixed to form new breeds of magneto-optic materials,[11] mixtures of different magnetic nanocrystals may lead to higher energy density magnetic properties,[30,33] and mixtures of semiconductors may be used for optoelectronic applications, like higher performance photovoltaics.[34] In one study that exemplifies this idea, BSLs of PbTe and Ag_2Te nanocrystals were over 100 times more electrically conductive than superlattices of only PbTe or Ag_2Te nanocrystals.[13]

To design and engineer BSL properties, their assembly must be well understood. Some BSL structures are expected based on geometrical packing arguments for spheres, as in the case of cubic AB (NaCl) and simple hexagonal AB_2 (AlB_2) structures in which nanocrystals fill space as efficiently as possible.[34] But many observed BSL structures, such as cub-AB_{13},[11] $CaCu_5$,[1-3,5,7,9,10], Fe_4C,[2,3] Cu_3Au,[2,3] are not *closest*-packed arrangements.[35] Therefore, a variety of other factors in addition to space-filling arguments have been proposed to be important in determining BSL structure, including size- and composition-dependent interparticle forces, including van der Waals attractions,[36,37] ligand-ligand interactions,[38] capillary forces,[39] electrostatic interactions,[2] and kinetic factors.[3,9,40] But the matter is complicated by the fact that the BSL structures reported thus far have had relatively short-range order (<3 μm) and structural characterization has been carried out almost exclusively by transmission electron microscopy (TEM) of relatively thin samples. To date, no scanning electron microscopy (SEM) images or small angle X-ray scattering patterns (SAXS) of BSLs have been published, and it is therefore possible that some observed BSLs are only metastable or stabilized/induced by the substrate; thus, making it more complicated to identify the underlying forces responsible for BSL structure.

Herein, SEM and grazing incidence small-angle X-ray scattering (GISAXS) measurements of sh-AB_2 BSLs are presented, which confirm the existence of long-range order in sh-AB_2 BSLs. This data provides evidence that the sh-AB_2 BSL phase is indeed a thermodynamically stable phase for the nanocrystal size ratio studied here (0.53). BSLs, however, only formed when nanocrystals were deposited onto a tilted substrate by controlled slow evaporation from dispersions with excess oleic acid. This indicates that the forces driving BSL formation are relatively weak. Some diversity in BSL structure was nonetheless also observed, including (1) uniaxial superlattice shrinkage normal to the substrate from residual solvent evaporation; (2) nearly periodic dislocations consisting of inserted half-planes of Au nanocrystals; and in thin BSL layers, (3) an analog of an AB_{13} phase in which Fe_2O_3 nanocrystals have substituted for Au nanocrystals in the 8a Wyckoff positions in the unit cell of space group 226, and (4) an "expanded" sh-AB_2 (100) plane.

5.2 EXPERIMENTAL SECTION

5.2.1 Materials and Supplies

All chemicals were used as received. Iron pentacarbonyl ($Fe(CO)_5$, 99.999%), oleic acid (99%), hydrogen tetrachloroaurate(III) hydrate (99.9+%), tetraoctylammonium bromide (TOAB, 98%), sodium borohydride ($NaBH_4$, 98+%), and dodecanethiol (≥98%) were purchased from Sigma-Aldrich. Dioctyl ether (>97%) was purchased from Fluka. Toluene (99.9%) was purchased from Fisher. Doubly-distilled deionized water (DI-H_2O) was used in all preparations.

5.2.2 Au Nanocrystal Synthesis

Dodecanethiol-coated 6.1 nm diameter Au nanocrystals were prepared as previously described.[41,42] In a 50 ml Erlenmeyer flask, 0.19 g of hydrogen tetrachloroaurate(III) hydrate was dissolved in 18 ml of DI water. 1.35 g of TOAB dissolved in 12.25 ml of toluene was added to the aqueous solution, and the mixture was stirred for one hour. The aqueous phase was discarded. A solution of 0.25 g of $NaBH_4$ dissolved in 15 ml of DI water was then added to the organic solution. This mixture was stirred for 20 hours. The aqueous phase was then discarded. 120 μL of dodecanethiol was added to the organic phase and the mixture was stirred for 1 hour.

The Au nanocrystals were isolated by first centrifuging the solution for 3 minutes at 8000 rpm and discarding the precipitate, which consists of poorly capped nanocrystals. The supernatant was collected and excess ethanol was added to precipitate the nanocrystals and separate them from molecular impurities in the reaction. After centrifuging the solution for 8 minutes at 8500 rpm, the precipitate was collected and the supernatant discarded. The nanocrystals were redispersed in chloroform, followed by size-selective precipitation using ethanol as an antisolvent.[36,43] 6.1±0.73 (±12%) nm diameter Au nanocrystals were used for superlattice self-assembly.

5.2.3 Fe_2O_3 Nanocrystal Synthesis

Oleic acid-coated 11.5 nm diameter Fe_2O_3 nanocrystals with a 6% polydispersity were prepared under inert (N_2) atmosphere using standard glovebox and Schlenk line techniques and published procedures.[44] In a 25 ml three neck flask, 10 ml of dioctyl ether and 960 μL (4.56 mmol) of oleic acid were heated to 100 °C under N_2 flow at atmospheric pressure. 0.2 ml (1.52 mmol) of $Fe(CO)_5$ was injected into this solution. [Caution must be taken when preparing $Fe(CO)_5$, as it is extremely volatile and potentially hazardous (refer to MSDS before use).] The solution was refluxed at 300 °C for one hour. The reaction flask was removed from the heating mantle and allowed to cool to room temperature. The flask was then opened to air for 30 minutes to oxidize the as-made Fe nanocrystals. This reaction solution containing the resulting Fe_2O_3 nanocrystals was then centrifuged for 5 minutes at 8000 rpm. The supernatant was collected and the precipitate, which consists of solid byproducts and poorly capped nanocrystals, was discarded. Excess ethanol was then added to the supernatant to precipitate the nanocrystals. This mixture was centrifuged for 10 minutes at 8000 rpm. The supernatant was discarded. The nanocrystals were further purified with two additional reprecipitation and centrifugation steps using hexane and ethanol as a solvent/antisolvent pair. 11.54±0.66 (±6%) nm diameter Fe_2O_3 nanocrystals were used for superlattice self-assembly.

5.2.4 Binary Nanocrystal Superlattice (BSL) Preparation

BSLs were deposited on various substrates, including TEM grids (carbon-coated copper 200 mesh, Electron Microscopy Sciences), Si wafers covered with native oxide (SEH America), or Si_3N_4-coated Si wafers, by immersing the substrate in a glass vial tilted at approximately 65° from vertical with a small volume of nanocrystal dispersion (See Appendix D for details). The nanocrystal dispersion was made by adding 0.12 mg of Au nanocrystals, 0.1 mg of Fe_2O_3 nanocrystals and 0.1 μl oleic acid in 440 μl of toluene, corresponding to a Fe_2O_3:Au nanocrystal number ratio of 1:2.5. The solvent was then allowed to evaporate over the course of several hours at 45 °C in air.

5.2.5 Materials Characterization

Transmission electron microscopy (TEM) was performed on either a Phillips EM208 TEM with 80 kV accelerating voltage or a JEOL 2010F with the field emission gun operated at 200 kV. Images were acquired digitally. Electron diffraction patterns were simulated using JEMS Electron Microscopy Software Package (Version 3.2710U2008, Copyright: P. Stadelmann, 1999-2008). Scanning electron microscopy (SEM) was performed on a Zeiss Supra 40 SEM with an in-lens arrangement at 10 keV working voltage and 5 mm lens to detector distance. Samples were grounded using copper tape to prevent charging.

Grazing incidence small angle X-ray scattering (GISAXS) measurements were performed on beam line D1 of the Cornell High Energy Synchrotron Source (CHESS) using monochromatic radiation of wavelength λ = 1.252 Å with a bandwidth $\Delta\lambda/\lambda$ of 1.5%. The x-ray beam was produced by a hardbent dipole magnet in the Cornell storage ring and monochromatized with $Mo:B_4C$ multilayers with a period of 30 Å. The D1 area detector (MedOptics) is a fiber coupled CCD camera with a pixel size of 46.9 μm by 46.9 μm and a total of 1024 x 1024 pixels with a 14-bit dynamical range per pixel.[45] Typical read-out time per image was below 5 sec. The images were dark current corrected, distortion-corrected, and flat-field corrected by the acquisition software. The sample to detector distance was 935 mm, as determined using a silver behenate powder standard. The incident angle of the x-ray beam was varied from 0.05 ° to 0.25° and typical exposure times were 100 seconds. Scattering images were calibrated and integrated using the Fit2D software.[46] The GISAXS diffraction peaks were indexed using the software package, NANOCELL.[47]

5.3 RESULTS AND DISCUSSION

5.3.1 TEM and SEM

Figure 5.1 shows SEM images of BSLs of (A) 11.5 nm Fe_2O_3 and (B) 6.1 nm Au nanocrystals. The BSLs have a simple hexagonal (sh) AB_2 (AlB_2, space group 191, *P 6/mmm*) structure as described in previous reports.[1-7] In the BSL, the large Fe_2O_3 nanocrystals occupy a simple hexagonal lattice with the smaller Au nanocrystals filling the trigonal prismatic interstitial spaces, as shown in Figure 5.2. Figure 5.3 shows TEM images of the (100), (110) and (001) surfaces of the BSLs. FFTs of the images index to the sh-AB_2 structure, and selected area electron diffraction (SAED) verified the presence of both Au and Fe_2O_3 nanocrystals in the BSLs (Figure 5.4). The (100) and (001) spacings measured in TEM images were 12.6 nm and 14.1 nm, corresponding to lattice dimensions, a=14.5 nm and c=14.1 nm. From SEM images, the (100) and (001) spacings were found to be 12.2 nm and 14.4 nm, corresponding to lattice dimensions a=14.1 nm and c=14.4 nm.

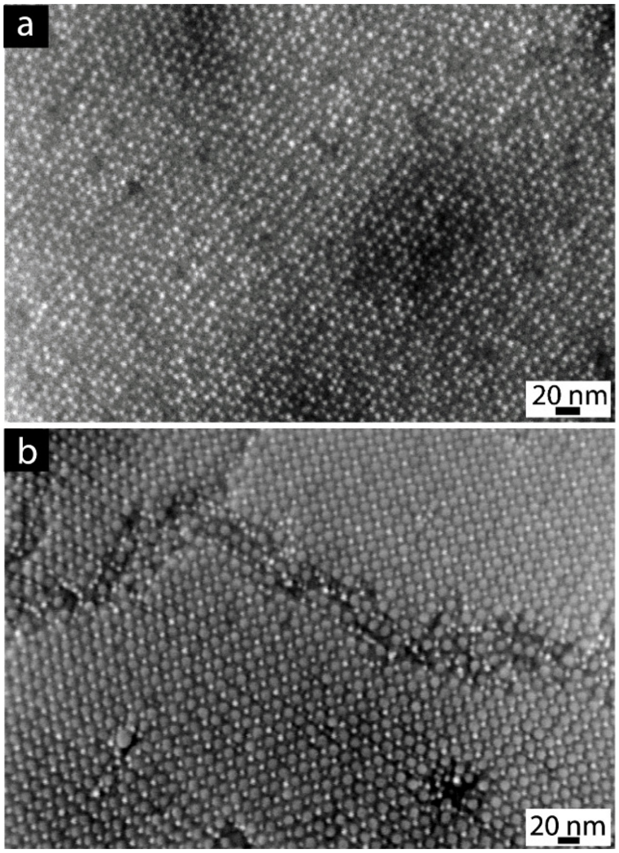

Figure 5.1. HRSEM images of sh-AB_2 BSLs on Si_3N_4-coated Si substrates with two different exposed BSL crystallographic surfaces: (a) (001) and (b) (100). Crystalline domains up to ~9 µm in diameter were observed.

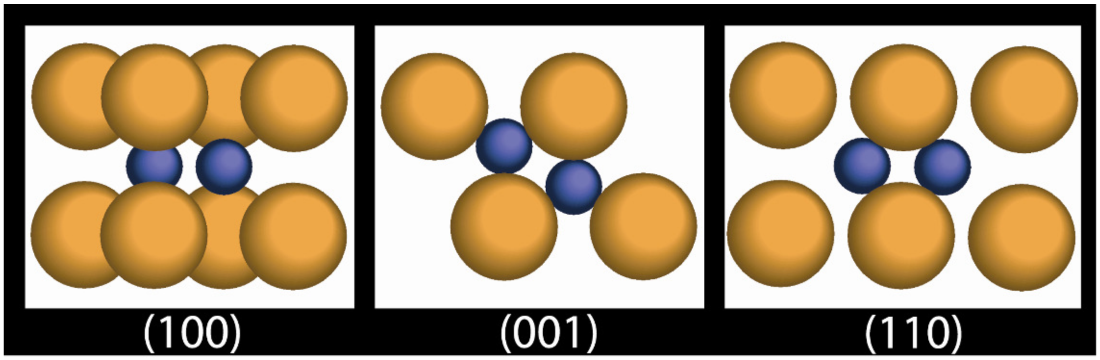

Figure 5.2. Different orientations of the sh-AB_2 (SG 191) unit cell. Orange spheres represent 11.5 nm Fe_2O_3 and blue spheres are 6.1 nm Au nanocrystals.

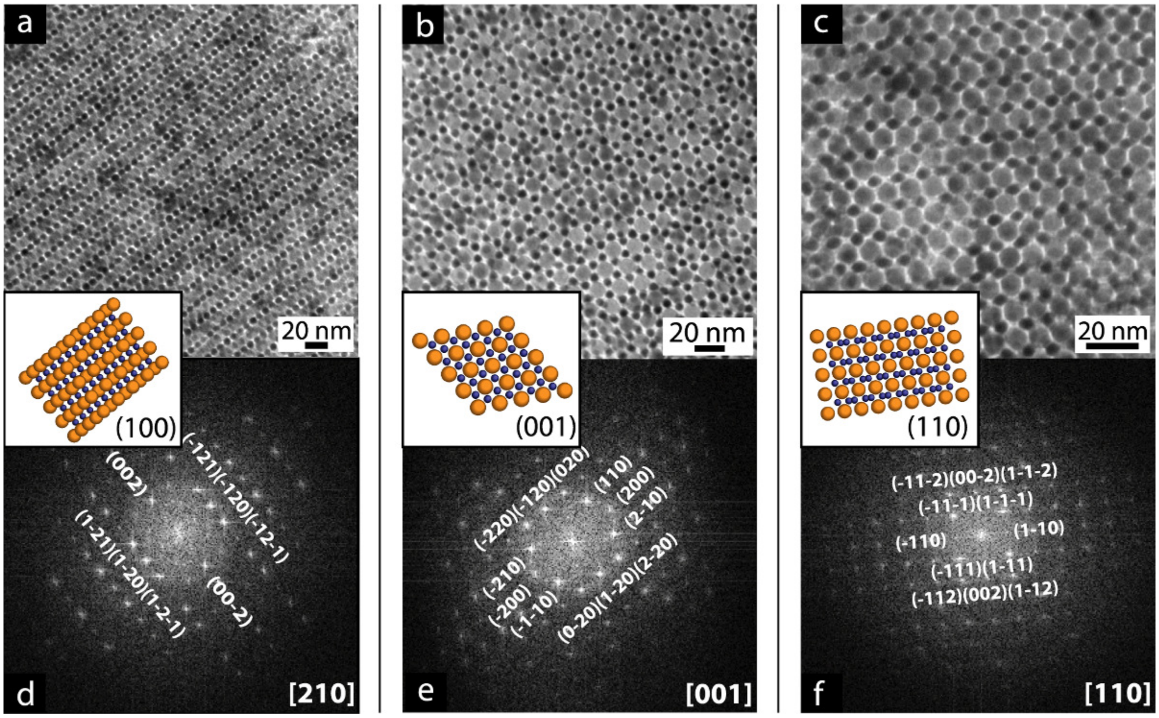

Figure 5.3. TEM images and FFTs of sh-AB_2 BSLs observed down three different zone axes to provide images of the corresponding lattice planes: (a,d) [210], (100); (b,e) [001], (001); and (c,f) [110], (110). The FFTs are indexed to sh-AB_2 lattice planes; the zone axes are given in the bottom right of the FFTs. Crystallographic models of the sh-AB_2 superlattices are provided in the insets; blue and orange spheres represent Au and Fe_2O_3 nanocrystals, respectively.

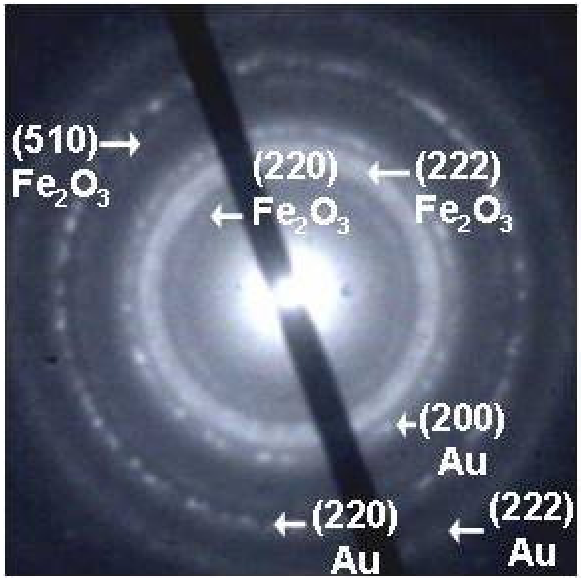

Figure 5.4. Wide-angle selective area electron diffraction acquired with the beam positioned down the [100] BSL sh-AB$_2$ BSL zone axis. The diffraction rings index to fcc Au and cubic γ-Fe$_2$O$_3$

5.3.2 Grazing Incidence Small Angle X-ray Scattering (GISAXS)

GISAXS measurements were performed on the BSLs and distinct diffraction spots were observed, thus confirming relatively long range order in the superlattices. Figure 5.5 shows examples of GISAXS measurements of the BSLs, along with an illustration of the experimental system. All of the measured GISAXS patterns indexed to an sh-AB$_2$ BSL structure (with a slight lattice contraction of 8-12% normal to the substrate as described below). The diffraction spot sizes varied from broad to narrow features, indicating variability in the size of crystalline BSL grains and their crystallographic superlattice orientations with respect to the substrate. Additional SEM images of BSLs are included in Appendix D, which clearly show that the BSL samples consist of multiple crystal grains with a variety of orientations on the substrate.

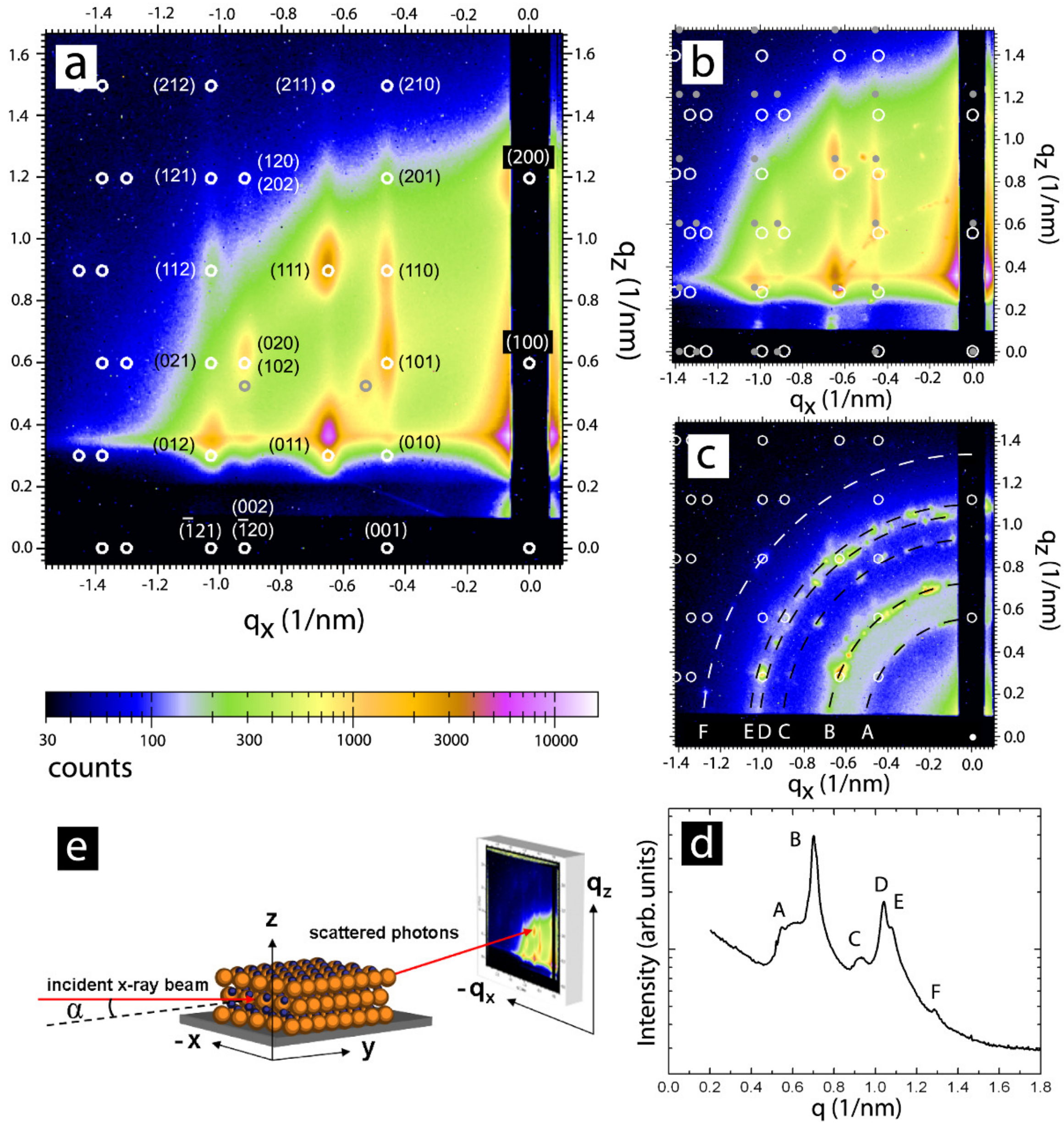
a
(212)
(211)
(210)
(121)
(120)
(202)
(201)
(200)
(112)
(111)
(110)
(021)
(020)
(102)
(101)
(100)
(012)
(011)
(010)
(002)
(̄121)
(̄120)
(001)
q_x (1/nm)
q_z (1/nm)
counts
30
100
300
1000
3000
10000
b
c
F
E D C
B
A
d
Intensity (arb. units)
q (1/nm)
e
z
-x
y
incident x-ray beam
α
scattered photons
q_z
-q_x

Figure 5.5. GISAXS measurements of BSLs assembled with 6.1 nm and 11.5 nm Au and Fe_2O_3 nanocrystals. The white circles in (a) correspond to the simulated diffraction spot pattern for a slightly distorted sh-AB_2 BSL with lattice dimensions b=c=13.8 nm, a=12.7 nm, γ=123.0°, which corresponds also to a centered orthorhombic (SG 65, *Cmmm*) unit cell oriented with the [010] direction normal to the substrate with dimensions a=c=13.8 nm, b=21.273 nm. The grey circles in (a) correspond to (011) and (111) spots of an sh-AB_2 lattice oriented with the crystallographic direction [001] normal to the substrate with unit cell dimensions of a=b=13.8 nm, c=12.3 nm. (See the Appendix D for a complete simulation and indexing of the (001) orientation, Figure D2.) (b) Simulated diffraction spots for sh-AB2 BSLs oriented on (100) planes with unit cell dimensions and a uniaxial lattice compression in the [210] direction of (grey dots) 13.8 nm, 12% and (white circles) 14.3 nm, 8% (which corresponds to a centered orthorhombic (SG65, *Cmmm*) lattice oriented in the [010] direction normal to the substrate with unit cell dimensions of (grey dots) a=c=13.8 nm, b=21.0 nm, and (white circles) a=c=14.3 nm, b=22.8 nm.) (c) Scattering pattern with rings of small spots indicated with dashed lines (A-F). (d) Radial integration of the scattering data in (c); Table 1 provides the q-values, d-spacings, and indices of the GISAXS data. (e) Schematic of the GISAXS configuration: incident x-ray beam, sample and sample manipulation, scattered beams, and area detector.

The GISAXS measurement in Figure 5.5a exhibits broad Bragg spots. These broad spots indicate that the scattering BSL grains are relatively small. The diffraction pattern indexes to a slightly distorted sh-AB_2 superlattice (AlB_2 analog, SG 191, *P 6/mmm*) oriented on its (100) plane on the substrate with unit cell dimensions of b=c=13.8 nm, a=12.7 nm and γ=123.0°. This structure corresponds to a simple hexagonal lattice with a uniaxial lattice contraction of 11% normal to the substrate in the [210] direction. This crystal structure is equivalent to a centered orthorhombic lattice (SG 65, *Cmmm*) oriented on a (010) plane with unit cell dimensions a=c=13.8 nm, b=21.273 nm (See Figure 5.6 and Figure D3 in Appendix D).

The GISAXS data in Figure 5.5a indicate that the sh-AB_2 BSL initially formed on the substrate with lattice dimensions of 13.8 nm and then contracted unidirectionally towards the substrate. This type of contraction normal to the substrate has been observed in other evaporated films as well, of ordered block copolymers,[50] mesoporous metal oxides,[51] and gold nanocrystal superlattices.[52] The lattice contraction results from the evaporation of residual solvent retained by the capping ligands just after BSL formation. As the residual solvent evaporates, the superlattice shrinks. But the nanocrystals cannot move laterally with respect to the substrate because their positions are fixed by adhesion to the substrate and as a result, the lattice decreases its total volume with a uniaxial compression towards the substrate.

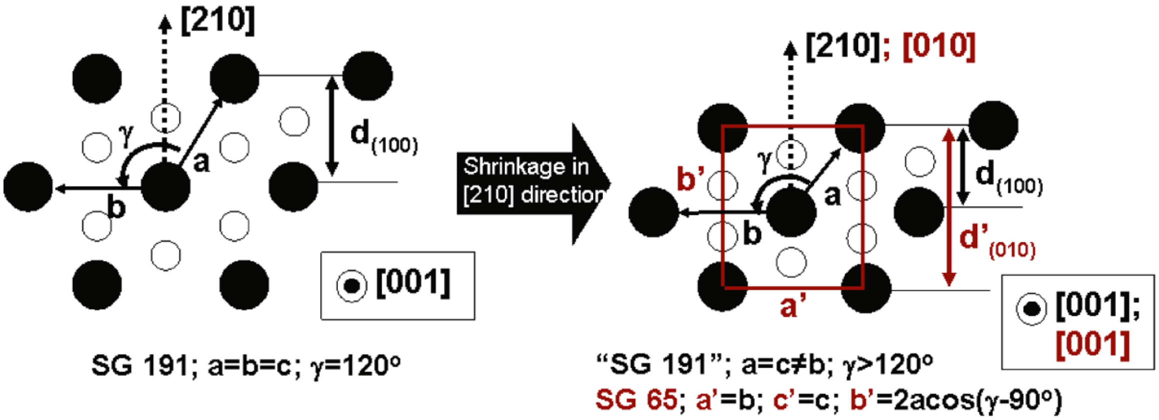

Figure 5.6. Depiction of the lattice contraction of a sh-AB_2 BSL that has contracted in the [210] direction during the late stages of drying. The BSL is oriented on its (100) plane and the contraction in the [210] direction changes the lattice symmetry from hexagonal to centered orthorhombic. The centered orthorhombic unit cell dimensions, *a*', *b*', *c*' are shown in red.

In addition to the diffraction spots in Figure 5.5a that index to sh-AB_2 BSL oriented on a (100) plane that has contracted in the [210] direction, there are two diffraction spots (labeled with gray circles) corresponding to sh-AB_2 BSL grains with a different crystallographic orientation on the substrate. These spots index to sh-AB_2 BSL grains oriented on their (001) planes that have contracted in the [001] direction, with unit cell dimensions of a=b=13.8 nm, c=12.3 nm. A complete simulation and indexing of the (001) orientation of a sh-AB_2 superlattice appears in Figure D2 of Appendix D.

The GISAXS patterns could not be indexed without considering the lattice contraction and the appropriate crystallographic orientation of the BSL grains on the substrate. Figure 5.5b provides another GISAXS example that reveals information about the superlattice orientation on the substrate and the uniaxial lattice compression that occurs perpendicular to the substrate. Both broad and narrow diffraction spots are present in Figure 5.5b, corresponding to relatively small and large superlattice grains, respectively. The broader diffraction spots indexed to a (100)-oriented sh-AB_2 BSL with lattice dimensions of 13.8 nm and a uniaxial lattice compression of 12% in the [210] direction. One set of the narrower diffraction spots indexed to a (100)-oriented sh-AB_2 superlattice with lattice dimensions of 14.3 nm that has contracted by 8% normal to the substrate in the [210] direction. These data indicate that more lattice shrinkage has occurred in the smaller BSL grains than in the larger grains.

Figure 5.5c shows another example of a GISAXS pattern obtained from an Au/Fe_2O_3 nanocrystal BSL sample. The "rings" of small spots suggest that a coexistence of many large superlattice grains with varying orientations exists on the substrate. One set of diffraction spots indexes to an orthorhombic BSL oriented in the [010] direction normal to the substrate with unit cell dimensions a=c=14.2 nm, b=22.628 nm (corresponding to a sh-AB_2 lattice with initial unit cell dimensions of 14.2 nm that has been compressed in the [210] direction by 8%). The ring-like diffraction pattern provides averaged information about the structure of the BSL grains since the grains have various crystallographic orientations. Indexing this pattern is complicated by the fact that BSL grains will have slightly different lattice *symmetry* depending on their orientation on the substrate due to the difference in the lattice direction of the uniaxial shrinkage. Nonetheless, the pattern can be approximately indexed to a simple hexagonal lattice, with the corresponding d-spacings obtained from the q-values of the diffraction rings,

$q = 2\pi/d$, provided in Table 1. Indexing the GISAXS data to a sh-AB$_2$ lattice gave lattice constants between 13.29 nm and 14.01 nm, which are consistent with what was found by TEM and SEM. But there is also a slight, but noticeable, anisotropy in the scattering rings. The diffraction features occur at slightly higher q in the x-direction than in the z-direction, which provides further indication of the lattice shrinkage normal to the substrate. Therefore, three different values of q (q_x, q_z and $<q>$) are provided in Table 5.1 for the scattering peak positions. The difference in these averaged lattice constants shows that the shrinkage is ~7%.

Table 5.1. Measured d-spacings from the GISAXS patterns in Figures 5.3c compared to the calculated d-spacings for a sh-AB$_2$ lattice (given in parentheses).

Ring	q_x (nm^{-1})	$d = \frac{2\pi}{q_x}$ (nm)*	q_z (nm^{-1})	$d = \frac{2\pi}{q_z}$ (nm)†	$<q>^{\S}$ (nm^{-1})	$d = \frac{2\pi}{\langle q \rangle}$ (nm)‡	Indexed planes
A	0.51	12.320 (12.134)	0.55	11.424 (11.510)	0.55	11.424 (11.668)	{100}
B	0.68	9.240 (9.172)	0.72	8.727 (8.701)	0.70	8.976 (8.820)	{101}
C	0.90	6.981 (7.006)	0.935	6.720 (6.646)	0.935	6.756 (6.737)	{110}
D	1.01	6.221 (6.266)	1.05	5.984 (5.944)	1.05	6.041 (6.025)	{111}
E	1.06	5.928 (6.067)	1.10	5.712 (5.755)	1.10	5.818 (5.834)	{200}
F	1.28	4.909 (4.954)	1.34	4.689 (4.699)	1.34	4.689 (4.764)	{112}

d-spacings calculated for a simple hexagonal lattice (SG191) with lattice constants *a*=*b*=*c*=14.01nm,* *a*=*b*=*c*=13.29nm,† and *a*=*b*=*c*=13.47nm.‡

§ Average q values obtained from the radial integration of the GISAXS data in Figure 5.5c.

5.3.3 Dislocations in sh-AB_2 BSLs

Bright stripes of nanocrystals were visible in SEM images of some BSLs formed on Si_3N_4 wafers, as shown in Figure 5.7. Additional SEM images of BSLs with these defects are provided in Appendix D. The stripes were observed in superlattices with the (100) plane parallel to the substrate and were identified to be superlattice dislocations consisting of gold nanocrystal half-planes inserted into the lattice as shown in Figure 5.7. Tilting the sample and imaging by SEM confirmed that the stripes were not step edges.

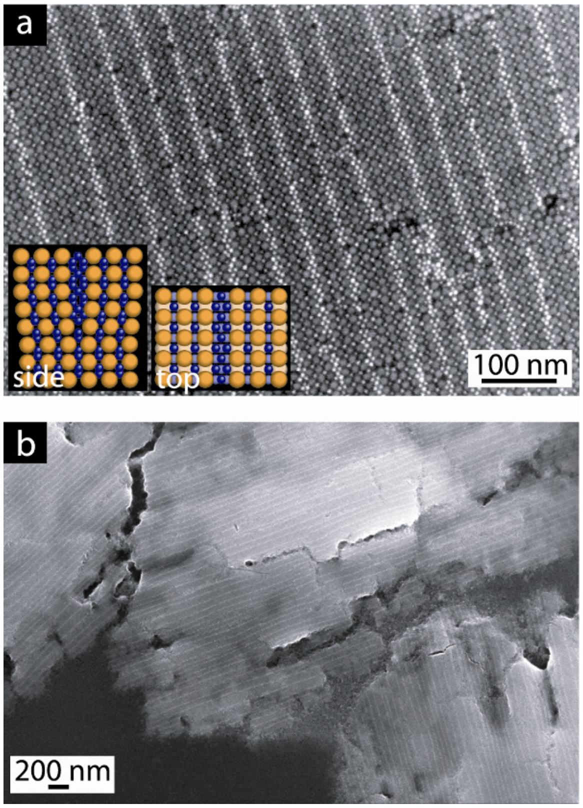

Figure 5.7. SEM images of superlattice dislocations: nearly periodic bright stripes are observed in these sh-AB_2 BSLs of 11.5 nm Fe_2O_3 and 6.1 nm Au nanocrystals oriented with (100) planes parallel to the substrate. The bright stripes are Au nanocrystal half-planes (dislocations) inserted into the lattice as illustrated in the inset in (a) as viewed from the side (looking at the (1-20) plane down the [010] axis) and from the top (looking at the (100) plane or down the [210] axis as viewed in the SEM images); the blue and orange spheres represent Au and Fe_2O_3 nanocrystals, respectively.

A correlation between the dislocation direction in neighboring superlattice islands, like those in Figure 5.7b and Figure 5.8, was observed. The inset in Figure 5.8 shows a histogram of the dislocation orientation measured from many BSL islands that were deposited on one substrate. The average dislocation orientation relative to the horizon in the figure is 37.3°. These islands appear to break off from a common BSL layer that forms at the air/solvent interface to deposit on the substrate. Although the drying direction is not known, the dislocation direction most likely occurs at 90° with respect to the drying direction, as illustrated in the figure, arising from the strain imposed on the BSL from the curved air/solvent interface as illustrated in Figure 5.9. The dislocations relieve this strain as the superlattice forms.

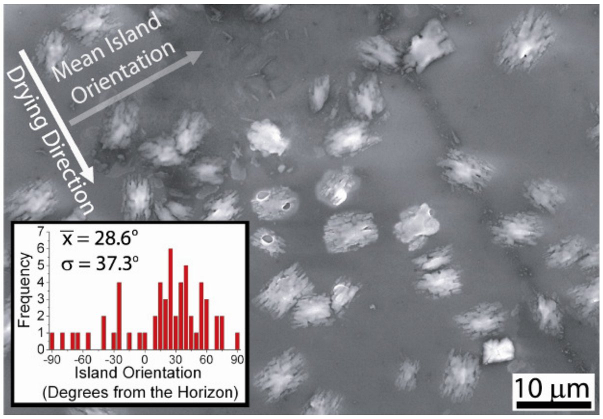

Figure 5.8. SEM image of BSL islands with visible inserted Au nanocrystal half-planes (dislocations). Inset: the orientational distribution of the dislocation direction with respect to the proposed drying direction indicated in the figure.

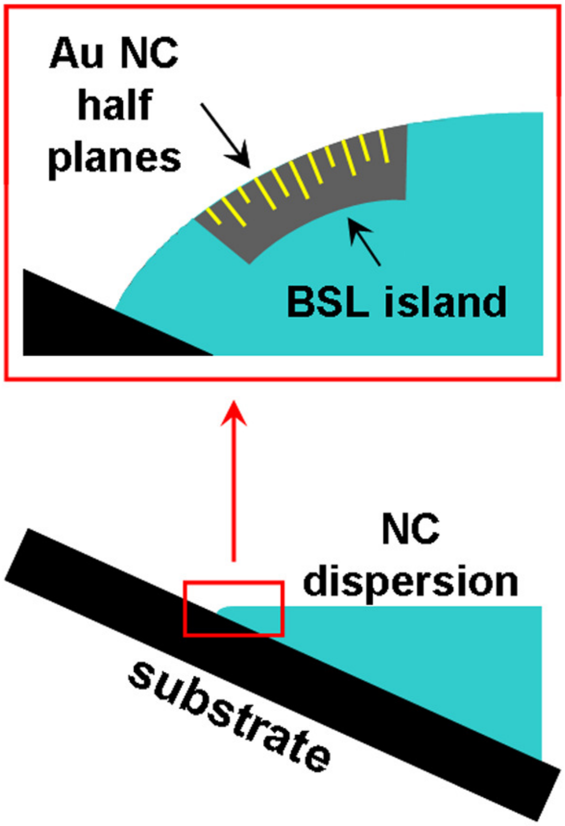

Figure 5.9 Illustration of the proposed mechanism of dislocation formation in the BSLs: gold nanocrystal half-planes insert into the crystallizing BSL to relieve strain at the curved air/solvent interface near the substrate.

5.3.4 Monolayers and Defects

An expansion of sh-AB_2 superlattice planes was observed in some thin superlattice layers. Figure 5.10a shows an example of such a sh-AB_2 superlattice, which has an unexpectedly large lattice constant of c=15.9 nm, compared to c=14.1 nm observed in thicker sh-AB_2 superlattice films such as those in Figures 5.10b and 5.10c. The thin nanocrystal layer in the lower right corner of Figure 5.10a corresponds to a (100) sh-AB_2 plane.

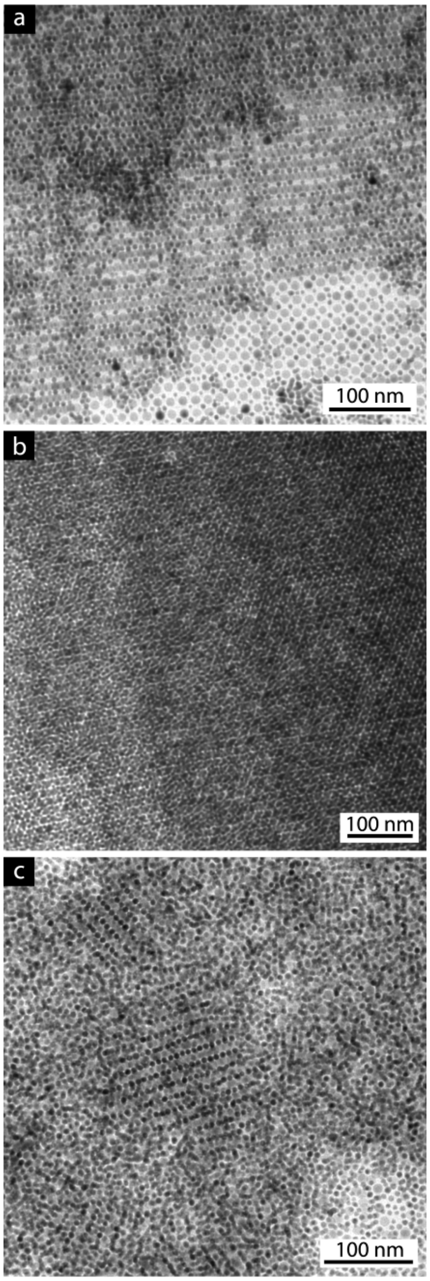

Figure 5.10. TEM images of thin sh-AB_2 BSLs. In (a) and (b) the superlattices appear to have nucleated on the substrate and crystallized from the bottom of the image to the top in (a) and from the left to the right in (b). The (100) plane is parallel to the substrate in image (a) and the (001) plane is parallel to the substrate in (b). In (c), the nanocrystals on the substrate are disordered and the BSL (with (100) orientation parallel to the substrate) does not appear to have nucleated on the substrate.

The TEM image in Figure 5.10a reveals a case in which the BSL structure (with the (100) plane parallel to the substrate) appears to assemble from a monolayer on the substrate into ordered multilayers. Another TEM image in Figure 5.10c shows an example of sh-AB_2 superlattices with lower nanocrystal layers that are disordered, suggesting that in this case the superlattices formed in solution and their assembly was not directed by the solution-substrate interface. Therefore, the influence of the substrate on BSL nucleation is presently not entirely clear, but perhaps when the superlattices nucleate on the substrate their lattice dimensions are directed by the substrate, which can give rise to an "expanded" unit cell like that in Figure 5.10a or a BSL structure different than the sh-AB_2 structure.

A new BSL structure was also observed that is similar to a (100) plane of a cuboctahedron AB_{13} superlattice (space group 226, $Fm\overline{3}c$) with Au nanocrystals substituted for Fe_2O_3 nanocrystals at the 8a Wyckoff positions in the unit cell (of space group 226). Figure 5.11 shows a TEM image of this structure. This BSL structure was observed only in thin nanocrystal layers. Although this structure is not equivalent to a cuboctahedron AB_{13} superlattice, it is structurally very similar and is not surprising that it coexists with the AB_2 superlattices since the coexistence of AB_2 and AB_{13} superlattices has been observed in a number of cases, including hard sphere colloidal particles[53-56] and binary nanocrystal superlattices.[2,3]

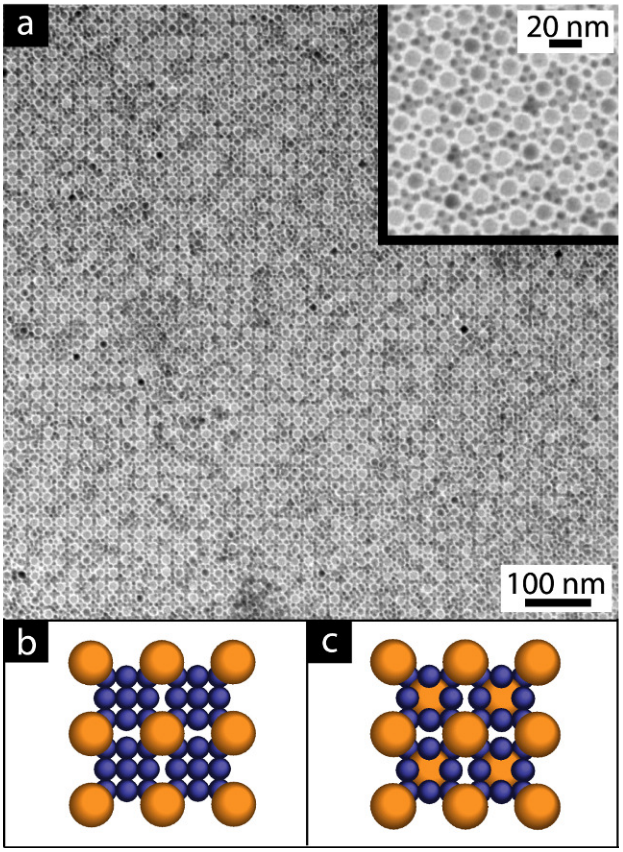

Figure 5.11. (a) TEM image of a two-dimensional BSL (a monolayer) with structure similar to the (100) plane of a cuboctahedron AB13 superlattice. The inset shows a higher magnification image. (b) Three-dimensional model of space group 226, a cuboctahedron AB_{13} superlattice. (c) Three-dimensional representation of a superlattice with Fe_2O_3 nanocrystals (orange) in place of Au nanocrystals (blue) at the 8a Wyckoff positions in the unit cell of space group 226.

5.3.5 BSL Formation and Space-Filling in the sh-AB2 Lattice.

All of the BSLs were made by slowly evaporating the solvent from concentrated dispersions with added oleic acid on tilted substrates. As shown in Figure 5.12, phase segregation of Au and Fe_2O_3 nanocrystal superlattices was regularly observed when oleic acid was not added in excess to the dispersion. Also, when the nanocrystals were deposited on flat substrates, BSLs were not observed. These observations indicate that the forces directing BSL formation are surprisingly subtle.

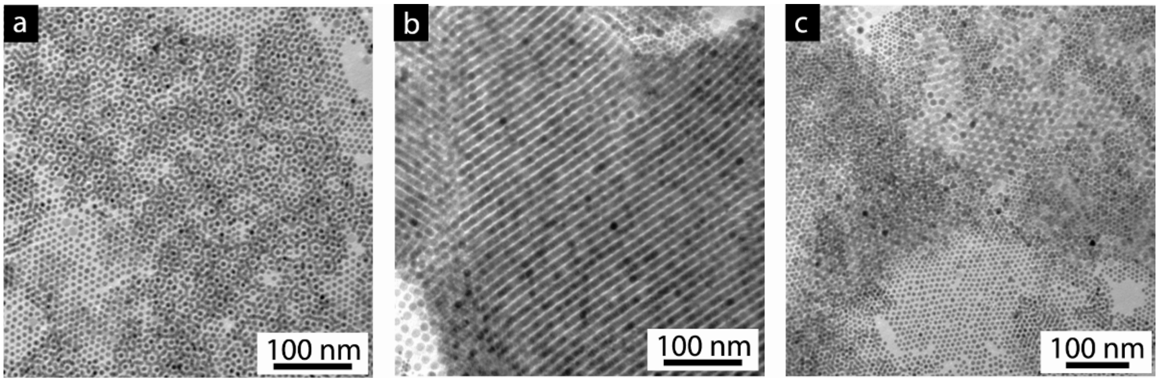

Figure 5.12. TEM images of phase separated regions of (a) Au and (b) Fe_2O_3 nanocrystals that formed when oleic acid was not added to the binary nanocrystal dispersion. Superlattices of Fe_2O_3 resulted as shown in (b), but no binary superlattices. Image (c) shows the phase separated regions are in close proximity.

Various driving forces for BSL formation have been mentioned in the literature,[2,3,7,8] but there is currently no consensus as to which forces are most influential. Some of this uncertainty probably stems from the complicating interactions of the deposition substrate, particularly in the case of thin BSL films, which have exhibited a variety of different structures. Certainly, one of the primary driving forces of BSL formation is the increase in “free volume” entropy that occurs when the bidisperse nanocrystals order into a lattice.[36,37,53,57] The sh-AB_2 lattice is a dense structure and spheres with the right size ratio (the radius ratio of large (R) and small (r) spheres that most efficiently fill space in a sh-AB_2 lattice is r/R=0.528) occupy 78% of the available volume when ordered into this lattice—this is denser than a face centered cubic (fcc) lattice (74%) of monodisperse spheres and nearly as dense as the closest-packed rock salt lattice (79%, but only for a radius ratio of 0.414; a rock salt lattice with a radius ratio of 0.528 is much less dense than the sh-AB_2 structure).

The Au and Fe_2O_3 nanocrystals used in this study are nearly perfectly size-matched for forming sh-AB_2 BSLs. From the interparticle spacing measured by GISAXS, the *effective* radii of Au and Fe_2O_3 nanocrystals are 3.8 nm and 7.15 nm, which corresponds to r/R=0.531. The nanocrystals exhibit an effective radius in the superlattice that consists of the inorganic cores, which are 3.05 nm and 5.75 nm for the Au and Fe_2O_3 nanocrystals, along with the additional space occupied by the ligands that intervene between the inorganic surfaces in the superlattice. The volume filled by ligands is determined experimentally from the combination of the GISAXS measurements that reveal the BSL unit cell dimensions and electron microscopy, which provides the inorganic core sizes. The experimentally determined ligand volume in the BSLs compares well to the expected excluded volume for nanocrystals with monolayer capping ligand coverage, to within ±10%.[49] The Au and Fe_2O_3 nanocrystals pack together into ordered superlattices of "soft spheres," as described previously for the case of superlattices of monodisperse ligand-stabilized nanocrystals.[36,37] For these nearly ideal sh-AB_2 BSLs, there is no need to believe that exotic forces between nanocrystals, such as electrostatic charging, is playing a role in their formation; although there is no evidence here that would discount their presence either.[58]

5.3.6 Depletion Attraction and its Possible Role on BSL Formation.

Additional attractive forces can further enhance BSL formation, as well as disrupt it. Van der Waals attractions,[36,37] ligand-ligand interactions,[38] capillary forces,[39] and electrostatic interactions[2] have been proposed to be important. One force that has not been discussed to any significant extent with respect to BSL formation is the *depletion attraction* between nanocrystals that can be induced by the excess free oleic acid in the dispersion. Depletion attraction forces are those that arise between two bodies—such as two nanocrystals—are immersed in a solution of macromolecules and the interparticle separation becomes less than the size of the macromolecule.[57,59] Depletion attraction forces are typically important when the macromolecule is less than about one tenth the size of the nanocrystal and can easily move out of the intervening space between the particles, which is certainly the case of an oleic acid molecule. When the interparticle separation is less than the diameter of the macromolecule, it becomes excluded from the intervening solvent, which leads to an osmotic force that drives the intervening solvent out from between the particles and pushes them together. Asakura and Oosawa[59] first that an attractive force *F*, develops between two spheres of diameter *D*, when the interparticle separation *d*, is less than the size of an intervening macromolecule *a*, that is also present in the solution:

$$F = -\frac{\pi}{4} p_0 \left\{ (D+d)^2 - a^2 \right\} \ , \quad D < a < D + d; \tag{1}$$

$$F = 0 \, , \qquad\qquad a > D + d \quad . \tag{2}$$

In Eqn (1), p_0 is the osmotic pressure of the macromolecular solution, $p_0 = kTN/V$, which in the case of interest is the oleic acid solution. kT is the thermal energy and N/V is the concentration. These expressions show how an increasing oleic acid concentration can enhance the depletion attraction force between nanocrystals. The depletion attraction between nanocrystals become increasingly significant as the solvent evaporates and concentrates the nanocrystals and the oleic acid. The fact that depletion attraction forces are relatively short range is also important for superlattice formation. These forces help squeeze the nanocrystals together as the solvent evaporates, but do not lead to irreversible particle aggregation—once the macromolecule becomes excluded from between the nanocrystals, the steric repulsion between nanocrystals due to the adsorbed ligands still prevents flocculation. This is important, as the nanocrystals need the ability to orient into their lowest energy structure (i.e., the superlattice).

5.3.7 The Evaporative Front

The other question about BSL formation regards the role of the evaporative front at the liquid-air and liquid-substrate interfaces. Some data indicate that BSLs assemble by nucleating from the substrate, as in the cases shown in Figures 5.10a and 5.10b. In other images, like Figure 5.10c, ordered BSL domains are resting on a layer of disordered nanocrystals, indicating that the BSLs formed in solution first before depositing on the substrate. The SEM images provided in Appendix D show that the BSLs crystallize from solution as grains resting on the substrate. Previous studies of gold nanocrystals have found that superlattice monolayers can assemble at the air-liquid interface of an evaporating dispersion.[60] Most of the BSLs studied here appear to crystallize at the air/solvent interface and then deposit onto the substrate as a floating interfacial layer. The curvature of the air/solvent interface leads to strain in the superlattice, which in some cases can lead to dislocations of inserted half-planes of Au nanocrystals in the BSLs with nearly periodic spacing.

5.4 CONCLUSIONS

Simple hexagonal (sh) AB_2 BSLs of 11.5 nm Fe_2O_3 and 6.1 nm Au nanocrystals were assembled and studied by TEM, SEM and GISAXS. BSL formation required the slow evaporation of a dispersing solvent with nanocrystal deposition on a tilted substrate. The addition of excess oleic acid to the dispersion solution was also found to be critically important for BSL formation. Excess oleic acid is believed to be inducing depletion attraction forces between the nanocrystals that help overcome the kinetic barrier to BSL formation. The solvent-air-substrate interface is also important, as the BSLs form at this interface.

The GISAXS data showed Bragg spots indicating relatively long-range order in the BSLs. GISAXS also revealed two predominant crystallographic orientations with of

(100) and (001) lattice planes on the substrate, but (110) oriented BSLs were also observed by TEM. GISAXS revealed a uniaxial shrinkage of 8 to 12% of the superlattice normal to the substrate that is not observable by TEM and SEM since these methods probe the structure by looking perpendicular to the substrate. The lattice shrinkage is the result of the evaporation of residual solvent that is retained in the superlattice right after deposition. For BSLs that have oriented on their hexagonal (100) planes on the substrate, this shrinkage changes the lattice symmetry to orthorhombic.

In addition to the relatively extended sh-AB2 BSLs, some defect BSL structures were also observed. Nearly periodic dislocations of inserted superlattice half-planes of Au nanocrystals were observed, appearing as bright stripes of nanocrystals in SEM images. A new thin film BSL structure was also observed that is similar to cuboctahedron AB_{13} structure with Fe_2O_3 nanocrystals in place of Au nanocrystals at the 8a Wyckoff positions in the unit cell of space group 226. A relatively large expansion of the sh-AB_2 lattice was also observed when deposited as a thin, near-monolayer film.

BSLs provide an exciting avenue for nanomaterials design. As synthetic methods and self-assembly approaches continue to develop, it is becoming increasingly likely that new materials might be designed systematically and rationally. Presently, however, further experiments are needed to elucidate in detail how BSLs nucleate, the driving forces for BSL formation and the role of the air-solvent-substrate interface on BSL formation. In situ GISAXS to follow BSL assembly in real time might be one next step. The SEM and GISAXS measurements presented here clearly show that BSLs are amenable to such studies.

5.5 REFERENCES AND NOTES

1. Redl, F. X.; Cho, K. S.; Murray, C. B.; O'Brien, S. *Nature* **2003,** *423*, 968-971.

2. Shevchenko, E. V.; Talapin, D. V.; Kotov, N. A.; O'Brien, S.; Murray, C. B. *Nature* **2006,** *439*, 55-59.

3. Shevchenko, E. V.; Talapin, D. V.; Murray, C. B.; O'Brien, S. *J. Am. Chem. Soc.* **2006,** *128*, 3620-3637.

4. Shevchenko, E. V.; Kortright, J. B.; Talapin, D. V.; Aloni, S.; Alivisatos, A. P. *Adv. Mater.* **2007,** *19*, 4183-4188.

5. Shevchenko, E. V.; Ringler, M.; Schwemer, A.; Talapin, D. V.; Klar, T. A.; Rogach, A. L.; Feldmann, J.; Alivisatos, A. P. *J. Am. Chem. Soc.* **2008,** *130*, 3274-3275.

6. Overgaag, K.; Evers, W.; de Nijs, B.; Koole, R.; Meeldijk, J.; Vanmaekelbergh, D. *J. Am. Chem. Soc.* **2008,** *130*, 7833-7835.

7. Chen, Z.; O'Brien, S. *ACS Nano* **2008**, *2*, 1219-1229.

8. Kiely, C. J.; Fink, J.; Brust, M.; Bethell, D.; Schiffrin, D. J. *Nature* **1998,** *396*, 444-446.

9. Chen, Z. Y.; Moore, J.; Radtke, G.; Sirringhaus, H.; O'Brien, S. *J. Am. Chem. Soc.* **2007,** *129*, 15702-15709.

10. Lu, C.; Chen, Z.; O'Brien, S. *Chem. Mater.* **2008,** *20*, 3594-3600.

11. Shevchenko, E. V.; Talapin, D. V.; O'Brien, S.; Murray, C. B. *J. Am. Chem. Soc.* **2005,** *127*, 8741-8747.

12. Saunders, A. E.; Korgel, B. A. *ChemPhysChem* **2005,** *6*, 61-65.

13. Urban, J. J.; Talapin, D. V.; Shevchenko, E. V.; Kagan, C. R.; Murray, C. B. *Nat. Mater.* **2007,** *6*, 115-121.

14. Lee, D. C.; Smith, D. K.; Heitsch, A. T.; Korgel, B. A. *Annu. Rep. Prog. Chem., Sect. C, Phys. Chem.* **2007,** *103*, 351-402.

15. Liz-Marzan, L. M. *Mat. Today* **2004,** *7*, 26-31.

16. Jun, Y. W.; Choi, J. S.; Cheon, J. *Angew. Chem., Int. Ed.* **2006,** *45*, 3414-3439.

17. Buonsanti, R.; Grillo, V.; Carlino, E.; Giannini, C.; Curri, M. L.; Innocenti, C.; Sangregorio, C.; Achterhold, K.; Parak, F. G.; Agostiano, A.; Cozzoli, P. D. *J. Am. Chem. Soc.* **2006,** *128*, 16953-16970.

18. Carbone, L.; Kudera, S.; Giannini, C.; Ciccarella, G.; Cingolani, R.; Cozzoli, P. D.; Manna, L. *J. Mater. Chem.* **2006,** *16*, 3952-3956.

19. Choi, J. S.; Jun, Y. W.; Yeon, S. I.; Kim, H. C.; Shin, J. S.; Cheon, J. *J. Am. Chem. Soc.* **2006,** *128*, 15982-15983.

20. Cozzoli, P. D.; Pellegrino, T.; Manna, L. *Chem. Soc. Rev.* **2006,** *35*, 1195-1208.

21. Kudera, S.; Carbone, L.; Casula, M. F.; Cingolani, R.; Falqui, A.; Snoeck, E.; Parak, W. J.; Manna, L. *Nano Lett.* **2005,** *5*, 445-449.

22. Kwon, K. W.; Lee, B. H.; Shim, M. *Chem. Mater.* **2006,** *18*, 6357-6363.

23. Pellegrino, T.; Fiore, A.; Carlino, E.; Giannini, C.; Cozzoli, P. D.; Ciccarella, G.; Respaud, M.; Palmirotta, L.; Cingolani, R.; Manna, L. *J. Am. Chem. Soc.* **2006,** *128*, 6690-6698.

24. Shi, W. L.; Zeng, H.; Sahoo, Y.; Ohulchanskyy, T. Y.; Ding, Y.; Wang, Z. L.; Swihart, M.; Prasad, P. N. *Nano Lett.* **2006,** *6*, 875-881.

25. Yu, H.; Chen, M.; Rice, P. M.; Wang, S. X.; White, R. L.; Sun, S. H. *Nano Lett.* **2005,** *5*, 379-382.

26. Alivisatos, A. P. *Nat. Biotechnol.* **2004,** *22*, 47-52.

27. Durr, N. J.; Larson, T.; Smith, D. K.; Korgel, B. A.; Sokolov, K.; Ben-Yakar, A. *Nano Lett.* **2007,** *7*, 941-945.

28. Lee, J. H.; Huh, Y. M.; Jun, Y.; Seo, J.; Jang, J.; Song, H. T.; Kim, S.; Cho, E. J.; Yoon, H. G.; Suh, J. S.; Cheon, J. *Nat. Med.* **2007,** *13*, 95-99.

29. Michalet, X.; Pinaud, F. F.; Bentolila, L. A.; Tsay, J. M.; Doose, S.; Li, J. J.; Sundaresan, G.; Wu, A. M.; Gambhir, S. S.; Weiss, S. *Science* **2005,** *307*, 538-544.

30. Zeng, H.; Li, J.; Liu, J. P.; Wang, Z. L.; Sun, S. *Nature* **2002,** *420*, 395-398.

31. Gur, I.; Fromer, N. A.; Geier, M. L.; Alivisatos, A. P. *Science* **2005,** *310*, 462-465.

32. Rogach, A. L. *Angew. Chem., Int. Ed.* **2004,** *43*, 148-149.

33. Cheon, J.; Park, J. I.; Choi, J. S.; Jun, Y. W.; Kim, S.; Kim, M. G.; Kim, Y. M.; Kim, Y. J. *Proc. Natl. Acad. Sci.* **2006,** *103*, 3023-3027.

34. Collier, C. P.; Vossmeyer, T.; Heath, J. R. *Annu. Rev. Phys. Chem.* **1998,** *49*, 371-404.

35. For example, the maximum packing fractions for superlattices with cub-AB (rock salt) and sh-AB_2 (AlB_2) structures are 0.793 and 0.778, respectively; whereas, the

maximum packing fractions of the ico-AB_{13}, cub-AB_{13} and $CaCu_5$ structures are 0.738, 0.7 and 0.7, respectively. A face center cubic lattice of monodisperse nanocrystals has a packing fraction of 0.74, which is more dense than the ico-AB_{13}, cub-AB_{13} and $CaCu_5$ lattices that would be formed by a bidisperse mixture of nanocrystals. The packing fractions also depend on the actual particle size ratio and are maximized when the smaller nanocrystals fit perfectly into the interstitial spaces within a lattice composed of the larger nanocrystals—i.e., 0.414 for cub-AB and 0.53 for sh-AB_2.

36. Korgel, B. A.; Fullam, S.; Connolly, S.; Fitzmaurice, D. *J. Phys. Chem. B* **1998,** *102*, 8379-8388.

37. Korgel, B. A.; Fitzmaurice, D. *Phys. Rev. B* **1999**, *59*, 14191-14201.

38. Luedtke, W. D.; Landman, U. *J. Phys. Chem.* **1996**, *100*, 13323-13329.

39. Rabideau, B. D.; Bonnecaze, R. T. *Langmuir* **2004,** *20*, 9408-9414.

40. The issue of how subtle forces and packing density influence superlattice structure is a rich topic. For example, the packing density, coordination number and local packing geometry are equivalent for face-centered cubic (fcc) and hexagonal close-packed (hcp) structures, yet fcc superlattices tend to be favored because there is a small entropy increase when the close packed planes of the superlattice stack into a cubic structure with *ABC* stacking instead of the *ABAB* stacking of an hcp lattice. Relatively slight differences in interparticle interactions have been shown to lead to changes in superlattice structure; for example, by increasing the ratio of the ligand length to the radius of the inorganic core, the superlattice changes from fcc to body-center cubic (bcc).[37,61]

41. Sigman, M. B.; Saunders, A. E.; Korgel, B. A. *Langmuir* **2004,** *20*, 978-983.

42. Brust, M.; Walker, M.; Bethell, D.; Schiffrin, D. J.; Whyman, R. *Chem. Commun.* **1994**, 801-802.

43. Murray, C. B.; Norris, D. J.; Bawendi, M. G. *J. Am. Chem. Soc.* **1993,** *115*, 8706-8715.

44. Hyeon, T.; Lee, S. S.; Park, J.; Chung, Y.; Bin Na, H. *J. Am. Chem. Soc.* **2001,** *123*, 12798-12801.

45. Gruner, S. M.; Tate, M. W.; Eikenberry, E. F. *Rev. Sci. Instrum.* **2002,** *73*, 2815-2842.

46. Hammersley, A.P. ESRF Internal Report, **1997,** *ESRF97HA02T*.

47. Tate, M. P.; Urade, V. N.; Kowalski, J. D.; Wei, T. C.; Hamilton, B. D.; Eggiman, B. W.; Hillhouse, H. W. *J. Phys. Chem. B* **2006,** *110*, 9882-9892.

48. The fully extended ligand length L, was computed using the fact that dodecanethiol and oleic acid have hydrocarbon chain lengths n, of 12 and 18: $L = 0.154 + 0.127n\,(\mathrm{nm})$.[62]

49. From TEM, the inorganic Au and Fe_2O_3 cores are 6.1 nm and 11.5 nm in diameter. Since the unit cell contains one Fe_2O_3 and two Au nanocrystals, the volume taken up by the inorganic cores of the Au and Fe_2O_3 nanocrystals in the unit cell is 1034.02 nm^3. The total unit cell volume determined from GISAXS is 2552.32 nm^3. Assuming that the Au and Fe_2O_3 nanocrystals are coated with a monolayer of ligands, the ligands have total excluded volumes of 233 nm^3 and 1209 nm^3, respectively. These values are calculated by using the relation, $v = (27.4 + 26.9n)\times 10^{-3}\,(\mathrm{nm}^3)$ for the excluded volume v, of each ligand molecule,[62] and estimating the number of ligands bound to each nanocrystal by taking a circular molecular "footprint" of 16 $Å^2$/molecule and assuming a close-packed monolayer with 91% surface coverage (the surface coverage of a hexagonal close-packed layer of disks).[36] From the GISAXS measurements of the BSL unit cell dimensions inorganic core sizes measured by TEM, the ligands must occupy (1990.81 nm^3 + 561.51 nm^3) - 1034.02 nm^3 = 1518.30 nm^3, which is very close to the estimated excluded volume of the ligands assuming close-packed capping ligand monolayers on the nanocrystals, which is 1209 nm^3 + (2×233 nm^3) = 1675 nm^3—a difference of ~9%.

50. Bosworth, J. K.; M. Y. Paik; Ruiz, R.; Schwartz, E. L.; Huang, J. Q.; Ko, A. W.; Smilgies, D. M.; Black, C. T.; Ober, C. K. *ACS Nano* **2008**, 2, 1396-1402.

51. Ruland, W.; Smarsly, B. M.; *J. Appl. Crystallogr.* **2007**, 40, 409-417.

52. Dunphy, D.; Fan, H.; Li, X.; Wang, J.; Brinker, C. J. *Langmuir* **2008**; *24*, 10575-10578.

53. Cottin, X.; Monson, P. A. *J. Chem. Phys.* **1995,** *102*, 3354-3360.

54. Murray, M. J.; Sanders, J. V. *Philos. Mag. A* **1980,** *42*, 721-740.

55. Schofield, A. B.; Pusey, P. N.; Radcliffe, P. *Phys. Rev. E* **2005,** *72*, 031407.

56. Bartlett, P.; Ottewill, R. H.; Pusey, P. N. *Phys. Rev. Lett.* **1992,** *68*, 3801-3804.

57. Gelbart, W. M.; Ben-Shaul, A. *J. Phys. Chem.* **1996**, *100*, 13169-13189.

58. The term, "nearly ideal," is used here to refer to the fact that the BSLs do not strictly have the simple hexagonal lattice symmetry because of their uniaxial lattice shrinkage perpendicular to the substrate that results during the late drying process when residual solvent entrained in the ligands evaporates after the BSL has formed and deposited on the substrate. This slight lattice distortion to an orthorhombic lattice itself is not predicted from simple sphere packing arguments,

but easily understood in terms of how the substrate pins the nanocrystals and prevents their restructuring during this late stage of the drying process.

59. Asakura, S.; Oosawa, F., *J. Chem. Phys.* **1954**, *22*, 1255-1256.

60. Bigioni, T. P.; Lin, X. M.; Nguyen, T. T.; Corwin, E. I.; Witten, T. A.; Jaeger, H. M. *Nat. Mater.* **2006,** *5*, 265-270.

61. Whetten, R. L.; Shafigullin, M. N.; Khoury, J. T.; Schaaff, T. G.; Vezmar, I.; Alvarez, M. M.; Wilkinson, A. *Acct. Chem. Res.* **1999**, *32*, 397-406.

62. Israelachvili, J. *Intermolecular & Surface Forces* (2nd ed., Academic Press, San Diego, CA, 1992).

Chapter 6: Conclusions and Future Research Directions

6.1 CONCLUSIONS

Carbon nanotubes, gold nanorods, silica coated magnetic nanocrystals, and binary nanocrystal superlattices possess interesting size, shape, and material properties. These interesting properties suggest that the nanomaterials may serve as novel components for new technologies with diverse applications including biology, microelectronics, optics, and photovoltaics. These applications will undoubtedly require production of the nanomaterials in high yield, with precise control over the reaction tunability and cost-effective methods. Optimization of the synthesis of carbon nanotubes was demonstrated, and factors significant to the synthesis of gold nanorods, silica coated magnetic nanocrystals, and binary nanocrystal superlattices were studied.

6.1.1 Carbon Nanotubes

Carbon nanotubes possess interesting mechanical, optical, and electronic properties which suggest they may be useful in a variety of applications. The primary route to carbon nanotube synthesis has been via the gas phase, where carbon sources are degraded over a catalyst bed at relatively high temperatures. Because gas phase synthesis is cost prohibitive and solution-phase synthetic routes can lead to continuous processability, we explored carbon nanotube synthesis in supercritical toluene, where toluene serves as both the reaction medium and carbon source for the reaction.

Multiwall carbon nanotubes (MWNTs) with outer diameters of 10 to 50 nm and wall thicknesses 5 to 20 nm were synthesized in supercritical toluene at temperatures ranging from 600 °C to 645 °C at 8.3 MPa. The nanotube formation was catalyzed by metallocenes such as cobaltocene, nickelocene, and ferrocene, or cobalt or iron nanocrystals. We found that supplemental carbon sources, either hexane or ethanol (~30 vol%), increased the yield of carbon nanotubes relative to pure toluene, and catalytic amounts of water (0.75 vol%) minimized the formation of carbon filaments and amorphous carbon.

Cobaltocene, with ethanol as a supplemental carbon source, gave the highest percentage of nanotubes in the product (~70%) and the highest conversion of toluene to MWNTs (~4%). Cobaltocene was also found to catalyze coiled nanotube formation, with the appearance of springs, hairpins, lassos, and coiled ropes arising from defects in the nanotube graphitic layers. The MWNTs tended to exhibit bamboo morphology and appear to grow by a folded-growth mechanism with graphitic sheets wrapped around the seed metal particles.

6.1.2 Gold Nanorods

Though the colloidal, seed-mediated synthesis of gold nanorods was developed in 2001 it is still not entirely understood. One important key to a reproducible synthesis is the purity of the surfactant precursor, cetyltrimethylammonium bromide (CTAB). Gold nanorods were synthesized using the colloidal seed-mediated, surfactant-assisted approach with CTAB obtained from ten different suppliers. The yield of gold nanorods depended strongly on the CTAB used: with the same recipe, three of the CTABs did not yield nanorods and produced only spherical gold particles, whereas the other CTABs yielded nanorods with nearly 100% yield. Inductively coupled plasma mass spectrometry revealed a trace iodide impurity in the CTABs that did not yield nanorods. Further experiments introducing potassium iodide to the nanorod synthesis verified the detrimental effect of iodide on nanorod formation. The nanorod morphology was also destroyed when potassium iodide was introduced post-synthesis.

6.1.3 Silica Coated Magnetic Nanocrystals and Gold Nanorods

Heterostructured nanomaterials possess the properties of each constituent and are exciting new candidates for biological imaging. Multifunctional colloidal core-shell nanoparticles of magnetic nanocrystals of iron oxide or FePt or gold nanorods encapsulated in silica shells doped with the fluorescent dye, Tris(2,2′-bipyridyl)dichlororuthenium(II) hexahydrate (Rubpy) were synthesized. The as-prepared magnetic nanocrystals were initially hydrophobic and were coated with silica using a microemulsion approach, while the as-prepared gold nanorods were hydrophilic and were coated with silica using a Stöber-type of process. Each approach yielded monodisperse nanoparticles with uniform fluorescent dye-doped silica shells. These colloidal heterostructures have the potential to be used as dual-purpose tags—exhibiting a fluorescent signal that could be combined with either dark-field optical contrast (in the case of the gold nanorods), or enhanced contrast in magnetic resonance images (in the case of magnetic nanocrystal cores). The optical and magnetic properties of the fluorescent silica-coated gold nanorods and magnetic nanocrystals are reported in Chapter 4.

6.1.4 Binary Nanocrystal Superlattices

When nanocrystals of the right size ratio are mixed in the correct proportions, they will self-assemble into binary nanocrystal superlattices (BSLs). BSLs of sterically-stabilized, hydrophobic, large (A; 11.5 nm diameter) iron oxide and small (B; 6.1 nm diameter) Au nanocrystals were assembled by slow evaporation of colloidal dispersions on tilted substrates. A detailed analysis of the BSL structure was carried out TEM and SEM and GISAXS. The BSLs were simple hexagonal (sh) AB2 superlattices (isostructural with the compound AlB2; space group 191, P 6/mmm) of large nanocrystals occupying a simple hexagonal lattice with small nanocrystals in the interstitial spaces. SEM and GISAXS confirmed long range order of the BSLs and GISAXS revealed that the superlattice is slightly contracted (8~12%) perpendicular to the substrate as a result of solvent drying in the deposition process. When the sh-AB2 superlattice deposits on a (100) plane, this shrinkage occurs in the [210] direction and changes the lattice symmetry to centered orthorhombic. Additionally, nearly periodic superlattice dislocations consisting of inserted half-planes of gold nanocrystals were observed by SEM in some BSLs.

6.2 FUTURE RESEARCH DIRECTIONS

6.2.1 Carbon Nanotubes

Multiwall carbon nanotubes were produced in high yield using supercritical toluene as a reaction medium. Supplemental carbon sources and catalytic amounts of water served to increase the nanotube yield and minimize amorphous carbon deposition on the nanotube sidewalls, respectively. These improvements are important initial steps towards a high-throughput solution phase synthesis of carbon nanotubes.

Another ultimate goal using this system is the production of single wall carbon nanotubes. Single wall carbon nanotubes were never observed in our syntheses, but possibly with the enhancement of reaction parameters such as temperature and/or seed nanocrystal diameter, they could be, and this is one major goal in this area of research. The necessity for higher temperatures might lead to an alternative supercritical fluid media. Toluene quickly degrades at temperatures over 640 °C, producing large populations of graphitic byproducts which may poison the catalyst seed particles. Alternative solvents that are more stable at temperatures greater than 640 °C could lead to a more controllable reaction environment.

Gas phase carbon nanotube synthesis has revealed that carbon nanotube diameter is often dictated by the seed nanocrystal size. In a supercritical fluid, the catalyst particles are freely floating, subject to agglomeration and Ostwald ripening in situ. Templated or patterned substrates with tethered catalysts seeds of fixed diameter could potentially lead to single wall carbon nanotubes formed in supercritical fluids.

One major challenge in the field of single wall carbon nanotubes synthesis is to synthesize nanotubes of only one chirality; i.e. nanotubes that are either all semiconducting or metallic. Alternatively, other strategies could be developed to separate tubes of different chiralities post-synthesis.

6.2.2 Gold Nanorods

Trace impurities of iodide in the surfactant precursor were found to disrupt the formation of gold nanorods made with a colloidal seed mediated synthesis. Previous work with semiconductor quantum dots revealed that trace impurities in tri-n-octylphosphine oxide, the capping ligand of these materials, also directed their final shape. These results suggest that nanomaterials are very sensitive to the presence of trace impurities during their growth process.

The significance of the iodide impurity in CTAB is an important discovery that furthers our understanding of the crystallization of rod-shaped nanocrystals from a cubic material such as gold. Further study to elucidate the differences in the growth directions between the step-wise additive and Ag(I)-assisted growth methods could lead to additional understanding of the nanorod growth mechanism. Additionally, experiments to verify the proposed model of nanorod inhibition by iodide binding to Au {111} could be performed.

6.2.3 Silica Coated Magnetic Nanocrystals and Gold Nanorods

As-prepared hydrophobic magnetic nanocrystals and hydrophilic gold nanorods were coated with fluorescent dye doped silica shells using the microemulsion and Stöber methods, respectively. These colloidal heterostructures have the potential to be used as dual-purpose tags, exhibiting a fluorescent signal that could be combined with either dark-field optical contrast or enhanced contrast in magnetic resonance imaging. Varying the heterostructure properties could lead to enhancement of the suitability of the dye-doped, silica coated magnetic nanocrystals as MRI contrast agents. For example, future MRI experiments could study the effect of the thickness of the silica shell, the nanocrystal core size, or surface functionalization to enhance the solubility and site specificity of these materials. There is an obvious tradeoff between overall particle size, which can hinder the heterostructure mobility in the body, and the intensity of the fluorescence signal, which corresponds to the thickness of the dye-doped silica shell. Perhaps *in vitro* or *in vivo* studies could be performed to determine the optimum particle size.

6.2.4 Binary Nanocrystal Superlattices

Simple hexagonal AB_2 BSLs of large iron oxide and small gold nanocrystals were assembled by slow evaporation of colloidal dispersions on tilted substrates. In some BSLs nearly periodic superlattice dislocations consisting of inserted half-planes of gold nanocrystals were observed. These half-planes are believed to arise from the strain induced by the curvature of the solution droplet at the air-liquid-substrate interface. Future experiments varying the sample tilt angle (and perhaps the radius of curvature of the droplet) might elucidate the onset of the insertion of such half-plane defects. In situ GISAXS would also be an interesting way to determine how BSLs nucleate and grow.

Additionally, further experiments varying the ratio and size of the nanocrystals could produce BSLs with AB (rock salt), AB_{13}, or other geometries. The introduction of a third nanocrystal size could potentially lead to the formation of ternary nanocrystal superlattices as well.

6.2.5 The Future of Nanotechnology

Interest in the field of nanotechnology is ever-growing. In 2000, the National Nanotechnology Initiative was founded by the United States federal government to encourage, conduct, and coordinate nanotechnology research and development. This establishment as well as growing corporate interest in nanotechnology research signifies the importance, great potential, and probable longevity of this field.

We know that many new nanomaterials undoubtedly show great promise for implementation in future technologies. However, the imperative further understanding and better characterization of these systems has also pointed out some of their potential limitations. For nanocrystals with biological imaging applications such as gold nanorods and silica coated magnetic nanocrystals, one key goal is to make these nanomaterials site specific with a high degree of accuracy. Developing biological recognition ligands that can effectively attach to nanocrystal surfaces *and* can target the nanocrystals to specific types of cells or even specific sites on a cell is a major challenge.

The health impact of nanomaterials is also a growing concern. For example, some data suggests that carbon nanotubes can induce asbestos-like toxicological symptoms when inhaled. The safe handling, disposal, environmental, and health effects of exposure to all types of nanomaterials are areas that need further study. This knowledge will only empower and reassure both the nanotechnology researchers and the public about all of the exciting benefits of nanomaterials applications.

Appendix A: Multiwall Carbon Nanotube Synthesis in Supercritical Fluids

PART 1: PHASE DIAGRAM OF TOLUENE

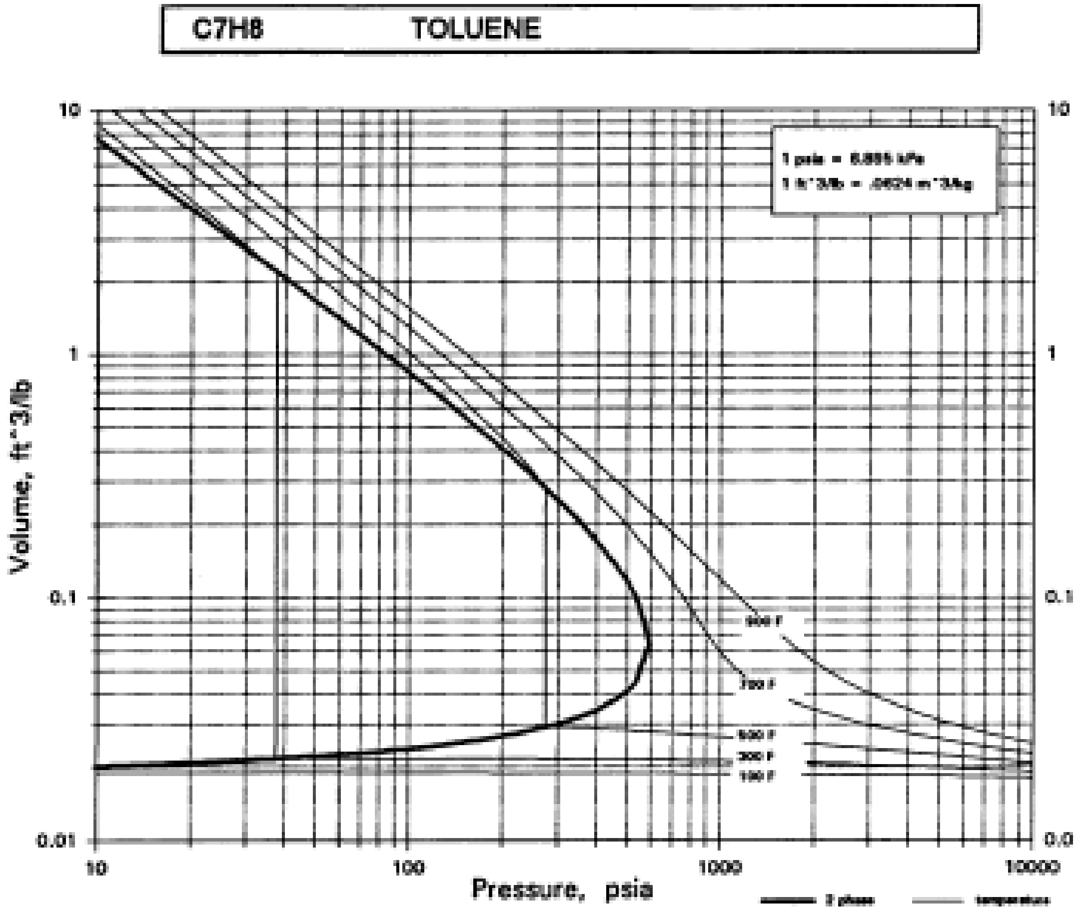

Figure A1. Volume versus pressure phase diagram of toluene. From reference[1].

PART 2: REFERENCES

1. Yaws, C. L., *Handbook of Thermodynamic Diagrams. Vol. 2: Organic Compounds C_5 to C_7*. Elsevier: Houston, 1996; Vol. 2.

Appendix B: The Influence of Iodide Impurities in CTAB on the Colloidal Seed-Mediated Synthesis of Gold Nanorods

PART 1: GOLD NANOROD OPTICAL PROPERTIES

The optical properties of dispersions of gold colloids can be predicted with Mie Theory[1, 2] through expressions for extinction cross section, C_{ext}.[3-5] For very small particles with a frequency dependent, complex dielectric function, ε:

$$\varepsilon = \varepsilon' + i\varepsilon''$$

which are embedded in a medium of dielectric constant ε_m, this can be expressed by:

$$C_{ext} = k\,\mathrm{Im}(\alpha)$$

where k is the wave vector and α is the polarizability of the colloid. The wave vector, k, is given by:

$$k = \left(\frac{2\pi\varepsilon_m^{1/2}}{\lambda}\right)$$

For a sphere, α is:

$$\alpha_{sphere} = \left(\frac{\varepsilon - \varepsilon_m}{\varepsilon + 2\varepsilon_m}\right) 4\pi r^3$$

where r is the sphere radius.

Gans[6] expanded upon Mie theory by predicting that for very small ellipsoids, the surface plasmon mode would split into two distinct modes. He quantified the response as function of the ellipsoid aspect ratio. Though nanorods are shaped more like cylinders than ellipsoids, analytical solutions of Mie theory for cylinders is not possible. Thus, the nanorods are represented as ellipses where the polarizability, α is:

$$\alpha_{nanorod} = \left(\frac{\alpha_1 + \alpha_2 + \alpha_3}{3}\right)$$

α_i corresponds to the polarizability of each of the nanorod dimensions and is given by:

$$\alpha_i = \left(\frac{\varepsilon - \varepsilon_m}{3\varepsilon_m + 3L_i(\varepsilon - \varepsilon_m)} \right) 4abc$$

where *a*, *b*, and *c* refer to the length of the ellipse (or nanorod) along the x, y, and z axes (a>b=c). The depolarization factor for the respective axes L_i are related by:

$$L_x + L_y + L_z = 1$$

and for an ellipsoidal particle such as a gold nanorod,

$$L_x = \frac{1-e^2}{e^2} \left(-1 + \frac{1}{2e} \ln\left(\frac{1+e}{1-e} \right) \right)$$

and

$$L_y = L_z = \frac{1-L_x}{2}$$

where *e* is the eccentricity of the ellipsoid and is related to the aspect ratio (*a*/*b*) by:

$$e^2 = 1 - \frac{b^2}{a^2}$$

For nanorods, there will be two plasmon resonances with energies of:

$$E = E_p \sqrt{L_i}$$

in the absorbance spectrum, where E_p is the bulk Au plasmon energy of 8.89 eV.

For bulk materials,

$$\varepsilon'_{\text{bulk}} = n^2 - k^2$$

and

$$\varepsilon''_{\text{bulk}} = 2nk$$

where *n* is the index of refraction and *k* is the extinction coefficient, which are both a function of photon energy *E*. For colloidal systems, the Drude free electron model[3, 7] can be used in conjunction with Mie Theory[1, 2] to approximate both the free electron (Drude,

D) and interband (IB) contributions to ε. The interband contribution accounts for the response of the 5d-electrons while the Drude contribution accounts for the electrodynamics of the nearly free conduction electrons.

$$\varepsilon' = \varepsilon'_D + \varepsilon'_{IB}$$

and

$$\varepsilon'' = \varepsilon''_D + \varepsilon''_{IB}$$

where

$$\varepsilon'_D = 1 - \frac{E_p^{\,2}}{E^2 + E_o^{\,2}}$$

and

$$\varepsilon''_D = \frac{E_p^{\,2} E_o}{E(E^2 + E_o^{\,2})}$$

where E_p is the bulk Au plasmon energy of 8.89 eV and $E_o = 0.027$ eV. The interband contribution, ε'_{IB} and ε''_{IB} for the nanocrystals can thus be calculated:

$$\varepsilon'_{IB} = \varepsilon'_{bulk} - \varepsilon'_D$$

$$\varepsilon''_{IB} = \varepsilon''_{bulk} - \varepsilon''_D$$

For nanocrystals, $E_o \approx 0.92/r$, where r is the radius in nanometers and E_o is in eV. Using the known dimensions of the nanorods, new values of ε'_D and ε''_D can then be calculated and summed with ε'_{IB} and ε''_{IB} to get nanorod specific values of ε' and ε'', respectively, for each nanorod dimension. Therefore there will be ε' and ε'' for both the longitudinal and transverse dimensions of the nanorod, corresponding to characteristic lengths L_x and L_y. The extinction cross section, C_{ext}, for a nanorod is then:

$$C_{ext,\,nanorod} = k\,\mathrm{Im}\left(\frac{\alpha_1 + 2\alpha_2}{3}\right) =$$

$$\frac{8\pi\varepsilon_m^{3/2}\cdot abc}{3\lambda}\left\{\left(\frac{\varepsilon_1''}{(\varepsilon_m + L_1(\varepsilon_1' - \varepsilon_m)^2 + L_1\varepsilon_1''^2}\right) + \left(\frac{2\varepsilon_2''}{(\varepsilon_m + L_2(\varepsilon_2' - \varepsilon_m)^2 + L_2\varepsilon_2''^2}\right)\right\}$$

Because gold nanorods are capped with a CTAB bilayer, $\varepsilon_m \approx 2.5$. The above equation can be used to solve for the plasmonic peak positions of gold nanorods of known aspect ratio. Alternatively, the nanorod aspect ratio can be determined from the absorbance spectra by setting one of the denominators of the polarizability expression equal to 0 and solving for either L_1 or L_2.

Using the above equations, El-Sayed's group[8] derived an empirical relationship between the aspect ratio and the wavelength λ_{max} of the longitudinal plasmon resonance:

$$\lambda_{\max} = 33.34\varepsilon_m \frac{b}{a} - 46.31\varepsilon_m + 472.31$$

PART 2: ADDITIVES AFFECTING THE SYNTHESIS OF GOLD NANORODS

Many factors can affect the synthesis of gold nanorods including the concentration of Ag(I) in the growth solution, the amount of seeds added to the growth solution, pH, and the addition of salts such as Na_2S. Some of these variables can be used to fine tune the position of the second plasmon peak. One such example is by varying the concentration of Ag added to the growth solution.[9] 75 µL was found to be optimum for producing nanorods with a peak in the near-infrared region.

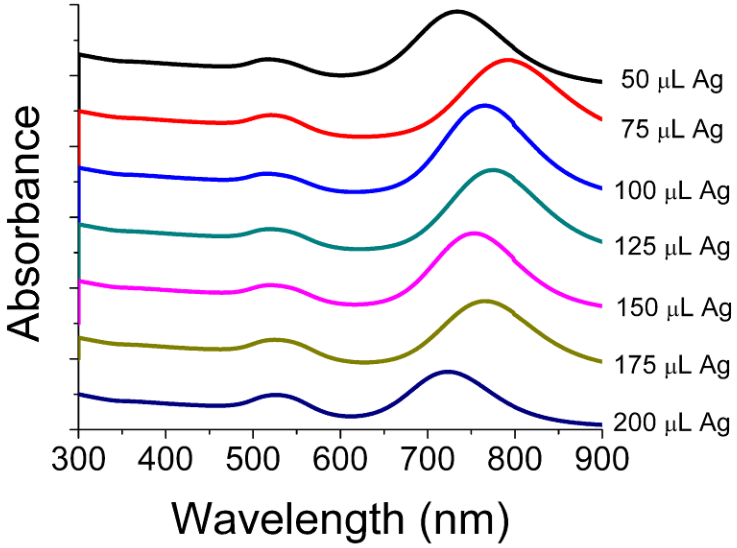

Figure B1. Au nanorods synthesized using the Ag(I)-assisted method with various amounts of $AgNO_3$ added to the reaction. Because 75 μL was found to be optimum for producing nanorods with a peak in the near-infrared region, all future control experiments used this amount of $AgNO_3$.

The second plasmon peak could also be tuned by varying the amount of gold nanoparticle seed solution added to the reaction. The second plasmon peak in the absorbance spectrum was found to redshift by increasing the amount of seeds added, but the peak height relative to that of the first plasmon peak was found to diminish with increasing seed volume addition. Therefore, though the peak is redshifted the overall yield of nanorods is not as high. We found the optimum nanorod production with 12 μL of seed as reported in the literature.

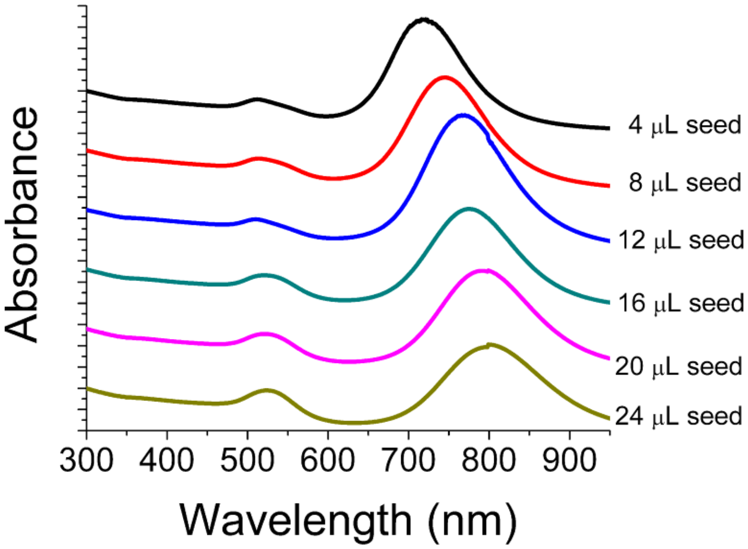

Figure B2. Au nanorods synthesized using the Ag(I)-assisted method with various amounts of seed gold solution added to the growth solution. The control is 12 μL of seed.

The effect of acidic and basic conditions on gold nanorod growth were also studied. By adding 55 μL of 0.1 M HCl or 0.1M NaOH, the solutions were made acidic and basic, respectively. Acidic conditions were found to slightly redshift the second plasmon peak while basic conditions destroyed the formation of nanorods. Changes in the pH affect the reducing ability of ascorbic acid and the reduction potentials of the gold and silver ions. Thus, when the solutions were too basic gold nanorods could not be made.

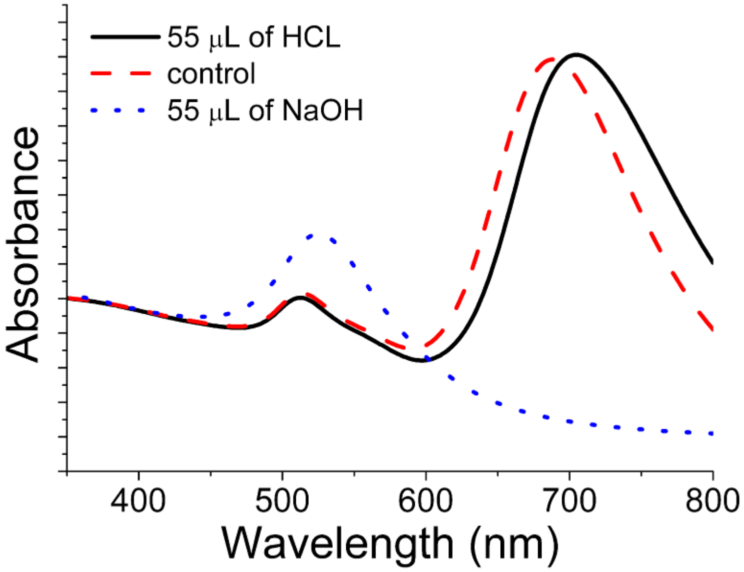

Figure B3. Au nanorods synthesized using the Ag(I)-assisted method in the presence of 0.1 M HCl or 0.1 M NaOH.

The addition of sodium sulfide (Na_2S) to the gold nanorod growth solution after seed addition can prevent the blueshifting of the second plasmon peak which occurs over time. Sulfide serves as a scavenger for Au and Ag ions, removing them from the reaction mixture and preventing them from later depositing on the nanorod side facets as the gold nanorods age in solution.

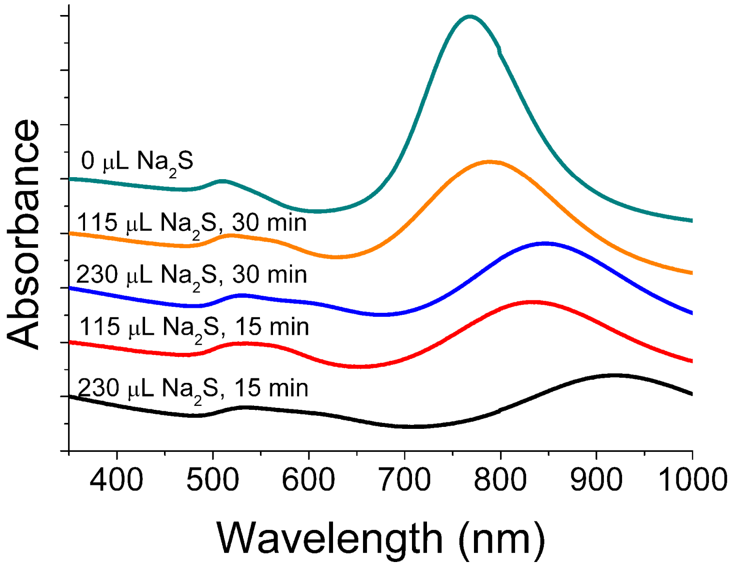

Figure B4. Au nanorods synthesized using the Ag(I)-assisted method with various amounts of seed sodium sulfide (Na_2S) added a specified period of time after gold seed addition.

Figure B5 shows an absorbance spectra and TEM images of Au nanorods that were synthesized without the addition of $Ag(NO_3)$. Although some very long nanorods are observed, the majority of the product consists of gold particles, as confirmed by the wavelength of the observed plasmon resonance. Figure B6 shows HRTEM images of gold seeds made from CTAB manufactured by (a) Acros and (b) MP Biomedicals that were used in the synthesis of gold nanorods. Gold nanorods resulted from the synthesis using MP Biomedicals CTAB but not Acros. Table 1 in the main text of the paper summarizes the results of the nanorod growth reactions carried out using all of these CTAB samples obtained from different suppliers.

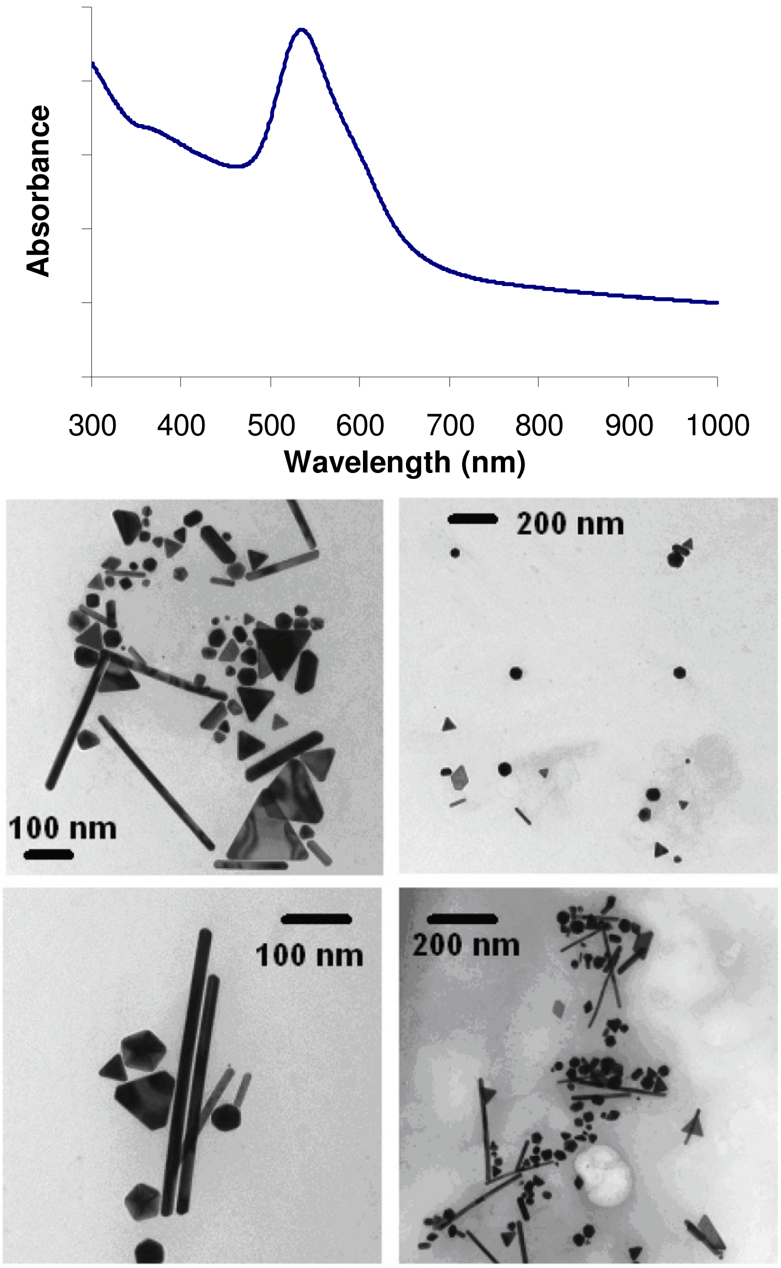

Figure B5. Au nanorods synthesized using the described recipe, but without the addition of Ag(NO_3) to the reaction. Although some very long nanorods (and triangles) are made, the majority of the product consists of spherical particles, as confirmed by the plasmon peak energy in the absorbance spectra (top).

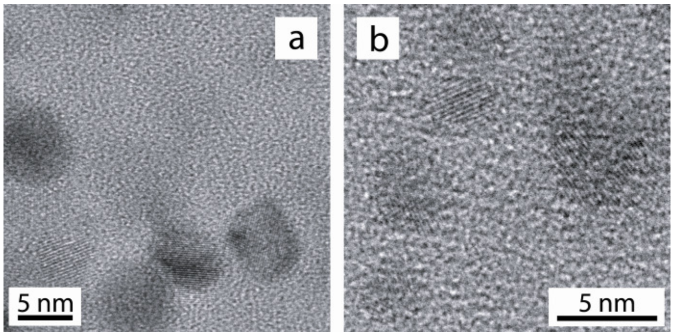

Figure B6. HRTEM images of gold seeds used in gold nanorod synthesis made from CTAB manufactured by (a) Acros and (b) MP Biomedicals.

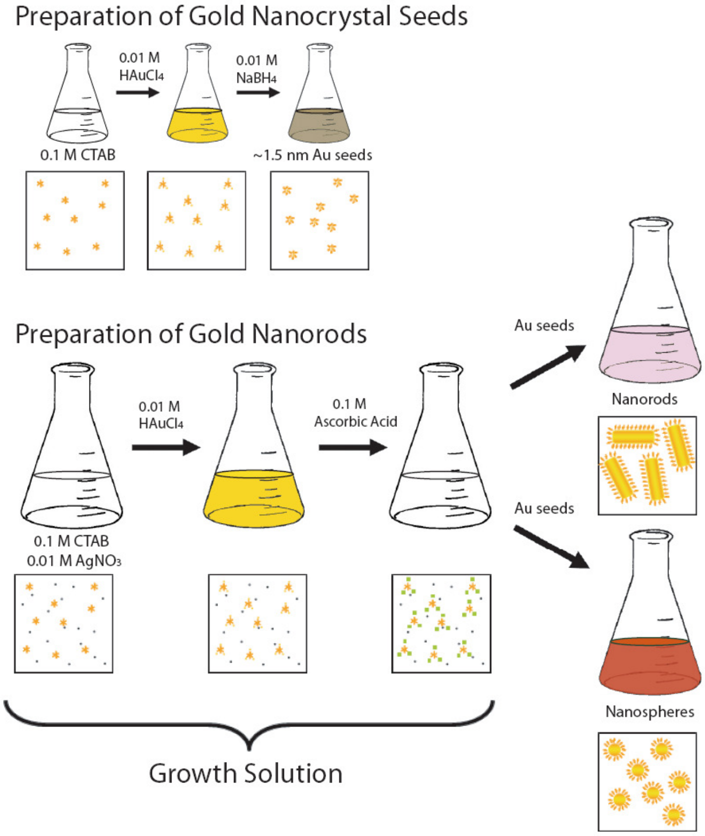

Figure B7. Seed-mediated, Ag(I)-assisted gold nanorod synthesis. Black dots represent Ag^+, the orange zig-zags are CTAB in the form of micelles, the yellow circles and green squares are $AuCl_4^-$, and $AuCl_2^-$, respectively, complexed with CTAB micelles. The gold nanocrystal seeds are injected into the growth solution in the final step of the nanorod synthesis. When iodide impurities are present, nanospheres will form instead of nanorods.

PART 3: ANALYTICAL TECHNIQUES

We employed several different analytical techniques including mass spectrometry, X-ray diffraction (XRD), hydrogen-1 nuclear magnetic resonance (^{1}H NMR), carbon-13 nuclear magnetic resonance, (^{13}C NMR), and size exclusion chromatography (SEC) to determine what impurities might be present in CTAB obtained from different suppliers. In summary, we did not observe any noticeable difference. Mass spectrometry, XRD, and SEC analysis resulted in identical spectra for all of the CTAB samples examined. There were subtle differences were between the ^{1}H NMR and ^{13}C NMR spectra, however, these were identified as either residual solvent (like ethanol) or as irreproducible noise in the measurement.

XRD data was acquired by drying an aqueous solution of concentrated CTAB into a film on a quartz slide using a Bruker-Nonius D8 Advance Theta-2Theta powder diffractometer with

Cu KAlpha radiation (Lambda = 1.5418 Å) and collecting with a scintillation detector for 8 h with an incremental angle of 0.02° at a scan rate of 10°/min. LC/MS (mass spectrometry) data was collected from a Thermo-Fisher LTQ Mass Spectrometer with a Surveyor Plus HPLC pump. The sample was prepared by dissolving 1 mg of CTAB in 1 mL of doubly-distilled, deionized water. The NMR measurements were made on a Varian Inova Unity Spectrometer at 500 MHz for ^{1}H NMR and 125 MHz for ^{13}C NMR. In each case, the sample was prepared by dissolving 10 mg of CTAB in 0.6 mL of D_2O. SEC (size exclusion chromatography) was acquired on 15 mg of CTAB dissolved in 1 g of DMF using a gel permeation column with an Optilab DSP refractometer and a DAWN EOS multi-angle laser light scattering detector. High-resolution transmission electron microscopy (HRTEM) imaging was performed on a JEOL 2010F transmission electron microscope operating at a voltage of 200 kV.

Figure B8 shows mass spectrometry data of CTAB supplied by Fluka (52370), MP Biomedicals, Acros, Sigma (H5882), and Aldrich. Figure B9 shows XRD data of CTAB supplied by Fluka (52370) and Sigma (H5882). Figure B10 shows ^{1}H NMR spectra of CTAB from Fluka (52370), Sigma (H5882), and Sigma (H6269). Figures B11 and B12 contains ^{13}C NMR spectra of CTAB supplied by Fluka (52370), Sigma (H5882), and Sigma (H6269). Figure B13 shows SEC data of CTAB supplied by Fluka (52370) and Sigma (H5882).

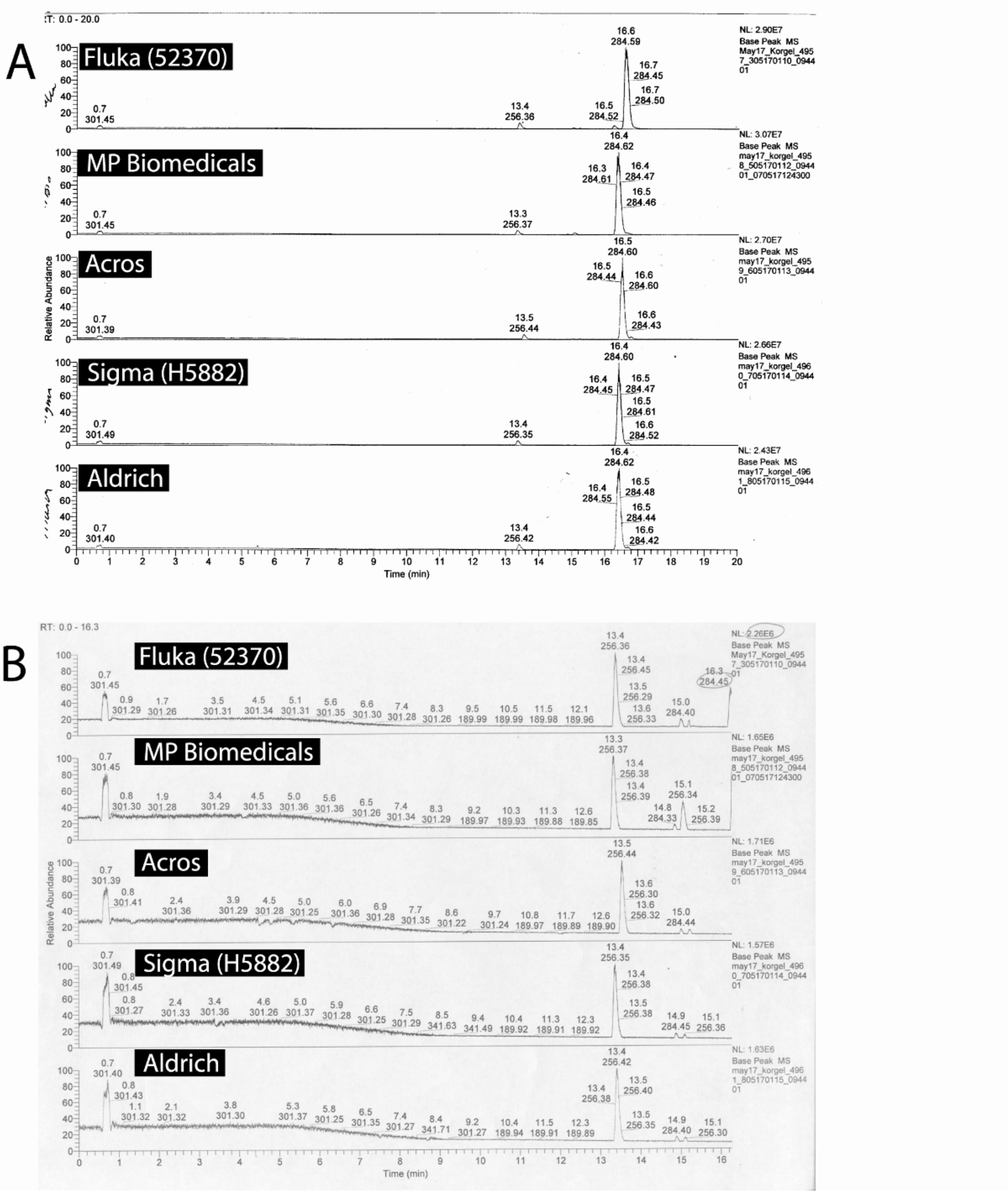
A
RT: 0.0 - 20.0
Fluka (52370)
MP Biomedicals
Acros
Sigma (H5882)
Aldrich
Relative Abundance
Time (min)
NL: 2.90E7 Base Peak MS May17_Korgel_4957_305170110_094401
NL: 3.07E7 Base Peak MS may17_korgel_4958_505170112_094401_070517124300
NL: 2.70E7 Base Peak MS may17_korgel_4959_605170113_094401
NL: 2.66E7 Base Peak MS may17_korgel_4960_705170114_094401
NL: 2.43E7 Base Peak MS may17_korgel_4961_805170115_094401
0.7 301.45
13.4 256.36
16.6 284.59
16.7 284.45
16.7 284.50
16.5 284.52
13.3 256.37
16.4 284.62
16.3 284.61
16.4 284.47
16.5 284.46
0.7 301.39
13.5 256.44
16.5 284.60
16.5 284.44
16.6 284.60
16.6 284.43
0.7 301.49
13.4 256.35
16.4 284.60
16.4 284.45
16.5 284.47
16.5 284.61
16.6 284.52
0.7 301.40
13.4 256.42
16.4 284.62
16.4 284.55
16.5 284.48
16.5 284.44
16.6 284.42
B
RT: 0.0 - 16.3
NL: 2.26E6
NL: 1.65E6
NL: 1.71E6
NL: 1.57E6
NL: 1.63E6
16.3 284.45
13.4 256.36
13.4 256.45
13.5 256.29
13.6 256.33
15.0 284.40
13.3 256.37
13.4 256.38
13.4 256.39
15.1 256.34
14.8 284.33
15.2 256.39
13.5 256.44
13.6 256.30
13.6 256.32
15.0 284.44
13.4 256.35
13.4 256.38
13.5 256.38
14.9 284.45
15.1 256.36
13.4 256.42
13.4 256.38
13.5 256.40
13.5 256.35
14.9 284.40
15.1 256.30

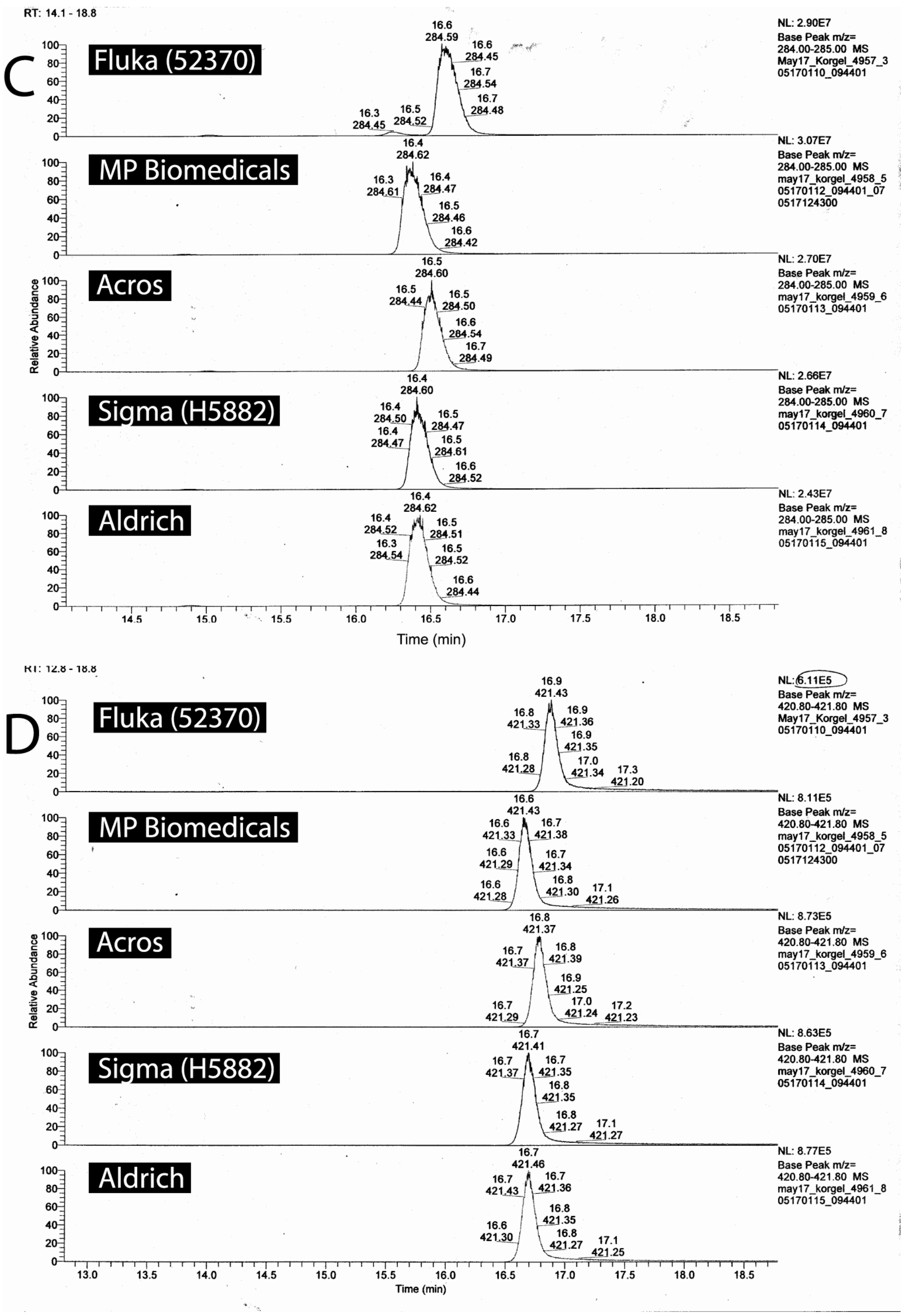
RT: 14.1 - 18.8
C
Fluka (52370)
MP Biomedicals
Acros
Sigma (H5882)
Aldrich
NL: 2.90E7 Base Peak m/z= 284.00-285.00 MS May17_Korgel_4957_3 05170110_094401
NL: 3.07E7 Base Peak m/z= 284.00-285.00 MS may17_korgel_4958_5 05170112_094401_07 0517124300
NL: 2.70E7 Base Peak m/z= 284.00-285.00 MS may17_korgel_4959_6 05170113_094401
NL: 2.66E7 Base Peak m/z= 284.00-285.00 MS may17_korgel_4960_7 05170114_094401
NL: 2.43E7 Base Peak m/z= 284.00-285.00 MS may17_korgel_4961_8 05170115_094401
16.6 284.59
16.4 284.62
16.5 284.60
16.4 284.60
16.4 284.62
Relative Abundance
Time (min)
RT: 12.8 - 18.8
D
Fluka (52370)
MP Biomedicals
Acros
Sigma (H5882)
Aldrich
NL: 6.11E5 Base Peak m/z= 420.80-421.80 MS May17_Korgel_4957_3 05170110_094401
NL: 8.11E5 Base Peak m/z= 420.80-421.80 MS may17_korgel_4958_5 05170112_094401_07 0517124300
NL: 8.73E5 Base Peak m/z= 420.80-421.80 MS may17_korgel_4959_6 05170113_094401
NL: 8.63E5 Base Peak m/z= 420.80-421.80 MS may17_korgel_4960_7 05170114_094401
NL: 8.77E5 Base Peak m/z= 420.80-421.80 MS may17_korgel_4961_8 05170115_094401
16.9 421.43
16.6 421.43
16.8 421.37
16.7 421.41
16.7 421.46
Relative Abundance
Time (min)

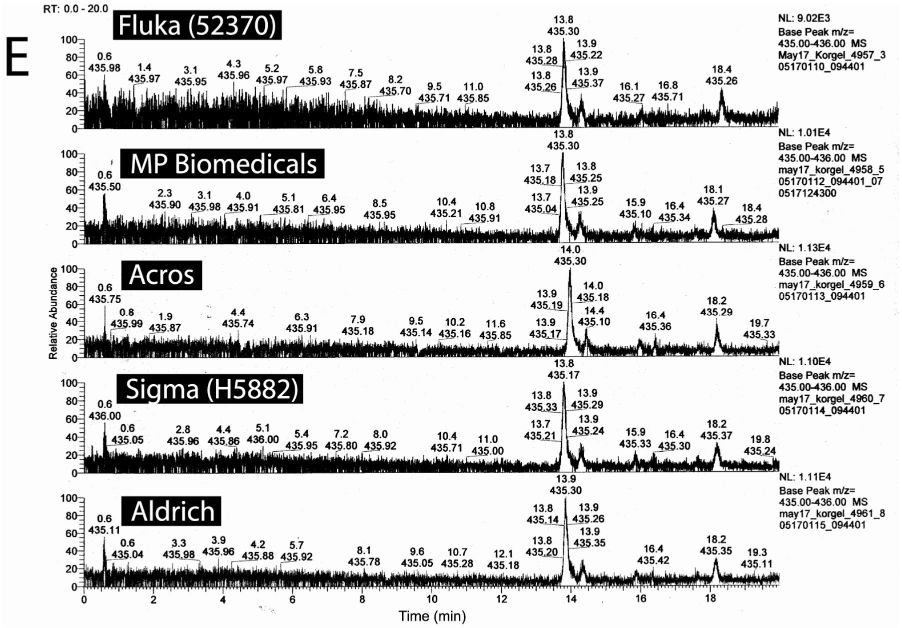

Figure B8. Mass spectrometry of CTAB supplied by Fluka (52370), MP Biomedicals, Acros, Sigma (H5882) and Aldrich. (A) The primary peak is centered at 284.6. Small peaks that might be impurities appeared at (B) 256 (C) 284 (D) and 421 (E) 435, but were found to be present in approximately the same amount in all of the CTAB samples.

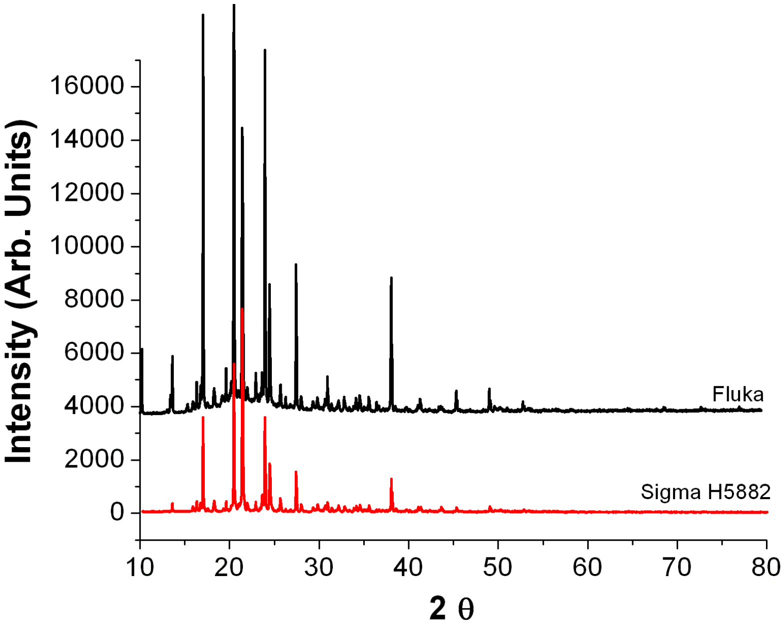

Figure B9. XRD of CTAB supplied by Fluka (52370) and Sigma (H5882). Peaks appear at the same positions in both samples.

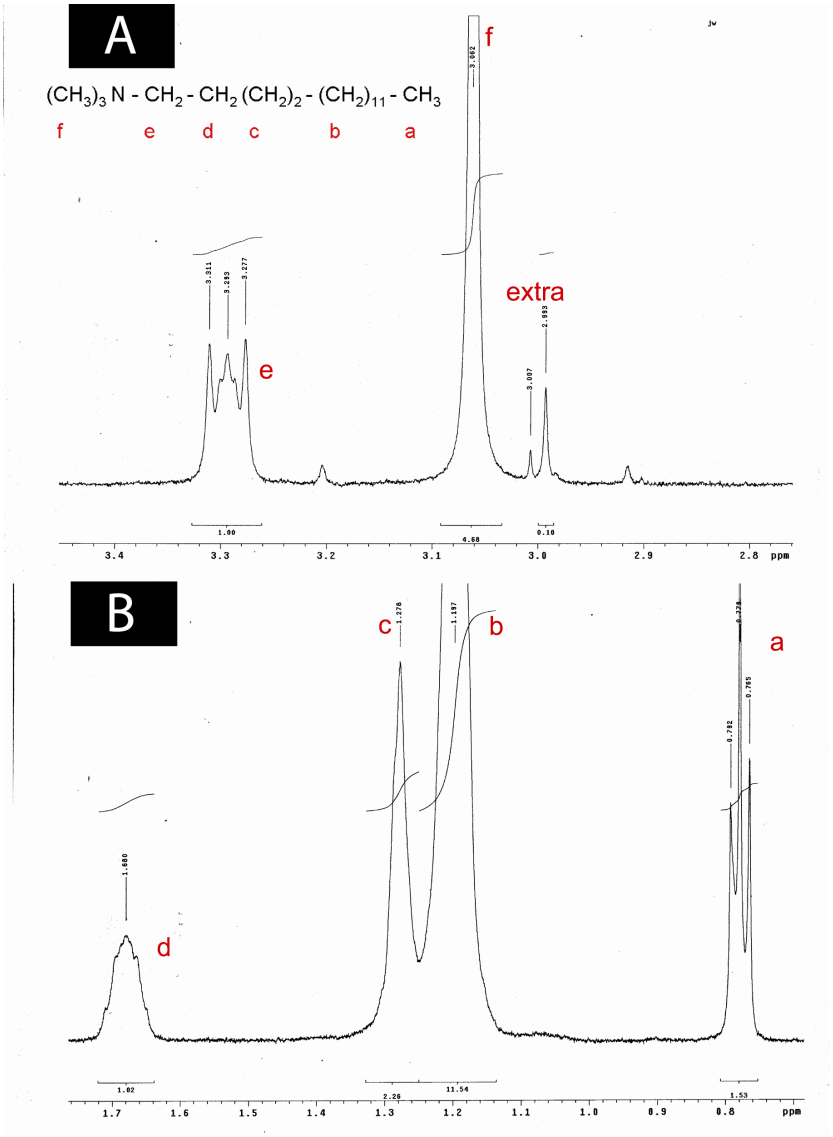
A
(CH3)3 N - CH2 - CH2 (CH2)2 - (CH2)11 - CH3
f e d c b a
jw
f
3.062
3.311
3.293
3.277
e
extra
3.007
2.993
1.00
4.68
0.10
3.4
3.3
3.2
3.1
3.0
2.9
2.8 ppm
B
c
1.278
1.197
b
a
0.778
0.765
0.792
1.680
d
1.02
2.26
11.54
1.53
1.7
1.6
1.5
1.4
1.3
1.2
1.1
1.0
0.9
0.8
ppm

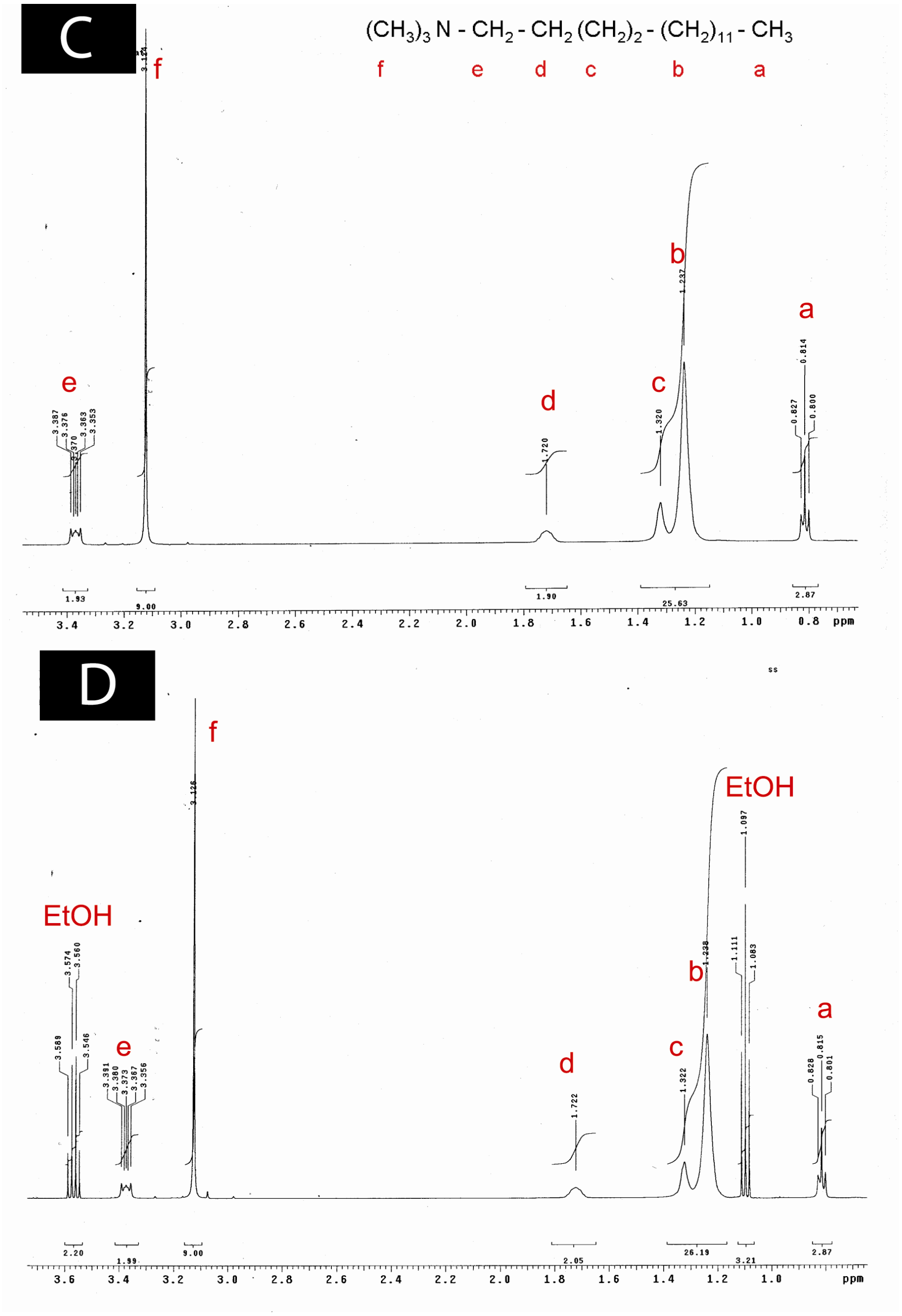

Figure B10. ^{1}H NMR spectra of CTAB supplied by (A) and (B) Fluka (52370), (C) Sigma (H5882), and (D) Sigma (H6269) in D_2O. The same major peaks were observed in each sample. Closer examination of the peaks at 3.007 and 2.993 ppm in figure S3A revealed that they were artifacts that did not appear in each spectrum. The quadruplet centered at 3.567 and the triplet centered at 1.097 in (D) correspond to ethanol.

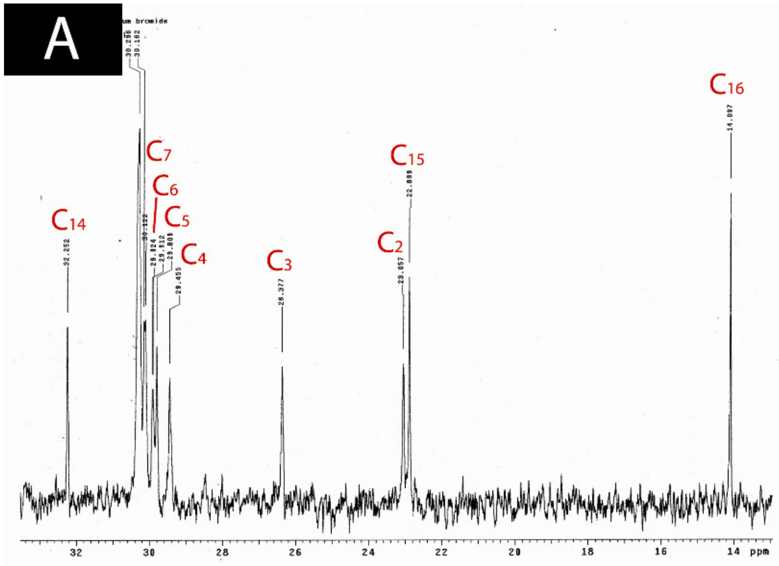
A
um bromide
30.286
30.162
C7
C6
30.122
29.924
29.912
29.809
C5
C4
29.455
C14
32.252
C3
26.377
C2
23.057
C15
22.899
C16
14.097
32
30
28
26
24
22
20
18
16
14 ppm

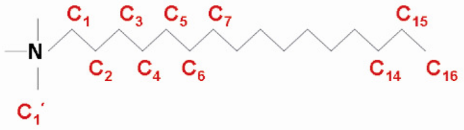
N
C1
C1'
C2
C3
C4
C5
C6
C7
C14
C15
C16

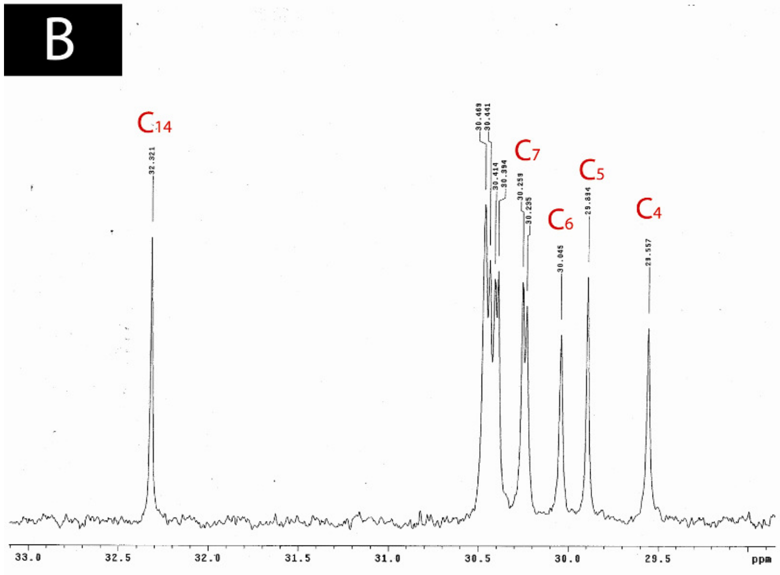
B
C14
32.321
30.469
30.441
30.414
30.394
C7
30.259
30.235
C6
30.045
C5
29.884
C4
29.557
33.0
32.5
32.0
31.5
31.0
30.5
30.0
29.5
ppm

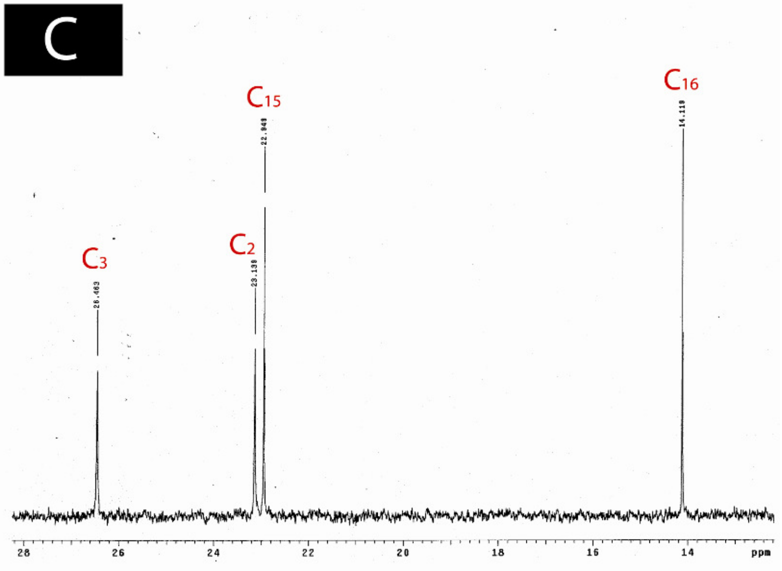
C
C3
26.463
C2
23.138
C15
22.948
C16
14.110
28
26
24
22
20
18
16
14
ppm

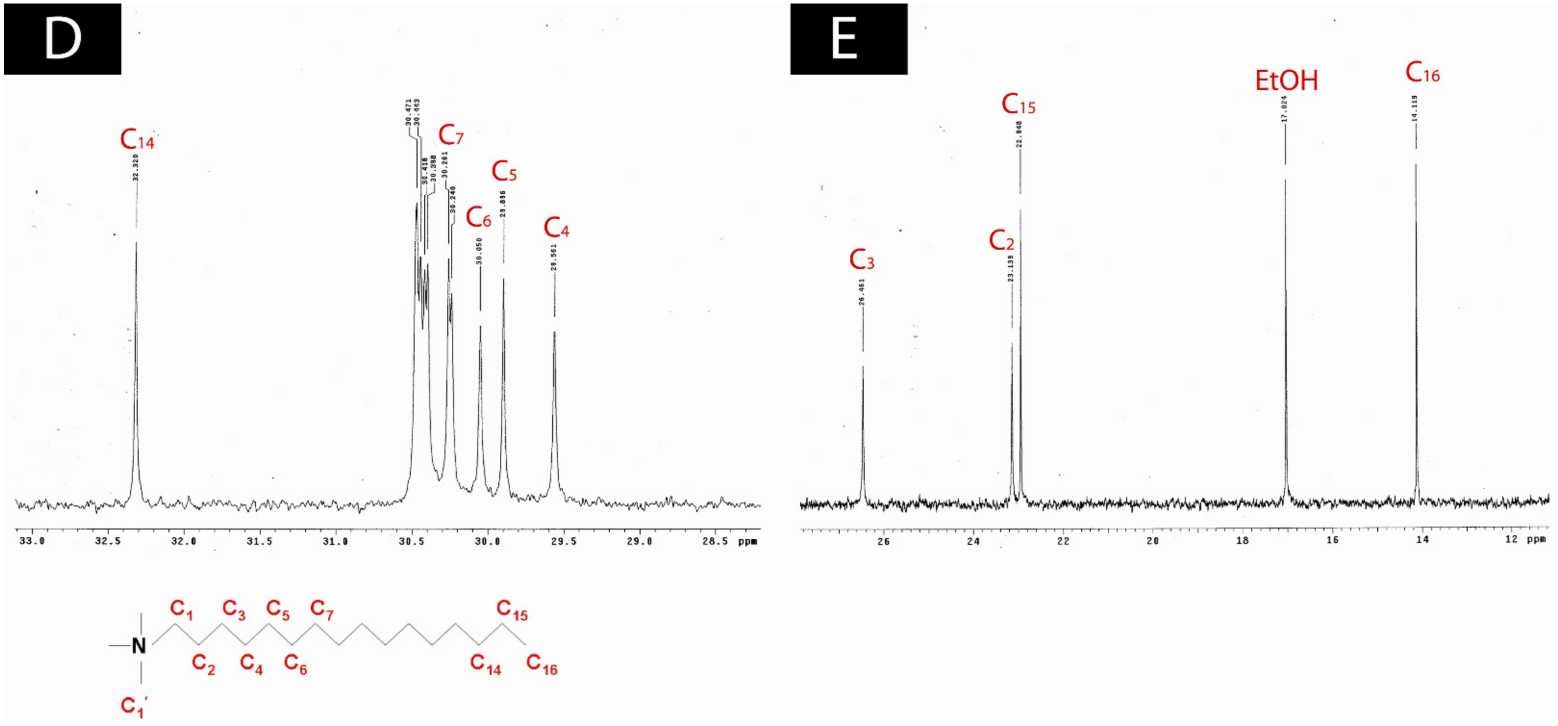

Figure B11. ^{13}C NMR spectra of CTAB supplied by (A) Fluka (52370), (B) and (C) Sigma (H5882), (D) and (E) Sigma (H6269) measured in D_2O. All of the same major peaks were found in each sample. The peak at 17.024 in (E) corresponds to ethanol. Unlabeled peaks near 30.4 correspond to the carbons 8-13 in the CTAB molecule.[10] The spectrum in (A) for CTAB from Fluka (52370) does not match exactly the spectra of the Sigma CTABs. We speculate that this was due to slight differences in calibration of the instrument, as the two Sigma CTABs were run in August 2007, whereas the Fluka (52370) CTAB was run in May 2006. Sigma (H5882) was also run in May 2006 and this spectra matched that of the Fluka (52370) spectra in (A).

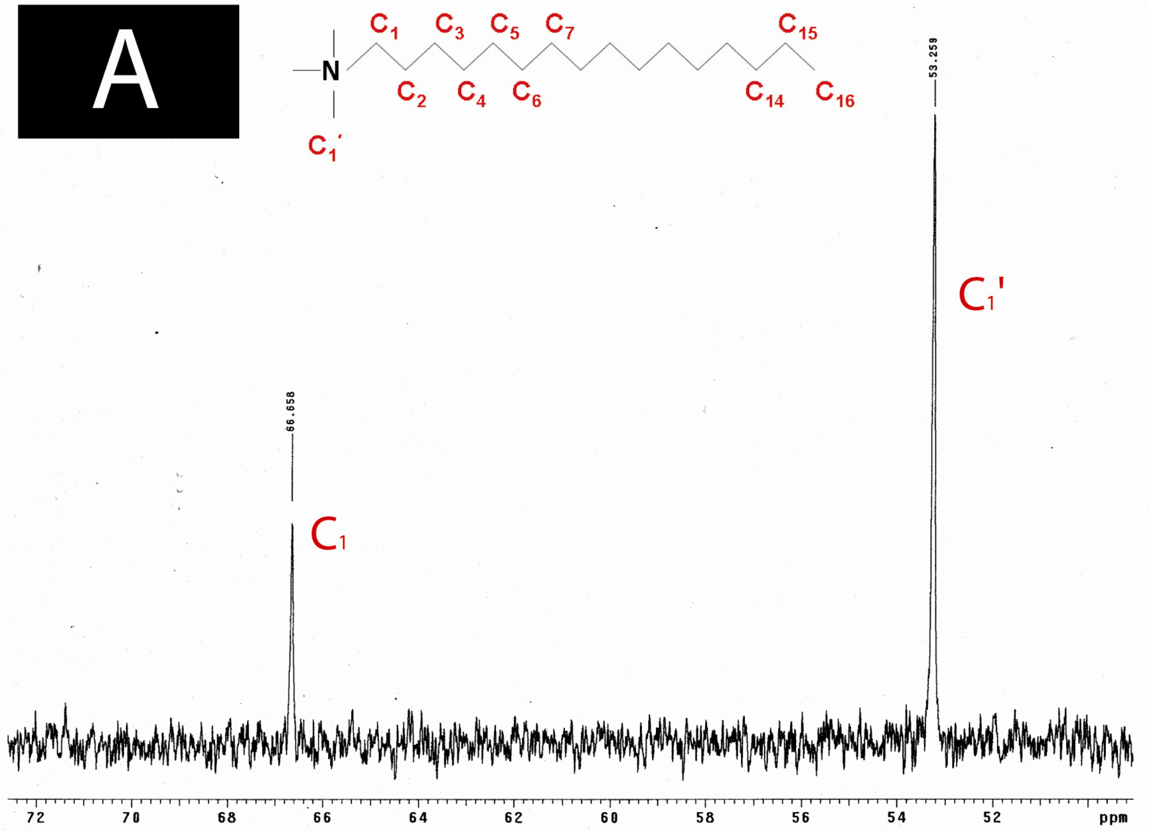
A
N
C1 C3 C5 C7 C15
C2 C4 C6 C14 C16
C1'
53.259
C1'
66.658
C1
72 70 68 66 64 62 60 58 56 54 52 ppm

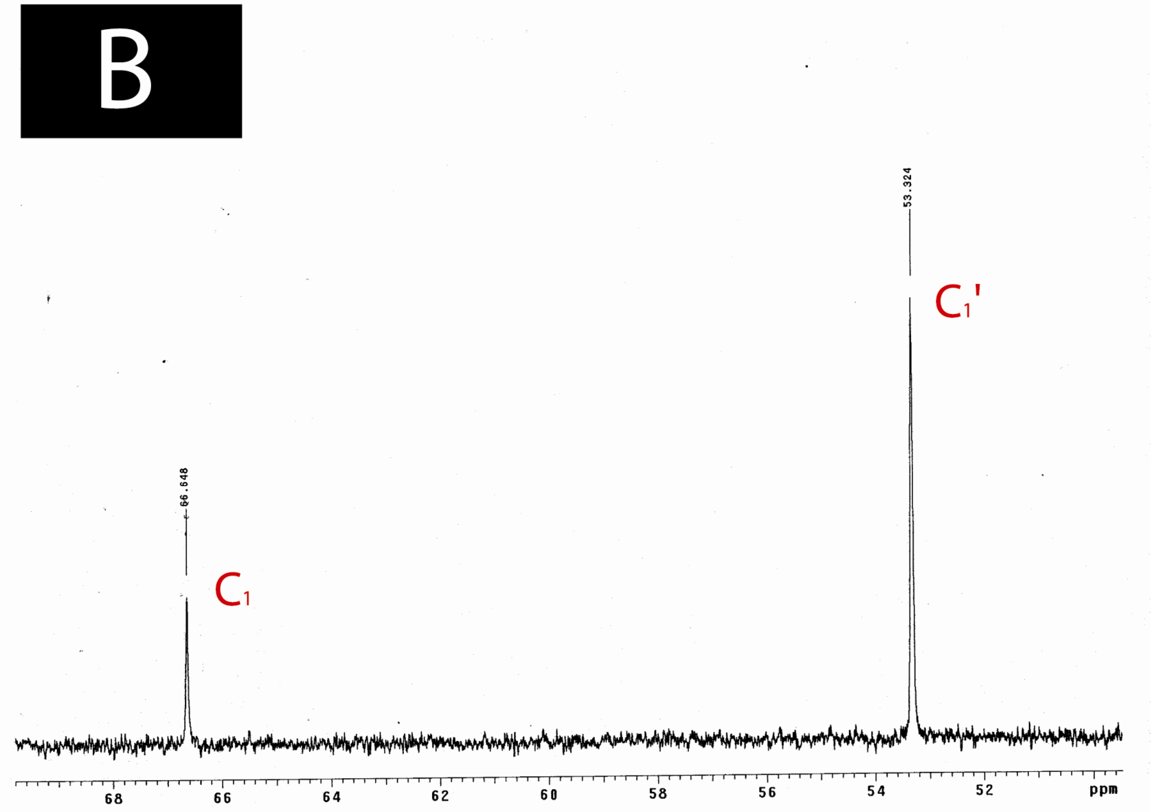
B
53.324
C1'
66.648
C1
68 66 64 62 60 58 56 54 52 ppm

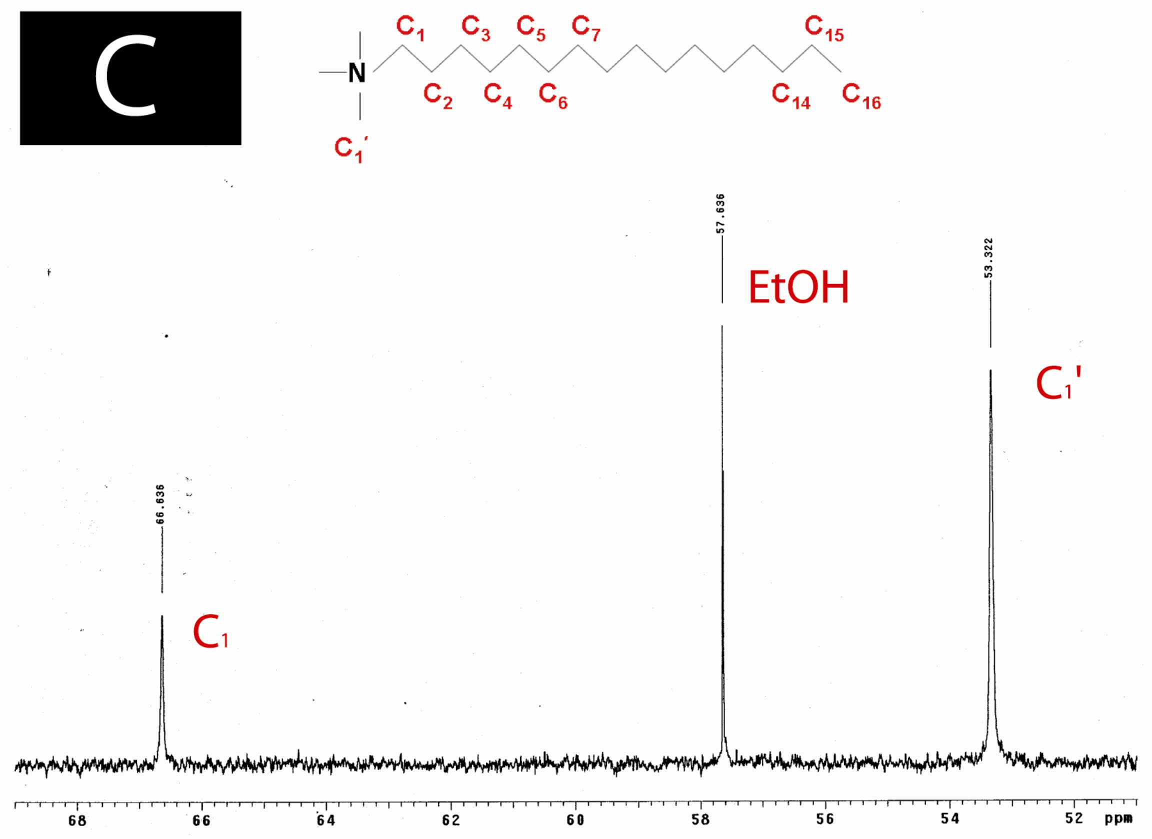

Figure B12. ^{13}C NMR spectra of CTAB supplied by (A) and (B) Fluka (52370), (C) Sigma (H5882), (D) and (E) Sigma (H6269) in D_2O. The peak at 57.636 ppm in (C) corresponds to ethanol.

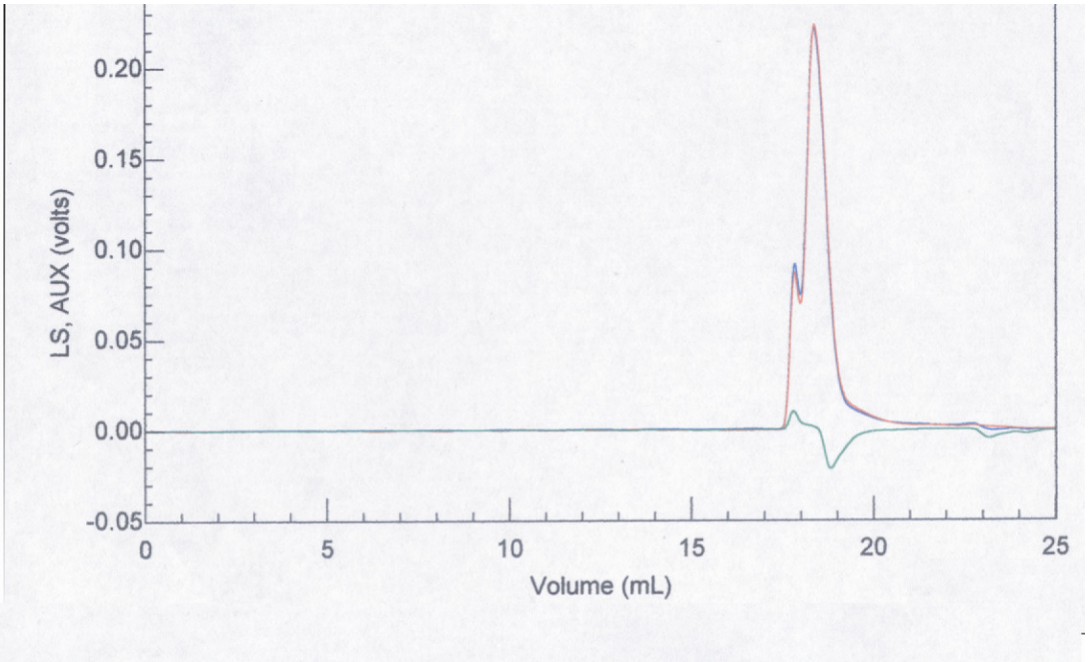

Figure B13. Size exclusion chromatography data of CTAB supplied by Fluka (52370) (blue line) and Sigma (H5882) (red line). The green line is for dimethylformamide (DMF), which was the solvent.

PART 4: REFERENCES

1. Bohren, C. F.; Huffman, D. F., *Absorption and Scattering of Light by Small Particles*. Wiley: New York, 1983.

2. Mie, G., *Ann. Phys.* **1908,** *25*, 377-455.

3. Alvarez, M. M.; Khoury, J. T.; Schaaff, T. G.; Shafigullin, M. N.; Vezmar, I.; Whetten, R. L., *J. Phys. Chem. B* **1997,** *101*, (19), 3706-3712.

4. Liz-Marzan, L. M., *Mater. Today* **2004,** *7*, (2), 26-31.

5. Perez-Juste, J.; Pastoriza-Santos, I.; Liz-Marzan, L. M.; Mulvaney, P., *Coord. Chem. Rev.* **2005,** *249*, (17-18), 1870-1901.

6. Gans, R., *Ann. Phys.* **1915,** *47*, 270-84.

7. Ziman, J. M., *Theory of Solids*. University Press: Cambridge, 1979; p 278.

8. Link, S.; Mohamed, M. B.; El-Sayed, M. A., *J. Phys. Chem. B* **1999,** *103*, (16), 3073-3077.

9. Nikoobakht, B.; El-Sayed, M. A., *Chem. Mater.* **2003,** *15*, 1957-1962.

10. Bacaloglu, R.; Bunton, C. A.; Cerichelli, G.; Ortega, F., *J. Phys. Chem.* **1989,** *93*, (4), 1490-1497.

Appendix C: Multifunctional Particles: Magnetic Nanocrystals and Gold Nanorods Coated with Fluorescent Dye-Doped Silica Shells

PART 1: SYNTHESIS OF MESOPOROUS SILICA COATED GOLD NANORODS

Gold nanorods and other CTAB-capped hydrophilic nanocrystals can be coated with a mesoporous layer of silica using a single step method.[1] As synthesized gold nanorods were centrifuged and redispersed in 10 ml of deionized water. 100 μL of a 0.1 M NaOH solution was added to adjust the pH to 10-11. Three injections of 30 μL of 20% TEOS in methanol were added in thirty minute intervals under gentle stirring. The final product consisted of mesoporous silica coated gold nanorods. The thickness of the mesoporous silica shell can be tuned by the number of TEOS injections.

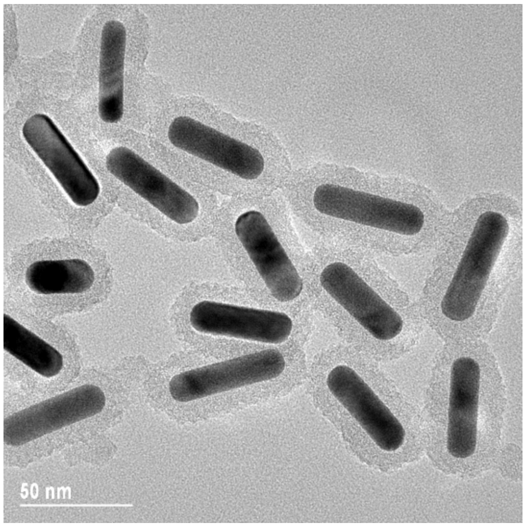

Figure C1. Gold nanorods coated with mesoporous silica.

PART 2: REFERENCES

1. Gorelikov, I.; Matsuura, N. *Nano Lett.* **2008,** *8*, 369-373.

Appendix D: Self-Assembled Simple Hexagonal AB_2 Binary Nanocrystal Superlattices: Synthesis, SEM, GISAXS and Defects

PART 1: BINARY SUPERLATTICE SYNTHESIS

BSLs were assembled onto tilted substrates by controlled evaporation of a dispersing solvent as illustrated in Figure D1. The substrate is immersed in the dispersion (40 μL for a TEM grid, 350 μL for a Si or Si_3N_4 wafer) and the solvent is evaporated in air at 45 °C. Table D1 shows the optimized solution conditions used to form sh-AB_2 BSLs. Extended BSL formation also required the addition of oleic acid to the nanocrystal dispersion. BSLs were not observed when dispersions were drop-cast onto flat TEM grids.

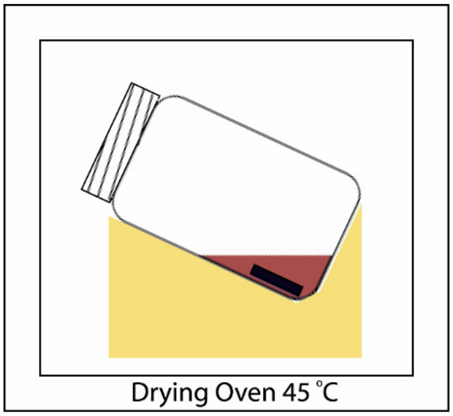

Figure D1. BSL self-assembly: A tilted vial with a substrate (black rectangle) immersed in the nanocrystal dispersion (shown in maroon) is placed in a drying oven at 45 °C in air as shown. The substrate is left undisturbed as the solvent evaporates over the course of several hours.

Table D1. Optimized solution conditions for formation of sh-AB_2 binary nanocrystal superlattices made from 11.5 nm Fe_2O_3 and 6.1 nm Au nanocrystals.

Binary Superlattice Preparation Parameters	
Solvent	toluene[†]
Fe_2O_3 stock solution conc. (mg/mL)	4.0
Au stock solution conc. (mg/ml)	4.0
Targeted total particle conc (mg/ml)	0.5
Targeted Fe_2O_3: Au Number Ratio	1:2.5
Volume of Fe_2O_3 added (μl)	25
Volume of Au added (μl)	30
Volume of toluene added (μl)	385
Final volume (μl)	440
Number of Fe_2O_3 particles	1.9×10^{13}
Number of Au particles	4.7×10^{13}
Volume of oleic acid solution added (μl)	15.0

[†] Previous reports indicated that tetrachloroethylene (TCE),[1-3] or mixtures of toluene and TCE[4-6] worked best for BSL formation, but we found that toluene gave BSLs with more extensive order.

PART 2: NANOCRYSTAL NUMBER CONCENTRATION CALCULATION

The weight of an individual nanocrystal (W_{nc}) was estimated by considering its volume, V_{nc}:

$$V_{nc} = \frac{4}{3}\pi r^3 \tag{1}$$

(r is the nanocrystal radius) and the density ρ, of the material:

$$W_{nc} = \rho V_{nc} \tag{2}$$

A 6.1 nm diameter Au nanocrystal has V_{nc} = 117.7 nm^3. ρ is 19.3 g/cm^3 for Au and 5.24 g/cm^3 for Fe_2O_3. A 6.1 nm diameter Au nanocrystal has W_{nc} = 2.3 x 10^{-18} g. The weight contribution of the ligands was estimated as follows. The surface area (SA_{nc}) of one nanocrystal was calculated:

$$SA_{nc} = 4\pi r^2 \tag{3}$$

The footprint of oleic acid (capping the Fe_2O_3) was taken to be equal to dodecanethiol (capping the Au), 0.16 nm^2.[7] The number of capping ligands ($N_{ligands}$) per nanocrystal was estimated by dividing the surface area of each nanocrystal (SA_{nc}) by the areal footprint of the ligand. The weight contribution of the ligands ($W_{ligands}$) per nanocrystal is:

$$W_{ligands} = \frac{N_{ligands}}{N_{Avogadro}} MW_{ligand} \tag{4}$$

where MW_{ligand} is the ligand molecular weight and $N_{Avagadro}$ is Avogadro's number. The number density N, of nanocrystals in the dispersion is:

$$N = \frac{c}{W_{nc} + W_{ligands}} \tag{5}$$

where c is the nanocrystal concentration. There are 4.7×10^{13} nanocrystals in 30 µl of a 4 mg/ml Au nanocrystal dispersion and 1.9×10^{13} nanocrystals in 25 µl of a 4 mg/ml dispersion of 11.5 nm diameter Fe_2O_3 nanocrystals.

PART 3: GISAXS SIMULATION OF THE [001] ORIENTATION

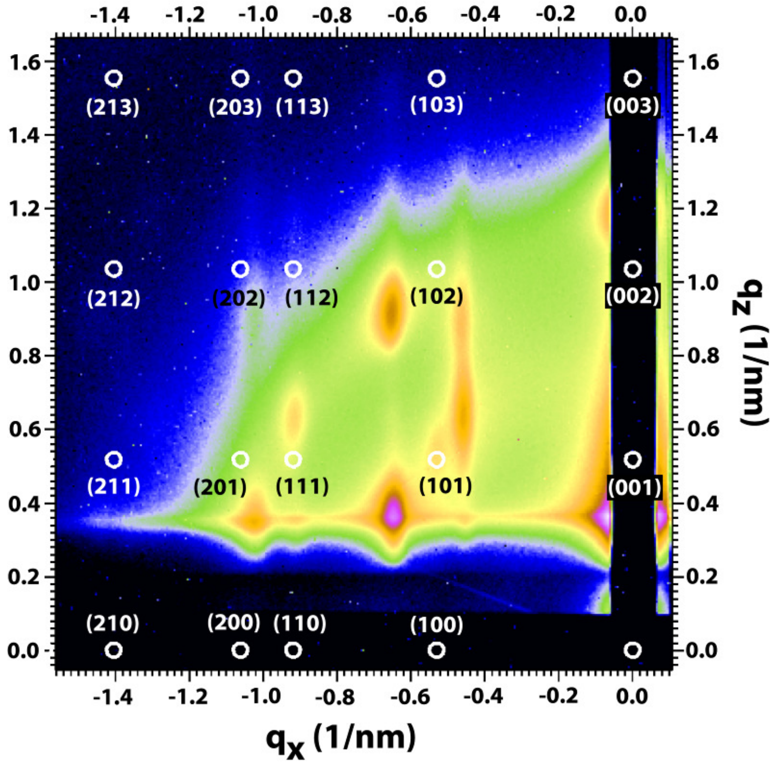

Figure D2. GISAXS simulation of the diffraction spot pattern produced from a sh-AB_2 (SG191; *P6/mmm*) lattice oriented with the (001) plane parallel to the substrate ([001] direction normal to the substrate) is overlaid onto GISAXS data of binary superlattices of 11.5 nm Fe_2O_3 and 6.1 nm Au nanocrystals. The lattice constants are a = 13.8 nm, b = 13.8 nm, and c = 12.28 nm, which corresponds to an 11% shrinkage along the c-axis.

PART 4: UNIAXIAL SHRINKING MODEL

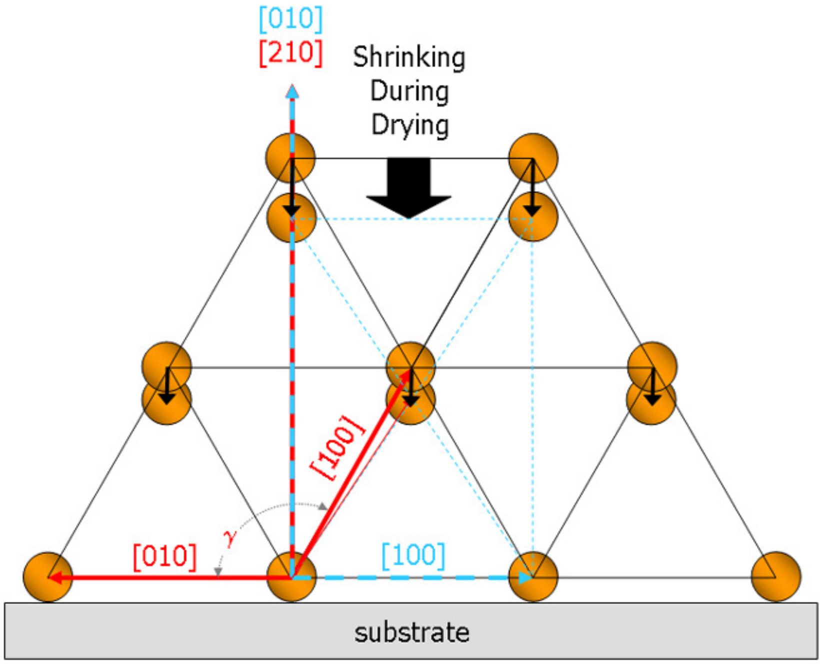

Figure D3. Model of the shrinkage of a binary superlattice of 11.5 nm Fe_2O_3 (orange) and 6.1 nm Au (not shown) nanocrystals with the crystallographic direction [210] normal to the substrate. While the superlattice is drying, excess solvent evaporates and causes the nanocrystals to shrink uniaxially along the [210] direction of the hexagonal lattice. The angle γ, changes as a result of the shrinkage and the lattice symmetry is no longer hexagonal, becoming orthorhombic SG 65. The red arrows and black lines correspond to the hexagonal unit cell of SG 191 (*P/6mmm*). The blue dashed lines represent the orthorhombic unit cell of SG 65 (*Cmmm*). The black arrows show the new location of the Fe_2O_3 nanocrystals after shrinkage.

PART 5: SEM IMAGES

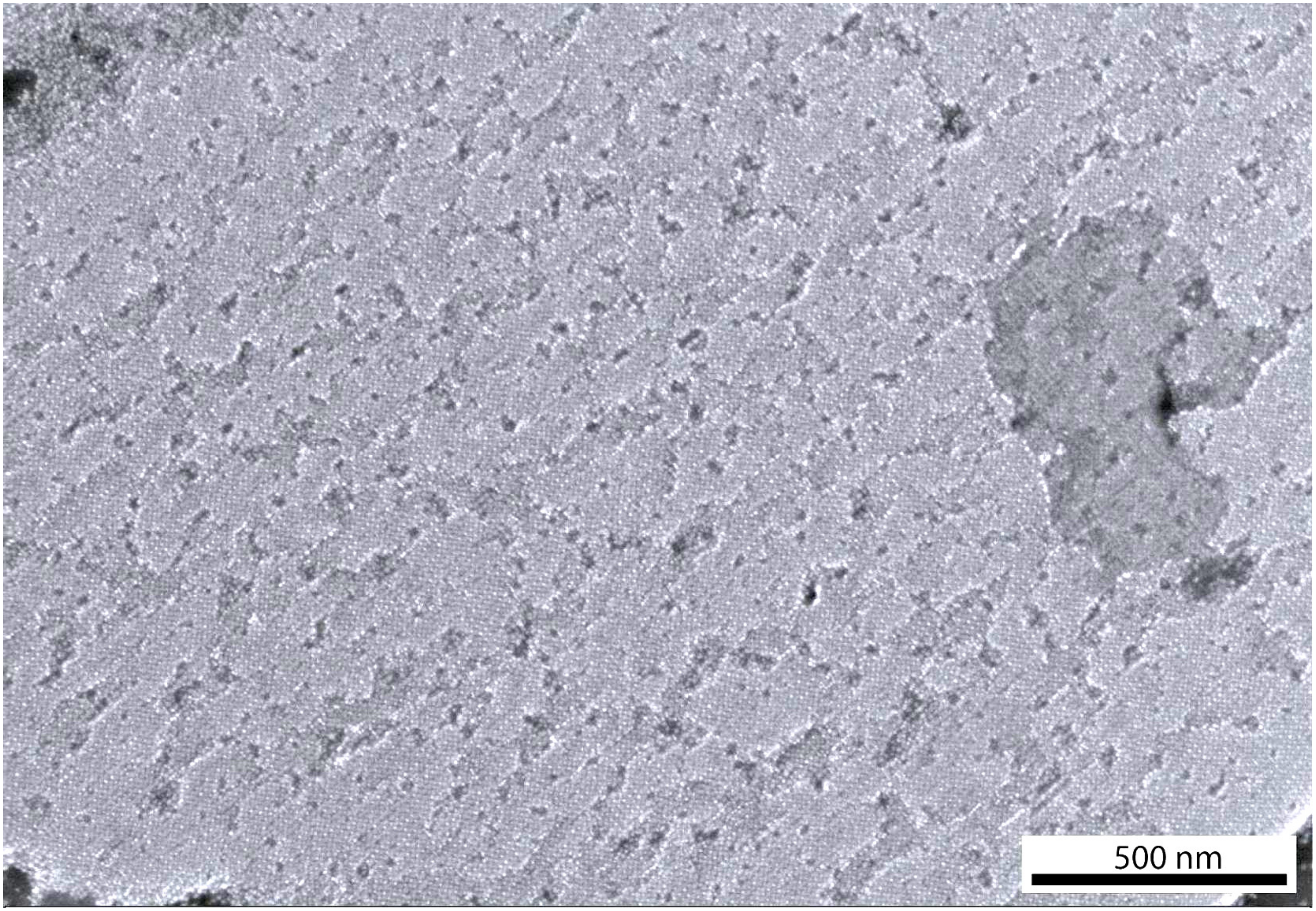

Figure D4. SEM image of sh-AB_2 binary superlattices assembled from 11.5 nm Fe_2O_3 and 6.1 nm Au nanocrystals.

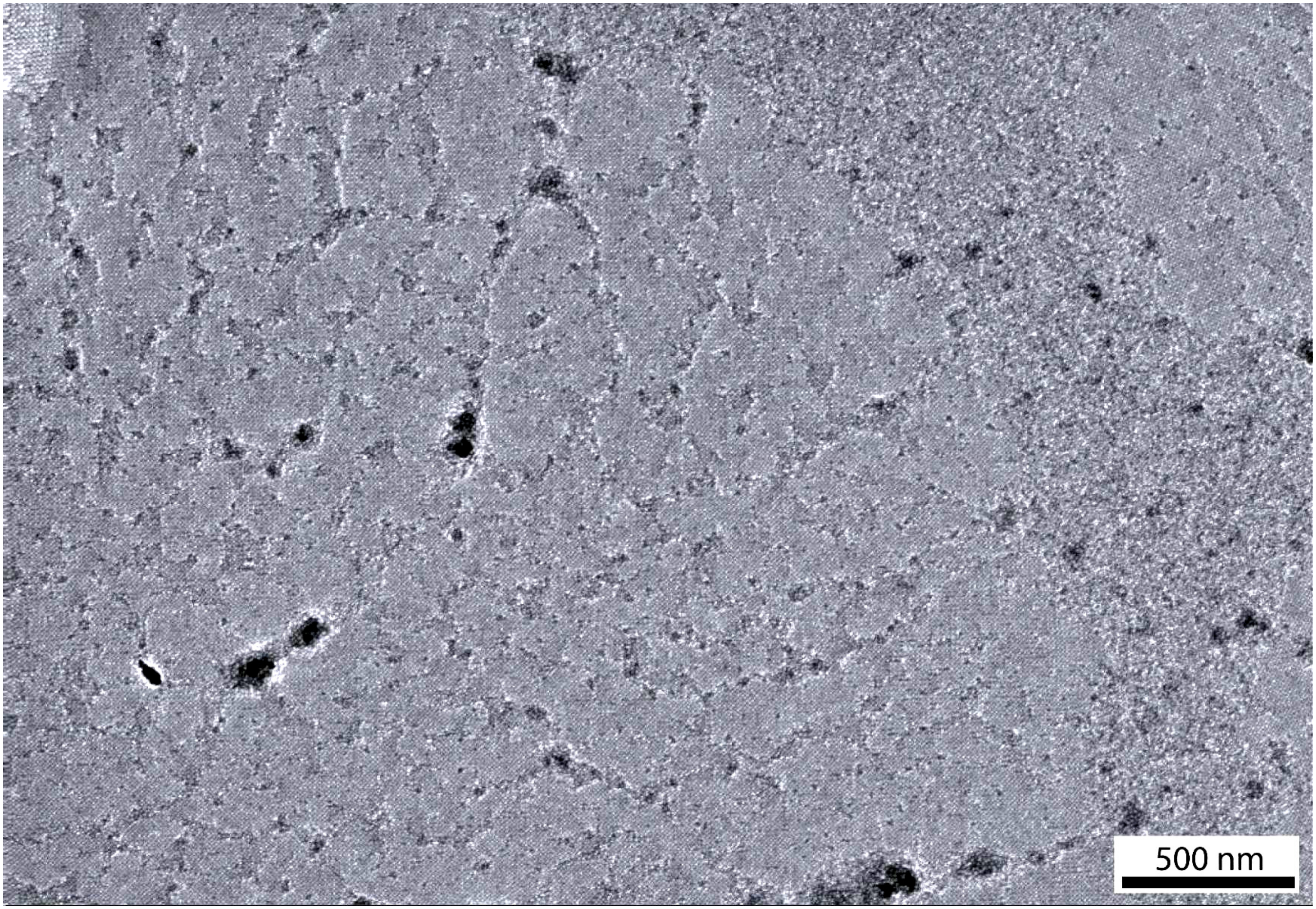

Figure D5. SEM image of sh-AB_2 binary superlattices assembled from 11.5 nm Fe_2O_3 and 6.1 nm Au nanocrystals.

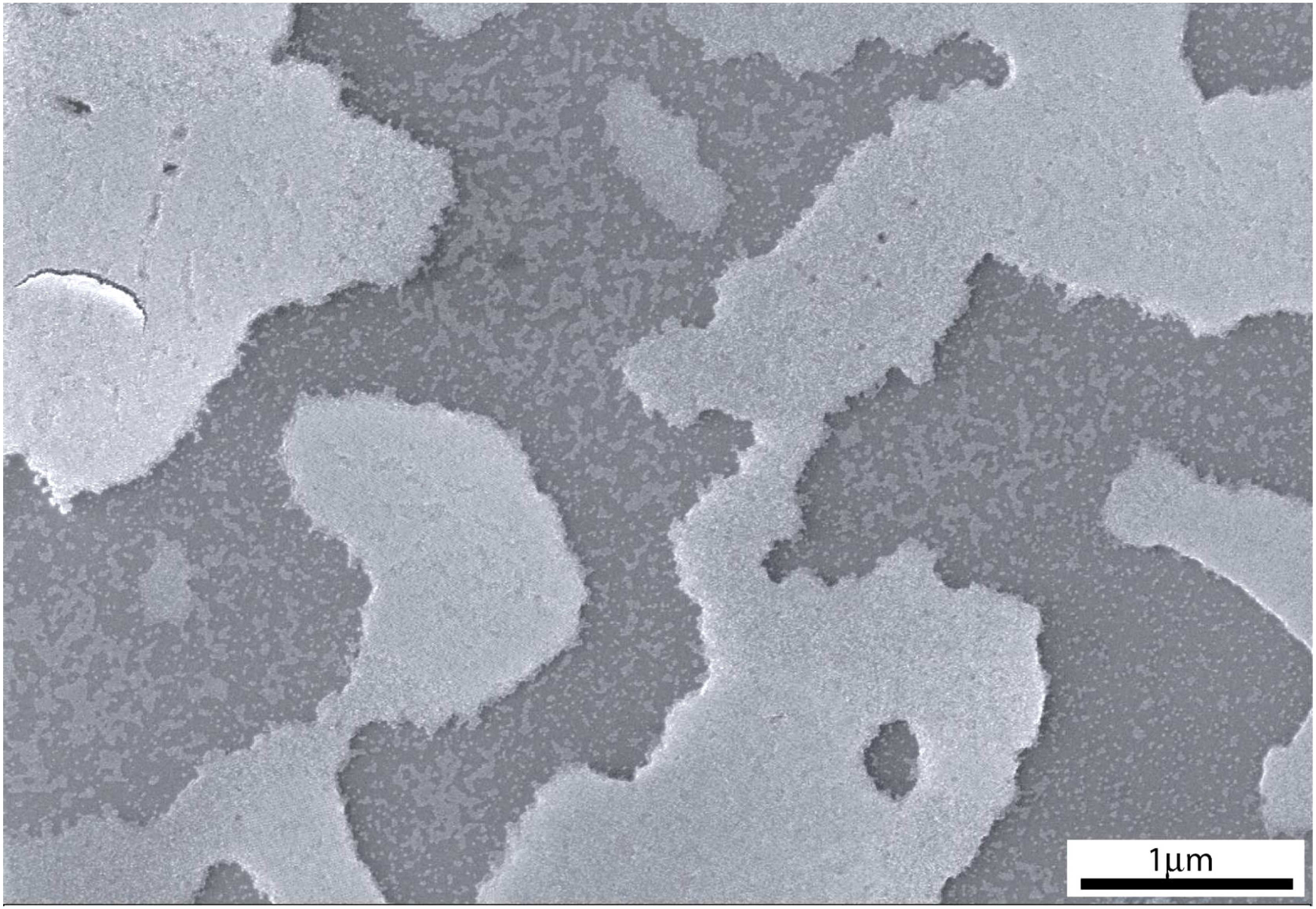

Figure D6. SEM image of sh-AB$_2$ binary superlattices assembled from 11.5 nm Fe$_2$O$_3$ and 6.1 nm Au nanocrystals.

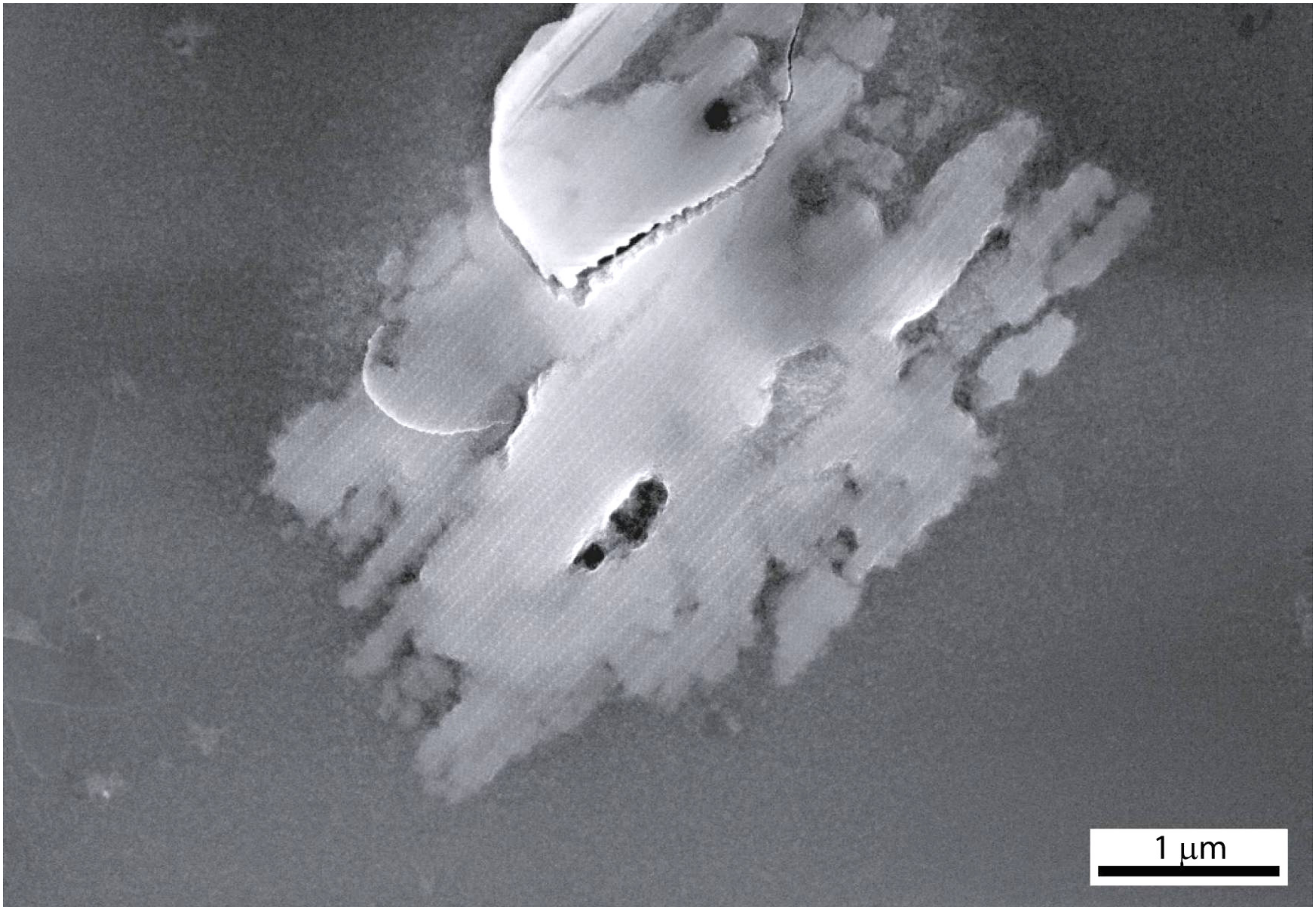

Figure D7. SEM image of sh-AB_2 binary superlattices assembled from 11.5 nm Fe_2O_3 and 6.1 nm Au nanocrystals.

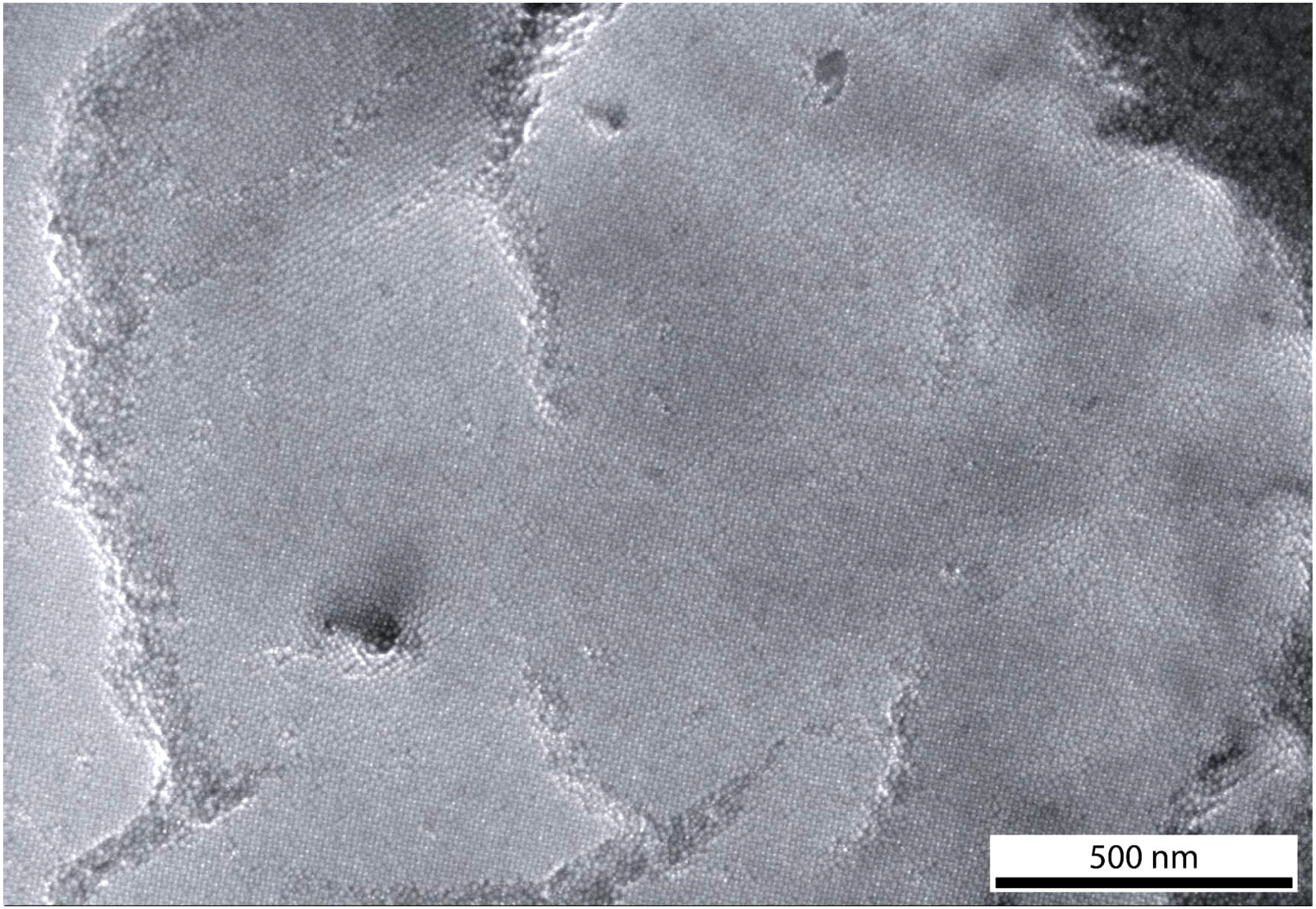

Figure D8. SEM image of sh-AB_2 binary superlattices assembled from 11.5 nm Fe_2O_3 and 6.1 nm Au nanocrystals.

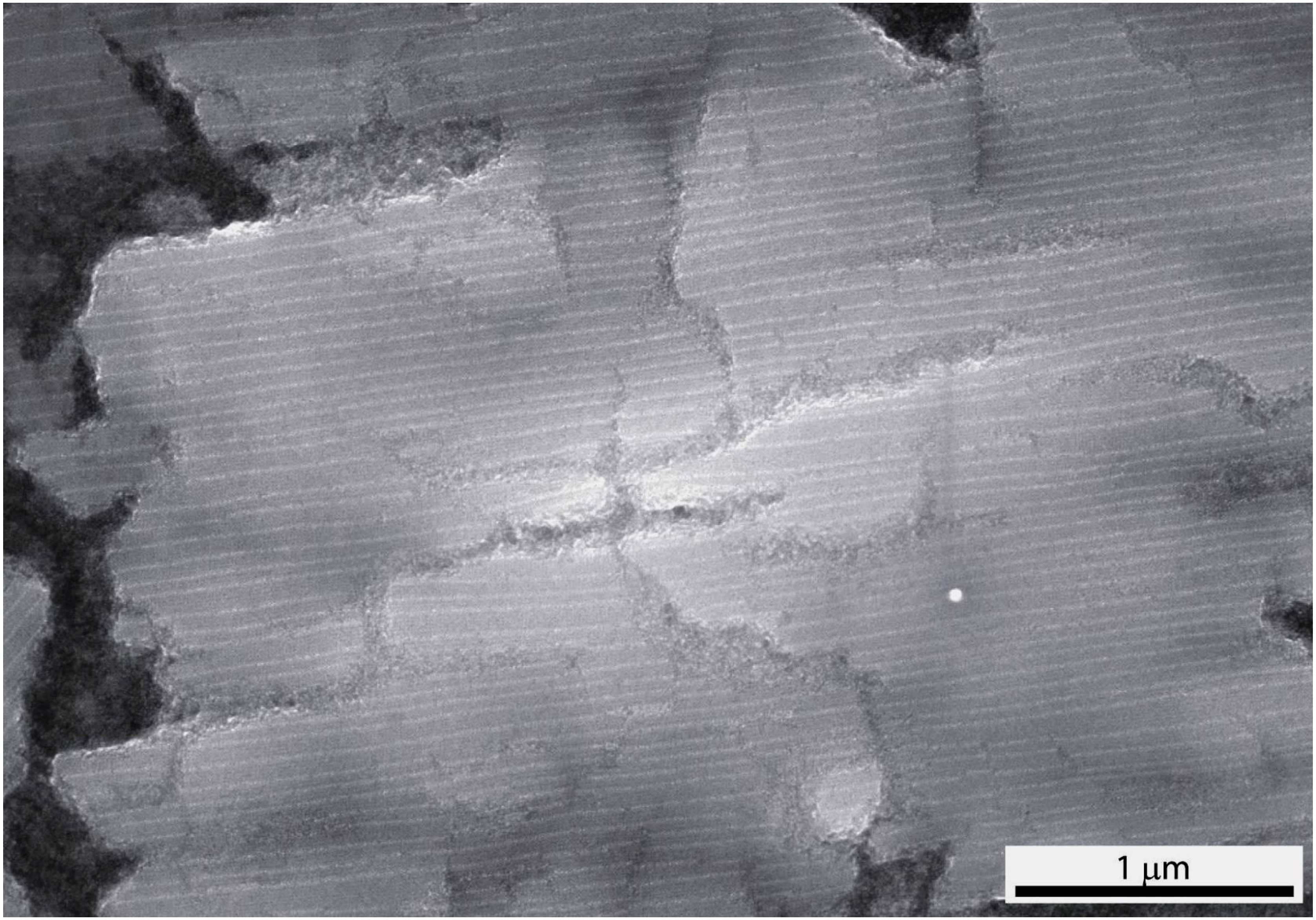

Figure D9. SEM image of sh-AB_2 binary superlattices assembled from 11.5 nm Fe_2O_3 and 6.1 nm Au nanocrystals.

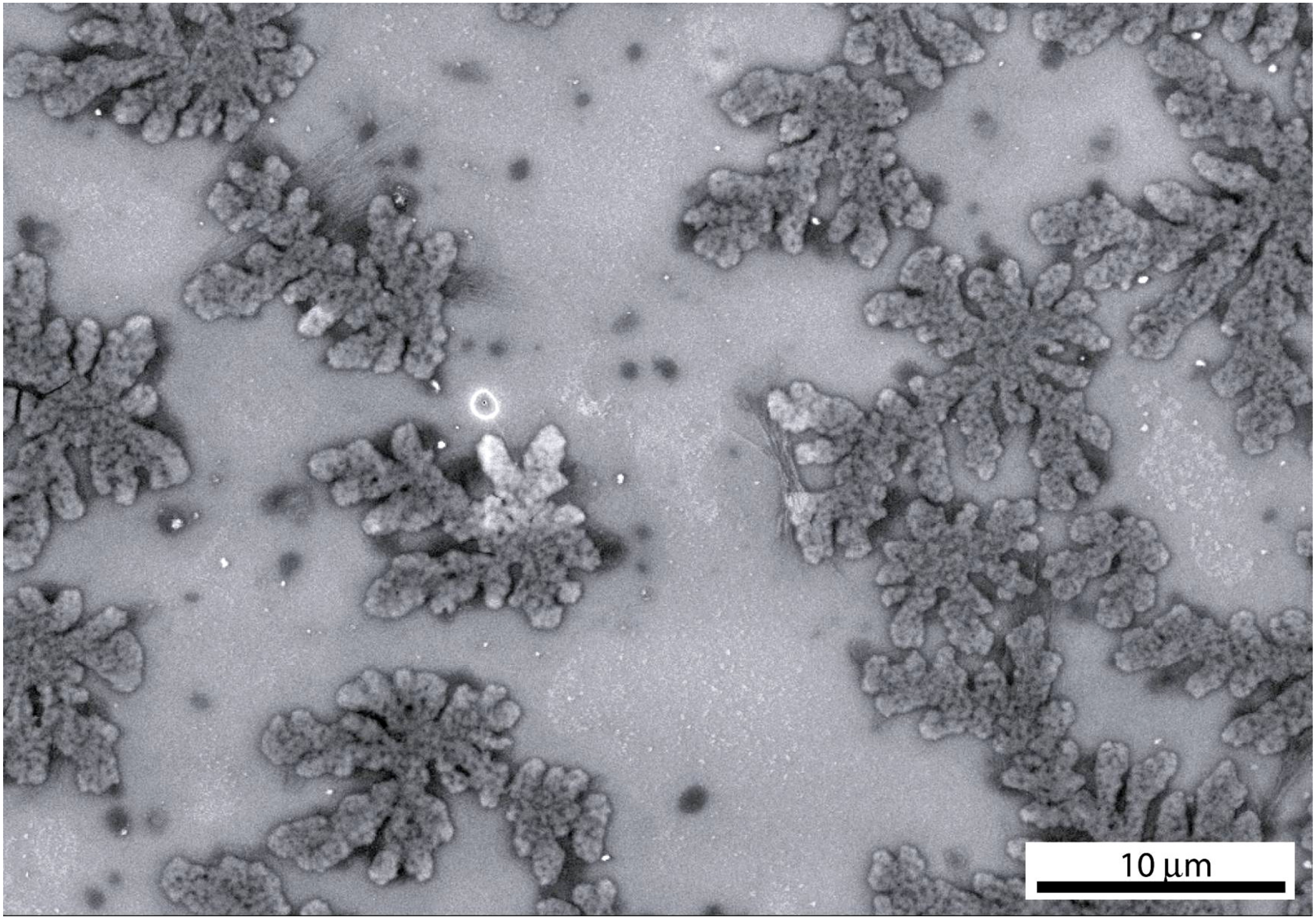

Figure D10. SEM image of sh-AB_2 binary superlattices assembled from 11.5 nm Fe_2O_3 and 6.1 nm Au nanocrystals.

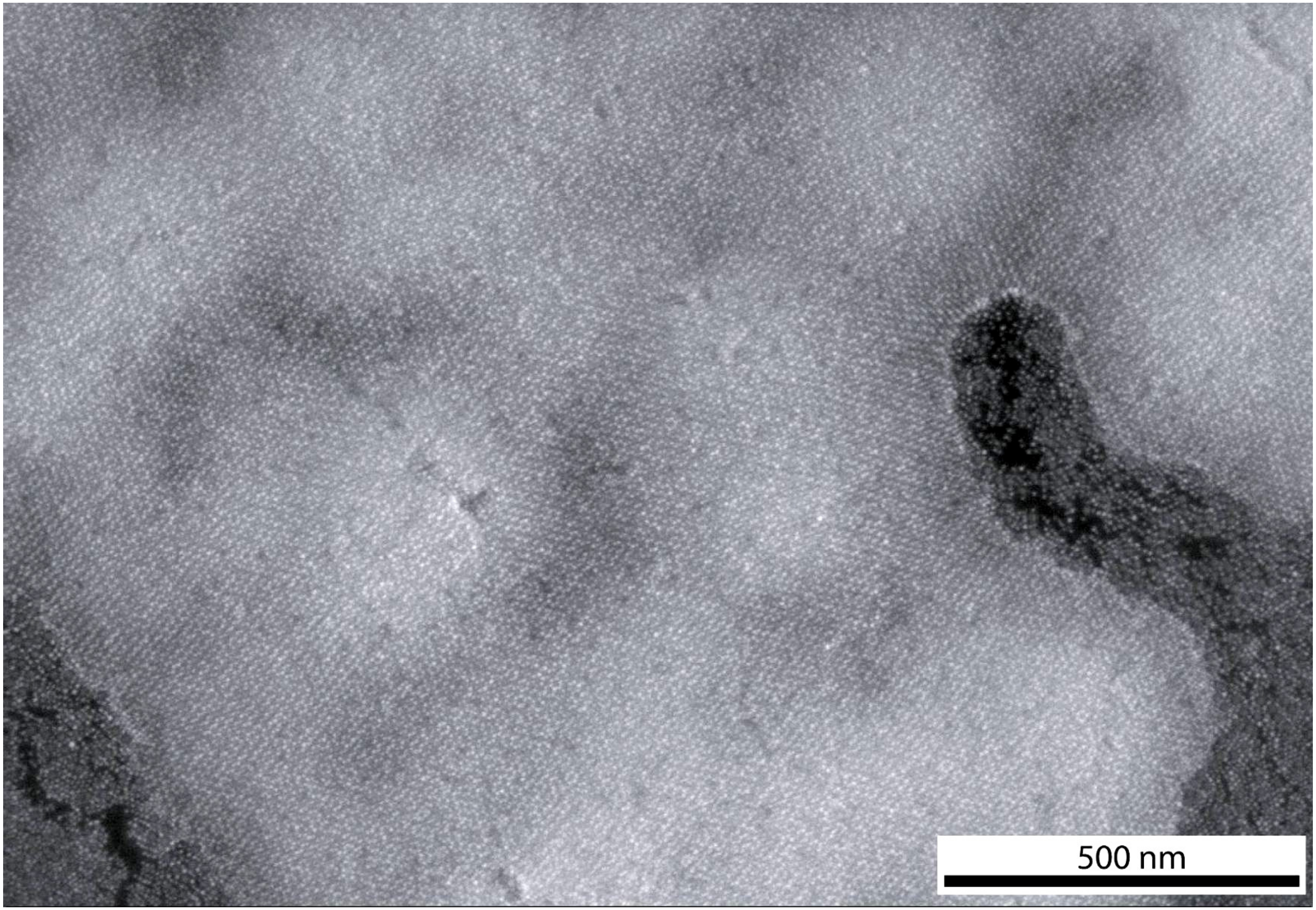

Figure D11. SEM image of sh-AB_2 binary superlattices assembled from 11.5 nm Fe_2O_3 and 6.1 nm Au nanocrystals.

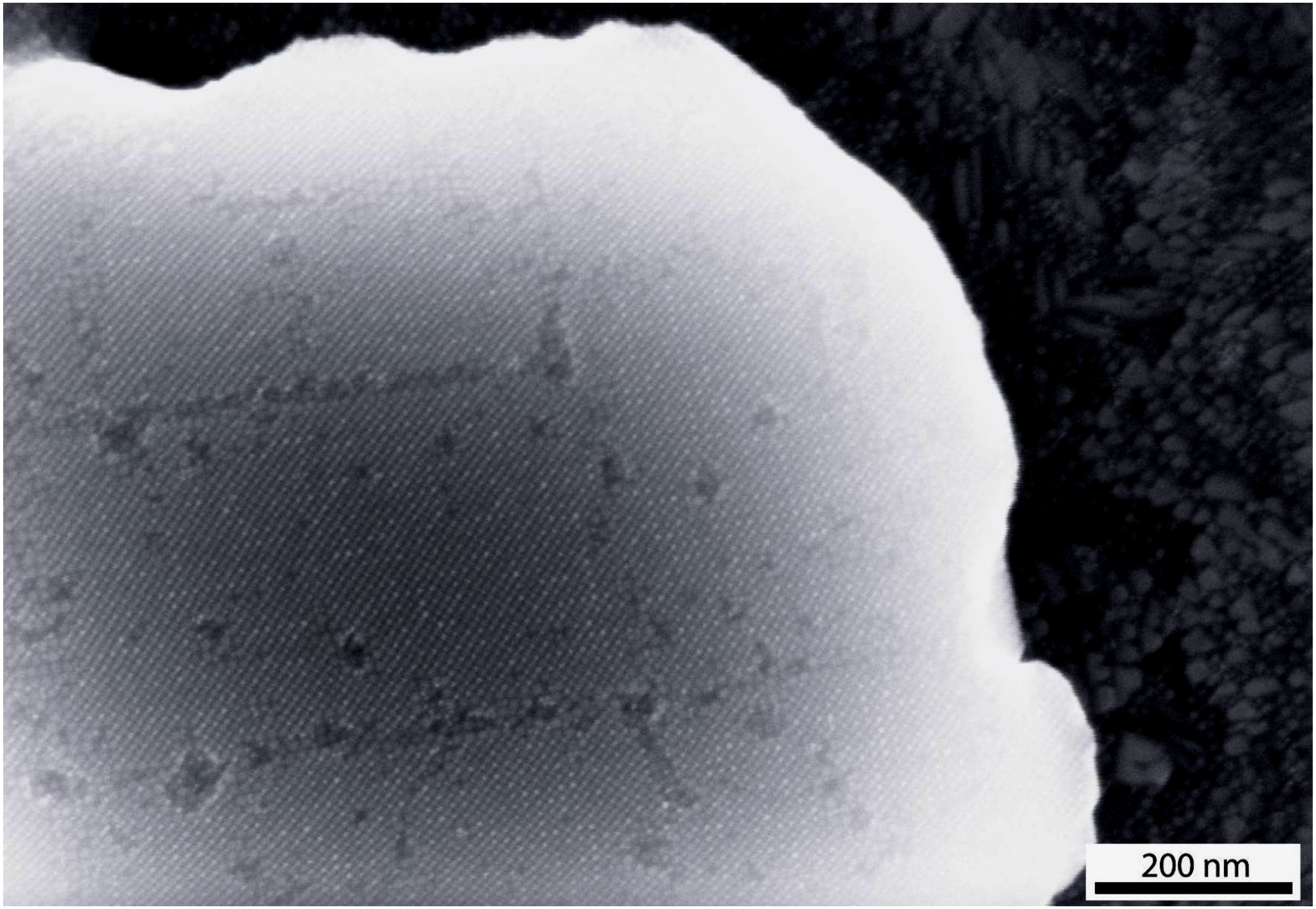

Figure D12. SEM image of sh-AB_2 binary superlattices assembled from 11.5 nm Fe_2O_3 and 6.1 nm Au nanocrystals.

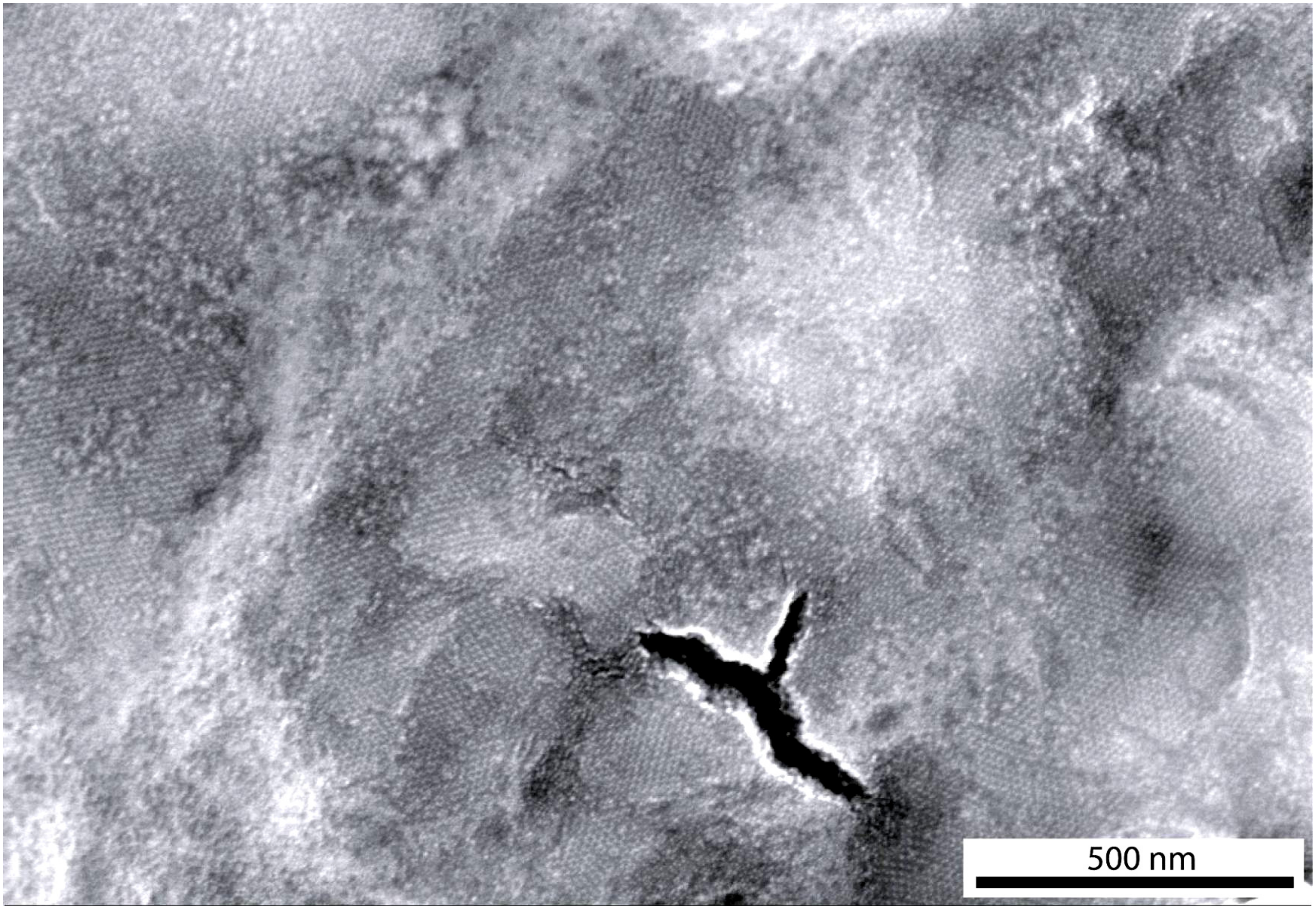

Figure D13. SEM image of sh-AB_2 binary superlattices assembled from 11.5 nm Fe_2O_3 and 6.1 nm Au nanocrystals.

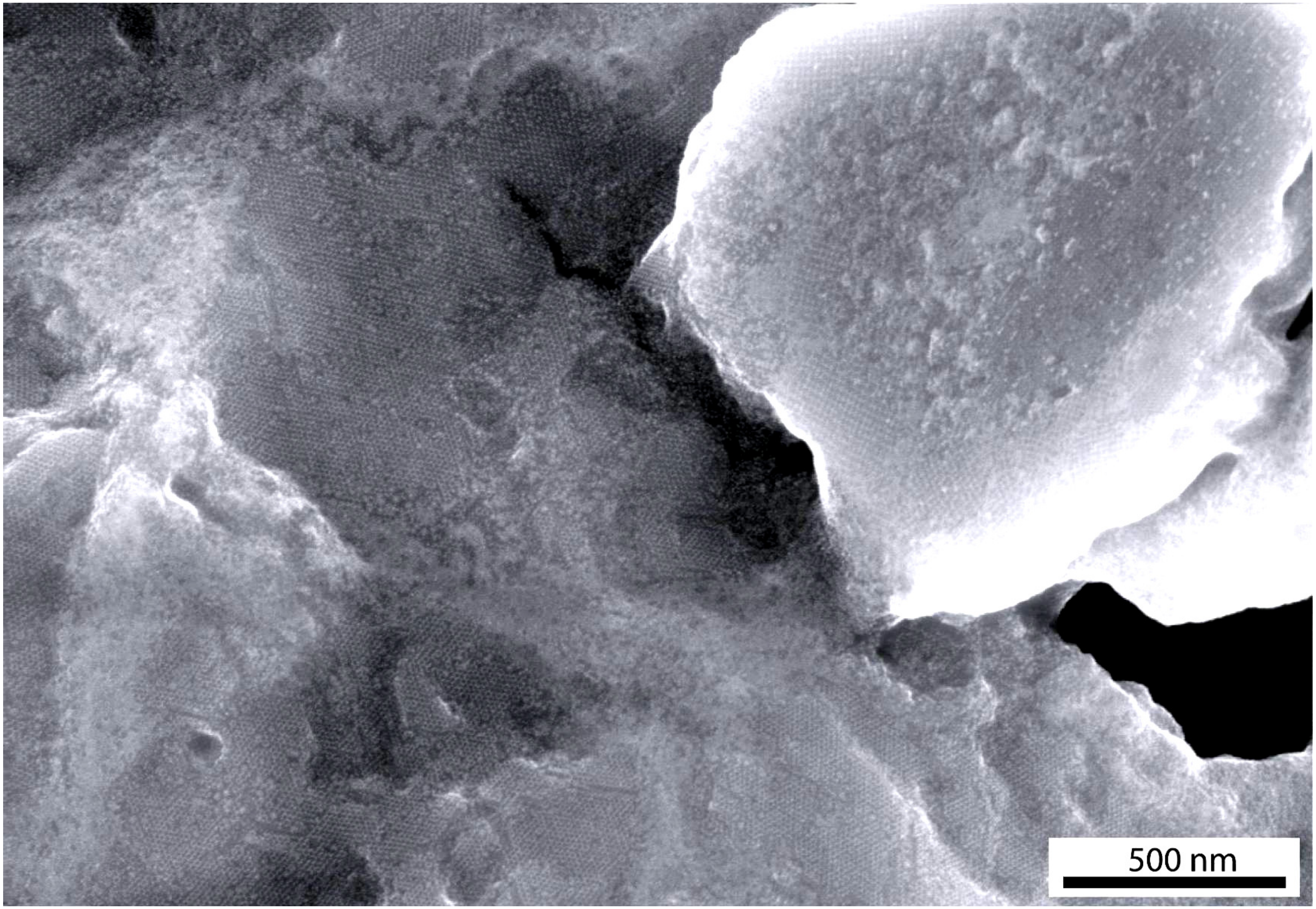

Figure D14. SEM image of sh-AB_2 binary superlattices assembled from 11.5 nm Fe_2O_3 and 6.1 nm Au nanocrystals.

PART 6: REFERENCES

1. Overgaag, K.; Evers, W.; de Nijs, B.; Koole, R.; Meeldijk, J.; Vanmaekelbergh, D. *J. Am. Chem. Soc.* **2008,** *130*, 7833-7835.

2. Chen, Z.; O'Brien, S. *ACS Nano* **2008**, *2*, 1219-1229.

3. Chen, Z. Y.; Moore, J.; Radtke, G.; Sirringhaus, H.; O'Brien, S. *J. Am. Chem. Soc.* **2007,** *129*, 15702-15709.

4. Shevchenko, E. V.; Talapin, D. V.; Kotov, N. A.; O'Brien, S.; Murray, C. B. *Nature* **2006,** *439*, 55-59.

5. Shevchenko, E. V.; Talapin, D. V.; Murray, C. B.; O'Brien, S. *J. Am. Chem. Soc.* **2006,** *128*, 3620-3637.

6. Shevchenko, E. V.; Kortright, J. B.; Talapin, D. V.; Aloni, S.; Alivisatos, A. P. *Adv. Mater.* **2007,** *19*, 4183-4188.

7. Korgel, B. A.; Fullam, S.; Connolly, S.; Fitzmaurice, D. *J. Phys. Chem. B* **1998,** *102*, 8379-8388.

Bibliography

Alexiou, C.; Jurgons, R.; Schmid, R. J.; Bergemann, C.; Henke, J.; Erhardt, W.; Huenges, E.; Parak, F. *J. Drug Targeting* **2003,** *11*, 139-149.

Alivisatos, A. P. *Nat. Biotechnol.* **2004,** *22*, 47-52.

Alvarez, M. M.; Khoury, J. T.; Schaaff, T. G.; Shafigullin, M. N.; Vezmar, I.; Whetten, R. L., *J. Phys. Chem. B* **1997,** *101*, (19), 3706-3712.

Andrews, R.; Jacques, D.; Qian, D. L.; Rantell, T., *Acc. Chem. Res.* **2002,** *35*, (12), 1008-1017.

Arruebo, M.; Fernandez-Pacheco, R.; Velasco, B.; Marquina, C.; Arbiol, J.; Irusta, S.; Ibarra, M. R.; Santamaria, J. *Adv. Funct. Mater.* **2007,** *17*, 1473-1479.

Asakura, S.; Oosawa, F., *J. Chem. Phys.* **1954**, *22*, 1255-1256.

Avouris, P., *Acc. Chem. Res.* **2002,** *35*, (12), 1026-1034.

Bacaloglu, R.; Bunton, C. A.; Cerichelli, G.; Ortega, F., *J. Phys. Chem.* **1989,** *93*, (4), 1490-1497.

Bagwe, R. P.; Hilliard, L. R.; Tan, W. H. *Langmuir* **2006,** *22*, 4357-4362.

Bagwe, R. P.; Yang, C. Y.; Hilliard, L. R.; Tan, W. H. *Langmuir* **2004,** *20*, 8336-8342.

Bao, J.; Chen, W.; Liu, T. T.; Zhu, Y. L.; Jin, P. Y.; Wang, L. Y.; Liu, J. F.; Wei, Y. G.; Li, Y. D. *ACS Nano* **2007,** *1*, 293-298.

Bartlett, P.; Ottewill, R. H.; Pusey, P. N. *Phys. Rev. Lett.* **1992,** *68*, 3801-3804.

Baughman, R. H.; Zakhidov, A. A.; de Heer, W. A., *Science* **2002**, *297*, 787.

Bigioni, T. P.; Lin, X. M.; Nguyen, T. T.; Corwin, E. I.; Witten, T. A.; Jaeger, H. M. *Nat. Mater.* **2006,** *5*, 265-270.

Binary Alloy Phase Diagrams. 2nd ed.; ASM International: Materials Park, OH, 1990; Vol. 1.

Bloembergen, N.; Purcell, E. M.; Pound, R. V. *Curr. Cont.* **1977,** 7.

Bohren, C. F.; Huffman, D. F., *Absorption and Scattering of Light by Small Particles*. Wiley: New York, 1983.

Bosworth, J. K.; M. Y. Paik; Ruiz, R.; Schwartz, E. L.; Huang, J. Q.; Ko, A. W.; Smilgies, D. M.; Black, C. T.; Ober, C. K. *ACS Nano* **2008**, 2, 1396-1402.

Bottini, M.; Cerignoli, F.; Mills, D. M.; D'Annibale, F.; Leone, M.; Rosato, N.; Magrini, A.; Pellecchia, M.; Bergamaschi, A.; Mustelin, T. *J. Am. Chem. Soc.* **2007,** *129*, 7814-7823.

Bravo, B. G.; Michelhaugh, S. L.; Soriaga, M. P.; Villegas, I.; Suggs, D. W.; Stickney, J. L. *J. Phys. Chem.* **1991,** *95*, 5245-5249.

Brust, M.; Walker, M.; Bethell, D.; Schiffrin, D. J.; Whyman, R. *Chem. Commun.* **1994**, 801-802.

Bulte, J. W. M.; Kraitchman, D. L. *NMR Biomed.* **2004,** *17*, 484-499.

Bunyakiat, K.; Makmee, S.; Sawangkeaw, R.; Ngamprasertsith, S., *Energy Fuels* **2006,** *20*, (2), 812-817.

Buonsanti, R.; Grillo, V.; Carlino, E.; Giannini, C.; Curri, M. L.; Innocenti, C.; Sangregorio, C.; Achterhold, K.; Parak, F. G.; Agostiano, A.; Cozzoli, P. D. *J. Am. Chem. Soc.* **2006,** *128*, 16953-16970.

Burda, C.; Chen, X.; Narayanan, R.; El-Sayed, M. A., *Chem. Rev.* **2005,** *105*, (4), 1025-1102.

Busbee, B. D.; Obare, S. O.; Murphy, C. J. *Adv. Mater.* **2003,** *15*, 414-416.

Bushong, S. *Magnetic Resonance Imaging: Physical and Biological Principles.* The C.V. Mosby Company: St. Louis, 1988.

Calderon Moreno, J. M.; Yoshimura, M., *J. Am. Chem. Soc.* **2001**, *123*, 741.

Carbone, L.; Kudera, S.; Giannini, C.; Ciccarella, G.; Cingolani, R.; Cozzoli, P. D.; Manna, L. *J. Mater. Chem.* **2006,** *16*, 3952-3956.

Carbone, L.; Nobile, C.; De Giorgi, M.; Sala, F. D.; Morello, G.; Pompa, P.; Hytch, M.; Snoeck, E.; Fiore, A.; Franchini, I. R.; Nadasan, M.; Silvestre, A. F.; Chiodo, L.; Kudera, S.; Cingolani, R.; Krahne, R.; Manna, L. *Nano Lett.* **2007,** *7*, 2942-2950.

Chen, M.; Kim, J.; Liu, J. P.; Fan, H. Y.; Sun, S. H. *J. Am. Chem. Soc.* **2006,** *128*, 7132-7133.

Chen, M.; Liu, J. P.; Sun, S. H. *J. Am. Chem. Soc.* **2004,** *126*, 8394-8395.

Chen, X. L.; Zou, J. L.; Zhao, T. T.; Li, Z. B. *J. Fluores.* **2007,** *17*, 235-241.

Chen, Z. Y.; Moore, J.; Radtke, G.; Sirringhaus, H.; O'Brien, S. *J. Am. Chem. Soc.* **2007,** *129*, 15702-15709.

Chen, Z.; O'Brien, S. *ACS Nano* **2008**, *2*, 1219-1229.

Cheng, W. L.; Dong, S. J.; Wang, E. K. *Angew. Chem., Int. Ed.* **2003,** *42*, 449-452.

Cheon, J.; Park, J. I.; Choi, J. S.; Jun, Y. W.; Kim, S.; Kim, M. G.; Kim, Y. M.; Kim, Y. J. *Proc. Natl. Acad. Sci.* **2006,** *103*, 3023-3027.

Cheung, C. L.; Kurtz, A.; Park, H.; Lieber, C. M., *J. Phys. Chem. B.* **2002,** *106*, (10), 2429-2433.

Cho, E. C.; Xie, J. W.; Wurm, P. A.; Xia, Y. N. *Nano. Lett.* **2009**, *9*, 1080-1084.

Cho, K. S.; Talapin, D. V.; Gaschler, W.; Murray, C. B., *J. Am. Chem. Soc.* **2005,** *127*, (19), 7140-7147.

Choi, J. S.; Jun, Y. W.; Yeon, S. I.; Kim, H. C.; Shin, J. S.; Cheon, J. *J. Am. Chem. Soc.* **2006,** *128*, 15982-15983.

Chu, T. C.; Shieh, F.; Lavery, L. A.; Levy, M.; Richards-Kortum, R.; Korgel, B. A.; Ellington, A. D. *Biosens. Bioelectron.* **2006,** *21*, 1859-1866.

Collier, C. P.; Vossmeyer, T.; Heath, J. R. *Annu. Rev. Phys. Chem.* **1998,** *49*, 371-404.

Connor, E. E.; Mwamuka, J.; Gole, A.; Murphy, C. J.; Wyatt, M. D. *Small* **2005,** *1*, 325-327.

Cordente, N.; Respaud, M.; Senocq, F.; Casanove, M.-J.; Amiens, C.; Chaudret, B. **2001,** *1*, 565-568.

Cortesi, R.; Esposito, E.; Menegatti, E.; Gambari, R.; Nastruzzi, C. *Int. J. Pharm.* **1996,** *139*, 69-78.

Cottin, X.; Monson, P. A., *J. Chem. Phys.* **1995,** *102*, (8), 3354-3360.

Cozzoli, P. D.; Pellegrino, T.; Manna, L. *Chem. Soc. Rev.* **2006,** *35*, 1195-1208.

Cui, H.; Eres, G.; Howe, J. Y.; Puretkzy, A.; Varela, M.; Geohegan, D. B.; Lowndes, D. H., *Chem. Phys. Lett.* **2003**, *374*, 222.

Dai, H. J., *Acc. Chem. Res.* **2002,** *35*, (12), 1035-1044.

Dai, H.; Rinzler, A. G.; Nikolaev, P.; Thess, A.; Colbert, D. T.; Smalley, R. E., *Chem. Phys. Lett.* **1996,** *260*, (3-4), 471-475.

Deck, C. P.; Vecchio, K. S., *J. Phys. Chem. B* **2005**, *109*, 12353.

Deng, T.; Li, J. S.; Jiang, J. H.; Shen, G. L.; Yu, R. Q. *Adv. Funct. Mater.* **2006,** *16*, 2147-2155.

Ding, H.; Yong, K. T.; Roy, I.; Pudavar, H. E.; Law, W. C.; Bergey, E. J.; Prasad, P. N. *J. Phys. Chem. C* **2007,** *111*, 12552-12557.

Dresselhaus, M. S.; Dresselhaus, G.; Avouris, P., *Carbon Nanotubes: Synthesis, Structure, Properties, and Applications*. Springer: New York, 2002.

Dubertret, B.; Skourides, P.; Norris, D. J.; Noireaux, V.; Brivanlou, A. H.; Libchaber, A. *Science* **2002,** *298*, 1759-1762.

Duguet, E.; Vasseur, S.; Mornet, S.; Devoisselle, J. M. *Nanomed.* **2006,** *1*, 157-168.

Dunphy, D.; Fan, H.; Li, X.; Wang, J.; Brinker, C. J. *Langmuir* **2008**; *24*, 10575-10578.

Durr, N. J.; Larson, T.; Smith, D. K.; Korgel, B. A.; Sokolov, K.; Ben-Yakar, A., *Nano Lett.* **2007,** *7*, (4), 941-945.

Ebbesen, T. W.; Ajayan, P. M., *Nature* **1992**, *358*, 220.

Figuerola, A.; Fiore, A.; Di Corato, R.; Falqui, A.; Giannini, C.; Micotti, E.; Lascialfari, A.; Corti, M.; Cingolani, R.; Pellegrino, T.; Cozzoli, P. D.; Manna, L. *J. Am. Chem. Soc.* **2008,** *130*, 1477-1487.

Figuerola, A.; Franchini, I. R.; Fiore, A.; Mastria, R.; Falqui, A.; Bertoni, G.; Bals, S.; Van Tendeloo, G.; Kudera, S.; Cingolani, R.; Manna, L. *Adv. Mater.* **2009,** *21*, 550-554.

Fu, A. H.; Gu, W. W.; Boussert, B.; Koski, K.; Gerion, D.; Manna, L.; Le Gros, M.; Larabell, C. A.; Alivisatos, A. P. *Nano Lett.* **2007,** *7*, 179-182.

Futaba, D. N.; Hata, K.; Yamada, T.; Mizuno, K.; Yumura, M.; Iijima, S., *Phys. Rev. Lett.* **2005**, *95*, 056104.

Gans, R., *Ann. Phys.* **1915,** *47*, 270-84.

Gao, J. X.; Bender, C. M.; Murphy, C. J. *Langmuir* **2003,** *19*, 9065-9070.

Gao, X. P.; Edens, G. J.; Liu, F. C.; Hamelin, A.; Weaver, M. J. *J. Phys. Chem.* **1994,** *98*, 8086-8095.

Gao, X. P.; Edens, G. J.; Weaver, M. J. *J. Phys. Chem.* **1994,** *98*, 8074-8085.

Gao, X. P.; Weaver, M. J. *J. Am. Chem. Soc.* **1992,** *114*, 8544-8551.

Gelbart, W. M.; Ben-Shaul, A. *J. Phys. Chem.* **1996**, *100*, 13169-13189.

Gobin, A. M.; Lee, M. H.; Halas, N. J.; James, W. D.; Drezek, R. A.; West, J. L. *Nano Lett.* **2007,** *7*, 1929-1934.

Gogotsi, Y.; Libera, J. A.; Yoshimura, M., *J. Mater. Res.* **2000**, *15*, 2591.

Gole, A.; Murphy, C. J. *Chem. Mater.* **2004,** *16*, 3633-3640.

Gole, A.; Murphy, C. J. *Chem. Mater.* **2005,** *17*, 1325-1330.

Gole, A.; Murphy, C. J. *Langmuir* **2005,** *21*, 10756-10762.

Gorelikov, I.; Matsuura, N. *Nano Lett.* **2008,** *8*, 369-373.

Goto, H.; Furuta, T.; Fujiwara, Y.; Ohashi, T. Method of purifying single wall carbon nanotubes from metal catalyst impurities. U.S. Patent Application 20030007924, January 9, 2003.

Gou, L. F.; Murphy, C. J. *Chem. Mater.* **2005,** *17*, 3668-3672.

Gruner, S. M.; Tate, M. W.; Eikenberry, E. F. *Rev. Sci. Instrum.* **2002,** *73*, 2815-2842.

Grzelczak, M.; Perez-Juste, J.; Mulvaney, P.; Liz-Marzan, L. M. *Chem. Soc. Rev.* **2008,** *37*, 1783-1791.

Grzelczak, M.; Perez-Juste, J.; Rodriguez-Gonzalez, B.; Liz-Marzan, L. M. *J. Mater. Chem.* **2006,** *16*, 3946-3951.

Grzelczak, M.; Sanchez-Iglesias, A.; Rodriguez-Gonzalez, B.; Alvarez-Puebla, R.; Perez-Juste, J.; Liz-Marzan, L. M. *Adv. Funct. Mater.* **2008,** *18*, 3780-3786.

Guo, T.; Nikolaev, P.; Thess, A.; Colbert, D. T.; Smalley, R. E., *Chem. Phys. Lett.* **1995,** *243*, (1-2), 49-54.

Gupta, A. K.; Naregalkar, R. R.; Vaidya, V. D.; Gupta, M. *Nanomed.* **2007,** *2*, 23-39.

Gur, I.; Fromer, N. A.; Geier, M. L.; Alivisatos, A. P. *Science* **2005,** *310*, 462-465.

Ha, T. H.; Koo, H. J.; Chung, B. H. *J. Phys. Chem. C* **2007,** *111*, 1123-1130.

Hammersley, A.P. ESRF Internal Report, **1997,** *ESRF97HA02T*.

Hanrath, T.; Korgel, B. A., *J. Amer. Chem. Soc.* **2002,** *124*, (7), 1424-1429.

Holmes, J. D.; Johnston, K. P.; Doty, R. C.; Korgel, B. A., *Science* **2000,** *287*, (5457), 1471-1473.

Hu, F. Q.; Wei, L.; Zhou, Z.; Ran, Y. L.; Li, Z.; Gao, M. Y. *Adv. Mater.* **2006,** *18*, 2553-2556.

Hu, G.; Cheng, M.; Ma, D.; Bao, X., *Chem. Mater.* **2003**, *15*, 1470.

Hu, J. T.; Odom, T. W.; Lieber, C. M., *Acc. Chem. Res.* **1999,** *32*, (5), 435-445.

Hu, S.-H.; Liu, T.-Y.; Huang, H.-Y.; Liu, D.-M.; Chen, S.-Y. *Langmuir* **2008,** *24*, 239-44.

Huang, X. H.; El-Sayed, I. H.; Qian, W.; El-Sayed, M. A. *Nano Lett.* **2007,** *7*, 1591-1597.

Huang, X. H.; El-Sayed, I. H.; Qian, W.; El-Sayed, M. A., *J. Am. Chem. Soc.* **2006,** *128*, (6), 2115-2120.

Hubert, F.; Testard, F.; Spalla, O. *Langmuir* **2008,** *24*, 9219-9222.

Huh, Y. M.; Jun, Y. W.; Song, H. T.; Kim, S.; Choi, J. S.; Lee, J. H.; Yoon, S.; Kim, K. S.; Shin, J. S.; Suh, J. S.; Cheon, J., *J. Am. Chem. Soc.* **2005,** *127*, (35), 12387-12391.

Hyeon, T.; Lee, S. S.; Park, J.; Chung, Y.; Bin Na, H. *J. Am. Chem. Soc.* **2001,** *123*, 12798-12801.

Iijima, S., *Nature* **1991,** *354*, (6348), 56-58.

Iijima, S.; Ajayan, P. M.; Ichihashi, T., *Phys. Rev. Lett.* **1992**, *69*, 3100.

Iijima, S.; Ishihashi, T.; Ando, Y., *Nature* **1992**, *356*, 776.

Iqbal, M.; Chung, Y. I.; Tae, G. *J. Mater. Chem.* **2007,** *17*, 335-342.

Israelachvili, J. *Intermolecular & Surface Forces* (2nd ed., Academic Press, San Diego, CA, 1992).

Jaiswal, J. K.; Goldman, E. R.; Mattoussi, H.; Simon, S. M. *Nat. Methods* **2004,** *1*, 73-78.

Jana, N. R.; Gearheart, L.; Murphy, C. J. *Adv. Mater.* **2001,** *13*, 1389-1393.

Jana, N. R.; Gearheart, L.; Murphy, C. J. *J. Phys. Chem. B* **2001,** *105*, 4065-4067.

Jebb, M.; Sudeep, P. K.; Pramod, P.; Thomas, K. G.; Kamat, P. V. *J. Phys. Chem. B* **2007,** *111*, 6839-6844.

Ji, X. J.; Shao, R. P.; Elliott, A. M.; Stafford, R. J.; Esparza-Coss, E.; Bankson, J. A.; Liang, G.; Luo, Z. P.; Park, K.; Markert, J. T.; Li, C. *J. Phys. Chem. C* **2007,** *111*, 6245-6251.

Jiang, X. C.; Brioude, A.; Pileni, M. P. *Colloids Surface* **2006,** *277*, 201-206.

Jiang, X. C.; Pileni, M. P. *Colloid Surface A* **2007,** *295*, 228-232.

Jiang, Y.; Wu, Y.; Zhang, S.; Xu, C.; Yu, W.; Xie, Y.; Qian, Y., *J. Am. Chem. Soc.* **2000**, *122*, 12383.

Johnson, C. J.; Dujardin, E.; Davis, S. A.; Murphy, C. J.; Mann, S. *J. Mater. Chem.* **2002,** *12*, 1765-1770.

Jun, Y. W.; Choi, J. S.; Cheon, J. *Angew. Chem., Int. Ed.* **2006,** *45*, 3414-3439.

Jun, Y. W.; Huh, Y. M.; Choi, J. S.; Lee, J. H.; Song, H. T.; Kim, S.; Yoon, S.; Kim, K. S.; Shin, J. S.; Suh, J. S.; Cheon, J. *J. Am. Chem. Soc.* **2005,** *127*, 5732-5733.

Kan, S.; Mokari, T.; Rothenberg, E.; Banin, U. *Nat. Mater.* **2003,** *2*, 155-158.

Kanzow, H.; Ding, A., *Phys. Rev. B* **1999**, *60*, 11180.

Khanal, B. P.; Zubarev, E. R. *Angew. Chem. Int. Edit.* **2007,** *46*, 2195-2198.

Kiely, C. J.; Fink, J.; Brust, M.; Bethell, D.; Schiffrin, D. J. *Nature* **1998,** *396*, 444-446.

Kim, J. S.; Rieter, W. J.; Taylor, K. M. L.; An, H.; Lin, W. L.; Lin, W. B. *J. Am. Chem. Soc.* **2007,** *129*, 8962-8963.

Koenig, S. H. *Invest. Radiol.* **1998,** *33*, 822-827.

Koenig, S. H.; Kellar, K. E. *Magn. Reson. Med.* **1995,** *34*, 227-233.

Koenig, S. H.; Schillin, W. *J. Biol. Chem.* **1969,** *244*, 6520-6526.

Korgel, B. A.; Fitzmaurice, D. *Phys. Rev. B* **1999**, *59*, 14191-14201.

Korgel, B. A.; Fullam, S.; Connolly, S.; Fitzmaurice, D. *J. Phys. Chem. B* **1998,** *102*, 8379-8388.

Kotz, J. C.; Treichel, P., *Chemistry and Chemical Reactivity*. 3rd ed.; Saunders College Publishing: Fort Worth, 1996; p 619.

Kou, X. S.; Zhang, S. Z.; Tsung, C. K.; Yang, Z.; Yeung, M. H.; Stucky, G. D.; Sun, L. D.; Wang, J. F.; Yan, C. H. *Chem-Eur. J.* **2007,** *13*, 2929-2936.

Kudera, S.; Carbone, L.; Casula, M. F.; Cingolani, R.; Falqui, A.; Snoeck, E.; Parak, W. J.; Manna, L. *Nano Lett.* **2005,** *5*, 445-449.

Kuperman, V. *MRI: Physical Principles and Applications*. Academic Press: Chicago, Illinois, 2000.

Kwon, K. W.; Lee, B. H.; Shim, M. *Chem. Mater.* **2006,** *18*, 6357-6363.

Kwon, S. G.; Hyeon, T. *Acc. Chem. Res.* **2008,** *41*, 1696-1709.

Lee, C. J.; Park, J. H.; Park, J., *Chem. Phys. Lett.* **2000**, *323*, 560.

Lee, C. J.; Park, J., *Appl. Phys. Lett.* **2000**, *77*, 3397.

Lee, C. J.; Park, J., *J. Phys. Chem. B* **2001**, *105*, 2365.

Lee, D. C.; Korgel, B. A., *Mol. Simul.* **2005**, *31*, 637.

Lee, D. C.; Mikulec, F. V.; Korgel, B. A., *J. Am. Chem. Soc.* **2004**, *126*, 4951.

Lee, D. C.; Mikulec, F. V.; Pelaez, J. M.; Koo, B.; Korgel, B. A. *J. Phys. Chem. B* **2006,** *110*, 11160-11166.

Lee, D. C.; Smith, D. K.; Heitsch, A. T.; Korgel, B. A. *Annu. Rep. Prog. Chem., Sect. C, Phys. Chem.* **2007,** *103*, 351-402.

Lee, G.-W.; Kumar, S., *J. Phys. Chem. B* **2005**, *109*, 17128.

Lee, J. H.; Huh, Y. M.; Jun, Y.; Seo, J.; Jang, J.; Song, H. T.; Kim, S.; Cho, E. J.; Yoon, H. G.; Suh, J. S.; Cheon, J. *Nat. Med.* **2007,** *13*, 95-99.

Lee, J. H.; Jun, Y. W.; Yeon, S. I.; Shin, J. S.; Cheon, J. *Angew. Chem., Int. Ed.* **2006,** *45*, 8160-8162.

Lee, S. M.; Cho, S. N.; Cheon, J. *Adv. Mater.* **2003,** *15*, 441-444.

Li, Y. M.; Kim, W.; Zhang, Y. G.; Rolandi, M.; Wang, D. W.; Dai, H. J., *J. Phys. Chem. B* **2001**, *105*, 11424.

Li, Y.; Liu, J.; Wang, Y. Q.; Wang, Z. L., *Chem. Mater.* **2001**, *13*, 1008.

Libera, J.; Gogotsi, Y., *Carbon* **2001**, *39*, 1307.

Lim, Y. T.; Kim, S.; Nakayama, A.; Stott, N. E.; Bawendi, M. G.; Frangioni, J. V. *Mol. Imaging* **2003,** *2*, 50-64.

Lin, Y. S.; Wu, S. H.; Hung, Y.; Chou, Y. H.; Chang, C.; Lin, M. L.; Tsai, C. P.; Mou, C. Y. *Chem. Mater.* **2006,** *18*, 5170-5172.

Link, S.; El-Sayed, M. A., *Annu. Rev. Phys. Chem.* **2003,** *54*, (1), 331.

Link, S.; Mohamed, M. B.; El-Sayed, M. A., *J. Phys. Chem. B* **1999,** *103*, (16), 3073-3077.

Liu, J.; Shao, M.; Chen, X.; Yu, W.; Liu, X.; Qian, Y., *J. Am. Chem. Soc.* **2003**, *125*, 8088.

Liu, J.; Xu, L.; Zhang, W.; Lin, W. J.; Chen, X.; Wang, Z.; Qian, Y., *J. Phys. Chem. B* **2004**, *108*, 20090.

Liu, M. Z.; Guyot-Sionnest, P. *J. Phys. Chem. B* **2005,** *109*, 22192-22200.

Liz-Marzan, L. M. *Mat. Today* **2004,** *7*, 26-31.

Liz-Marzan, L. M.; Giersig, M.; Mulvaney, P., *Langmuir* **1996,** *12*, (18), 4329-4335.

Lofton, C.; Sigmund, W. *Adv. Funct. Mater.* **2005,** *15*, 1197-1208.

Louchev, O. A., *Phys. Status Solidi A* **2002**, *193*, 585.

Louchev, O. A.; Hester, J. R., *J. Appl. Phys.* **2003,** *94*, (3), 2002-2010.

Lu, C. W.; Hung, Y.; Hsiao, J. K.; Yao, M.; Chung, T. H.; Lin, Y. S.; Wu, S. H.; Hsu, S. C.; Liu, H. M.; Mou, C. Y.; Yang, C. S.; Huang, D. M.; Chen, Y. C. *Nano Lett.* **2007,** *7*, 149-154.

Lu, C.; Chen, Z.; O'Brien, S. *Chem. Mater.* **2008,** *20*, 3594-3600.

Lu, X.; Hanrath, T.; Johnston, K. P.; Korgel, B. A., *Nano Lett.* **2003**, *3*, 93.

Luedtke, W. D.; Landman, U. *J. Phys. Chem.* **1996**, *100*, 13323-13329.

Maruyama, S.; Kojima, R.; Miyauchi, Y.; Chiashi, S.; Kohno, M., *Chem. Phys. Lett.* **2002**, *360*, 229.

McCarley, R. L.; Bard, A. J. *J. Phys. Chem.* **1991,** *95*, 9618-9620.

McGrew, K. J.; Murphy, J. W. Iodine leach for the dissolution of gold. US Patent 4557759, **1985**.

McKee, G. S. B.; Vecchio, K. S., *J. Phys. Chem. B* **2006**, *110*, 1179.

Meyyappan, M., *Carbon Nanotubes: Handbook of Nanoscience, Engineering, and Technology.* CRC Press: Boca Raton, 2003.

Meyyappan, M.; Delzeit, L.; Cassell, A.; Hash, D., *Plasma Sources Sci. Technol.* **2003**, *12*, 205.

Michalet, X.; Pinaud, F. F.; Bentolila, L. A.; Tsay, J. M.; Doose, S.; Li, J. J.; Sundaresan, G.; Wu, A. M.; Gambhir, S. S.; Weiss, S. *Science* **2005,** *307*, 538-544.

Mie, G., *Ann. Phys.* **1908,** *25*, 377-455.

Millstone, J. E.; Wei, W.; Jones, M. R.; Yoo, H. J.; Mirkin, C. A. *Nano Lett.* **2008,** *8*, 2526-2529.

Miranda, O. R.; Dollahon, N. R.; Ahmadi, T. S. *Cryst. Growth Des.* **2006,** *6*, 2747-2753.

Mirska, D.; Schirmer, K.; Funari, S. S.; Langer, A.; Dobner, B.; Brezesinski, G., *Colloids Surf., B* **2005,** *40*, (1), 51-59.

Mizuno, K.; Hata, K.; Saito, T.; Ohshima, S.; Yumura, M.; Iijima, S., *J. Phys. Chem. B* **2005**, *109*, 2632.

Murphy, C. J.; Sau, T. K.; Gole, A. M.; Orendorff, C. J.; Gao, J.; Gou, L.; Hunyadi, S. E.; Li, T. *J. Phys. Chem. B* **2005,** *109*, 13857-13870.

Murray, C. B.; Norris, D. J.; Bawendi, M. G. *J. Am. Chem. Soc.* **1993,** *115*, 8706-8715.

Murray, M. J.; Sanders, J. V. *Philos. Mag. A* **1980,** *42*, 721-740.

Murray, M. J.; Sanders, J. V., *Philos. Mag.* **1980,** *42*, (6), 721-40.

Nikoobakht, B.; El-Sayed, M. A. *Chem. Mater.* **2003,** *15*, 1957-1962.

Nikoobakht, B.; El-Sayed, M. A. *Langmuir* **2001,** *17*, 6368-6374.

Niidome, Y.; Nakamura, Y.; Honda, K.; Akiyama, Y.; Nishioka, K.; Kawasaki, H.; Nakashima, N. *Chem. Commun.* **2009,** *13*, 1754-1756.

Nolan, P. E.; Schabel, M. J.; Lynch, D. C., *Carbon* **1995**, *33*, 79.

Orendorff, C. J.; Hankins, P. L.; Murphy, C. J. *Langmuir* **2005,** *21*, 2022-2026.

Orendorff, C. J.; Murphy, C. J. *J. Phys. Chem. B* **2006,** *110*, 3990-3994.

Ouyang, M.; Huang, J. L.; Lieber, C. M., *Acc. Chem. Res.* **2002,** *35*, (12), 1018-1025.

Overgaag, K.; Evers, W.; de Nijs, B.; Koole, R.; Meeldijk, J.; Vanmaekelbergh, D. *J. Am. Chem. Soc.* **2008,** *130*, 7833-7835.

Ow, H.; Larson, D. R.; Srivastava, M.; Baird, B. A.; Webb, W. W.; Wiesner, U. *Nano Lett.* **2005,** *5*, 113-117.

Pal, T.; Jana, N. R.; Sau, T. K. *Corros. Sci.* **1997,** *39*, 981-986.

Park, H. J.; Ah, C. S.; Kim, W. J.; Choi, I. S.; Lee, K. P.; Yun, W. S. *J. Vac. Sci. Technol. A* **2006,** *24*, 1323-1326.

Park, J.; Koo, B.; Yoon, K. Y.; Hwang, Y.; Kang, M.; Park, J.-G.; Hyeon, T. **2005,** *127*, 8433-8440.

Pastoriza-Santos, I.; Perez-Juste, J.; Liz-Marzan, L. M. *Chem. Mater.* **2006,** *18*, 2465-2467.

Pellegrino, T.; Fiore, A.; Carlino, E.; Giannini, C.; Cozzoli, P. D.; Ciccarella, G.; Respaud, M.; Palmirotta, L.; Cingolani, R.; Manna, L. *J. Am. Chem. Soc.* **2006,** *128*, 6690-6698.

Peng, X. G. *Adv. Mater.* **2003,** *15*, 459-463.

Peng, X. G.; Manna, L.; Yang, W. D.; Wickham, J.; Scher, E.; Kadavanich, A.; Alivisatos, A. P. *Nature* **2000,** *404*, 59-61.

Peng, Z. A.; Peng, X. G. *J. Am. Chem. Soc.* **2002,** *124*, 3343-3353.

Perez-Juste, J.; Liz-Marzan, L. M.; Carnie, S.; Chan, D. Y. C.; Mulvaney, P. *Adv. Funct. Mater.* **2004,** *14*, 571-579.

Pierrat, S.; Zins, I.; Breivogel, A.; Sonnichsen, C. *Nano Lett.* **2007,** *7*, 259-263.

Puntes, V. F.; Zanchet, D.; Erdonmez, C. K.; Alivisatos, A. P., *J. Am. Chem. Soc.* **2002**, *124*, 12874.

Qin, J.; Laurent, S.; Jo, Y. S.; Roch, A.; Mikhaylova, M.; Bhujwalla, Z. M.; Muller, R. N.; Muhammed, M. *Adv. Mater.* **2007,** *19*, 1874-1878.

Qin, L. C., *J. Mater. Sci. Lett.* **1997**, *16*, 457.

Quarta, A.; Di Corato, R.; Manna, L.; Ragusa, A.; Pellegrino, T. *IEEE T. Nanobiosci.* **2007,** *6*, 298-308.

Rabideau, B. D.; Bonnecaze, R. T. *Langmuir* **2004,** *20*, 9408-9414.

Rai, A.; Singh, A.; Ahmad, A.; Sastry, M. *Langmuir* **2006,** *22*, 736-741.

Rao, C. N. R.; Govindaraj, A.; Sen, R.; Satishkumar, B. C., *Mater. Res. Innovations* **1998**, *2*, 128.

Redl, F. X.; Cho, K. S.; Murray, C. B.; O'Brien, S., *Nature* **2003,** *423*, (6943), 968-971.

Rodriguez-Fernandez, J.; Perez-Juste, J.; Mulvaney, P.; Liz-Marzan, L. M. *J. Phys. Chem. B* **2005,** *109*, 14257-14261.

Rogach, A. L. *Angew. Chem., Int. Ed.* **2004,** *43*, 148-149.

Ruland, W.; Smarsly, B. M.; *J. Appl. Crystallogr.* **2007**, 40, 409-417.

Ruoff, R. S.; Lorents, D. C., *Carbon* **1995**, *33*, 925.

Santra, S.; Tapec, R.; Theodoropoulou, N.; Dobson, J.; Hebard, A.; Tan, W. H. *Langmuir* **2001,** *17*, 2900-2906.

Santra, S.; Wang, K. M.; Tapec, R.; Tan, W. H. *J. Biomed. Optics* **2001,** *6*, 160-166.

Santra, S.; Yang, H. S.; Holloway, P. H.; Stanley, J. T.; Mericle, R. A. *J. Am. Chem. Soc.* **2005,** *127*, 1656-1657.

Santra, S.; Zhang, P.; Wang, K. M.; Tapec, R.; Tan, W. H. *Anal. Chem.* **2001,** *73*, 4988-4993.

Satishkumar, B. C.; Govindaraj, A.; Sen, R.; Rao, C. N. R., *Chem. Phys. Lett.* **1998**, *293*, 47.

Sau, T. K.; Murphy, C. J. *Langmuir* **2004,** *20*, 6414-6420.

Saunders, A. E.; Korgel, B. A. *ChemPhysChem* **2005,** *6*, 61-65.

Saunders, A. E.; Sigman, M. B.; Korgel, B. A. **2004,** *108*, 193-199.

Schaaff, T. G.; Shafigullin, M. N.; Khoury, J. T.; Vezmar, I.; Whetten, R. L.; Cullen, W. G.; First, P. N.; Gutierrez-Wing, C.; Ascensio, J.; Jose-Yacaman, M. J., *J. Phys. Chem. B* **1997,** *101*, (40), 7885-7891.

Schofield, A. B.; Pusey, P. N.; Radcliffe, P. *Phys. Rev. E* **2005,** *72*, 031407.

Schwartzberg, A. M.; Zhang, J. Z., *J. Phys. Chem. C* **2008,** *112*, (28), 10323-10337.

Selvan, S. T.; Patra, P. K.; Ang, C. Y.; Ying, J. Y., *Angew. Chem.* **2007,** *46*, (14), 2448-2452.

Seo, J.-w.; Jun, Y.-w.; Ko, S. J.; Cheon, J. **2005,** *109*, 5389-5391.

Shah, P. S.; Hanrath, T.; Johnston, K. P.; Korgel, B. A., *J. Phys. Chem. B* **2004**, *108*, 9574.

Shah, P. S.; Husain, S.; Johnston, K. P.; Korgel, B. A. **2001,** *105*, 9433-9440.

Shevchenko, E. V.; Kortright, J. B.; Talapin, D. V.; Aloni, S.; Alivisatos, A. P. *Adv. Mater.* **2007,** *19*, 4183-4188.

Shevchenko, E. V.; Ringler, M.; Schwemer, A.; Talapin, D. V.; Klar, T. A.; Rogach, A. L.; Feldmann, J.; Alivisatos, A. P. *J. Am. Chem. Soc.* **2008,** *130*, 3274-3275.

Shevchenko, E. V.; Talapin, D. V.; Kotov, N. A.; O'Brien, S.; Murray, C. B. *Nature* **2006,** *439*, 55-59.

Shevchenko, E. V.; Talapin, D. V.; Murray, C. B.; O'Brien, S. *J. Am. Chem. Soc.* **2006,** *128*, 3620-3637.

Shevchenko, E. V.; Talapin, D. V.; O'Brien, S.; Murray, C. B. *J. Am. Chem. Soc.* **2005,** *127*, 8741-8747.

Shi, W. L.; Zeng, H.; Sahoo, Y.; Ohulchanskyy, T. Y.; Ding, Y.; Wang, Z. L.; Swihart, M.; Prasad, P. N. *Nano Lett.* **2006,** *6*, 875-881.

Shieh, F.; Saunders, A. E.; Korgel, B. A. *J. Phys. Chem. B* **2005,** *109*, 8538-8542.

Sibbald, M. S.; Chumanov, G.; Cotton, T. M. *J. Phys. Chem.* **1996,** *100*, 4672-4678.

Sigman, M. B.; Saunders, A. E.; Korgel, B. A. *Langmuir* **2004,** *20*, 978-983.

Singh, S.; Pasricha, R.; Bhatta, U. M.; Satyam, P. V.; Sastry, M.; Prasad, B. L. V. *J. Mater. Chem.* **2007,** *17*, 1614-1619.

Smith, D. K.; Korgel, B. A. *Langmuir* **2008,** *24*, 644-649.

Smith, D. K.; Rasch, M. R.; Korgel, B. A. *Nanomed.* **2007,** *2*, 943-9.

Sokolov, K.; Nida, D.; Descour, M.; Lacy, A.; Levy, M.; Hall, B.; Dharmawardhane, S.; Ellington, A.; Korgel, B.; Richards-Kortum, R., In *Adv. Cancer Res.*, 2007; Vol. 96, pp 299-344.

Song, H. T.; Choi, J. S.; Huh, Y. M.; Kim, S.; Jun, Y. W.; Suh, J. S.; Cheon, J. *J. Am. Chem. Soc.* **2005,** *127*, 9992-9993.

Spuch-Calvar, M.; Perez-Juste, J.; Liz-Marzan, L. M. *J. Colloid Interface Sci.* **2007,** *310*, 297-301.

Stewart, M. E.; Anderton, C. R.; Thompson, L. B.; Maria, J.; Gray, S. K.; Rogers, J. A.; Nuzzo, R. G. *Chemical Reviews* **2008,** *108*, 494-521.

Stöber, W.; Fink, A.; Bohn, E. *J. Colloid Interface Sci.* **1968,** *26*, 62-9.

Stowell, C. A.; Korgel, B. A., *Nano Lett.* **2005**, *5*, 1203.

Suchanek, W. L.; Libera, J. A.; Gogotsi, Y.; Yoshimura, M., *J. Solid State Chem.* **2001**, *160*, 184.

Tago, T.; Hatsuta, T.; Miyajima, K.; Kishida, M.; Tashiro, S.; Wakabayashi, K. *J. Am. Ceram. Soc.* **2002,** *85*, 2188-2194.

Tao, N. J.; Lindsay, S. M. *J. Phys. Chem.* **1992,** *96*, 5213-5217.

Tate, M. P.; Urade, V. N.; Kowalski, J. D.; Wei, T. C.; Hamilton, B. D.; Eggiman, B. W.; Hillhouse, H. W. *J. Phys. Chem. B* **2006,** *110*, 9882-9892.

Treacy, M. M. J.; Ebbesen, T. W.; Gibson, J. M., *Nature* **1996**, *381*, 678.

Tromsdorf, U. I.; Bigall, N. C.; Kaul, M. G.; Bruns, O. T.; Nikolic, M. S.; Mollwitz, B.; Sperling, R. A.; Reimer, R.; Hohenberg, H.; Parak, W. J.; Forster, S.; Beisiegel, U.; Adam, G.; Weller, H. *Nano Lett.* **2007,** *7*, 2422-2427.

Umeno, A.; Hirakawa, K. *Appl. Phys. Lett.* **2005,** *86*.

Urban, J. J.; Talapin, D. V.; Shevchenko, E. V.; Kagan, C. R.; Murray, C. B. *Nat. Mater.* **2007,** *6*, 115-121.

Vial, S.; Pastoriza-Santos, I.; Perez-Juste, J.; Liz-Marzan, L. M. *Langmuir* **2007,** *23*, 4606-4611.

Vivekchand, S. R. C.; Cele, L. M.; Deepak, F. L.; Raju, A. R.; Govindaraj, A., *Chem. Phys. Lett*. **2004**, *386*, 313.

Wan, J.; Cai, W.; Meng, X.; Liu, E. *Chem. Comm.* **2007,** 5004-5006.

Wang, C. G.; Wang, T. T.; Ma, Z. F.; Su, Z. M. *Nanotechnology* **2005,** *16*, 2555-2560.

Wang, F. D.; Tang, R.; Buhro, W. E. *Nano Lett.* **2008,** *8*, 3521-3524.

Wang, H. F.; Huff, T. B.; Zweifel, D. A.; He, W.; Low, P. S.; Wei, A.; Cheng, J. X. *Proc. Natl. Acad. Sci. U. S. A.* **2005,** *102*, 15752-15756.

Wang, J.; Li, Y. F.; Huang, C. Z. *J. Phys. Chem. C* **2008,** *112*, 11691-11695.

Wang, J. X.; Watson, G. M.; Ocko, B. M. *J. Phys. Chem.* **1996,** *100*, 6672-6677.

Wang, L.; O'Donoghue, M. B.; Tan, W. H. *Nanomed.* **2006,** *1*, 413-426.

Wang, L.; Tan, W. H. *Nano Lett.* **2006,** *6*, 84-88.

Wang, W.; Huang, J. Y.; Wang, D. Z.; Ren, Z. F., *Carbon* **2005**, *43*, 1328.

Wang, W.; Kunwar, S.; Huang, J. Y.; Wang, D. Z.; Ren, Z. F., *Nanotechnology* **2005**, *16*, 21.

Wang, X.; Lu, J.; Xie, Y.; Du, G.; Guo, Q.; Zhang, S., *J. Phys. Chem. B* **2002**, *106*, 933.

Wang, Y. X. J.; Hussain, S. M.; Krestin, G. P. *Eur. Radiol.* **2001,** *11*, 2319-2331.

Wang, Y. Y.; Tang, G. Y.; Koeck, F. M.; Brown, B.; Garguilo, J. M.; Nemanich, R. J., *Diamond Relat. Mater.* **2004**, *13*, 1287.

Weissleder, R., *Nat. Biotechnol.* **2001,** *19*, (4), 316-317.

Weissleder, R.; Elizondo, G.; Wittenberg, J.; Rabito, C. A.; Bengele, H. H.; Josephson, L. *Radiology* **1990,** *175*, 489-493.

Whetten, R. L.; Shafigullin, M. N.; Khoury, J. T.; Schaaff, T. G.; Vezmar, I.; Alvarez, M. M.; Wilkinson, A. *Acct. Chem. Res.* **1999**, *32*, 397-406.

Winter, J. O.; Liu, T. Y.; Korgel, B. A.; Schmidt, C. E. *Adv. Mater.* **2001,** *13*, 1673-1677.

Wu, H. Y.; Huang, W. L.; Huang, M. H. *Cryst. Growth Des.* **2007,** *7*, 831-835.

Xia, Y. N.; Halas, N. J., *MRS Bull.* **2005,** *30*, (5), 338-344.

Xing, Y.; Chaudry, Q.; Shen, C.; Kong, K. Y.; Zhau, H. E.; Wchung, L.; Petros, J. A.; O'Regan, R. M.; Yezhelyev, M. V.; Simons, J. W.; Wang, M. D.; Nie, S. *Nat. Protocols* **2007,** *2*, 1152-1165.

Yamamoto, S.; Morimoto, Y.; Tamada, Y.; Takahashi, Y. K.; Hono, K.; Ono, T.; Takano, M. *Chem. Mater.* **2006,** *18*, 5385-5388.

Yan, J. L.; Estevez, M. C.; Smith, J. E.; Wang, K. M.; He, X. X.; Wang, L.; Tan, W. H. *Nano Today* **2007,** *2*, 44-50.

Yang, H.; Deschatelets, P.; Brittain, S. T.; Whitesides, G. M. *Adv. Mater.* **2001,** *13*, 54-58.

Yang, Z. S.; Lin, Y. W.; Tseng, W. L.; Chang, H. T. *J. Mater. Chem.* **2005,** *15*, 2450-2454.

Yantasee, W.; Warner, C. L.; Sangvanich, T.; Addleman, R. S.; Carter, T. G.; Wiacek, R. J.; Fryxell, G. E.; Timchalk, C.; Warner, M. G. *Environ. Sci. Technol.* **2007,** *41*, 5114-5119.

Yao, G.; Wang, L.; Wu, Y. R.; Smith, J.; Xu, J. S.; Zhao, W. J.; Lee, E. J.; Tan, W. H. *Anal. Bioanal. Chem.* **2006,** *385*, 518-524.

Yavuz, C. T.; Mayo, J. T.; Yu, W. W.; Prakash, A.; Falkner, J. C.; Yean, S.; Cong, L. L.; Shipley, H. J.; Kan, A.; Tomson, M.; Natelson, D.; Colvin, V. L. *Science* **2006,** *314*, 964-967

Yaws, C. L., *Handbook of Thermodynamic Diagrams. Vol. 2: Organic Compounds C_5 to C_7.* Elsevier: Houston, 1996; Vol. 2.

Yi, D. K.; Lee, S. S.; Papaefthymiou, G. C.; Ying, J. Y. *Chem. Mater.* **2006,** *18*, 614-619.

Yin, Y.; Alivisatos, A. P. *Nature* **2005,** *437*, 664-670.

Yong, K.-T.; Sahoo, Y.; Choudhury, K. R.; Swihart, M. T.; Minter, J. R.; Prasad, P. N. **2006,** *6*, 709-714.

Yoshimatsu, N.; Kawasaki, T.; Ban, K.; Kusaka, T.; Ikeda, T. E. *J. Surf. Sci. Nanotechnol.* **2005,** *3*, 524-526.

Yu, C. X.; Irudayaraj, J. *Anal. Chem.* **2007,** *79*, 572-579.

Yu, C. X.; Nakshatri, H.; Irudayaraj, J. *Nano Lett.* **2007,** *7*, 2300-2306.

Yu, C. X.; Varghese, L.; Irudayaraj, J. *Langmuir* **2007,** *23*, 9114-9119.

Yu, H.; Chen, M.; Rice, P. M.; Wang, S. X.; White, R. L.; Sun, S. H. *Nano Lett.* **2005,** *5*, 379-382.

Zeng, H.; Li, J.; Liu, J. P.; Wang, Z. L.; Sun, S. H., *Nature* **2002,** *420*, (6914), 395-398.

Zhang, L. H.; Liu, B. F.; Dong, S. J. *J. Phys. Chem. B* **2007,** *111*, 10448-10452.

Zhang, M.; Yudasaka, M.; Iijima, S., *J. Phys. Chem. B* **2004**, *108*, 149.

Zhang, W.; Ma, D.; Liu, J.; Kong, L.; Yu, W.; Qian, Y., *Carbon* **2004**, *42*, 2341.

Zhang, X.; Sreekumar, T. V.; Liu, T.; Kumar, S., *J. Phys. Chem. B* **2004**, *108*, 16435.

Zhao, X. J.; Bagwe, R. P.; Tan, W. H., *Adv. Mater.* **2004,** *16*, (2), 173-176.

Zhao, X. J.; Hilliard, L. R.; Mechery, S. J.; Wang, Y. P.; Bagwe, R. P.; Jin, S. G.; Tan, W. H. *Proc. Natl. Acad. Sci. U. S. A.* **2004,** *101*, 15027-15032.

Zhao, X. J.; Tapec-Dytioco, R.; Tan, W. H. *J. Am. Chem. Soc.* **2003,** *125*, 11474-11475.

Ziman, J. M., *Theory of Solids*. University Press: Cambridge, 1979; p 278.

Zweifel, D. A.; Wei, A. *Chem. Mater.* **2005,** *17*, 4256-4261.

Vita

Danielle Kristin Smith graduated from Logan-Rogersville High School in 1998 and went on to attend the University of Missouri-Columbia in the fall of that year. She graduated *summa cum laude* with a Bachelor of Science in Chemical Engineering in May of 2003. Upon graduation, she accepted a job in the BioPharm division of the Paul Mueller Company in Springfield, MO. She worked there until her enrollment at the University of Texas at Austin in August of 2004. Danielle earned her Ph.D. while studying under the supervision of Dr. Brian Korgel in nanomaterials chemistry and engineering.

Permanent address: 3819 South Fairwood, Rogersville, MO 65742 USA

This dissertation was typed by the author.